Search for a cumulative neutrino flux from 2LAC-blazar populations using 3 years of IceCube data

DISSERTATION
zur Erlangung des akademischen Grades

doctor rerum naturalium
(Dr. rer. nat.)

im Fach Physik

eingereicht an der
Mathematisch-Naturwissenschaftlichen Fakultät
der Humboldt-Universität zu Berlin

von

Herrn Dipl.-Phys. Thorsten Glüsenkamp

Präsident der Humboldt-Universität zu Berlin
Prof. Dr. Jan-Hendrik Olbertz

Dekan der Mathematisch-Naturwissenschaftlichen Fakultät
Prof. Dr. Elmar Kulke

Gutachter:
1. Prof. Dr. Alexander Kappes
2. Prof. Dr. Lutz Köpke
3. Prof. Dr. Marek Kowalski

Tag der mündlichen Prüfung: 26.1. 2016

ZUSAMMENFASSUNG

Blazare sind aktive galaktische Kerne mit relativistischen Plasmajets, deren Symmetrieachse in Richtung Erde zeigt. Sie sind primäre Kandidaten für die Produktion von hochenergetischen Neutrinos.

Diese Arbeit umfasst die Suche nach einem kumulativen Neutrinofluss von allen 862 Fermi-LAT 2LAC Blazaren und vier spektral ausgewählten Unterpopulationen. Selektierte Myonspuren aus drei Jahren IceCubedaten werden mit einer ungebinnten "Stacking"-Punktquellenanalyse untersucht. Zwei unterschiedliche Gewichtungen werden benutzt, um den unbekannten relativen Anteil jeder Quelle am Gesamtneutrinofluss der jeweiligen Population zu berücksichtigen. Neun der zehn resultierenden Tests zeigen leichte Überfluktuationen, von denen keine statistisch signifikant ist. Das Ergebnis erlaubt es, den Maximalanteil der 2LAC-Blazare zum kürzlich entdeckten astrophysikalischen TeV-PeV Neutrinofluss auf 23% einzuschränken. Diese Grenze gilt unter der Annahme des momentan favorisierten Spektralindex des astrophysikalischen Neutrinoflusses von -2.5 und bei einem Flavorverhältnis von 1:1:1 bei Erreichen der Erde. Die Ergebnisse erfordern keine rein hadronische Produktion der beobachteten Gammastrahlung und bleiben, bis auf einen Faktor zwei, für moderat härtere Spektren oder für kleinere Unterpopulationen, wie z.b. die GeV-detektierten TeV-Cat Quellen, gültig.

Zusätzlich werden obere Flussgrenzen für generische Spektren, die einem Potenzgesetz folgen, sowie für konkrete spektrale Modelle der diffusen Neutrinoemission von Blazaren, ausgerechnet. 12 von 14 dieser Modelle können eingeschränkt oder ausgeschlossen werden.

Wenn die größte Überfluktuation als physikalischer Effekt interpretiert wird, findet man einen weichen Fluss in der 5-10 TeV Region, welcher mit Gammastrahlenbeobachtungen kompatibel ist. Mehr Daten sind bereits verfügbar und erlauben es, dieses Szenario in der nahen Zukunft zu testen. Falls es bestätigt wird, könnten Blazare der erste bekannte extragalaktische Ort hadronischer Beschleunigung werden.

ABSTRACT

Blazars are active galactic nuclei with relativistic plasma jets whose symmetry axis is pointing towards Earth. They are a prime source candidate for the production of high-energy neutrinos.

This work describes the search for a cumulative neutrino flux from all 862 Fermi-LAT 2LAC blazars and four spectrally defined sub-populations. Selected muon-track events from three years of IceCube data are analyzed with an unbinned likelihood stacking approach. Two different weighting schemes are used to account for the unknown relative flux contributions of each source. Nine of ten tests show slight overfluctuations, none of which are statistically significant. An upper flux limit is calculated constraining the maximal contribution of the 2LAC blazars to the recently discovered diffuse TeV-PeV neutrino flux to be 23% or less assuming the currently favored spectral index for the astrophysical flux of around -2.5 and an equal composition of neutrino flavors arriving at Earth. The results do not require a purely hadronic production of the observed gamma rays and remain valid for moderately harder spectra or smaller sub-populations, e.g. the TeVCat sub-sample, up to a factor of around 2.

Additionally, upper limits are calculated for generic power-law spectra and for concrete spectral models of the diffuse neutrino emission of blazar populations. 12 out of 14 of these models are either constrained or excluded.

If the largest overfluctuation is interpreted as a physics effect, one finds a soft flux in the 5-10 TeV region that is compatible with gamma-ray observations. Further years of data are already available which makes this scenario testable in the near future. If confirmed, blazars might become the first known extragalactic hadronic acceleration site.

CONTENTS

1 OVERVIEW 1

2 COSMIC MESSENGER PARTICLES 5
- 2.1 Cosmic rays 5
- 2.2 Photons 11
- 2.3 Neutrinos 15
- 2.4 Complementarity 17

3 BLAZARS 21
- 3.1 Astronomical classification 21
- 3.2 Blazars in the unified picture of AGN 22
- 3.3 Spectral energy distribution 25
- 3.4 Luminosity function, source counts and cosmic evolution 28
- 3.5 Neutrino emission 30

4 THE ICECUBE NEUTRINO OBSERVATORY 37
- 4.1 Neutrino detection fundamentals 37
  - 4.1.1 Neutrino interactions 37
  - 4.1.2 Energy losses and Cherenkov light 38
  - 4.1.3 Event signatures 41
    - 4.1.3.1 Neutrino-induced events 41
    - 4.1.3.2 Atmospheric muons 43
- 4.2 The detector 44
  - 4.2.1 Construction 44
  - 4.2.2 Properties of the Antarctic ice 46
  - 4.2.3 Data acquisition and data processing 48
- 4.3 Software and simulation 50

5 ANALYSIS OVERVIEW 53
- 5.1 Scientific questions 53
- 5.2 The "stacking" approach 53
- 5.3 Differences to previous blazar stackings 54
- 5.4 Technical prerequisites 55
  - 5.4.1 The Likelihood Ratio 56
  - 5.4.2 Obtaining error estimates on parameters 57

6 MUON TRACK DATA 59
- 6.1 Important likelihood reconstructions 59
  - 6.1.1 Directional reconstruction 59
  - 6.1.2 Energy reconstruction 62
- 6.2 Selection strategy 64
- 6.3 Properties 64

7 BLAZAR SELECTION 69
- 7.1 The Fermi 2LAC catalog 69
- 7.2 Definition of samples 70
- 7.3 Completeness 73

8 A LIKELIHOOD ANALYSIS FOR POINT SOURCE STACKING 75
8.1 The likelihood function 75
8.1.1 Signal and background PDF 76
8.2 Estimating Flux Confidence Intervals 78
8.3 Software Implementation 81
8.4 Features of the standard method 84
8.4.1 Background injection from data 84
8.4.2 Maximal number of sources in a stacking search 84
8.4.3 Derivation of the PDFs 85
8.4.4 Disagreement between injected and fitted parameters 88
8.4.5 Energy pdf and applicability of Wilks' theorem: the "undersampling problem" 89
8.4.5.1 Correct description of the PDFs 89
8.4.5.2 Parameter bounds 90
8.4.5.3 Large sample limit 90
8.4.6 Background pdf from data 92
9 VARIATIONS OF THE STANDARD METHOD 93
9.1 Reversing PDF approximations 93
9.1.1 Extension to a 3-d PDF 93
9.1.2 Estimating the point spread function from Monte Carlo 94
9.1.3 Non-gaussianity due to the curved celestial sphere: the Fisher-von-Mises distribution 96
9.2 The background PDF from Monte Carlo 97
9.3 Negative n_s in the minimization 99
9.3.1 Application for differential sensitivities 102
9.4 Conclusions 104
10 RESULTS 107
10.1 P-values 107
10.1.1 "Integral" searches 107
10.1.2 "Differential" searches 108
10.1.3 Robustness 109
10.2 Flux upper limits 110
10.2.1 Systematic errors 110
10.2.2 Energy range 112
10.2.3 Limit construction in the equal weighting scheme 113
10.2.4 Generic flux upper limits 115
10.2.5 Blazar contribution to the diffuse neutrino flux 117
10.2.6 Upper limits on models of neutrino emission from blazars 118
11 DISCUSSION 123
11.1 Implications for models of neutrino emission 123
11.2 Implications for the observed diffuse neutrino flux 123
11.3 A potential physical nature of the observed excess 125
12 SUMMARY AND OUTLOOK 131
A SUPPLEMENTARY INFORMATION 135

A.1 Analysis framework 135
A.2 Supplementary figures 141
B LIGHTYIELD STUDIES 147
B.1 Implementation of a min.-bias trigger 147
B.2 Relative DOM efficiency 147
B.3 Absolute Optical Efficiency 150
C OUTLOOK ON THE DIRECTIONAL RECONSTRUCTION 153
D STUDIES ON THE FISHER-VON-MISES DISTRIBUTION 155

BIBLIOGRAPHY 167

1 OVERVIEW

The beginning of the 20th century marked a new era in physics with the emerging understanding of the atomic and subatomic phenomena of our world. During this epoch, the study of ionizing radiation with electrometers, a rather mundane and earthly activity, opened the first window to the high energy cosmos by the unexpected discovery of cosmic rays. A remark by J.J. and G.P Thomson in 1928 foreshadowed the developments over the coming decades:

It would be one of the romances of science if these obscure and prosaic minute leakages of electricity from well-insulated bodies should be the means by which the most fundamental problems in the evolution of the cosmos had to be investigated.[1]

Indeed, nowadays, observations of high energy cosmic rays in conjunction with photons and neutrinos provide complementary information about the high energy universe, which is ultimately linked to fundamental questions about the evolution of the cosmos itself. For example, γ-ray and neutrino observations can put constraints on the properties of dark matter which plays an important role for structure formation in the early universe. Many questions, however, remain unanswered. One of them concerns the origin of the highest energy cosmic rays itself, which has been a mystery since their initial discovery over 100 years ago. Neutrinos might potentially provide an answer to this question since they uniquely point back to cosmic ray interactions and are not deflected by magnetic fields. Recently, IceCube has detected the astrophysical neutrino background at TeV-PeV energies, opening a new energy domain in neutrino astronomy. An effort is now underway to associate this apparent diffuse flux with particular source classes which might in turn have implications for possible cosmic ray acceleration sites.

One candidate for cosmic ray acceleration and subsequent high energy neutrino production are blazars. These objects constitute highly collimated plasma outflows ("jets") from the active central regions of distant galaxies, whose directions closely coincide with the line-of-sight as seen from Earth. Possible neutrino emission from these objects arises from cosmic ray interactions with gas or photon fields within the jets which produce neutrinos via resulting charged pion decay. Calculations which quantify the neutrino emission go under the name "hadronic" models and additionally predict gamma ray emission from neutral pion decay.

Interestingly, at gamma ray energies above a few GeV, the extra-galactic diffuse γ-ray background is known to be dominated by blazars. Assuming a naive translation of this fact to the neutrino sector via hadronic models,

1 Quote from *Conduction of Electricity through Gases* Vol. 1, 1928, Cambridge University Press, page 12

one could also expect a large contribution of blazars to the diffuse neutrino background measured by IceCube, under the assumption that this flux is of extragalactic origin. On the other hand, the γ-ray emission in blazars can also be explained via so-called "leptonic" models which would not produce any neutrino signal at all. Additionally, the γ-ray background is measured in a different energy range, about 1-2 orders of magnitude lower than the energies of the IceCube signal. An experimental statement for the contribution (or maximal contribution) of blazars to the diffuse neutrino flux is required to further constrain possible connections between the two sectors.

Furthermore, the diffuse neutrino flux predictions from blazar populations span several orders of magnitude due to the different assumptions that go into the calculations. An experimental measurement or upper limit of the diffuse flux produced by a given blazar population would help to constrain this parameter space directly.

This thesis investigates the cumulative neutrino emission from blazar populations, defined with the 2nd Fermi AGN catalog (2LAC), using three years of IceCube muon-track data in an unbinned likelihood point-source stacking analysis. The 2LAC covers the sky for Galactic latitudes $|b| > 10^\circ$ in the energy range between 100 MeV and 100 GeV. It comprises 862 blazar positions with minimal source confusion and resolves the majority of the total γ-ray flux from blazars in the universe into distinct sky positions with errors smaller than the spatial resolution for muon neutrinos in the dataset used in this thesis (the ν_μ track resolution is between 0.7° and 0.4° in the energy range from 1 TeV to 1 EeV). The largest population investigated are all blazars combined, which comprises a factor 40 more sources in a single sample than in previous stacking searches. We call this search type "population search". For this purpose, a framework is developed which can handle thousands of sources efficiently and supports multiple extensions to the standard point source method, whose strengths and weaknesses are evaluated. Any stacking analysis has to assume relative weights for each source in the population, where each weight is proportional to the expected number of neutrinos from the given source. Two different weighting schemes are applied in this analysis: the first assumes neutrino emission for a source follows the measured γ-ray luminosity, the other neglects the gamma ray emission completely in order to minimize bias from possible non-hadronic contributions. Finally, the implications for the prevailing models of neutrino emission from blazars are discussed and the result is put into context with the recently detected diffuse extraterrestrial neutrino signal whose origin is a matter of current debate.

Chapter 2 gives a short overview over the different messenger particles from the cosmos, their relevant properties and the special role of neutrinos. Chapter 3 discusses blazars, their properties and prevailing neutrino emission models. Chapter 4 introduces the IceCube detector, neutrino event signatures and the data processing chain. Chapter 5 summarizes the goals of this analysis, how it differs from previous approaches and introduces the Maximum Likelihood method, which is a central technical aspect of

individual event reconstructions and the final analysis itself. Chapter 6 describes the properties of the muon-track data. Chapter 7 describes the blazar populations that are being studied. Chapter 8 introduces the standard point source likelihood method and discusses its properties. Chapter 9 discusses possible variations of the standard method which are being analyzed. Chapter 10 presents the results of the analysis and Chapter 11 closes with a discussion.

2 COSMIC MESSENGER PARTICLES

The outgoing particles of particle collisions in distant places of the cosmos act as messengers if they eventually cross the path of the Earth. These messenger particles can then be detected in experiments and be used to understand the particles taking part in the primary interaction. The standard model provides us with a menu of all the particles that we can possibly detect from extragalactic sources. Most importantly, they must be stable to survive the journey. At high energies ($\gg$ GeV), the only known particles that can do so are photons, neutrinos, electrons and all stable atomic nuclei, where the last two are usually called cosmic rays[1]. This chapter summarizes the relevant properties of these particles at $\gg$ GeV energies, states some open questions, and points out the importance of a complementary usage of information with a focus on neutrinos.

2.1 COSMIC RAYS

High-energy cosmic rays above GeV energies dominantly consist of all known atomic nuclei up to iron, while electrons and anti particles are subdominant by at least a factor of 10 [Bei+09]. The major contribution, around 80 % [Oli14], comes from protons. Because cosmic rays are charged, they do not follow straight paths during interstellar or intergalactic traversal due to magnetic fields. For a 6×10^{18} eV Proton one expects on average a deflection of about 4° over a distance of 100 Mpc [Aug08]. For higher energies the deflection is reduced, while it increases with higher nuclear charge Z. Recent measurements of cosmic rays have not seen any significant correlation with large scale structure [Aug10] or a distinct point source. The diffuse spectrum and composition of primary cosmic rays has been measured over many orders in energy up to 2×10^{20} eV. A recent compilation of measurements of the all-particle cosmic ray spectrum up to the highest energies is shown in figure 1. The overall shape can be approximated by different power-law spectra, starting with a spectral index of -2.6 around 100 TeV and getting softer on average towards higher energies. There are three structures in the overall spectrum that should be emphasized. The first one is the region around 4×10^{15} eV, which is called the "knee region". Up to this region, the dominant contribution is expected to be of Galactic origin, probably due to acceleration in supernova remnants.

1 This includes the corresponding anti particles. Gravitational waves have not been directly detected yet and are therefore not part of the discussion here.

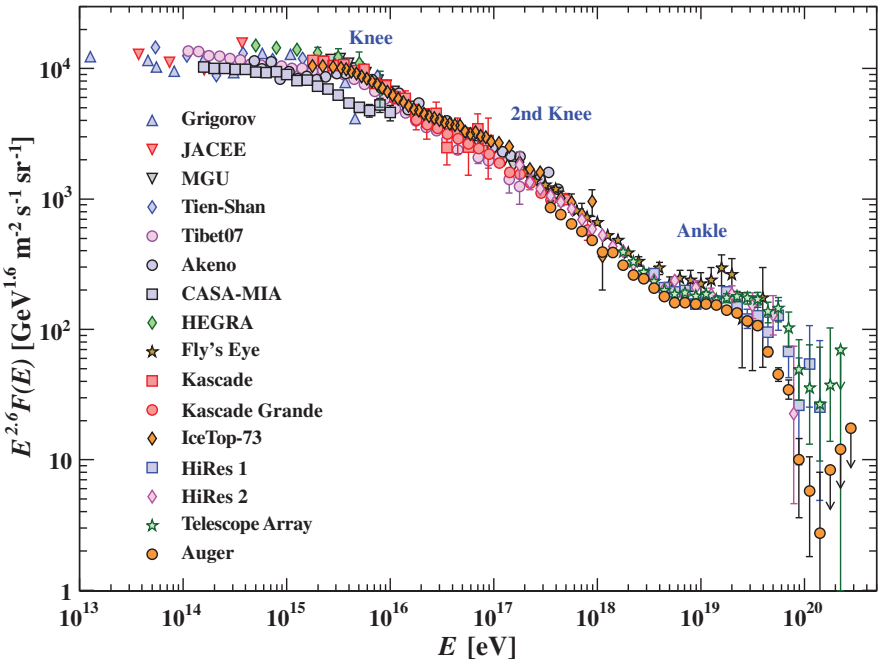

Figure 1: The primary cosmic ray spectrum between 1×10^{13} eV and 2×10^{20} eV. The spectrum is multiplied by $E^{2.6}$ to emphasize spectral features. Taken from [Oli14].

The energy balance works out if only a few percent of the kinetic energy of average supernova explosions is used to accelerate cosmic rays [GS64]. Recently, there has been the detection of gamma-ray spectra characteristic for hadronic acceleration in two supernovae remnants which supports this connection [Fer13]. Above the knee the overall spectral index becomes steeper which can be explained by an element-wise cutoff at different energies [Pet61], starting with protons and ending with iron nuclei. At around 30PeV a "second knee" is observed which could indicate a second Galactic component, e.g. a Galactic source nearby [Gai12]. The third feature is an apparent hardening of the spectrum around 6×10^{18} eV (6 EeV), also called the "ankle region", which is usually assumed to be the energy range at which the extra-galactic cosmic rays start to dominate, although the relative contributions of specific source classes are unknown. At even higher energies a suppression of the cosmic ray flux due to photo hadronic interactions with the **C**osmic **M**icrowave **B**ackground (CMB) is expected to happen and possibly seen in the cutoff starting at around 8×10^{19} eV.

High energy cosmic rays are produced by acceleration from lower energies. The acceleration mechanisms that are studied most in the literature are variants of collision-less diffusive shock acceleration [Bel78] since they naturally lead to the power-law spectra which are observed in nature.

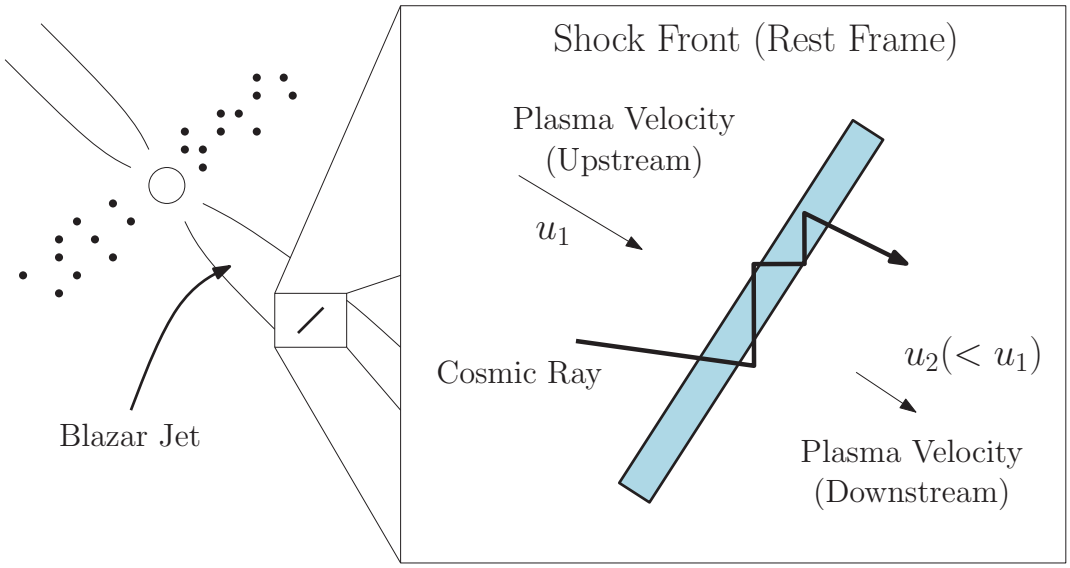

Figure 2: Sketch of a shock front (blue) in its rest frame, examplified for a plasma environment within a blazar jet (see chapter 3 for a description of blazars). Adapted from [Bel78].

The environment for such acceleration are shocks, which form whenever a plasma cloud moves supersonically through the surrounding medium. At the boundary of such a shocked region, the shock front, particle acceleration takes place. The basic mechanism is sketched in figure 2. In the rest frame of this shock front one can divide the plasma flow into an "upstream" region (velocity u_1) before the shock, and a "downstream" region (with a slower velocity u_2) which corresponds to the inside of the shocked region. Such a system can be described analytically by a differential equation for $f(x, p, t)$, the pitch-angle averaged distribution of particles which impinge on the shock and perform scattering on either side of the shock front on magnetic field turbulences [BO78]. This distribution is assumed isotropic because the individual velocities u_1 and u_2 are assumed to be smaller than the individual particle velocities. A stationary solution for f then has the power-law form

$$f = f_0 \cdot p^{-q} \tag{1}$$
$$q = \frac{3 \cdot r}{r-1}, r = \frac{u_1}{u_2}$$

depending only on the ratio of up- and downstream velocities r, called the "compression ratio". Typical values of of this ratio of 3-4 lead to values for q of 4-4.5 [BO78] . This translates via

$$\frac{dN}{dp} \propto f_0 \cdot p^{-q+2} \tag{2}$$

to power-law spectra with spectral indices between -2 and -2.5 for the differential particle flux. A similar result is obtained when looking at the

energy gain of individual shock front crossings of a charged particle [Bel78]. This result is in rather close agreement with the observations (figure 1), if one takes into account further softening of the spectrum due to propagation and energy loss.

The specific Ansatz described here is only valid for planar and non-relativistic shocks. More complicated **M**agneto **H**ydro **D**ynamic (**MHD**) calculations [MD01] including numerical simulations which also encompass relativistic shock environments [MBQ08] indicate that relativistic shocks do also yield power-law spectra. Particle acceleration is discussed again (setion 3.5) in the context of neutrino emission from blazar jets.

Acceleration sites for the highest energetic cosmic rays have not been identified yet. The question of potential candidate sources can be addressed by looking at the size of the acceleration region and the local magnetic field strengths. If the magnetic fields are not strong enough, it becomes impossible to confine particles within the acceleration region and continue the acceleration to higher energies. Thus, there is a maximum energy that can be reached under very generic assumptions, independent of the detailed acceleration processes, given these two quantities. This can be quantified in the so called "Hillas Criterion" [Hil84] (eq. 3)

$$B_{\mu G} \cdot L_{pc} > \frac{2 \cdot E_{15}}{Z \cdot \beta} \tag{3}$$

where $B_{\mu G}$ is the magnetic field in the source in units of micro Gauss, L_{pc} is the characteristic size of the source in units of parsec, E_{15} is the energy of the particle in units of 1×10^{15} eV and β and Z are the velocity and charge of the particle.

Plotting the characteristic acceleration size versus local magnetic field strength for a given acceleration region, the inequality is represented by diagonal lines for a given fixed energy. This is shown in figure 3 which includes the inequality for a 1×10^{20} eV proton and iron nucleus as well as potential cosmic accelerators. Any source below a particular diagonal line does not fulfill the inequality and thus does not qualify for a source candidate for the given energy. Blazars, the objects of study in this thesis, populate the region between AGN and "radio lobes" and are a source candidate for particles up to 1×10^{20} eV.

Cosmic rays interact via two processes in the source and when they travel in intergalactic space:

- Hadronuclear interactions: cosmic rays interacting with gas

  In the following we will restrict ourselves to the simplified case of proton-only interactions (p-p) which dominate hadro-nuclear interactions. Interactions with heavier nuclei are usually accounted for by

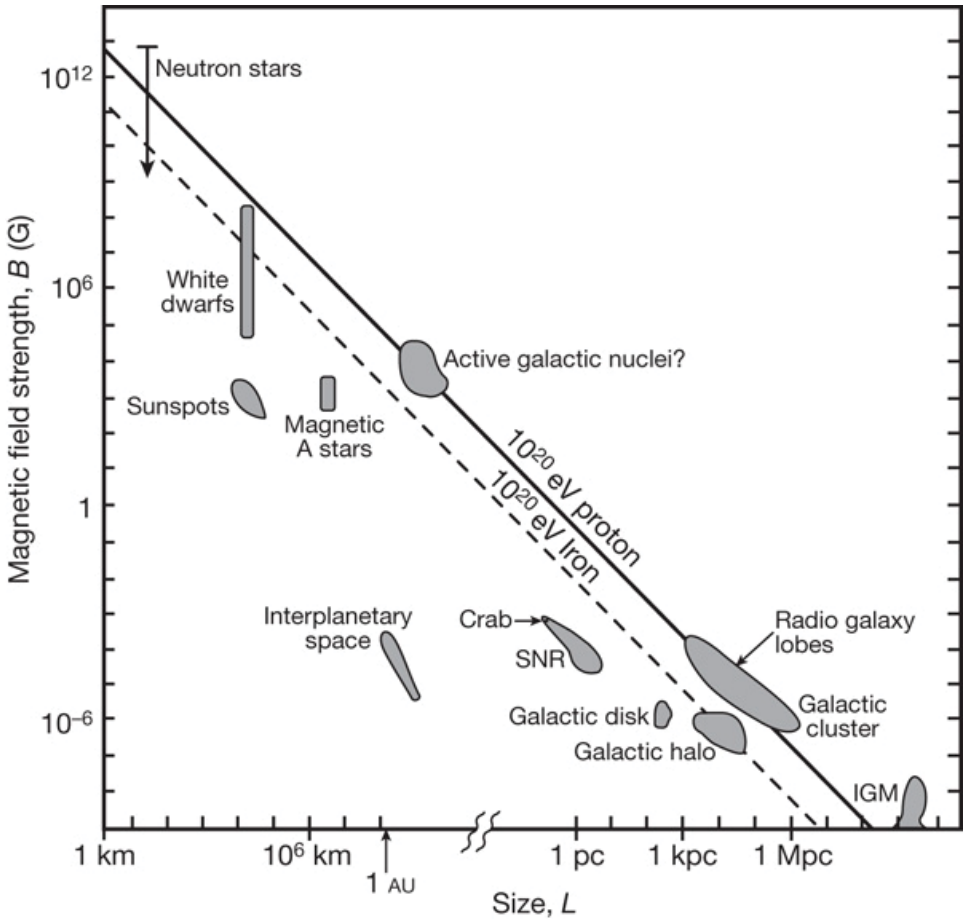

Figure 3: The local magnetic field strength versus typical accelerator sizes defined via the Larmor radius (The "Hillas" plot). Diagonal lines depict the Hillas criterion (eq. 3) for a 1×10^{20} eV proton and iron nucleus. Taken from [BM09].

scaling relations [KMO14]. The proton-proton interaction can be written as

$$p + p \rightarrow \begin{cases} \pi^{\pm} + \boldsymbol{X} \\ \quad \hookrightarrow \mu^{\pm} + \nu_{\mu}(\overline{\nu}_{\mu}) \\ \quad\quad \hookrightarrow e^{\pm} + \nu_{e}(\overline{\nu}_{e}) + \overline{\nu}_{\mu}(\nu_{\mu}) \\ \pi^{o} + \boldsymbol{X} \\ \quad \hookrightarrow 2 \cdot \gamma \end{cases} \tag{4}$$

X stands for all hadronic secondaries except pions. The resulting neutral pions subsequently decay into photons while the charged ones produce neutrinos.

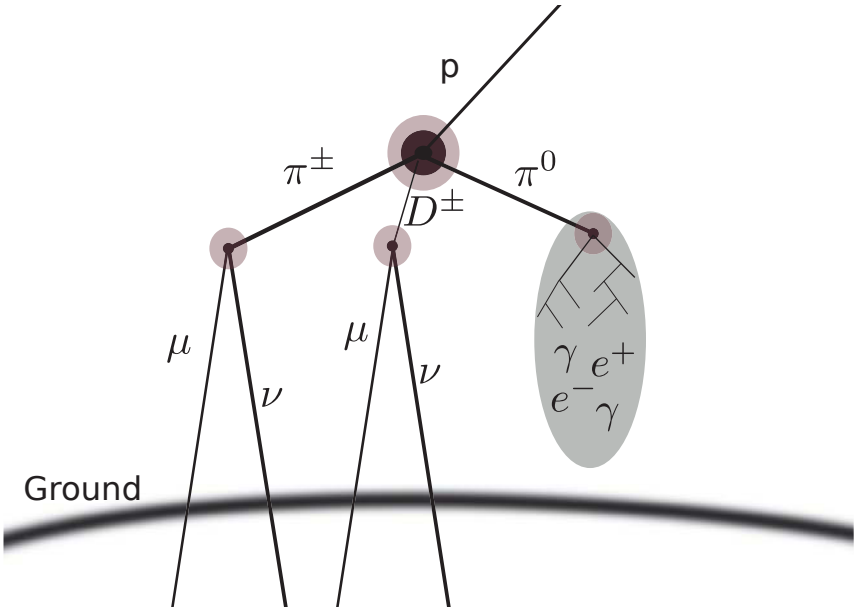

Figure 4: A schematic of a cosmic ray shower. A primary proton interacts with an air molecule and produces secondary particles (here only mesons are visualized). Neutral mesons, mostly pions, decay electromagnetically whose corresponding electromagnetic component resides within the atmosphere above the ground. Charged mesons decay and produce muons and neutrinos which can reach underground detectors.

- Photo-meson interactions : cosmic rays interacting with photons

  Photo-meson (p-γ) interactions often produce an intermediate hadronic short-lived resonance which decays into lighter mesons. The most common reaction of this type involves a proton and a photon producing a Δ^+ resonance (equation 5).

$$p + \gamma \to \Delta^+ \to \begin{cases} \boldsymbol{\pi^{\pm}} + [\boldsymbol{n}] \to \pi^{\pm} + [p^+ + e^- + \overline{\nu}_e] \\ \qquad\qquad \hookrightarrow \mu^{\pm} + \nu_\mu(\overline{\nu}_\mu) \\ \qquad\qquad\qquad \hookrightarrow e^{\pm} + \nu_e(\overline{\nu}_e) + \overline{\nu}_\mu(\nu_\mu) \\ \boldsymbol{\pi^0} + \boldsymbol{p} \\ \hookrightarrow 2 \cdot \gamma \end{cases} \quad (5)$$

  Again, photons arise from neutral pion decays and neutrinos from charged pion decays.

Once the cosmic rays reach the Earth, they interact via the hadronuclear channel with a molecule in the Earth's atmosphere. The process induces a particle shower, as schematically visualized in figure 4.

The electromagnetic component of the shower is quickly attenuated when it reaches the ground. On the other hand, charged meson decays lead to muons and neutrinos which can penetrate several kilometers (thousands of

kilometers for neutrinos) below the ground and form the background for astrophysical neutrino searches. More details are given in section 6.

2.2 PHOTONS

Unlike Cosmic Rays, photons are neutral and therefore not deflected by magnetic fields. As such, many point sources of high energy gamma rays have been identified. At energies above 100 MeV, the extragalactic photon sky can be divided into two components: resolved sources (1) and a diffuse unresolved signal (the **I**sotropic diffuse **G**amma-**R**ay Background - **IGRB**). The total emission of point sources and diffuse signal together form the **E**xtragalactic **G**amma-Ray **B**ackground - **EGB**. The most recent measurement of these components was performed by the Fermi collaboration [Fer15] and is shown in figure 5.

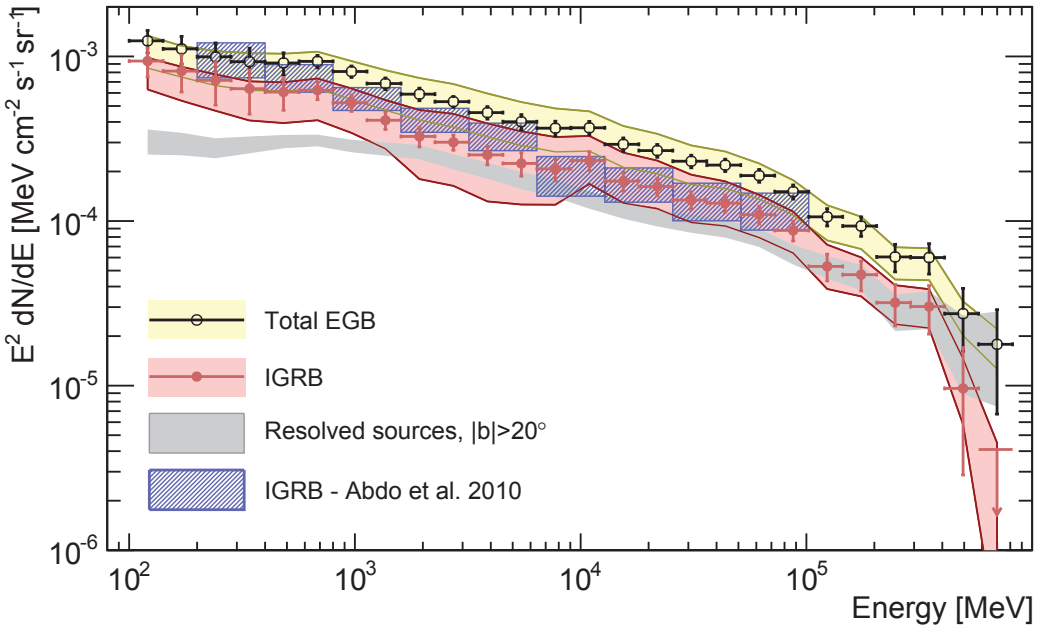

Figure 5: The Extragalactic Gamma-Ray Background measured between 100 MeV and 820 GeV. Also depicted are the contributions of the unresolved isotropic component (IGRB) and the resolved extragalactic sources. Taken from [Fer15].

Around 100 GeV, resolved sources make up about 50 % of the total EGB. Since more than 90 % of the resolved sources are blazars, their contribution is substantial and is discussed in section 3 in more detail.

Within standard model physics five scenarios for gamma-ray generation should be mentioned which are potentially of relevance for this thesis. The first scenario generates gamma rays as the end products of mesons following hadronic interactions (equations 4 and 5), typically from the decay of a π^0 (figure 6a). The second involves **I**nverse **C**ompton (IC) scattering with electrons in which photons gain energy up to GeV energies and be-

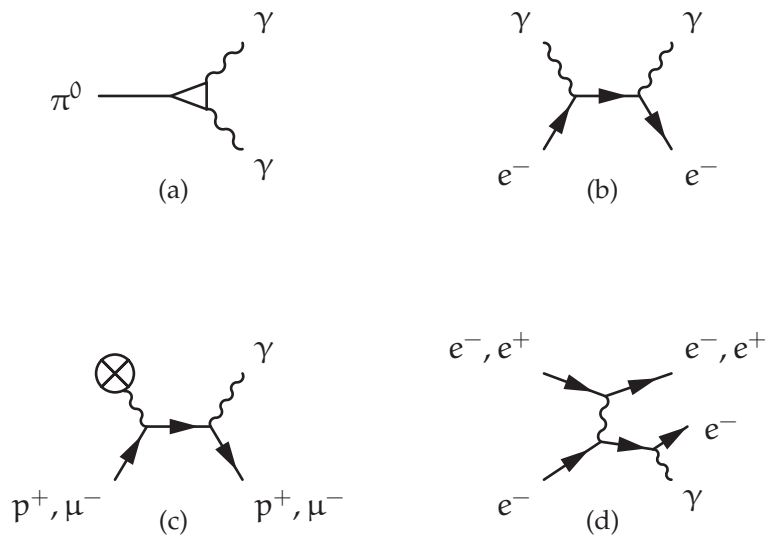

Figure 6: Four distinct astrophysical scenarios to produce high energy photons: (a) neutral pion decay (b) inverse compton scattering of electrons (c) synchroton emission and (d) bremsstrahlung emission.

yond (figure 6b). The corresponding diagram can be flipped by crossing symmetry and describe the process of pair annihilation, a mechanism that normally only produces a line signal but which can be broadened in astrophysical environments [BS96]. The fourth mechanism generates gamma rays as synchroton radiation from charged particles via interaction with a magnetic field (figure 6c). At ultra-relativistic energies this can typically happen to heavier particles like protons and muons which is relevant in certain blazar neutrino emission models (see section 3.5). The fifth scenario is bremsstrahlungs emission of a charged particle in the electric field of another charged particle (see figure 6d). In the context of this thesis, pair-bremsstrahlung of the type $e^- + e^-$ or $e^- + e^+$ [BS95] is a process which can lead to photons in blazar environments (see section 3 for the theoretical introduction to blazars).

Once high energy gamma rays are created they have to be able to leave the source region and travel unhindered trough intergalactic space. On Earth, their intensity is reduced dominantly by compton scattering up to around 1GeV and by Bethe-Heitler pair production on nuclei and bound electrons at higher energies [Oli14]. In typical cosmic environments, however, Bethe-Heitler pair production and Compton scattering play a subdominant role since the electron- and baryon densities are many orders of magnitude lower. Photon fields are then the dominant absorption target via pair production in reactions of the type: $\gamma\gamma \rightarrow e^+ + e^-$. The newly created electron and positron can in turn emit synchroton photons (magnetic field) or generate IC photons (ambient photon fields) which can annihilate with other photons and the process starts all over again: an electromagnetic cas-

cade developes[2][AKC08] (see figure 7). The gamma rays that emerge are not all aligned with primary gamma ray direction anymore or might even be isotropized [RB10]. This means it is more and more unlikely the higher the energy to observe the primary photon, since it would "cascade down" and leave the source region split up over many photons of lower energies. Also, because of isotropization only a fraction of the primary gamma ray energy can be inferred from observing on-source photons.

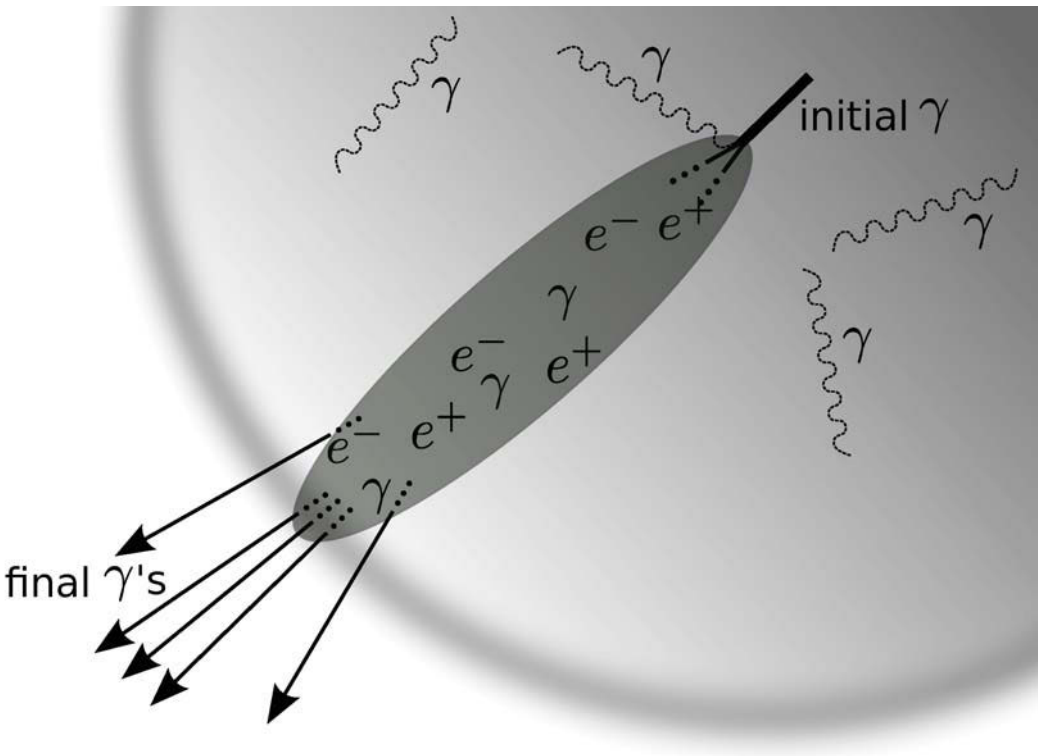

Figure 7: Reprocessing of a gamma ray within a source environment via $\gamma\gamma$ pair production ending in an electromagnetic cascade. The reprocessed escaping gamma rays (thin solid lines) are lower in energy than the initial one (thick solid line).

Once high energy gamma rays are leaving the source region, $\gamma\gamma$ absorption with so called "**E**xtra galactic **B**ackground **L**ight" (EBL) becomes dominant [GS67]. The EBL is the thermal radio to UV emission of all stars and dust plus a contribution from AGN (section 3.2) integrated over the whole universe [Dom+11]. After the CMB it exhibits the second largest energy density in extragalactic photon fields. The threshold for $\gamma\gamma \rightarrow e^+ + e^-$ from relativistic kinematics is given by

$$E_1 \cdot E_2 \cdot (1 - \cos(\theta)) > 2 \cdot {m_e}^2 \approx 0.5 \cdot MeV^2 \tag{6}$$

Here, E_1 and E_2 are are the respective photon energies, θ is the relative angle between the two, m_e is the electron rest mass and the speed of light

2 Electromagnetic cascades in dense materials at Earth are different in the respect that Bethe-Heitler pair production and bremsstrahlung dominate. See section 4.1.2 for cascades in ice.

is set to unity. The cross section for e+/e- pair production sharply peaks just above the threshold of this kinematic condition [GS66], which means one can approximately use equation 6 to read off the corresponding photon energies which will dominantly absorb gamma rays of a given energy. For high GeV up to TeV gamma rays the corresponding photon energies fall into the energy regime of the EBL, which means ultraviolet to infrared wavelengths. For 100 TeV gamma rays and beyond, the CMB becomes the dominant absorption target.

For a given energy, one can now calculate the distance at which only $1/e$ of the initial gamma ray flux survives if one assumes a particular model of the EBL. This distance is called the "gamma-ray horizon". In general, one can describe the gamma-ray absorption process with the optical depth $\tau_{\gamma\gamma}$, which is defined via

$$I_f = I_i \cdot \exp(-\tau_{\gamma\gamma}(E, z)) \tag{7}$$

and contains the gamma-ray horizon as a special case when the optical depth is unity. A recent model-independent measurement of the gamma ray horizon [Dom+13] is shown in figure 8. At 100 GeV the universe is

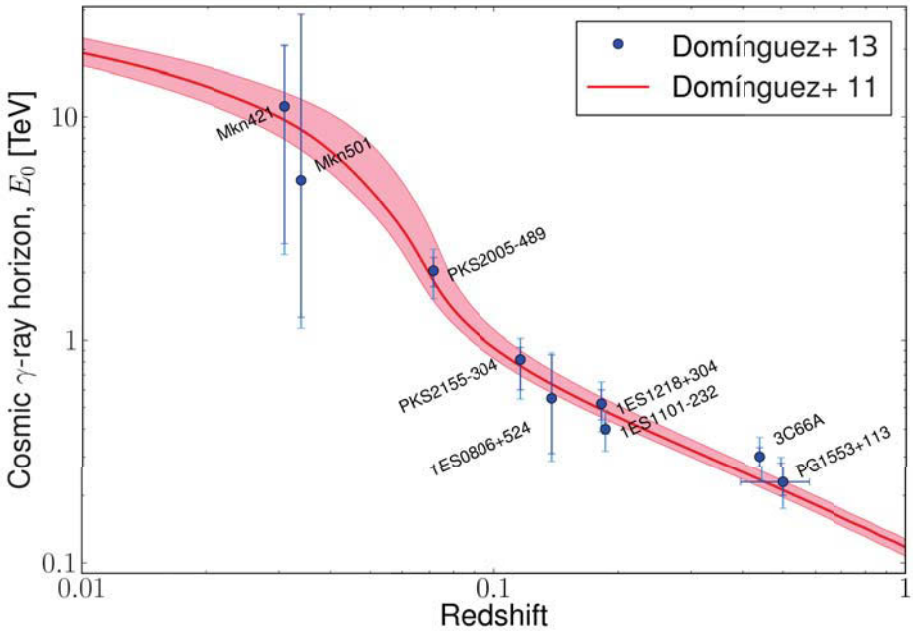

Figure 8: The cosmic gamma ray Horizon measured from blazars (data points[Dom+13]) and from theoretical EBL modeling (red curve[Dom+11]). Figure taken from [Dom+13].

practically completely transparent up to a redshift of 1, while at 1 TeV it becomes opaque above a redshift of around 0.1. At the energies observed by the LAT on the Fermi Gamma-Ray Space Telescope considered in this thesis (< 100 GeV), EBL absorption should thus become relevant only for sources with a redshift larger than one.

2.3 NEUTRINOS

Neutrinos interact only via weak interaction processes and travel nearly unhindered and at straight paths over intergalactic distances until they are eventually detected at Earth. This makes them interesting messenger particles, but their elusive nature makes it also hard to detect them in the first place. Over the past 50 years, only three distinct extraterrestrial neutrino fluxes have been identified.

At low energies in the kev-MeV range solar neutrinos were the first extraterrestrial neutrinos to be discovered in the late 1960's [Cle+98], providing the first observational view into the interior of the sun.

In 1987 several underground detectors measured a burst of neutrino events at MeV energies in close temporal coincidence with a SuperNova explosion in the large magellanic cloud[IMB87] [Kam87] [UNO87] [Ale+87]. The neutrinos reached the Earth hours before the optical light due to the fact that they could escape the explosion region unhindered.

In 2013, IceCube detected a diffuse neutrino signal, a billion times more energetic than the neutrinos from the sun or from SN1987a with energies between hundreds of TeV and arround 1 PeV [Ice13a]. The latest measurement of this diffuse astrophysical flux with an extension down to around 20 TeV [Ice15] is depicted in figure 9.

The best fit power-law gives a spectral index of around -2.5. The origin of these neutrinos has not been identified yet and is still open for debate. Compatibility with an isotropic flux suggests an extragalactic component. A possible contribution of blazars to this diffuse signal is investigated in this thesis (see section 5).

In the energy range of the IceCube diffuse signal, neutrinos from standard model interactions are exclusively produced in the decay chains of hadronic interactions which have been discussed in section 2.1. In general, neutrinos occur in three flavors (e, μ, τ), although only the first two are typcially produced in hadronic interactions. On their propagation to Earth neutrinos oscillate from one flavor to another. The oscillations have the consequence that the flavor ratio with which neutrinos leave a distance source is usually not the same as the ratio one observes in an Earth-bound experiment. For a neutrino source at cosmological distances one can show [Win12] that the observed flux of a given neutrino flavor β behaves like

$$\Phi_{\nu_\beta} \propto \sum_{\alpha=e,\mu,\tau} P_{\alpha\beta} \cdot \Phi_{\nu_\alpha} \tag{8}$$

where Φ_{ν_α} is the flux of flavor α at the source and $P_{\alpha\beta} = \sum_{i=1}^{3} |U_{\alpha i}|^2 |U_{\beta i}|^2$ is a function of the PMNS-mixing matrix U. One can take the proton-proton (eq. 4) or photo-meson (eq. 5) processes and look only at the ratio of emerging neutrino flavors from the charged pion decays assuming these dominate the processes. This yields a flavor ratio $(e : \mu : \tau)$ at the source of 1:2:0 which, after application of oscillations, results in a 1:1:1 ratio at Earth, shown in table 1.

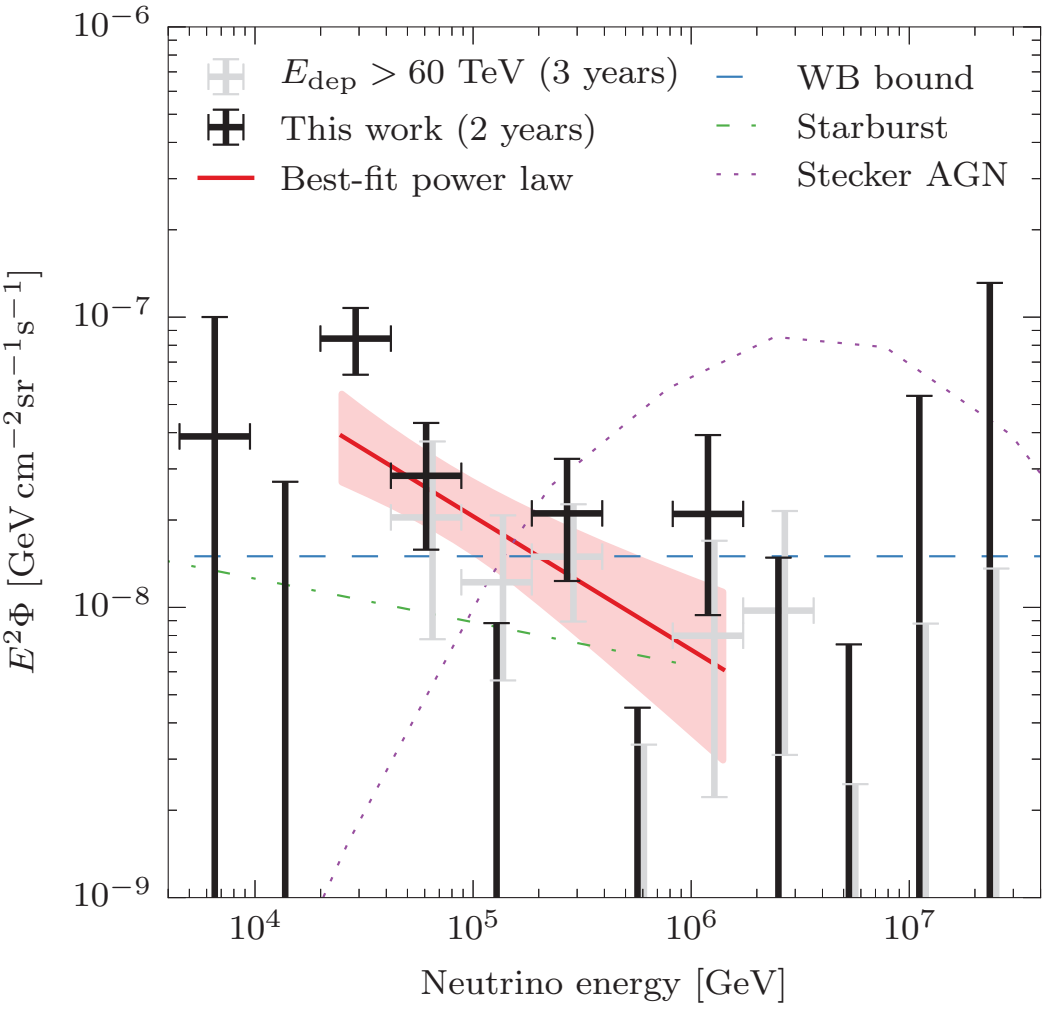

Figure 9: The cosmic neutrino background above 1 TeV as measured by IceCube. The best fit power-law is depicted as the red line (spectral index -2.46). An unfolded spectrum is shown in black. Also shown are an upper bound derived from the observed CR flux (blue) and particular models for neutrinos from Starburst galaxies (green) and AGN cores (magenta). Figure taken from [Ice15]

There are two other flavor ratios which can be seen as extremal cases of neutrino production in astrophysical sources: a pure electron neutrino beam (1:0:0) and a pure muon neutrino beam (0:1:0). These limiting cases would in principal occur if the muons loose energy inside the source before they decay, thus the pion decay dominates the neutrino spectrum at high energies (muon-neutrino dominated) or if the neutron decay dominates and the pions for some reason can be neglected (electron-neutrino dominated). The resulting ratios at Earth can differ substantially. In a realistic, more complicated environment, though, these extreme cases are usually not expected to occur. For an optically thin source (no muon damping) where the primaries follow an E^{-2} spectrum, it can be shown [LLM07] that one reaches a ratio

Pion and muon decay		
1 : 2 : 0 @ source	→	1 : 1 : 1 @ detector
Pion-Decay dominated (muon damped)		
0 : 1 : 0 @ source	→	0.2 : 0.4 : 0.4 @ detector
Neutron decay dominated		
1 : 0 : 0 @ source	→	0.5 : 0.2 : 0.2 @ detector

Table 1: Different flavor ratio scenarios showing the ratio at the source and at Earth. Calculations use the values given in [FTV14].

of 1:1.9:0, rather close to the generic scenario discussed at the beginning. Therefore, the standard assumption for the neutrino flavor ratio to arrive at a detector at Earth is usually 1:1:1. Significant deviations, if detected, would give immediate insight into the conditions at the source.

2.4 COMPLEMENTARITY

All messenger particles carry complementary information which allows to infer the maximal knowledge about astrophysical processes if the different channels are combined. Their different messenger properties are schematically summarized in figure 10.

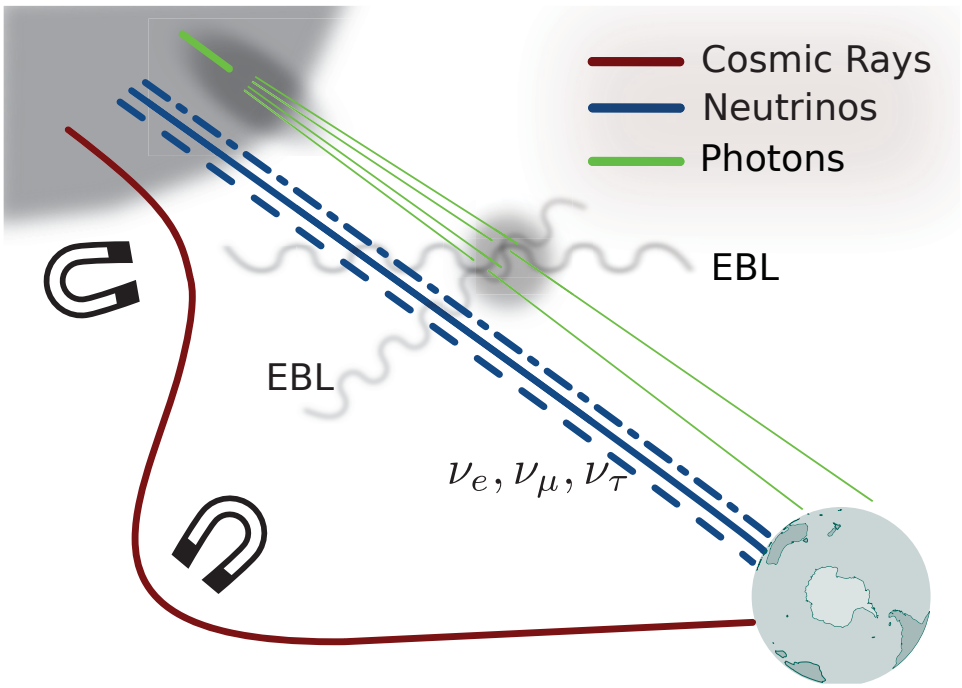

Figure 10: Schematic of the three basic messenger particles in the high energy regime. The gray area in the upper left corner represents some arbitrary cosmic source region. Reprocessing of photons inside the source region or absorption via the EBL is indicated by dark grey blobs.

Cosmic rays (section 2.1) are charged and lose their directional information due to magnetic deflection or interact along the way. Gamma rays (section 2.2) might not leave the source region, are absorbed at the highest energies due to the EBL, and are not uniquely related to hadronic interactions. Neutrinos (section 2.3) essentially overcome all these weaknesses since they are neutral, point back to the primary interaction within the source, come in three flavors and are hardly attenuated along the way. Because they are intertwined in their generation with photons and cosmic rays (see equations 4 and 5), they offer a complementary window that puts constraints on the interpretation of both gamma ray and cosmic ray observations. This includes a possible answer to the origin of the highest energy cosmic rays.

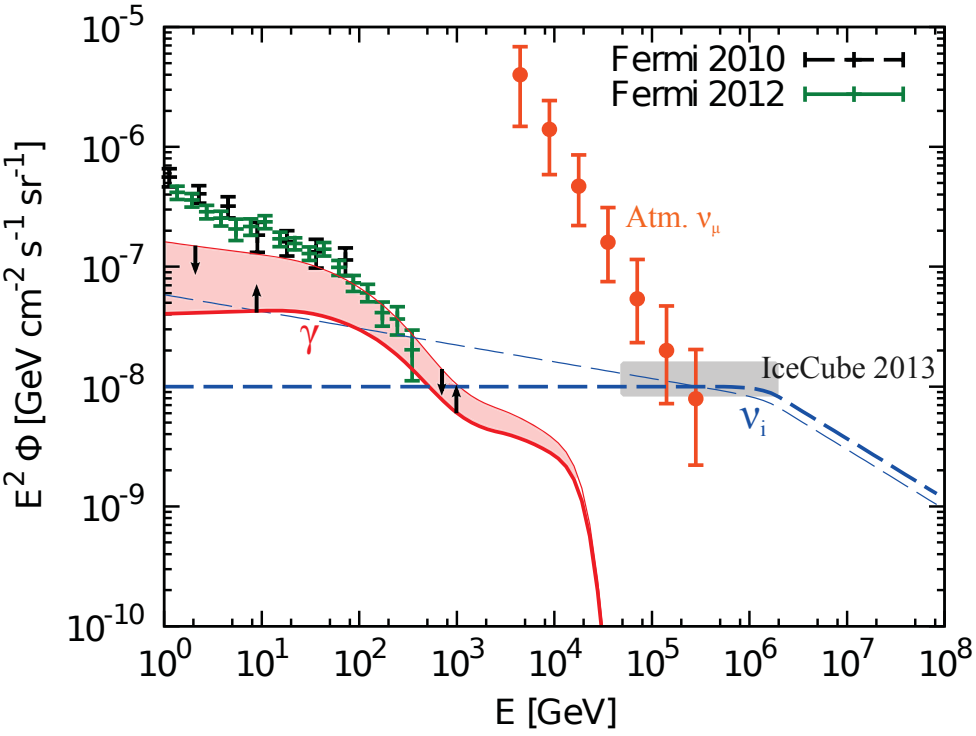

Figure 11: Compatibility of the IceCube signal (gray band) with the EGB measurements (green and black data points) in p-p scenarios. A variation of the primary proton spectral index between $\Gamma = 2.0$ and $\Gamma = 2.14$ leads to the depicted neutrino spectra (blue dashed) and photon spectra (red band). Figure taken from [MAL13].

As an example for complementarity reasoning, one can try to model the EGB and the diffuse neutrino signal in a common production scenario. If hadronuclear interactions are dominantly responsible for the diffuse neutrinos, it can be shown [MAL13] that the spectral index of the astrophysical diffuse flux has to be harder than -2.2 to not overshoot the gamma ray observations in the GeV and TeV regime (see figure 11). The newest IceCube measurements (figure 9 in section 2.3), however, indicate a spectral index of around -2.5, which makes a proton/proton origin within the context of the preceding argumentation unlikely. Blazars (see chapter 3) are

objects which are usually modeled with photomeson interactions and are not prone to the constraint in figure 11, although here the expected neutrino spectra from models in the literature (see section 3.5) typically peak at higher energies than a few PeV, which is above the highest measured energies of the astrophysical flux. Experimental constraints for blazars are required for further argumentation, especially since the existing neutrino model fluxes span several orders of magnitude and provide no coherent expectation. Additionally, given that blazars already constitute a large fraction of the EGB (see section 2.2), it is desirable to know how much they eventually contribute to the astrophysical neutrino flux, as neutrinos and gamma rays are fundamentally linked via hadronic processes.

3

BLAZARS

The astrophysical objects studied in this thesis are blazars. This chapter gives an overview over their discovery, how they are connected to galaxies and what is expected from these objects in terms of neutrino emission from the literature.

3.1 ASTRONOMICAL CLASSIFICATION

The line of research that ultimately led to the discovery of the objects that we call blazars was initiated by emission line spectroscopy of objects in the sky over 60 years ago. In 1943 it was discovered by Seyfert [Sey43] that a particular subclass of galaxies show strong and broad emission lines from the central nucleus. Emission lines are a tracer of ionized material and broad lines indicate high relative velocities (observed are velocities much larger than from a thermal broadening alone [Pet97]). Such "active" cores are known today as **A**ctive **G**alactic **N**uclei (AGN). A subset of these AGN show enhanced radio emission [BM54]. One can define "radio-loudness" as a classification parameter, for example as the ratio of radio to optical flux $R_{r/o}$ [Kel+89].

$$R_{r/o} = \frac{F_{5GHz}}{F_{440nm}} \tag{9}$$

One typically calls an AGN radio-loud if $R_{r/o} \geqslant 10$ [Pet97]. Radio-loud AGN comprise around 10% on average [Vel+12] [1] of all AGN while radio-quiet AGN (denoted as Seyfert Galaxies) comprise the rest.

In the 1960's, a seemingly disconnected class of objects was discovered [Sch63] [San65] whose characteristic was a large redshift of optical emission lines of 0.1 or more, hinting at distances of billions of light years which was more distant than usual Seyfert galaxies. Since they looked like stars in ordinary light, they were dubbed "Quasi Stellar Objects" (QSO's). Again, these fall into radio-quiet and radio-loud categories [2]. A peculiar radio-loud QSO ("BL LACERTAE") was identified in 1968 whose optical properties marked it as different from other ones known at the time [Sch68]. It had a continuum polarized radio emission, strong optical variability and showed no hints of emission lines, which had been *the* defining criterion for previously detected QSO's. Over the following years, many similar objects with no detectable emission lines were discovered and were subsequently given the

1 The fraction is a strong function of luminosity. It is lower than 10% for low luminosity galaxies and higher for the highest luminosity ones.

2 Radio-loud QSO's are also called Quasars. These were the first QSO's to be discovered.

name BLLac-objects[Str+72]. In the 70's, astronomers found mounted evidence for radio-loud QSO's which showed normal strong emission lines, but which shared the variability,radio and polarization properties of the BLLacs. Thus, as these seemed to stem from the same underlying class of objects, the term "**blazar**" was put forward to denote all optically variable, often polarized sources with a continuous radio spectrum, regardless of the presence of emission lines or not [AS80]. The seemingly different sub populations in terms of broad lines are still used for classification nowadays. The dividing line between the two is usually set to 5 Å [Sti+91] in terms of the rest-frame **e**quivalent **w**idth (EW) [3] of the broadest optical emission line. Objects with narrower line widths are still denoted as BLLac objects, while the others are called **F**lat **S**pectrum **R**adio **Q**uasars (FSRQs). Figure 12 illustrates the spectral differences for a typical FSRQ and BLLac. In the next

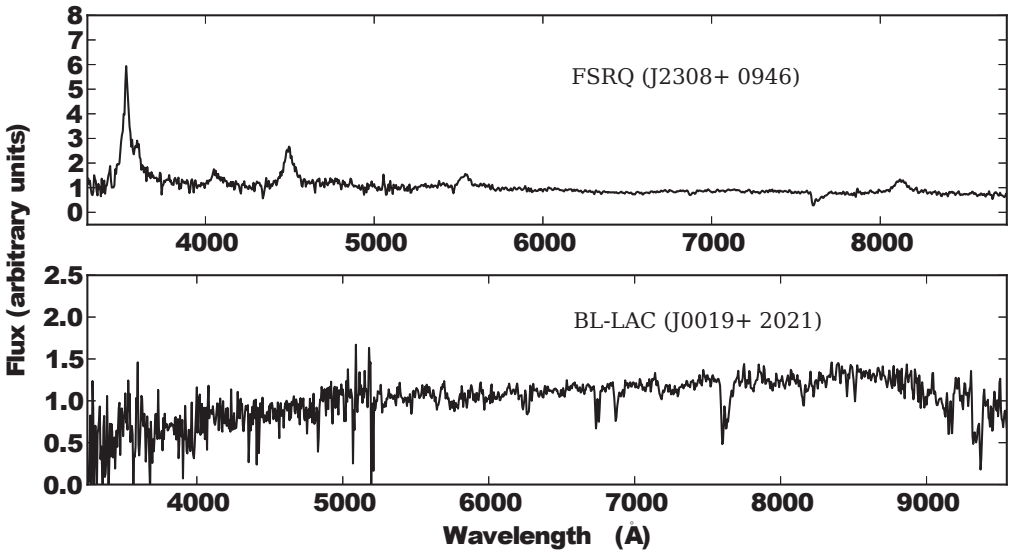

Figure 12: Optical rest-frame spectra of FSRQ (J2308+ 0946) and BLLac object (J0019+ 2021). Strong broad emission lines can be seen around 3500 Å and 4500 Å for the FSRQ, while they are absent for the BLLac. The figure is adapted from [Pur+13].

section it will be described how blazars can be physically understood in a unified context that also encompasses the seemingly different phenomena of AGN and QSO's in one scheme.

3.2 BLAZARS IN THE UNIFIED PICTURE OF AGN

By the end of the 70's it became clear that the observational characteristics of blazars could be explained by the assumption that one looks straight

3 Equivalent width is defined as the width of a rectangle with the same area as the continuum subtracted area below the emission line.

into the direction of an "astrophysical jet" [BK79], emerging from a compact region. Such jets had been known to exist from observations for a long time [Cur18], especially in the context of extended radio sources [MHB70], and had also been theoretically understood as an emerging bipolar Poynting flux-dominated[4] plasma outflow via magnetic energy extraction from a spinning black hole and the matter surrounding it [BZ77] [BP82]. The variability aspect of blazars can be understood, if particles are accelerated in confined regions within the jet plasma (e.g. in shock fronts, see section 2.1), which would also explain the observed polarization via synchroton emission [BK79]. A complete understanding of jet dynamics, however, is still lacking due to the complexity of plasma modeling over many different orders of intrinsic distance scales (see section 3.5). The "jet-on" (because one looks directly into the jet) picture for blazars was subsequently embraced and combined with the other known AGN and radio-loud QSO spectral features to formulate a unified model based on the observer's line-of-sight on a single class of objects, the AGN itself, which became the prevailing paradigm in the 90's [UP95]. The idea is schematically depicted in figure 13.

The center of an AGN hosts a $10^6 - 10^8$ solar mass black hole which is surrounded by an accretion disk of matter. The broad emission lines stem from fast moving material which is likely close to the black hole and might be part of the outer accretion disk itself [Pet06]. This region of fast moving matter is commonly referred to as the "**B**road **L**ine **R**egion" (**BLR**). Some of this material moves towards the line of sight, some away, thus creating broad emission lines whose widths indicate relative velocity differences of often 10000km/s or more [Pet97]. On the other hand, observationally it is found that in some AGN only narrow emission lines exist (so called type-2 objects). This is explained by an obscuring dust torus, which prevents observations of the inner-most region from edge-on viewing angles [Ant82] [Ant83]. The **N**arrow **L**ine **R**egion (**NLR**), on the other hand, is thought to consist of ionized matter that extends beyond the torus and is thus visible even at edge-on angles. This picture is independently valid for radio-quiet and radio-loud objects. Radio-quiet Seyfert-type galaxies represent low-luminosity AGN of the local universe. Radio-quiet QSO represent higher-luminosity AGN that are more distant. For radio-loud AGN, radio galaxies represent the local low-luminosity counterparts of more distant radio-loud QSO. Astrophysical jets, however, are only observed in radio-loud AGN. Going to very small viewing angles with respect to the jet axis for such objects, at some point the blazar characteristics begin to dominate as one observes the emission from the jet.

4 Poynting flux-dominated means most of the energy of the plasma is in photons instead of the kinetic energy of particles.

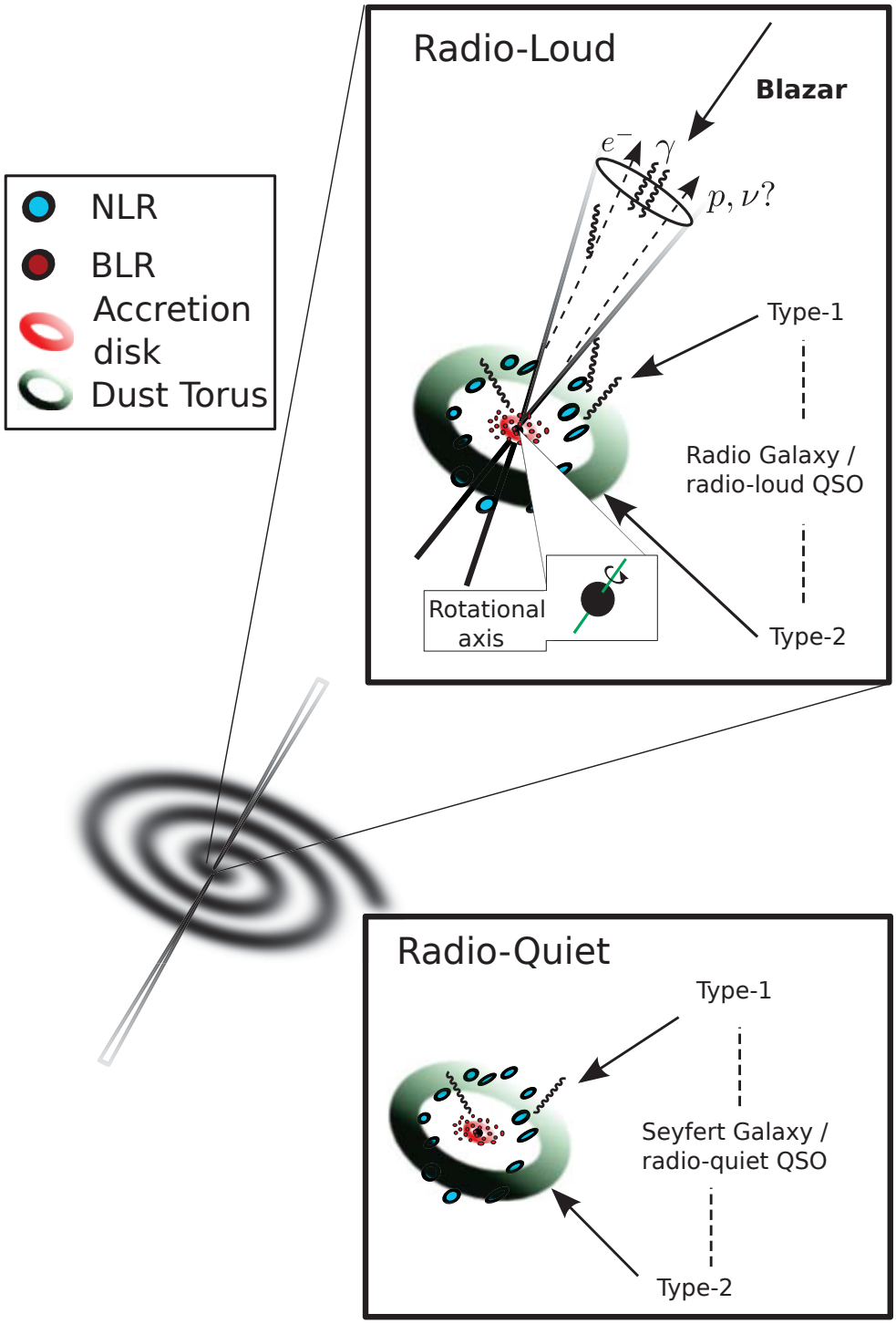

Figure 13: The unified picture for radio-loud AGN. The Narrow Line Region (NLR) is depicted as blue clouds. The Broad Line Region (BLR) is closer inward, depicted as red clouds and connects to the accretion disk. Emerging electrons, protons or neutrinos are depicted as dashed arrows, while photons are depicted as wiggly lines. The lines-of-sight (viewing angles) from earth are shown as solid arrows together with the corresponding classification names.

The blazar characteristics can be explained by relativistic beaming effects which modify the observed flux compared to the jet-frame.It can be shown that an observed energy flux at Earth is related via

$$F_{\nu,\mathrm{obs.}}(E_0) = \frac{D^3}{(1+z)^3} \cdot F_{\nu,\mathrm{jet}}(E_0 \cdot \frac{1+z}{D}) \tag{10}$$

to an energy flux measured in the jet system [HBW10], where E_0 is the energy measured by the observer and D is the relativistic Doppler factor defined as $D = 1/(\Gamma \cdot (1 - \beta\cos(\theta)))$ which stems from a combination of time retardation and Lorentz contraction. The factor $1+z$ is included here and describes the effect of cosmological redshift. Typical values for blazars, $D \approx 10$ and a redshift of $0-3$ can result in flux amplifications of a few hundred. Slight changes in the jet velocity or direction can drastically change the Doppler factor and thus lead to the observed flux variability in blazars. The same considerations apply to a possible neutrino flux from these objects. Equation 10 is strictly only valid for an isotropic emissivity with a power-law spectrum originating within the jet. For different scenarios, e.g. more sophisticated emission geometries [LB85] or external radiation impinging onto the jet (EC models) [Der95], the relation differs.

There are also approaches to take effects of the evolution of AGN over cosmic history into account [Hop+05]. These address problems with the standard unified scheme, e.g. that there are objects which are intrinsically lacking a BLR [Tra01]. A potential evolution scenario for blazars is described in section 3.4.

3.3 SPECTRAL ENERGY DISTRIBUTION

Observations of hundreds of blazars have been performed at radio, optical, x-ray and and gamma-ray wavelengths. The characteristic **S**pectral **E**nergy **D**istribution (**SED**)[5] consists of two peaks separated by several orders of magnitude in energy, and is often called a "double hump" spectrum. As an example, figure 14 shows the SED of blazar *1ES-0229*.

In general, the peak at lower energies is usually located between radio to x-ray frequencies while the peak at higher energies is located in the gamma-ray regime. In order to explain this spectral behavior, two different sets of approaches have been developed over the last decades: *leptonic* and *hadronic* models. In both classes of models, the low-energy peak is explained by relativistic electrons that move in the jet and emit synchroton radiation, giving the reason why this peak is also called "synchroton peak". The difference between both approaches arises in the explanation of the "gamma-ray peak". In leptonic models, the electrons that are responsible for the synchroton

5 An SED curve for radio and optical observations is usually defined in units νF_ν versus ν and is equivalent to $E^2 \cdot \Phi$ which is used for high energy photon or neutrino observations (see section 2.3). The area below the SED (if the previously mentioned units are used) is directly proportional to the overall energy stored in the particles up to a factor of $\log(10)$.

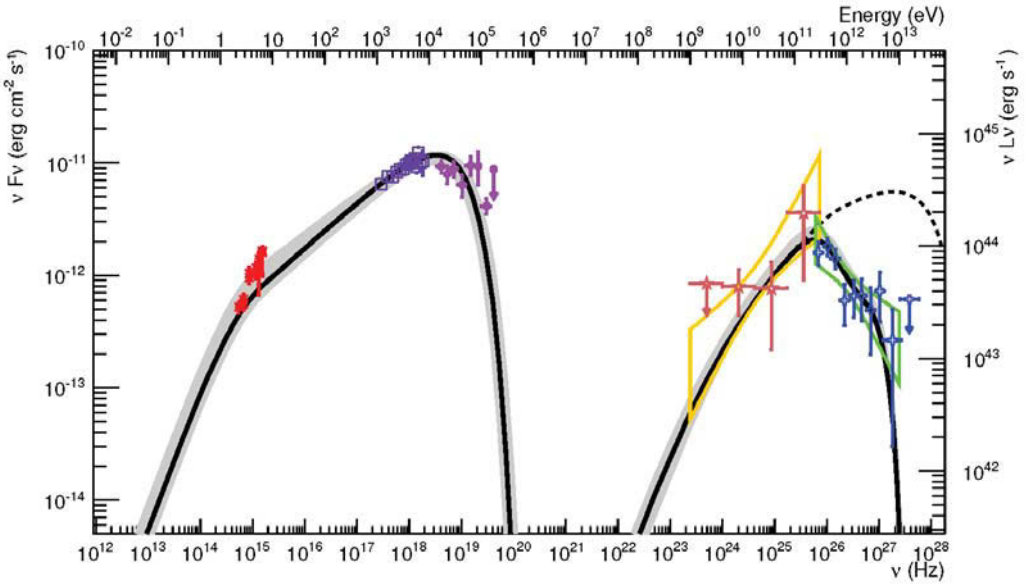

Figure 14: SED of the blazar *1ES-0229*. The data is collected by Swift (red, purple, magenta), Fermi (brown points and yellow butterfly) and Veritas (blue points and green butterfly). The gray band shows several models (of the SSC-type, see text) which all fit the data, while the solid black line indicates the model fit with the lowest χ^2. The dotted black line represents the intrinsic spectrum corrected for absorption effects in the EBL (see section 2.2). Figure taken from [Ali+14].

peak interact with ambient photons via IC-scattering which gain energy in this process (see figure 6b in section 2.2) and end up forming the gamma-ray peak. This has been proposed in various versions, depending on the nature of the photons that take part in the IC-process. **S**elf-**S**ynchroton **C**ompton (SSC) models invoke the synchroton photons generated by the electrons within the jet [Ghi89], and are therefore also called "internal" models. In **e**xternal **c**ompton (**EC**) models photons impinge on the jet from the outside, e.g. originating from the accretion disk [DS93] or the BLR [SBR94] (see figure 13).

The second class of models is called "hadronic models", and explains the gamma rays as outcomes of hadronic interactions (see section 2.1). As a consequence such models also predict neutrinos. The prevailing hadronic models with explicit neutrino flux predictions will be discussed in more detail in section 3.5.

The structure of the SED is used for further classifications. Originally, a classification based on the position of the synchroton peak existed only for BLLac objects. This differentiation into **H**igh-Peaked **BL**-LAC's (HBL's) and **L**ow-Peaked **BL**-LAC's (LBL's) [PG95] was further generalized in 2010 to **L**ow-/**I**ntermediate- and **H**igh-**S**ynchroton **P**eaked Objects (LSP/ISP/HSP) which also includes FSRQs[Fer10b]. The exact definitions of these various classifications, including the BLLac/FSRQ distinction introduced in section 3.1, are summarized in table 2. The combination of the FSRQ/BLLac

Type: Spectral lines [Sti+91]	
Classification	Definition
BLLac	optical EW < 5 Å
FSRQ	optical EW > 5 Å

Type: Synchroton peak [PG95] [Fer10b]	
Classification	Definition
LSP	$\nu_{sync,peak} < 1 \times 10^{14}$ Hz
ISP	1×10^{14} Hz $< \nu_{sync,peak} < 1 \times 10^{15}$ Hz
HSP	$\nu_{sync,peak} > 1 \times 10^{15}$ Hz

Table 2: Summary of of the two blazar classification schemes used in this thesis.

classification and the SED-based LSP/ISP/HSP classification will be used throughout this thesis except when references to older publications require otherwise.

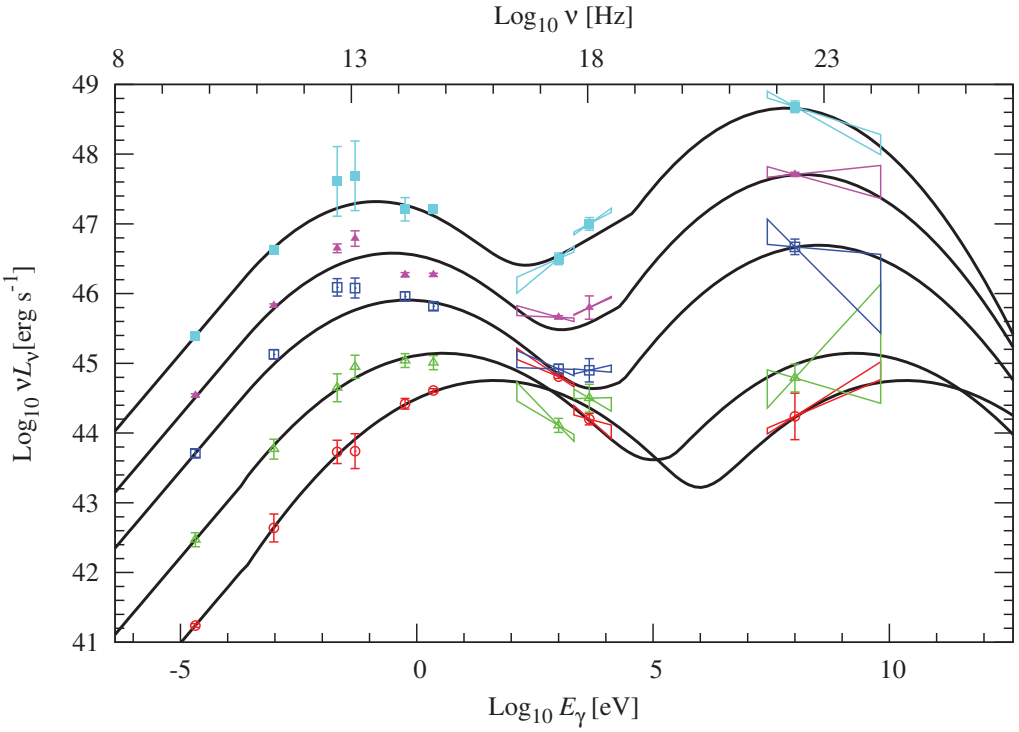

Figure 15: Averaged blazar SED's from over 100 blazars with data from [Fos+98] binned in 5 luminosity categories. The black lines indicate the empirical SED model from [IT09], showing bolometric luminosities of 49.50, 48.64, 47.67, 46.37, and 45.99 (from top to bottom in units $\log_{10}(L_{bol}/\mathrm{erg\,s^{-1}})$. Figure taken from [Ino+10].

Fossati et al. [Fos+98] observed a sequential behavior in the SED positions and peak-to-peak luminosity ratio of over 100 blazars. The higher the bolometric luminosity, the more do the peaks shift towards lower frequencies

and the more the gamma peak seems to gain dominance over the synchroton peak. Figure 15 shows this "blazar sequence" for average spectra of blazars of different bolometric luminosities. The light blue and magenta data corresponds to average LSP spectra, the blue data to an ISP spectrum and the green and red data to HSP spectra. The blazar sequence is an empirical observation but is connected to further studies on evolution, as described in the next section.

3.4 LUMINOSITY FUNCTION, SOURCE COUNTS AND COSMIC EVOLUTION

To describe the cosmological behavior of a class of astronomical objects one defines the Luminosity function $\rho_L(z) = dN/dLdV$, the density of objects over luminosity and volume (comoving volume in the following). The luminosity function is defined for a given energy interval and depends on redshift. When it is integrated over luminosity, it has units of number density, usually referred to in units of Mpc^{-3}. If the number density increases with larger z, one speaks of positive evolution, otherwise of negative evolution. The most general behavior of a luminosity function is called **L**uminosity **D**ependent **D**ensity **E**volution (LDDE), a change of number density and luminosity distribution simultaneously [6]. Blazars in general show LDDE behavior [Aje+12] while sub-populations differ from each other (see end of this section). One can integrate the luminosity function over redshift and/or luminosity, weighted with various functions, to obtain more meaningful "observables". Three such quantities shall be discussed in the following.

The first observable is the flux per steradian observed at earth from the whole population of sources, where the "weighting function" is the observed differential flux of a single source with a given spectral shape. This single-source flux depends linearly on the intrinsic luminosity L_γ and has redshift corrections already included [VPR09]

$$\begin{aligned}\frac{d\Phi}{dE_{0\,\mathrm{iso.}}} &= \frac{1}{4\pi}\int_V dV_{\mathrm{com.}}\int_L \rho_L \frac{d\Phi}{dE_{0\,\mathrm{single}}}\,dL \\ &= \frac{1}{4\pi}\int_z \frac{dV_{\mathrm{com.}}}{dz}dz\int_L \rho_L \frac{d\Phi}{dE_{0\,\mathrm{single}}}\,dL \end{aligned} \tag{11}$$

E_0 is the energy measured in the observer system and $V_{\mathrm{com.}}$ is the comoving volume element that depends on redshift and the cosmological model. The neutrino emission models discussed in section 3.5 make use of this calculation.

The second observable is the luminosity density, defined as

$$\Phi_L(z) = \int_L L \cdot \rho_L\, dL \tag{12}$$

6 This implies a change of normalization and shape of the luminosity function. Shape variation comes from a varying luminosity distribution for different z. Normalization changes if the number of objects per comoving volume depends on z.

It is useful when discussing the total luminosity output at a given redshift, as done towards the end of this section.

The third observable is the "source count distribution" $N(>S)$, the number of sources detectable at Earth above a given integrated photon flux S. It is related to the luminosity function via [Aje+12]

$$N(>S) = \int_z \frac{dV_{com.}}{dz} dz \int_{L_{min.}=f(S,z)}^{\infty} \rho_L \, dL \tag{13}$$

Here, the lower integration bound over luminosity is parametrized as a function of the observed integrated flux S that arrives at earth for the given luminosity L and redshift z. Starting with $N(>S)$, one can construct the differential source count dN/dS via differentiation and the corresponding quantity $S \cdot dN/dS$. The latter is discussed again in section 7.3 as it can be used to determine the respective fractions of the intensity of a population (e.g. of gamma-ray blazars) that can and cannot be resolved into particular sources.

The blazar sequence described in section 3.3 has been the starting point for the consideration of a generalized evolutionary scenario (the "evolutionary blazar sequence"), in which FSRQs are thought to evolve into BLLacs over cosmic time, changing from rapid accretion during a FSRQ phase which dominates for around one billion years, to a long-lived "starvation" phase which is represented by the majority of the BLLacs, the HSP-BLLacs [BD02], [CD02]. The observed blazar sequence in figure 15 is thought to contain all intermediate stages [Ghi+11] of the evolutionary sequence: FSRQs $\rightarrow$ LSP-BLLacs $\rightarrow$ ISP-BLLacs $\rightarrow$ HSP-BLLacs.

Recently, this picture got further observational support [Aje+14] by comparing the luminosity and number density evolution of the two blazar subclasses in gamma-ray emission. Figure 16 shows the luminosity density and number density of FSRQs and BLLacs in dependence on the redshift. A part of the luminosity output of BLLacs (the LSPs) is peaking at similar redshifts as the FSRQs, while towards lower redshifts a complete reverse in the BLLac curve indicates the dominance of another BLLac sub-population (figure 16a). This can be attributed to the HSP objects, which gain in number density towards $z = 0$, i.e. show negative evolution (figure 16b). It should be mentioned that there are also authors [Gio+12] which interpret the blazar sequence to come about due to selection effects, mostly by missing high redshift BLLac objects. In this picture, there exist two separate groups of blazars which are not connected via evolution: One are the HSP-BLLacs, which generally show lower total luminosity. The other group combines FSRQs and LSP-BLLacs, and the difference between them only comes about due to jet emission in LSP-BLLacs which swamps any emission lines. In all other properties they are assumed to be physically equivalent, which is a rather similar interpretation as in the standard evolutionary blazar sequence. Some of the aspects of the evolutionary blazar sequence and the close similarity between FSRQs and LSP-BLLacs are considered in the definition of the blazar populations for this analysis in section 7.2.

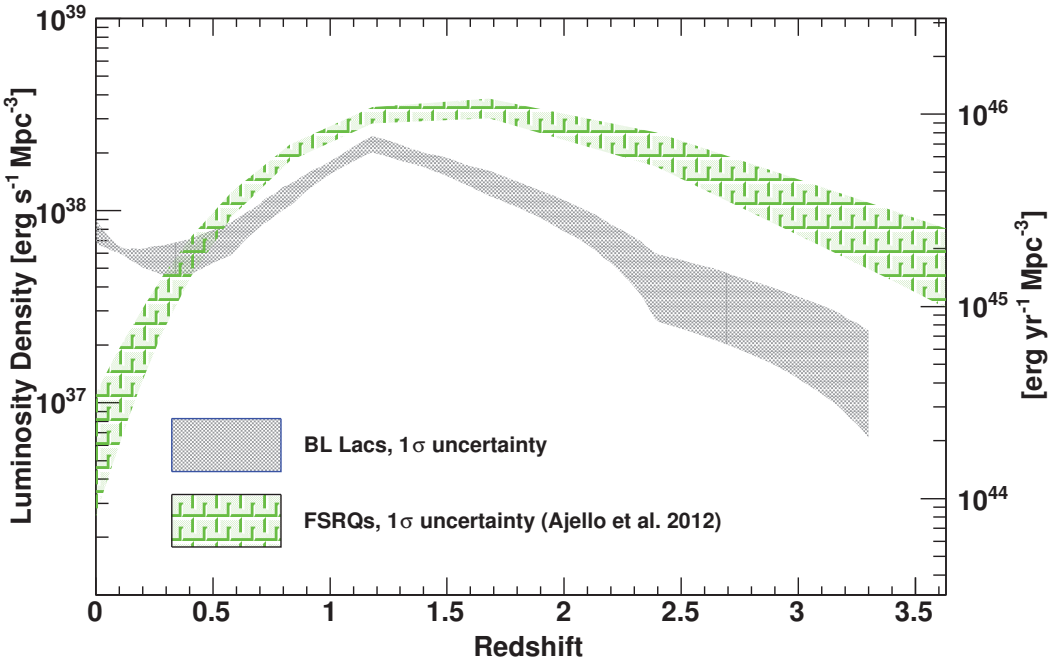

(a)

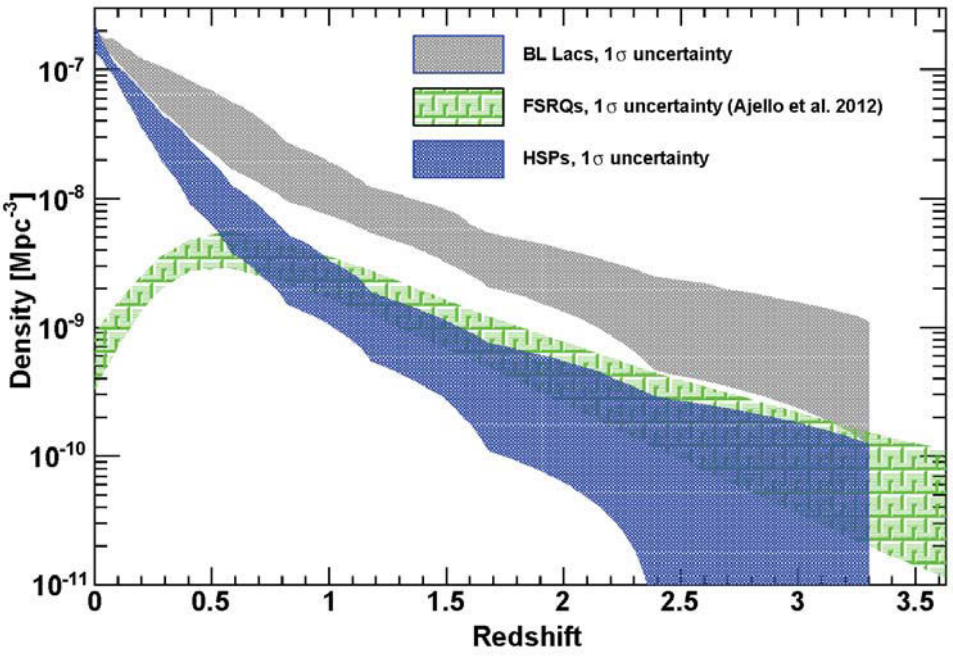

(b)

Figure 16: Luminosity (a) and density (b) evolution for BLLacs and FSRQs. The figures are taken from [Aje+14].

3.5 NEUTRINO EMISSION

In order to produce high energy neutrinos, hadrons (or for simplicity protons) have to be accelerated to sufficiently high energies within the jet. In all

the models that will be discussed in this section, the high energy protons are simply "injected" by some unspecified mechanism, as particle acceleration within jets and jet dynamics itself are complex, and usually treated separately. Nontheless, the possible origin of high energy protons within a jet shall be briefly discussed here.

If the jet is Poynting-Flux dominated at its base [BZ77], the energy needs to be transferred to the kinetic energy of particles. This might happen in gradual "bulk acceleration" of the whole jet as inferred from MHD solutions [Gra12] or in isolated acceleration regions within the jet. One potential mechanism might be acceleration in shock fronts (described in section 2.1), which occur within the jet. These could be present due to shocks formed by MHD instabilities [BK79] or due to stochastic jet launching events that interfere in the outer parts of the jet and form random patterns of shocked regions [Spa+01] [Rac+10]. Another potential mechanism is magnetic reconnection, a phenomenon originally developed to explain solar flares [Par57]. Here, electromagnetic energy is dissipated over a short timescale into kinetic particle energy due to interacting boundaries of different field configurations, which accelerate particles in rather confined E-field geometries when the boundaries interact. Both shocks (section 2.1) and magnetic reconnection [SS14] can naturally lead to power-law proton spectra which potentially serve as the basis for neutrino emission models.

Neutrino emission models can be either of the p-p or p-γ type, referring to the primary hadronic interaction (see section 2.1).

p-p scenarios for blazars [SPS02] [NR09] are under-represented in the literature, because the matter density in jets is assumed to be too low [Man95] and they do not naturally require high energy protons and thus not necessarily offer an explanation for UHECRs.

More prominent are p-γ neutrino models, which naturally require UHE protons for typical photon energies in the jet environment to surpass the photo-production threshold and produce gamma rays that explain the gamma-ray peak. For example, protons above an energy of $\approx 10\,\mathrm{PeV}$ are required for interactions with UV photons and even higher for lower photon energies [NMB93]. The p-γ models are categorized in a similar fashion as leptonic models (see section 3.3) based on the target photon fields. Target photons can stem from "generic regions"[7] [HZ97], from inside the jet [Man95] [Mue+03] [BBR05] [TGG14] , from the accretion disk [Pro97], from the BLR [AD01] , from internal and several external regions combined [MID14] or from the EBL when the interaction happens outside the generation region [Ess+10]. Nearly all models assume a simple jet (with one radiation zone). The exception is the *Tavecchio et al.* model [TGG14][TG15] where the dominant target photon field stems from an outer layer (the sheath) in an overall two-zone model with a spine-sheath geometry. The case where the target photons stem from the EBL would predict more "fuzzy" sources

7 "Generic regions" in this context means that the photons can come from any region within the AGN and a particular origin is not explicitly mentioned.

due to magnetic deflection during the propagation of the protons. In addition to the previous models, there are also calculations which implicitly make use of the possible correlation between AGN and high energy cosmic rays (e.g. [BB09]) , which are not considered in the following.

Among all models in the literature, the ones of interest for this thesis are the ones that have been calculated for an entire class of blazars, not just a particular single source. Table 3 summarizes the different diffuse predictions and their respective normalization mechanism.

Publication	Source photons	Calculation
Mannheim (1995) [Man95]	synchrotron	generic lum. function, normalized on EGB for (A) E > 100 MeV (B) 1 - 100 MeV
Protheroe (1997) [Pro97]	accretion disk	γ lum. function ν/γ-correlation
Halzen et al (1997) [HZ97]	generic	normalized on γ-flux ratio EGB/Mkn421
Mücke et al. (2003) [Mue+03]	synchroton	radio lum. function, ν/radio-correlation (no primary γ-correlation)
Becker et al. (2005) [BBR05]	synchroton	radio lum. function normalize via model in [FB95] (no primary γ-correlation)
Murase et al. (2014) [MID14]	synchr./BLR/ Torus/ Accretion Disk	γ and X-Ray lum. function for numerical modeling (no primary γ-correlation)
Tavecchio et al. (2014) [TGG14][TG15]	layer radiation (Spine-Sheath-geometry)	GeV-blazar number density function for numerical modelling (no primary γ-correlation)

Table 3: Overview of models for the diffuse $\nu_\mu + \overline{\nu}_\mu$-flux from blazar populations. The middle column lists the source photons taking part in the photo-meson interaction. The right column summarizes the flux calculation and a potential correlation to gamma-rays.

These "population predictions" can be broadly classified into two groups. In the first group, one calculates the neutrino spectrum for a single source, given specific assumptions about the geometry and physical processes. Then, one takes this spectrum as the defining one for the population and assumes a correlation to gamma-ray emission from neutrino pion decay via the same

parent process. Finally, one integrates over the corresponding gamma-ray luminosity function and eventually normalizes the result to match the EGB. A strict proportionality of the resulting neutrino flux to the γ-ray flux is implicit in these models. All predictions from the 1990's share this property.

In the second group, which consists of all the newer models starting with the one by *Muecke et al.*, the neutrino flux is primarily proportional to a quantity other than γ-rays. A strict proportionality of the resulting neutrino flux to the γ-ray flux is therefore not implicit in this case, but can still happen indirectly. For example, in the *Murase et al.* model, while the dominant gamma-ray emission is leptonic, the brightest gamma-ray emitters are still expected to produce the largest neutrino flux[MID14].

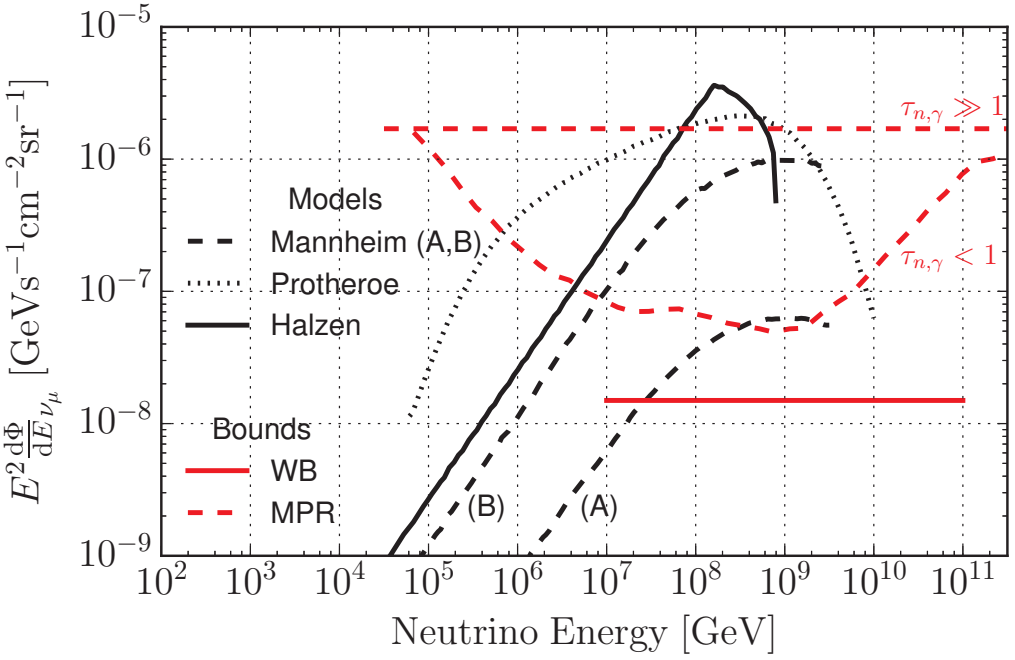

Figure 17: Models (black) and upper bounds (red) for the diffuse $\nu_\mu + \overline{\nu}_\mu$-flux emission from generic blazars. Predictions are plotted as shown in the original publications.

In addition to these specific models, two usually cited "neutrino upper bounds" do exist that apply to the maximum allowed diffuse neutrino flux from AGN jets[8]. The first one ("WB-bound", from Waxman,Bahcall) [WB99] is based on the cosmic ray production rate above EeV energies which is then translated to the maximal neutrino energy production rate and an upper bound on the diffuse neutrino flux given the observed $\geqslant$ EeV cosmic-ray flux. The derivation assumes optical thin photo-meson sources, such that

8 Strictly speaking, the model calculations that normalize the neutrino expectation to the observed gamma-ray background (e.g. *Mannheim*) are in principle also "upper bounds", since they imply that the total blazar gamma-ray emission is of hadronic origin and explains the total EGB.

the majority of protons can escape at the highest energies without interacting. Also, it is strictly only valid above neutrino energies of 10 PeV but can be interpolated to lower energies under the assumption of an E^{-2} spectrum [BW01].

The second one ("MPR-bound"[MPR01], from Mannheim, Protheroe, Rachen) assumes that strong magnetic fields in the source prevent protons from escaping at high energies, thus the connection to high energy cosmic rays is drawn via neutron escape. The neutron production rate places the central role which is then related to the emerging neutrino, gamma-ray and cosmic-ray flux flux. The resulting bounds are then normalized via both gamma-ray and cosmic-ray observations for different energy regimes, depending which one is more constraining. The superposition of all energy regimes gives the upper bound. Additionally, upper bounds for generic optically thick sources and specifically for BLLacs/FSRQs are calculated.

Figures 17, 18 and 19 summarize the previously described theoretical models or upper bounds for the diffuse 1-flavor neutrino flux from generic blazars, from BLLacs and from FSRQs, respectively.

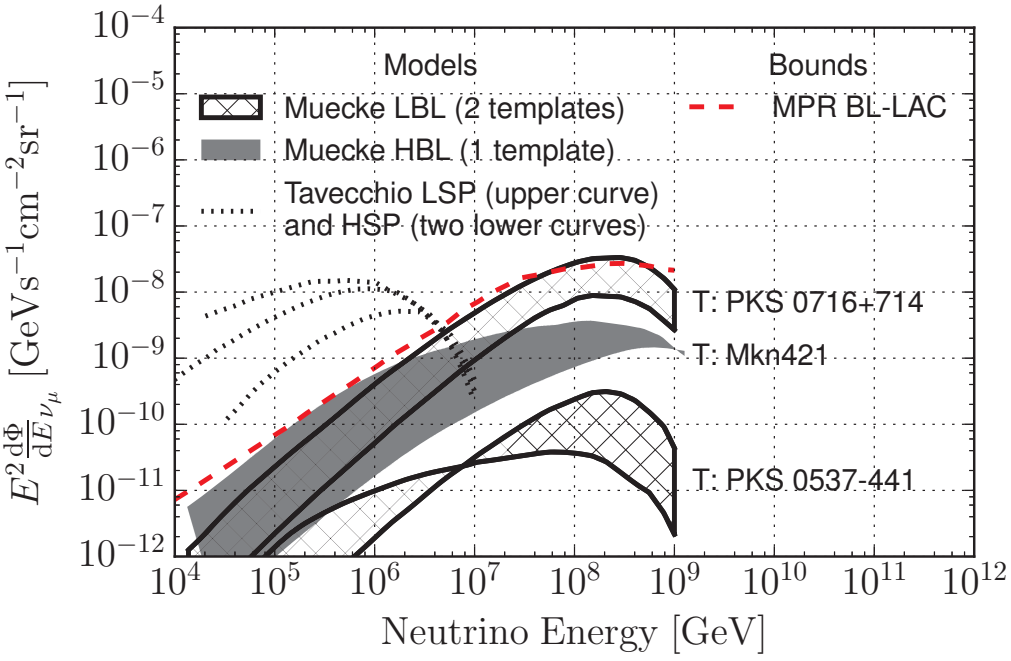

Figure 18: Models (black) and upper bounds (red) for the diffuse $\nu_\mu + \overline{\nu}_\mu$-flux emission from BLLac objects. Predictions are plotted as shown in the original publications, modified to the 1-flavor expectation if necessary[a].

a This assumes an equal partition of flavors for the neutrinos arriving at Earth. The *Tavecchio et al.* per-flavor flux is plotted with equal magnitude as the all-flavor prediction in the publication due to a normalization mistake in the paper.

For the BLLac models from *Muecke et al.*, the specific source templates from numerical modelling of PKS 0716+714/PKS 0537-441 (LBL) and Mkn421

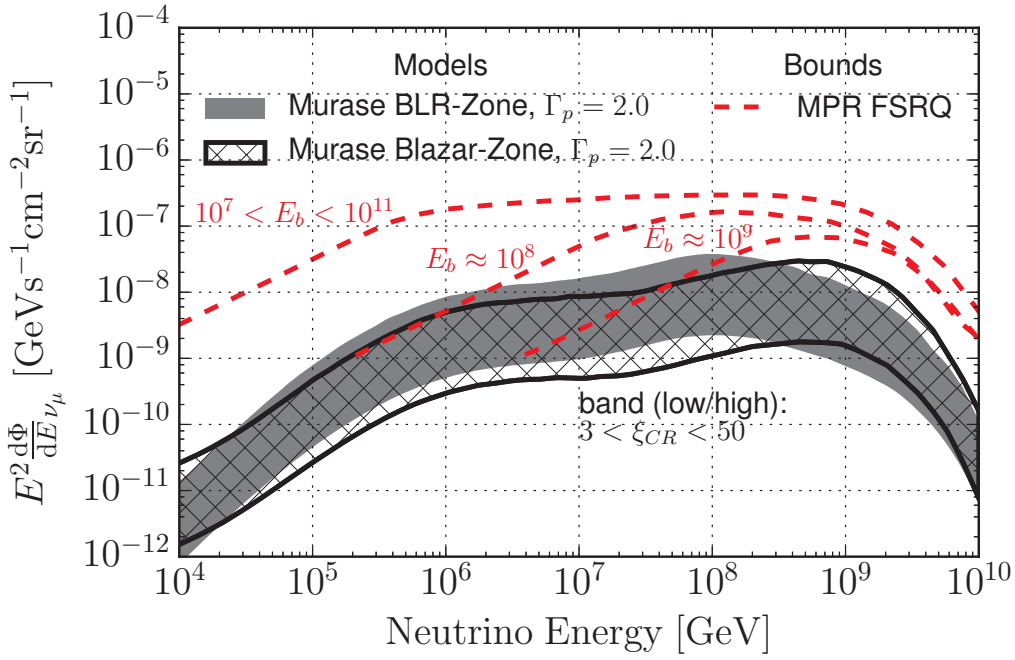

(a)

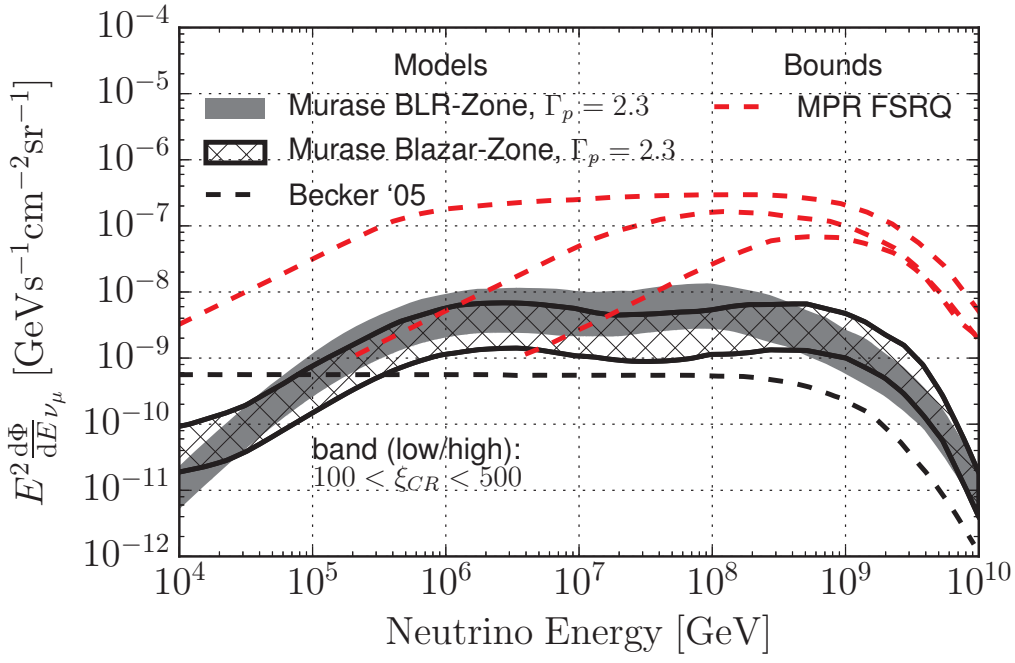

(b)

Figure 19: Models (black) and upper bounds (red) for the diffuse $\nu_\mu + \overline{\nu}_\mu$-flux emission from FSRQs. Predictions are plotted as shown in the original publications, modified to the 1-flavor expectation if necessary[a].

a This assumes an equal partition of flavors for the neutrinos arriving at Earth. The calculation applies to the *Murase et al.* model.

(HBL) are being used. The depicted model ranges come from variations of the target photon density and emission region size. The predictions from *Tavecchio et al.* are plotted a factor of three larger than in the original paper due to a normalization error.

The FSRQ models from *Murase et al.* are shown for different proton spectral indices of -2.0 and -2.3. Two neutrino production scenarios are considered for the former one. 'BLR-Zone' denotes a model in which neutrons escape the inner jet and subsequently interact with external radiation fields in the the BLR/dust torus to produce neutrinos. 'Blazar-Zone' denotes neutrino production within the jet, involving internal synchroton fields and external radiation impinging onto the jet. ξ_{CR} denotes the "Cosmic-ray loading factor", and is defined via $\xi_{CR} = L_{CR}/L_{Rad}$ as the ratio between cosmic-ray and radiation luminosity within the source. The expected neutrino flux is directly proportional to this factor, where the band in the plots denotes the values for ξ_{CR} that have been considered in the publication.

The MPR FSRQ bounds are derived for different break energies E_b (below which the proton flux becomes very hard). Shown is the result for $E_b \approx 10^9$GeV, $E_b \approx 10^8$GeV and for a superposition of the bounds derived for break energies between 10^7GeV and 10^{11}GeV. The WB-bound in principle already excludes the predictions of the generic blazar models (as emphasized by the authors). However, due to the assumptions being made, e.g. the escape of high energy protons from the jet, such statements have been criticized by the MPR authors [MPR01].

The different implicit assumptions for the models and bounds that are being made are the reason all the results differ by 2-3 orders of magnitude. An experimental check is desired. The implications from this work are discussed in section 10.2.6.

4

THE ICECUBE NEUTRINO OBSERVATORY

This chapter describes the detection principles, structure and data acquisition of the "IceCube Neutrino Observatory", a 1 km^3 sized neutrino detector located a few hundred meters away from 0°0′0″ S within the Antarctic ice.

4.1 NEUTRINO DETECTION FUNDAMENTALS

4.1.1 *Neutrino interactions*

Neutrino interactions are broadly classified into "Charged Current" (CC) and "Neutral Current" (NC) modes. Figure 20 displays schematically the scattering of a muon neutrino with a nucleus. The exchange via a W (CC-mode) or Z (NC-mode) boson are the only two possibilities neutrinos can interact with other matter. The large masses (>80 GeV) of these two gauge bosons appear in the respective Feynman propagator in the denominator and effectively lead to small cross sections and the elusive nature of neutrinos. While the NC reaction is characterized only by momentum transfer to the scattering target, the neutrino additionally transforms into its corresponding lepton (e, μ, τ) in the CC reaction. Figure 21 shows the cross sections for the **d**eep **i**nelastic **s**cattering (**DIS**) with nuclei, the dominant interaction mode above 10 GeV [FZ12] which is relevant for IceCube. Elastic scattering with bound electrons at these energies is in general more than an order of magnitude suppressed, except for the case of resonant W production from $\overline{\nu_e}$ around 6 PeV [Bha+11] which is not included in the plot. Generally, CC interactions are a factor three more likely to happen than NC interactions. Also shown is the threshold line where the Earth becomes optically thick for a neutrino traveling through it at a given direction (zenith angle) and energy from the viewpoint of a detector 2 km below the surface.

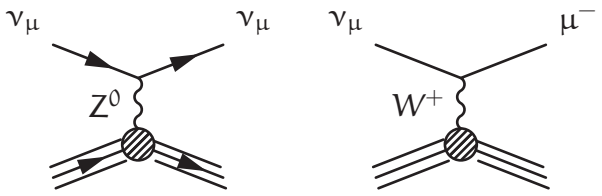

(a) Neutral Current interaction

(b) Charged Current interaction.

Figure 20: Feynman diagrams depicting inelastic neutral and charged current interactions of a muon-neutrino interacting with a nucleus.

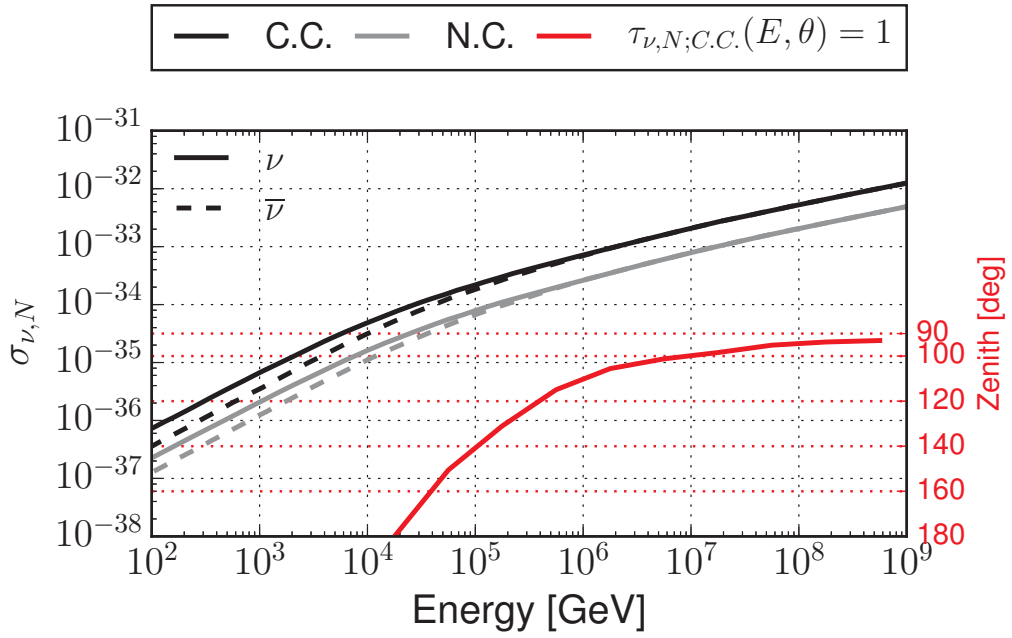

Figure 21: DIS Cross sections between 100 and 1×10^9 GeV. The red curve indicates where the optical depth for neutrinos crossing the earth is equal to unity given a particular direction and energy (using the PREM [DA81] Earth density model).

4.1.2 *Energy losses and Cherenkov light*

Once an interaction has taken place, the energy depositions by the subsequently created charged particles are the means by which IceCube detects a neutrino. These charged particles are typically relativistic and move faster than the speed of light in ice, which results in emission of so called "Cherenkov light" [Čer37]. Cherenkov light is emitted in a coherent light front at a certain angle with respect to each charged particle that depends on the refractive index n and velocity β via $\cos(\theta) = \frac{1}{\beta \cdot n}$, and can thus be used to infer the particles direction if measured accurately. This relation can also geometrically be understood as the superposition of Huygens elemental waves as depicted in figure 22. The spectrum of the emitted light peaks in the optical and UV regimes, following a power law spectrum as [Oli14]

$$\frac{d^2N}{dx d\lambda} = \frac{2\pi\alpha z^2}{\lambda^2}\left(1 - \frac{1}{\beta^2 n(\lambda)^2}\right) \tag{14}$$

, i.e. short wavelengths dominate.

One can categorize the possible energy deposits in IceCube into three generic classes.

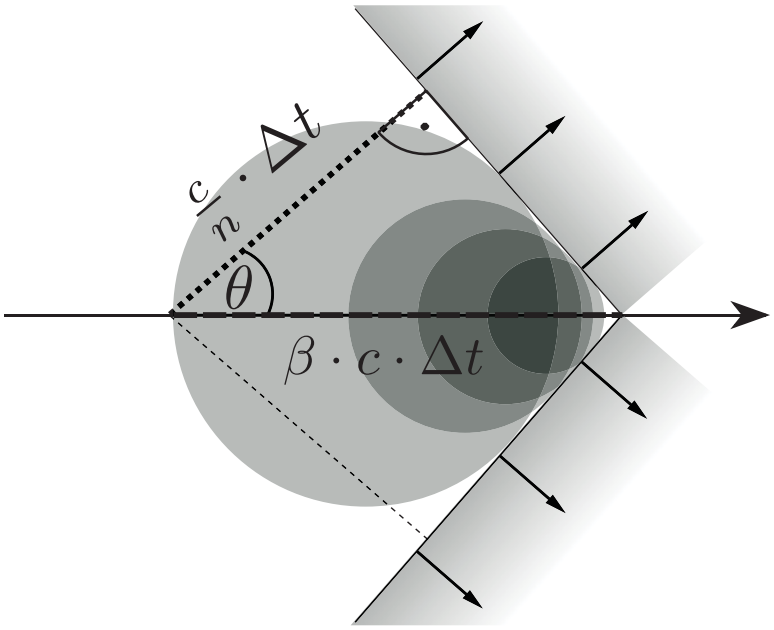

Figure 22: Schematic depiction of Cherenkov radiation. In a fixed time interval Δt the particle traverses a larger distance (dashed) than light in the medium (dotted).

- Hadronic showers/cascades

  Hadronic showers are generated when a nucleus is destroyed during a neutrino interaction or when a charged secondary particle (i.e. a muon) interacts inelastically with a nucleus. They dominantly consists of the secondary hadrons emerging from the reaction and their corresponding decay chains.

- Electromagnetic showers/cascades

  An electromagnetic shower is initiated by an electron or photon (EM sub-showers from π^0 are usually called "hadronic"), which developes as a shower in the interplay between bremsstrahlungs losses of electrons and pair production by photons. Because of the relatively high density of ice, an electromagnetic shower in ice is confined to a few meters at TeV energies. Only at multi-PeV to EeV energies the shower gets spread out due a decrease in bremsstrahlungs and pair production cross sections [Mis93] which results in a longitudinal extension of around 100 m at several EeV.

- quasi-continuous energy loss of a track

  In addition to rather confined showers, muons and tau leptons exhibit quasi-continuous energy loss regimes, in which they loose their energy predominantly via ionization smoothly along the track. For muons in ice, for example, this happens below the "critical energy" of around 1 TeV, while for τ-leptons this threshold is higher [CR04] . Ionization processes can incidentally still result in electrons with rel-

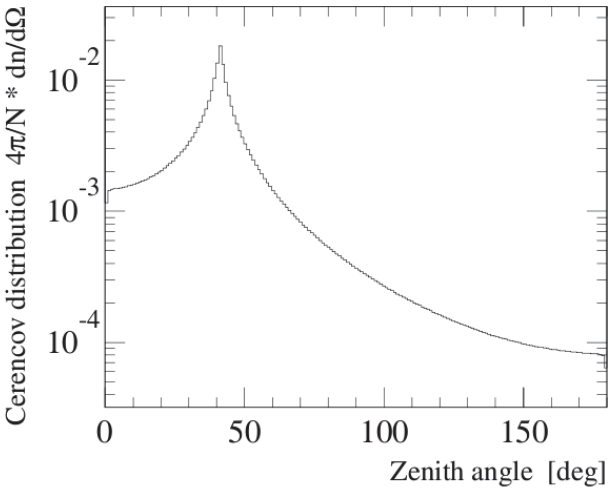

(a)

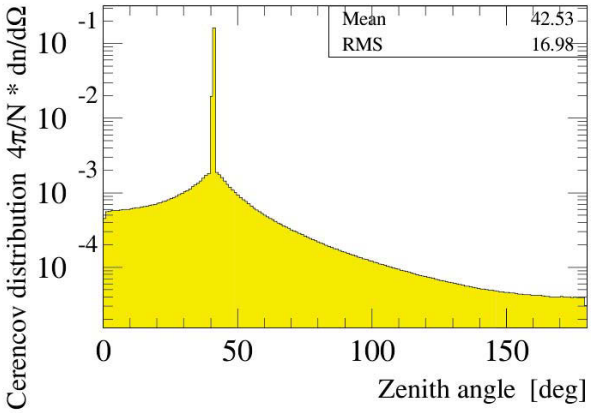

(b)

Figure 23: Normalized angular Cherenkov profiles for (a) an electromagnetic shower and (b) a minimally ionizing muon track. Adapted from [Wie95].

ativistic energies, so called δ-electrons, but a quasi-continuous view is usually applicable. This quasi-continuous energy loss is in fact always present, even at higher energies, but it becomes subdominant compared to stochastic losses (see next section).

Since all the above energy losses involve a multitude of charged particles, sometimes slightly offset from the initial particle direction, one can describe the resulting Cherenkov Light with effective Cherenkov profiles emerging as the superposition from the individual particles. Figure 23 depicts results from simulations [Wie95] showing this effective emission angle profile for Cherenkov light for an electromagnetic shower and a quasi-continuous energy loss of a muon track. The track profile is sharply peaked at the nominal Cherenkov angle since the muon dominates the emission over additional δ-electrons. In contrast, the shower emission is more spread out. At energies above 100 GeV, the general shape of the Cherenkov profile of a

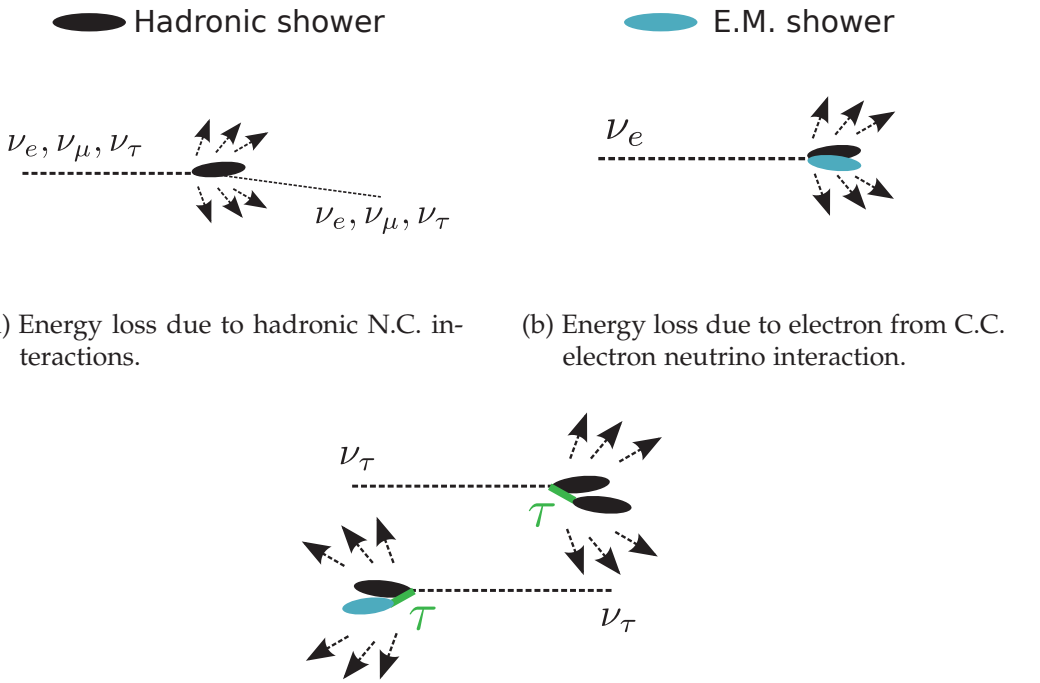

(a) Energy loss due to hadronic N.C. interactions.

(b) Energy loss due to electron from C.C. electron neutrino interaction.

(c) The dominant energy deposition of a tau: shower signature either via hadronic decay or leptonic decay into an electron.

Figure 24: Shower-like event signatures from neutrino interactions. Arrows indicate emerging Cherenkov light.

hadronic shower can be assumed to be similar to its electromagnetic counterpart, while the light yield is typically lower.

4.1.3 *Event signatures*

Event signatures in IceCube emerge as superpositions of the energy losses described in the previous section. These can be classified into two classes: Shower-like and Track-like event signatures. In the following, the most common physical origins for these signatures are outlined. [1]

4.1.3.1 *Neutrino-induced events*

The shower- and track-like signatures for neutrino-induced events are summarized in figures 24 and 25.

N.C.-interactions transfer a fraction of the neutrino energy to the nucleus which is destroyed and leaves behind a hadronic shower (figure 24a).

1 Only idealized signatures are covered, while in general a continuous transition between observed track-like and shower-like signatures exist. Tracks can always appear fractional within the active volume either because they are starting or ending within, or because they are clipping a corner.

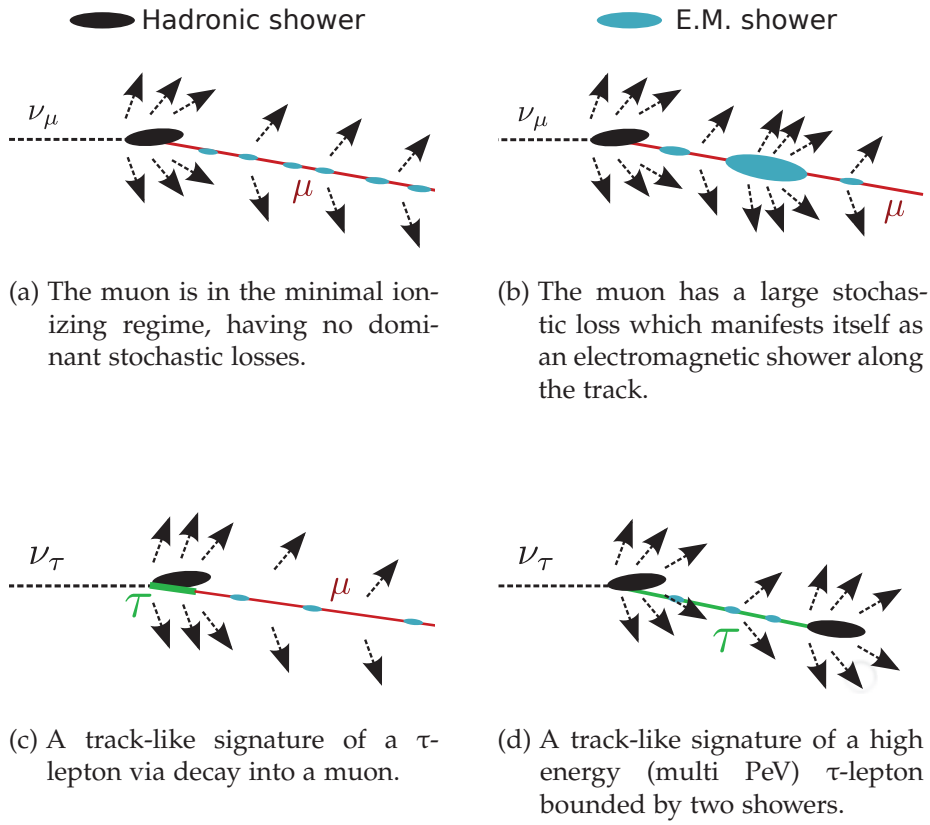

(a) The muon is in the minimal ionizing regime, having no dominant stochastic losses.

(b) The muon has a large stochastic loss which manifests itself as an electromagnetic shower along the track.

(c) A track-like signature of a τ-lepton via decay into a muon.

(d) A track-like signature of a high energy (multi PeV) τ-lepton bounded by two showers.

Figure 25: Track-like event signatures from neutrino interactions. Arrows indicate emerging Cherenkov light.

This type of interaction affects all neutrino species in a similar way which means shower-type signatures might stem from any neutrino species. C.C.-interactions also produce a hadronic shower, but the corresponding charged lepton will also be visible. Depending on the species (e, μ, τ) the emerging energy loss patterns have to be differentiated.

ELECTRON NEUTRINOS An electron will always initiate an electromagnetic shower (see figure 24b).

MUON NEUTRINOS A muon has a much higher mass than the electron and consequently has much lower Bremsstrahlungs losses which leads to its penetrating character. In the quasi-continuous regime stochastic losses are not relevant (see figure 25a) and smooth track-like signature is visible. Above the critical energy, however, stochastic losses along the track can substantially contribute to the Cherenkov emission (see figure 25b). The stochastic losses split up into bremsstrahlung, photo-nuclear losses and e^+/e^- pair production [CR04]. Muon signatures represent the most relevant ones for this thesis.

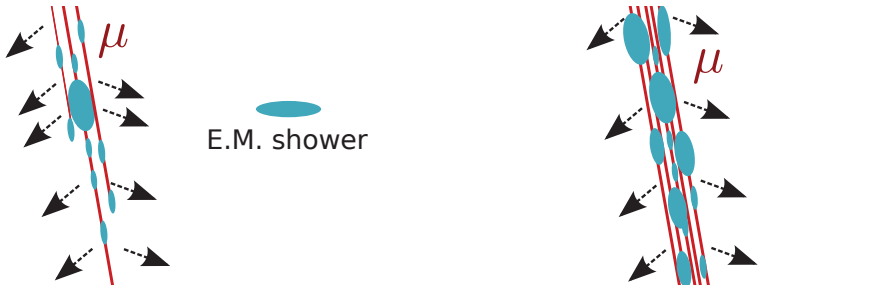

(a) One muon dominates the bundle and the track signature is dominated by its stochastic losses.

(b) The energy losses of individual muons average out.

Figure 26: Illustration of typical stochastic and smooth event signatures of muon-bundles.

τ-NEUTRINOS A τ-lepton has a much shorter lifetime and will thus dominantly decay before travelling a large distance. In 65% of the cases, the $\tau-$decay will proceed hadronically, leading to a hadronic shower at the decay point. The other 35% split up almost equally between the leptonic decays to $e + \nu_e$ and $\mu + \nu_\mu$ [Oli14]. Thus, in 83% of all cases a singular shower (electromagnetic/hadronic) will emerge at the decay point (fig. 24c) while in 17% a muon track will continue (fig. 25c). Importantly, the length of the tau before decay is a function of its energy, reaching a length of $50\,\mathrm{m}$ at 1 PeV or $500\,\mathrm{m}$ at 10 PeV (the length growing linearly up to 1 EeV) [CR04] which results in (semi)track-like τ-lepton signatures bounded by showers. The τ-signatures thus vary strongly with energy and exhibit many different topologies. Assuming a 1/1/1 flavor composition, track-like ν_τ-signatures are sub-dominant in a track selection by at least a factor of 6 compared to ν_μ, and would additionally only contribute at very high energies. In this analysis they will be neglected. The effect will be discussed again in the context of systematics in section 10.2.1.

4.1.3.2 *Atmospheric muons*

As already depicted in figure 4 in section 2.1, muons from charged meson decays originating in cosmic ray showers can penetrate kilometers below the surface. In general, several such decays can happen from one primary interaction and form a bundle of muons that arrives at the detector. For low-mass primaries (e.g. protons) these bundles tend to be energetically dominated by a single muon while for higher mass primaries (e.g. iron) the bundles often consist of many muons with comparable energies. This results in a family of track-like signatures, starting from the case where one muon in the stochastic regime dominates the bundle energy loss (figure 26a) up to the case where the whole bundle appears as a quasi-continuous track either because the individual muons are not yet in the stochastic regime or their stochastic losses average out (figure 26b).

In contrast to neutrino-induced signatures, muon bundles can only arrive as down-going tracks (zenith angles < 90°) because the overburden of rock and ice stops all muons for upgoing directions. Atmospheric muons are an important background for this thesis and are discussed again in section 6.

4.2 THE DETECTOR

4.2.1 *Construction*

GEOMETRY The Observatory consists of an "In-Ice" Cherenkov detector and a surface Air Shower Array called "Ice-Top". The In-Ice detector consists of 2.5 km long cables ("strings") buried vertically in the ice. Attached to each of these strings are 60 Digital Optical Modules (DOMs) between 1450 m and 2450 m depth that serve as light detection units. It has been constructed over a period of several years starting in late 2005 and finishing in early 2011. During this phase data has already been collected while each year a certain amount strings were added to the array. A side view of the final detector is shown in figure 27a and a top view of the geometrical configuration for the last 3 years of construction is depicted in figure 27b.

The work described in this thesis makes use of these last 3 years until completion, called "IC-59", "IC-79" and "IC-86" respectively, where the number behind the "IC" stands for the number of total strings deployed in the particular configuration. The horizontal module spacing between strings is about 125m while the vertical spacing between modules is about 17m, leading to an effective minimal neutrino energy threshold of about 100GeV. A few hundred meter separate the lower end of the detector from the bedrock. In the inner part of the detector in the final configuration, 8 strings have been submerged with a denser spacing and using higher Quantum Efficiency DOMs. The instrumented depth of these "DeepCore" DOMs is chosen such, that it lies in a particular dust-free region of the ice (see section 4.2.2). At the surface above 81 strings, 2 Surface "tanks" have been constructed. Each of them contains two of the same types of DOMs that were lowered into the ice. The total of 162 of these tanks makes up the "Ice-Top" surface array, a surface detector for air shower measurements which is utilized for muon background reduction in this thesis.

THE DIGITAL OPTICAL MODULE The Digital Optical Module (DOM) is the elementary detection unit of the detector, see figure 27a. It contains a 25 cm diameter **p**hoto**m**ultiplier **t**ube (PMT), UV/optical LED's for calibration, and an on-board mainboard for immediate digitization of observed signals [Ice09] . The whole structure is housed in a pressure sphere to resist the hydrostatic pressure of the deep ice. In order to allow an optimal photon transmission from the glass sphere to the PMT, an optical gel layer is inserted that reduces photon loss between the different surfaces. A metal grid surrounding the PMT ensures an optimal shielding from the

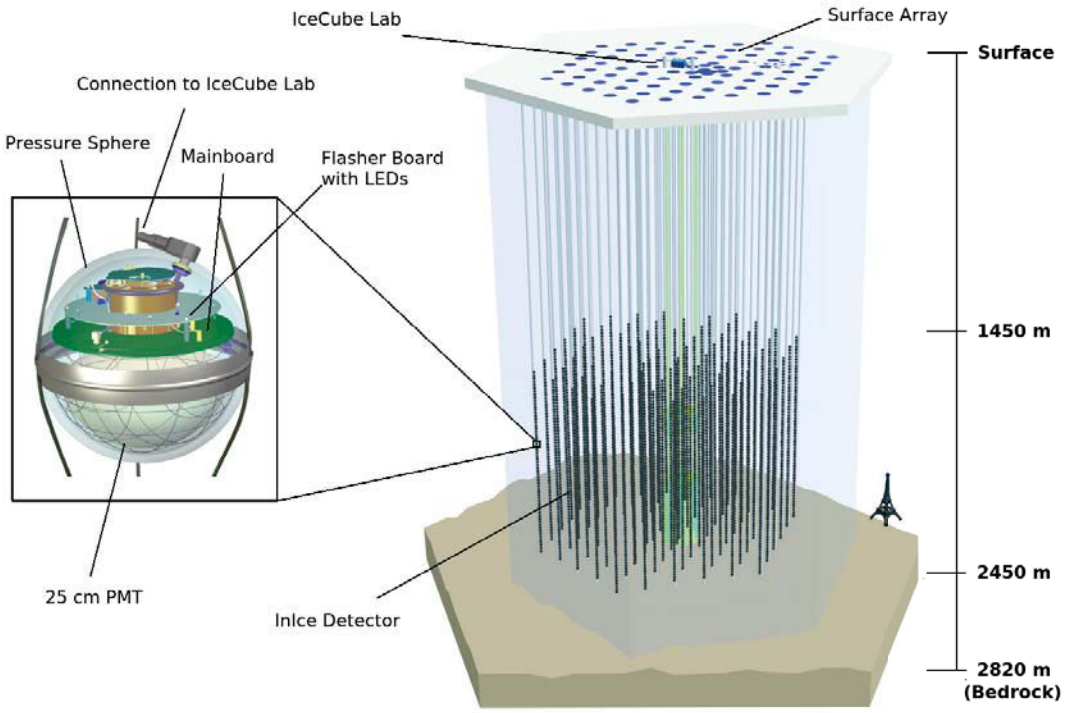

(a) Side sketch of full detector with a zoom-in onto a DOM and its vital components.

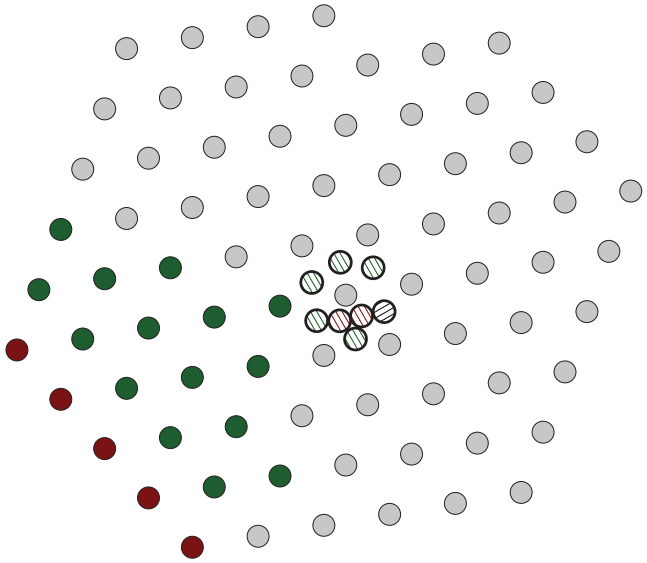

(b) Top sketch of the detector. The color coding shows the strings that have been added in the respective configuration: gray for IC-59, green for IC-79 and red for IC-86. The DeepCore strings are highlighted.

Figure 27: Geometry and construction of the IceCube Neutrino Observatory.

Earth magnetic field. The photon detection efficiency for the PMT is peaking at 25% at wavelengths around 390 nm [Ice10]. PMTs that are used in the DeepCore DOMs have a quantum efficiency that is roughly 40% higher relative to the standard PMTs. PMT noise due to cathode thermionic electron emission, radioactive decay of ^{40}K and scintillation in the glass sphere and ranges between 500Hz for normal PMTs up to 700Hz for "High-**QE** (**Q**uantum **E**fficiency)" PMTs [Sch10].

Each DOM acts as an independent detector that works autonomously and sends its digitized output via cable to the IceCube laboratory at the surface where the data is studied collectively. A description of the data acquisition starting with photons hitting the DOM, digitization and the subsequent data processing is given in section 4.2.3.

4.2.2 *Properties of the Antarctic ice*

The Antarctic ice represents the active volume of the detector and therefore needs to be studied in terms of its optical properties for Cherenkov photons. Below 1400m where the ice pressure has practically eliminated all air bubbles, it is one of the most transparent solids known for the frequency range from 200-400 nm [Pri06]. On the other hand, so called "dust-logger" measurements have revealed volcanic ashes and dust deposits in different depths [Bra+05] rendering the exact understanding of light propagation highly non-trivial. In general, the properties of interest for photon propagation in a transparent medium are scattering and absorption behavior. The scattering in the Antarctic ice can be modelled by MieScattering [Mie08] on target air bubbles or dust grains. The interesting quantity in this respect is the effective scattering length [AMA06] (and its inverse, the effective scattering coefficient), which is defined as

$$\lambda_e = \lim_{n\to\infty} \lambda_s \cdot \sum_{i=0}^{n} \langle \cos(\theta) \rangle^i = \lambda_s \cdot \frac{1}{1 - \langle \cos(\theta) \rangle} \tag{15}$$

λ_e is the effective scattering length, λ_s the average scattering length between two consecutive scattering points and $\langle \cos(\theta) \rangle$ the average of the cosine of the scattering angle between two consecutive scatter points. It describes the average distance after which the intensity has dropped by a factor of e due to scattering. The interesting quantity in the context of absorption is the absorption length (and its inverse, the absorption coefficient), defined as the distance after which the an incoming light beam has dropped in intensity by a factor of e due to absorption. Based on LED "flashing" events at particular DOM positions, one of the latest fit results to determine the ice properties over the whole vertical length of IceCube is described in [Ice13b]. For this fit, the ice is modelled in 10 m layers, where each layer is assumed to be homogeneous along the horizontal direction and shares one common absorption and scattering coefficient. Additionally, four other parameters are fitted to capture normalization factors and

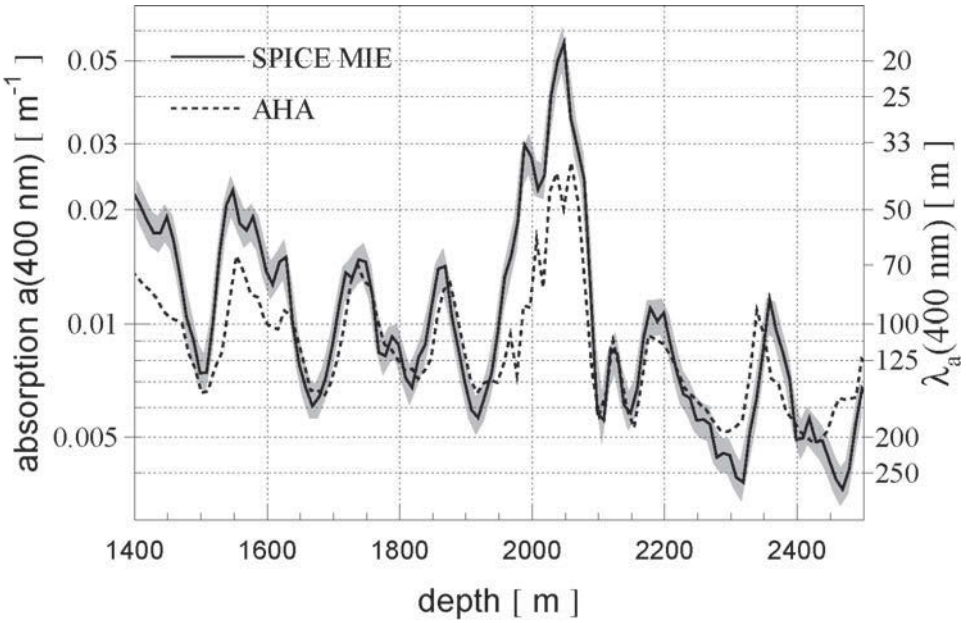

(a) Absorption coefficient vs depth.

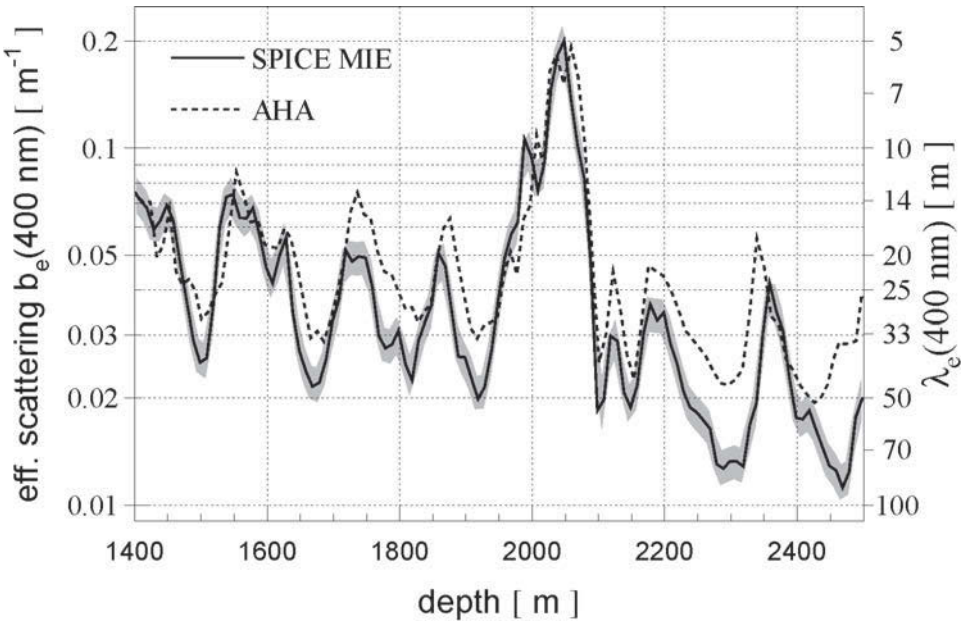

(b) Effective scattering coefficient vs depth.

Figure 28: Ice properties (scattering and absorption coefficients) which are used in simulation. Shown is an older ice model (AHA) and the one used for this work (SPICE MIE). Figures are taken from [Ice13b].

the shape of the scattering function, which is modelled as a superposition between two analytic functions to capture the expected profile from Mie Scattering [Ice13b]. A 1st order effect , dust layer tilting by up to 70 m over the width of the detector towards SE/NW [Bay+10] is also included in the model. This ice model is commonly referred to as "SPICE MIE", and is the one being used for all standard simulations in this thesis. The scattering and absorption coefficients in this model are shown in figure 28. The best

conditions exist in a depth around 2300 m, the DeepCore region. The worst optical conditions appear in a depth between 1950-2100 m, a region that is colloquially called the "dust-layer".

4.2.3 *Data acquisition and data processing*

When a photon hits the PMT and produces a signal above a certain charge threshold, around 0.25 **P**hoto **E**lectrons (PE - the elementary charge unit of the PMT) [Ice10], the signal is further processed by the DOM mainboard for digitization. The primary digitization mode has a time resolution of 3.3 ns and is performed by a 128-sample ATWD (**A**nalog **D**igitwal **W**aveform **D**igitization) chip allowing to capture up to 422.4 ns of the signal waveform. In fact, two such chips are running in "ping-pong" mode to reduce dead time, because the readout of a waveform takes about 29 µs [Ice09]. In addition, a second digitization mode is performed simultaneously without dead time by a FADC (**F**lash **A**nalog To **D**igital **C**onverter) chip with a lower resolution of 25 µs and a total waveform length of up to 6400 µs. Waveforms are only digitized if at least one ATWD chip is available, thus FADC-only waveforms can not be produced. Such a digitized combined ATWD+FADC waveform is also called a "DomLaunch". These DomLaunches are the raw data that get transferred to the IceCube Laboratory at the surface, where further centralized processing takes place. They are the starting point of the data processing scheme as described in figure 29.

DOMLaunches that are fired within 1 µs of another DOMlaunch not more than 2 DOMs apart on the same string are called HLC (Hard Local Coincidence) Launches. Isolated DOMLaunches are called SLC (Soft Local Coincidence) instead. HLC Launches form the basis for trigger algorithms, motivated by that fact that physics events usually produce clustered launches. The trigger algorithm of interest for this thesis is called "SMT-8" (Single Multiplicity Trigger). It triggers when 8 HLC launches reside within a sliding time window of 5 µs length. Using the trigger information, events are constructed from all launches (SLC+HLC) by overlapping the trigger readout windows and combining the corresponding launches into one event. In this way, one ends up with roughly 2 kHz of events containing an SMT-8 trigger, nearly all of them triggered by cosmic-ray muons. At this point the waveforms for each event are calibrated and so-called "hits" are extracted. This procedure is crucial since it forms the basis for almost all the following reconstructions. The calibration takes care of the DOM to DOM variations of the PMTs in terms of fundamental hardware properties like PMT gain, discriminator threshold, or charge offsets. The hit extraction converts the calibrated waveform into hits - tuples that contain a charge and the extracted photon arrival time. Each hit corresponds to the average waveform for a **S**ingle **P**hoto **E**lectron [Ice10]. The superposition of several such SPE templates, weighted by the charge of the hits, is fitted to the overall waveform. The final steps in the data processing chain involve reconstructions

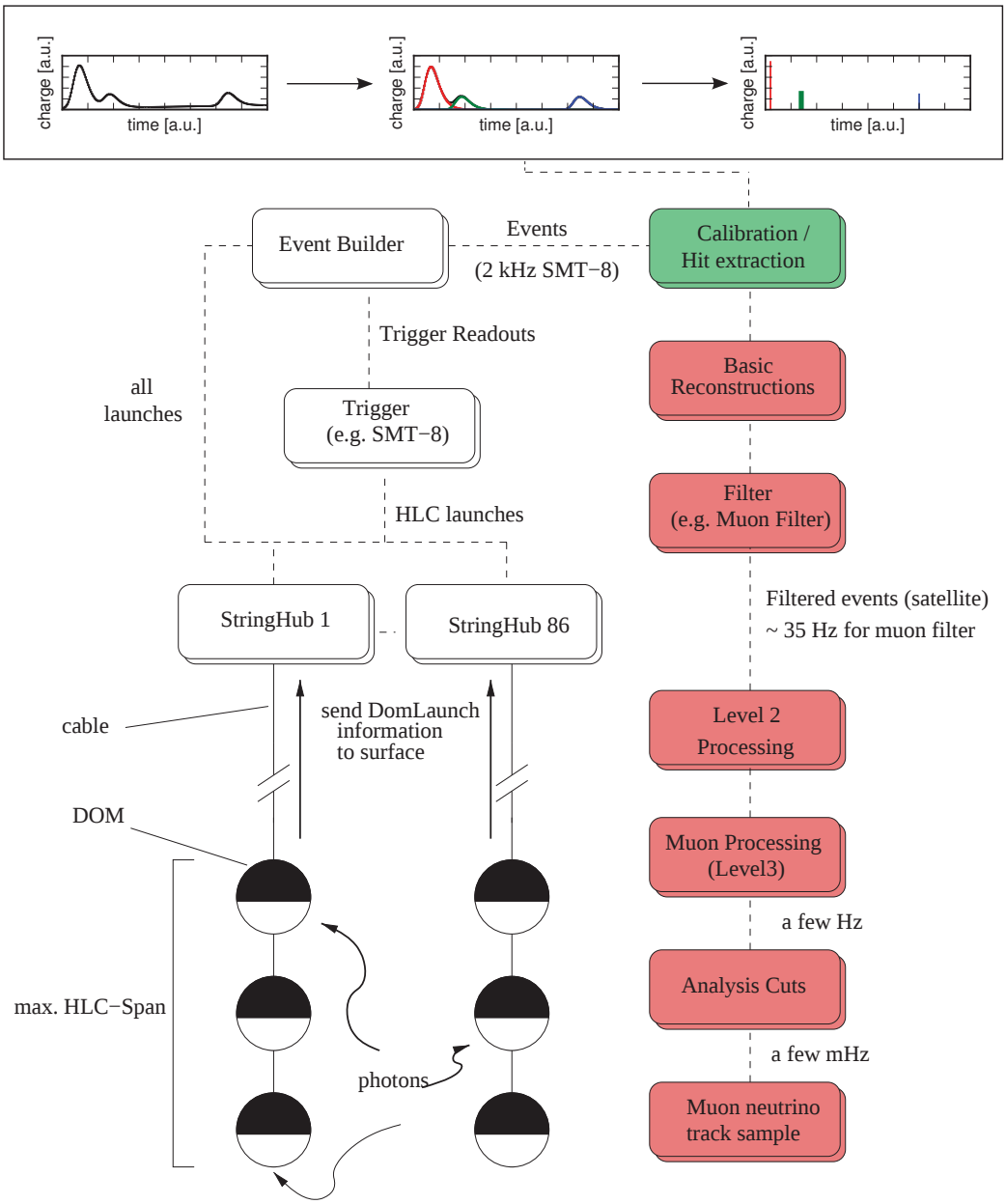

Figure 29: The data acquisition chain and data processing from photons to final event level. The hit extraction (green) is emphasized schematically, showing how individual hits correspond to waveforms. See the text for a detailed description of the individual steps.

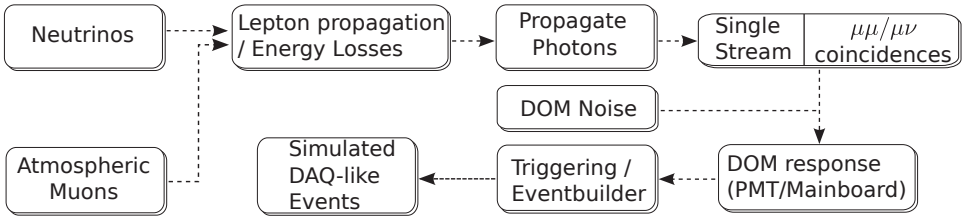

Figure 30: Individual steps to simulate neutrinos and atmospheric muons from air showers. $\mu\nu$-coincident events are only simulated in IC-86. The final events are equivalent to the DAQ Event Builder output.

and calculation of various topological variables. Based on these, a filter (muon filter for muon track data) and subsequent event selections reduce the rate from around 2 kHz at trigger level down to a few mHz at a final analysis level. This scheme generally holds for IC-59, IC-79 and IC-86. The properties of the data at final analysis level for the different years are discussed in section 6.

4.3 SOFTWARE AND SIMULATION

The IceCube collaboration uses a script-based work-flow engine, called Icetray [DeY05], to simulate physics events and perform reconstructions. Individual IceTray-modules are chained one after the other to produce a final simulation result that eventually looks like the output from the DAQ chain just before calibration and hit extraction (see section 4.2.3). The processing and reconstruction steps that follow are then applied both to data and simulated events.

The simulation procedure is schematically shown in figure 30 for neutrino signal and cosmic-ray simulation. For neutrinos, an isotropic flux with a given spectrum is simulated starting at the Earth's surface (distributed over the whole globe), and then subsequently tracked towards the IceCube detector taking the relevant cross sections into account. The procedure makes use of the software package ANIS [GK05] embedded inside an IceTray module and uses the PREM earth density model [DA81]. Neutrinos that enter the relevant volume around IceCube are forced to interact. The actual interaction probability is calculated and applied to the event as a weight.For cosmic-ray simulations the chain starts with a module employing a modified version of Corsika [Hec+98] [Chi03] which simulates cosmic ray interactions in the atmosphere and outputs the muons from the resulting showers that enter the relevant volume around the detector (usually a cylinder centered at IceCube with radius 700 m and height 1400 m). Similar to neutrino simulations, the resulting events can be re-weighted to different primary cosmic ray spectra if desired.

Af this stage the neutrino and CR simulation can proceed in a similar fashion. The muon- and possibly tau-tracks are propagated taking into ac-

count the relevant energy losses as described in section 4.1.2 using a software called MMC [CR04]. Afterwards, Cherenkov photons are produced for the three generic energy depositions (quasi-continous track/EM shower/hadronic shower) according to the profiles described in section 4.1.2. The photon propagation in the ice is performed in one of two distinct ways. The first makes use of a table lookup of previously created tables containing photon arrival probabilities [Lun+07] for showers and quasi-continuous track segments for all relevant (non-negligible light yield) geometrical orientations and positions with respect to the DOM positions. This way is computationally fast, since the probability for the photons to arrive at a given DOM position only amounts to a table lookup. The second way amounts to do the photon propagation for each event individually during the simulation chain using a code called PPC [Chi13]. The direct photon propagation is more accurate than the tabulated approach, but it comes with higher computational load. For the primary neutrino datasets that are being used in this thesis, the table approach has been used since the datasets cover energies up to 1×10^9 GeV and the corresponding computational load for direct photon propagation would have been too high. Some datasets to evaluate systematic uncertainties are produced via direct photon propagation up to energies of 1×10^7 GeV. The photon propagation step yields all the photons that produce a signal in the PMT within a given DOM, thus this step includes glass transmissivity and the quantum efficiency of the PMT. At this stage, individual muon bundles from air showers are mixed with neutrino events to simulate the fraction of neutrino events which possess simultaneous air shower signatures (only present in the IC-86 simulation). Cosmic-ray simulations contain $\mu - \mu$ coincident events in the datasets of all years. Noise hits are added to simulate the dark count PMT signals. Afterwards, the PMT response and successive FADC/ATWD digitization are simulated, yielding the raw uncalibrated waveforms (DomLaunches). Finally, the trigger algorithms and the event builder from the DAQ chain are emulated to end up with events similar to data. In this thesis, cosmic-ray simulations are only used for verification purposes, not for the final analysis itself.

5 ANALYSIS OVERVIEW

The goal of the analysis presented here is to search for statistically significant overfluctuations of track-like neutrino events from the directions of GeV-detected blazar populations. The GeV-detected blazars are selected from the 2LAC catalog (see section 7). This chapter explains briefly the two main scientific questions to be addressed by the analysis. The analysis method is an "unbinned likelihood stacking" (see section 8), whose advantages and disadvantages are shortly evaluated. The differences to previous applications of the stacking approach are pointed out. Finally, the likelihood method is explained, which is a reoccuring method not only for the analysis itself but also for specific event reconstructions, and is put into context with its concrete applications in this work.

5.1 SCIENTIFIC QUESTIONS

The analysis is driven by two main questions:

- The model predictions for the diffuse flux of blazar populations outlined in section 3.5 require an experimental check. How strongly can these models be constrained?
- What is the contribution of 2LAC blazars (and GeV-emitting blazars in general) to the IceCube diffuse flux in the TeV-PeV regime?

The origin of high-energy cosmic rays is directly connected to these questions. A positive neutrino detection would point to blazars as the first established extragalactic acceleration site for cosmic rays. Section 10 presents the results on these issues and section 11 discusses them.

5.2 THE "STACKING" APPROACH

The analysis is performed as a "stacking analysis", in which one looks towards all source directions simultaneously. One treats the regions around all sources as one combined signal region and tests the whole population of sources for neutrino emission only once. While the technical details will be introduced later (see section 8), it is important to emphasize at this point the benefits and drawbacks of such an approach.

BENEFITS

- Usually, the largest flux contribution of a population of objects is not emitted by the strongest source, but spread out over several weaker

ones (see section 7.3). Thus, if blazars emit neutrinos as a class, a stacking analysis will most likely be the most sensitive to find them.

- If a significant overfluctuation is found, it is reasonable to assume that this overfluctuation is indeed caused by the blazars in question. It is unlikely that random sources which have aligned by chance in the search region around the blazar-positions would have caused the signal. This is to be contrasted with a standard point source search, which can only identify a significant spot in the sky, but most likely can not pinpoint with certainty the exact source where the overfluctuation comes from.

DRAWBACK

- A stacking search **has** to assume so-called "source weights", which correspond to an assumed relative neutrino emission within the population (see section 8.1.1 for the technical details of the weighting procedure) [1]. If applied naively, it limits the generality of the end result since it is only valid if the particular weighting scheme is realized in nature.

5.3 DIFFERENCES TO PREVIOUS BLAZAR STACKINGS

This analysis differs from previous stacking searches mainly in two aspects:

I The weighting scheme is designed to produce end results that are not necessarily limited to apply only to the assumed weighting scheme. This is achieved by two features.

- Traditionally, it is assumed that the neutrino emission is proportional to gamma-ray emission (see e.g. [Ice06], [Ice14d]). While this is also done here (assuming proportionality to the gamma-ray energy flux), a second weighting scheme is used which neglects the observed gamma-ray flux of the sources completely and gives each source the same weight. This is the most unbiased weighting approach one can take.
- The analysis framework (see section 8.3) allows to produce skymaps that have a different injected relative neutrino emission within the sources than is assumed with the weighing scheme. In this way, one does not restrict oneself to set a limit that is only valid for the assumed weighting (equal weights are unrealistic, no population consists of sources with equal emission), but one can set a limit that is valid for a different neutrino emission or for a whole ensemble of possible neutrino emissions.

1 In the further discussion, weights will always denote the relative neutrino emission within the population. There is also a contribution within the total weight that is fixed by the source position. This is most manifest if the spectral index is assumed similar in each source and the total weight factorizes into two (see section 8.1.1).

II The size of the chosen blazar populations are as large as possible (typically more than a hundred sources) and the selection is based on spectral properties only. No selection based on the gamma-ray flux is applied. The reasons for this choice are explained in section 7.1.

Furthermore, some technical aspects like the simulation framework (section 8.3), the confidence interval estimation (section 8.2), the calculation of differential limits (9.3.1) and the valid energy range of the limits (10.2.2) are handled differently than in previous approaches.

The event selections in point source searches have matured to the point that dramatic improvements seem unlikely. For this thesis, it was decided to use existing track selections [Ice14d] which results in three years of data from 2009 to 2011 (see section 6).

The angular resolution is one of the most important aspects of a point source search. It has recently been improved to include ice properties, directionality of the Cherenkov emission and some handle on systematic uncertainties and stochastic energy losses in the reconstruction [Sch14]. There is general hope to have further improvements in the future, mostly based on an extension of the track hypothesis to include full stochastic energy loss treatment [Ice14a]. So far, however, all studies in this regard have not yet succeeded, although there are still possible routes which might potentially work out (see appendix C). The main technical focus of this work has been to understand the likelihood-based search method in detail, analyze its strengths and weaknesses and potentially find points of improvements. This is described in sections 8 and 9. The technical prerequisites to understand likelihood-based methods in general are explained in the next section.

5.4 TECHNICAL PREREQUISITES

Throughout this thesis the "**M**aximum **L**ikelihood (**ML**) Method" will be utilized in various contexts. The ML-Method is an approach to estimate parameters of a model or hypothesis given discrete, uncorrelated data events [Jam06]. It can also be used to compare models directly. The method revolves around the likelihood function L. L consists of the product of individual data-point evaluations with respect to a **P**robability **D**ensity **F**unction (**PDF**) that describes the given problem and depends on some parameters θ, usually very generally stated as $L = \prod f(x_i; \theta)$. The best estimates for the parameters θ are those which maximize L. In practice, this amounts to minimizing the negative likelihood function, or the negative **l**og-likeli**h**ood (**LLH**) function which possesses the same minima due to the monotonicity of the logarithm. An overview of generic likelihood functions and their applications in this thesis is given in figure 31. For counting experiments with independent data events that are observed via continuous observables (e.g. a position in the sky), the likelihood functions can generically be written down in four different forms (the outer boxes) as will be argued in the following. A PDF of a continuous parameter can either be evaluated as a

continuous function (unbinned) or it can be transformed into a form with discrete bins (binned) which has to be ensured to be normalized to unity. Mathematically, the unbinned PDF can always be derived as the infinite bin case of the binned PDF. While in the standard likelihood formulation (left side of figure 31) the binned and unbinned cases contain information about the shape of the PDF, one can additionally add information about the normalization. This is accomplished via multiplication ("extension") with a Poisson factor and gives rise to the binned and unbinned "extended" likelihood formulations [Bar90]. Thus, one ends up with four generic formulations or "building blocks"[2].

Any concrete likelihood function that is applied to a given problem is a derivation or modification of at least one of these basic formulations or can be constructed out of a product of these. The resulting likelihood function inherits the strengths and weaknesses of the individual building blocks. Unbinned formulations, for example, do not allow rigorous "Goodness of Fit" tests [Raj03], but are in principle the most sensitive ones as they do not imply a "binned approximation" to the PDF. If one uses the extended formalism, one must be aware that possible systematic uncertainties in the expected number of events can further worsen the result, while such systematics might not play such a big role when relying only on the shape of the PDF.

In the context of this thesis, likelihood functions are used for directional and energy reconstruction (see section 6.1) and for the point source analysis itself (see section 8).

5.4.1 *The Likelihood Ratio*

It is useful to define a likelihood ratio for nested hypotheses as

$$R = \frac{\max.(L[\theta_{1..m}; \theta_1 = \theta_{1,0}, .., \theta_d = \theta_{d,0}])}{\max.(L[\theta_{1..m}])} \tag{16}$$

where L depends on m parameters of which in the numerator d are fixed and $m - d$ take the values that maximize L, while in the denominator all m parameters take the values that maximize L. "Nested" in this context means that the parameter space of allowed parameters in the numerator is always a sub-manifold of the parameters in the denominator where the d fixed parameters can vary freely. In the limit of high statistics, $N \Rightarrow \infty$, the quantity $\lambda = -2 \cdot \ln(R)$ behaves approximately like a χ^2-distribution with d **d**egrees **o**f **f**reedom (**DOF**) according to Wilks' Theorem [Wil38]. The DOF amount to the number of fixed parameters in the numerator. The quantity λ can be used as a so-called **t**est **s**tatistic (TS), a distribution to discriminate between two competing models. The TS-distribution can also be used to estimate parameters via a confidence interval construction (see next section).

2 For intrinsically discrete observables, for example binary output, only the lower row of this picture exists and there are only two possible formulations.

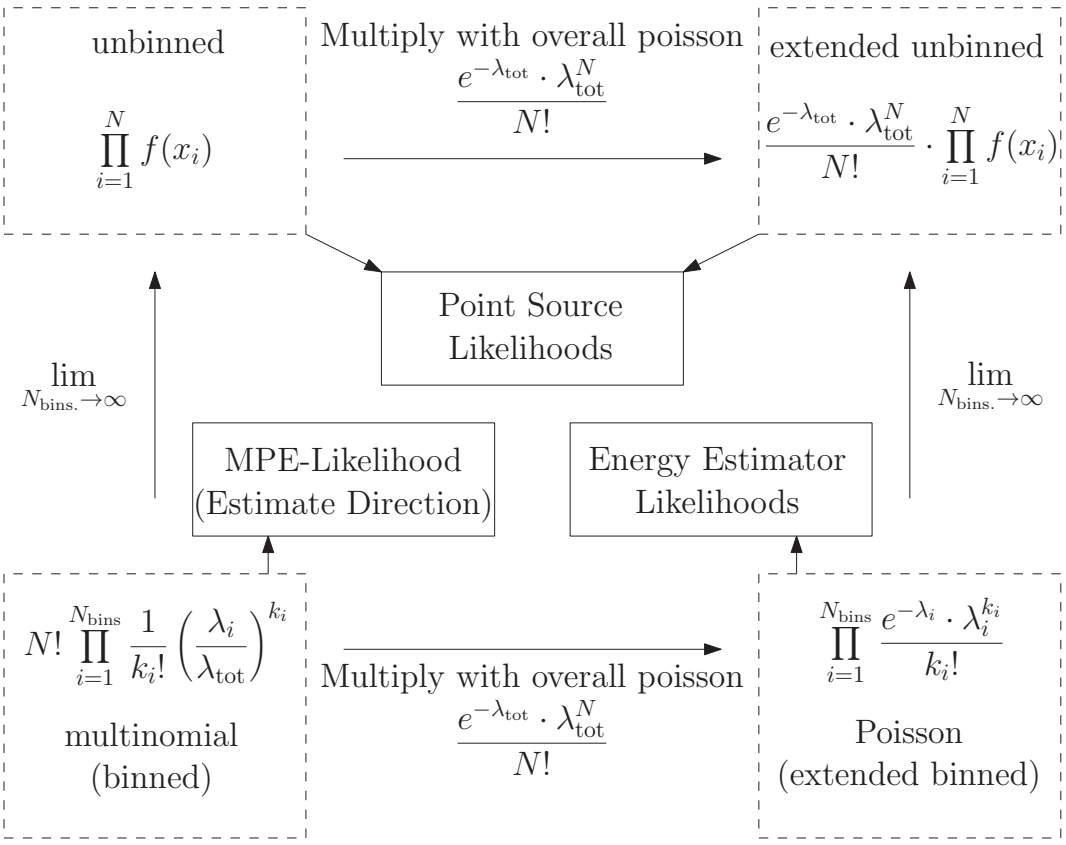

Figure 31: Relations between the four possible generic likelihood approaches (dashed boxed) and various applications thereof in the context of this thesis (solid boxed). N denotes the number of uncorrelated data events and f(x) is a continuous PDF defined in the observable space.

5.4.2 *Obtaining error estimates on parameters*

In the context of frequentist probability theory, one is interested in the best estimate of a a given parameter and its so called n% confidence interval. This interval contains the best estimate for the parameter in n% of repeated pseudo-experiments and can be interpreted as an error estimate. There are two ways this confidence interval is calculated for the purpose of this thesis. The first involves a "profile likelihood scan" around the maximum of the likelihood function, in which the parameter of interest is varied in an interval around the best-fit value while all other parameters are set to the values that maximize the likelihood function. For example, the 1σ interval is chosen such that the LLH function at the interval boundaries is lower by 0.5 for 1 DOF or 1.17 for 2 DOF compared to its value at the maximum. This method is applied to estimate an error of the directional reconstruction of muon tracks (see section 6.1.1) and has the advantage that it only requires one set of data points for the estimate. On the other hand, the profile likelihood is relying on Wilk's theorem [Ran12]. If the event counts are small or the PDFs defining the likelihood function are wrong, Wilk's theorem does not apply (see section 8.4.5) and the profile likelihood estimation can yield

wrong results. The other method involves the interval construction via a so-called "confidence belt". While being computationally more expensive, this also works if the PDFs of the problem are only approximates of the true PDFs small event counts are present. For the unbinned stacking analysis the CL_s confidence belt construction [Reaoo] is chosen. For further discussion and implementation of the confidence belt construction see section 8.2.

6 MUON TRACK DATA

In order to look for spatial correlations with potential point source positions in the sky, one requires a reconstruction of the incoming neutrino directions that is as precise as possible. Track-like event signatures in general offer better angular resolutions than cascades and are the selection of choice. This analysis is based on track event selections of the datasets recorded in 2008/2009 (IC-59), 2009/2010 (IC-79) and 2010/2011 (IC-86).

The first part of this chapter introduces the likelihood reconstructions which are of importance for the point source analysis. This includes directional reconstruction, energy reconstruction and the directional error estimator. The second part of this chapter sketches the general selection strategy and properties of the final data sample.

6.1 IMPORTANT LIKELIHOOD RECONSTRUCTIONS

In order to understand event reconstructions in IceCube, the notion of the "time residual PDF" has to be introduced. The time residual PDF describes the probability distribution for Cherenkov photons to arrive at a given DOM over time. It depends on a given physics hypothesis, e.g. the position, orientation and energy losses of a muon track in the detector. By varying the parameters of the hypothesis, one minimizes a (usually modified) variant of one of the four likelihood functions described in figure 31 (section 5), where the time residual PDF is the PDF which is evaluated. The best fit values of the parameters determine the final event reconstruction. For the different problems of energy and directional reconstruction, different likelihoods and hypotheses are used as described in the following.

6.1.1 *Directional reconstruction*

- MPE-Likelihood Reconstruction The so-called MPE (**M**ulti **PE**) likelihood is used for the final directional reconstruction. It is derived from the multinomial likelihood (see figure 31, section 5) with three bins per DOM.

$$
\begin{aligned}
L &= \prod_{j=1}^{N_{DOM}} \frac{N!}{0!1!(N-1)!} \cdot {w_0}^0 \cdot {w_1}^1 \cdot {w_2}^{N-1} \\
&= \prod_{j=1}^{N_{DOM}} N \cdot \left(\int_{t_1-\Delta t}^{t_1+\Delta t} p_j(t)\,dt \right) \left(\int_{t_1+\Delta t}^{\infty} p_j(t)\,dt \right)^{N-1} \\
&\underset{\Delta t \to 0}{=} \prod_{j=1}^{N_{DOM}} N \cdot p_j(t_1) \cdot \left(1 - P_j(t_1)\right)^{N-1}
\end{aligned}
\tag{17}
$$

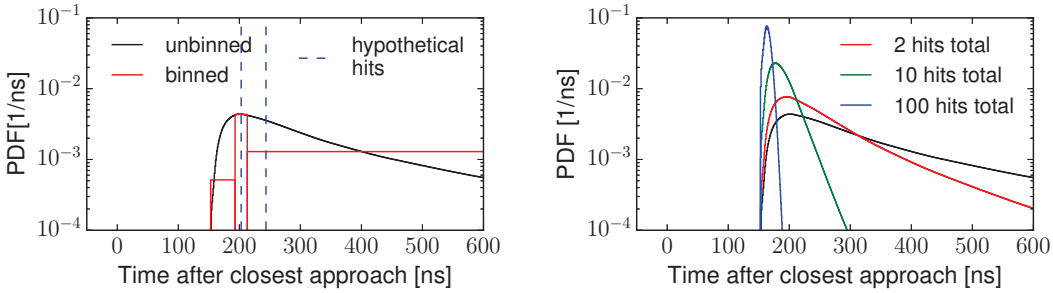

(a) (b)

Figure 32: Time residual PDF for an infinite track hypothesis passing a DOM at 50 m on closest approach. a) Unbinned version and a specific binned form used for the multinomial probability calculation in the context of the MPE derivation. (b) The time residual PDF for the first hit (MPE PDF) for different number of total hits within the DOM.

Here N is the number of hits for the given DOM, w_i is the probability for a hit to land in bin i, p_j and P_j denote the time residual PDF and CDF (**C**umulative **D**istribution **F**unction) for DOM j and t_1 is the hit time of the first hit in the given DOM.

The binning is chosen such that the first bin contains no hit, the second bin one hit and the last bin the remaining $N-1$ hits (see figure 32a). In the last step, the width of the second bin is sent to zero. The result effectively describes the probability density for the first hit only, depending on how many photons the DOM has seen in total, and is called MPE PDF. It partly mitigates uncertainties in the ice, since the first hit is the least scattered one and more likely to be less scattered the more photons the DOM has seen, which is immediately reflected in the sharpening of the peak with an increase in the number of photons in the DOM (see figure 32b). The particular derivation shown here assumes that each hit has an associated charge of 1 PE. Each extracted hit in reality can carry arbitrary charges, so in practice N is replaced by the total charge.

The likelihood minimization involves finding 5 parameters (position for a given point of the track and two angles). While in IC-59 the time residual PDF is calculated analytically (as described in [JR07]) as an isotropic cascade sitting on an imaginary muon track, in IC-79 and IC-86 it is calculated from a multi-dimensional spline [WSL13] fitted to simulated photon arrival probabilities for an infinite track hypothesis which takes into account the directionality of the emitted photons and the ice properties. The spline-version also includes further modifications as described in [Sch14] which can better handle stochastic outliers which are not part of the infinite track hypothesis or systematic effects due to uncertainties in the ice.

- Error estimate of the directional reconstruction

  A 1-σ error estimate for the position is calculated via a 2-d profile likelihood scan around the best fit direction in the two space angles, as first introduced in [Neu06]. The scan is performed for a rotated version of the track at the equator, where the two angle coordinates can be treated quasi-euclidean, and the log-likelihood is fitted internally with a paraboloid whose semi-major and semi-minor axes can then be used to define the 1-σ error contours. In the end, the two errors are combined via $\sqrt{\frac{{\sigma_1}^2+{\sigma_2}^2}{2}}$ to yield an average estimator for the 1-σ width of a symmetric 2-d gaussian PSF. This error estimator is called "paraboloid" error (or σ_{pb}). Simulations show that the paraboloid error is usually smaller than the true error $\Psi(\nu_\mu, \mathrm{MPE})$, its deviation depending on the deposited energy and consequently also on the neutrino energy, as depicted in figure 33. This bias, which gets larger for higher energies, is not completely understood. It is unwanted behavior in the standard point source approach (see section 8), since the spacial PDF is calculated analytically as a 2-d gaussian which depends only on σ_{pb} and neglects any energy dependence. To mitigate this effect, a correction function that depends on the deposited energy has to be applied to both data and simulation to make the ratio $\Psi(\nu_\mu, \mathrm{MPE})/\sigma_{pb}$ flat. The ideal central value after this correction is 1.177 , since σ_{pb} is supposed to estimate the 39% quantile of the 2d-gaussian, but $\Psi(\nu_\mu, \mathrm{MPE})$ on average corresponds to the 50% quantile, which is a factor of 1.177 larger. For the exact definition of the correction functions the reader is referred to [Ice14d]. As can be seen in fig. 33, the corrected curves are flat above 10 TeV and slightly below the optimal value of 1.177. This is conservative, since it is better to assume a slightly larger PSF than a smaller one. The rising ratio below a few TeV is due to a rising contribution of the kinematic angle between neutrino and emerging muon. This effect is not correctable, since all the muons below the critical energy (in the minimally ionizing regime) are indistinguishable and reconstructed to similar energies.

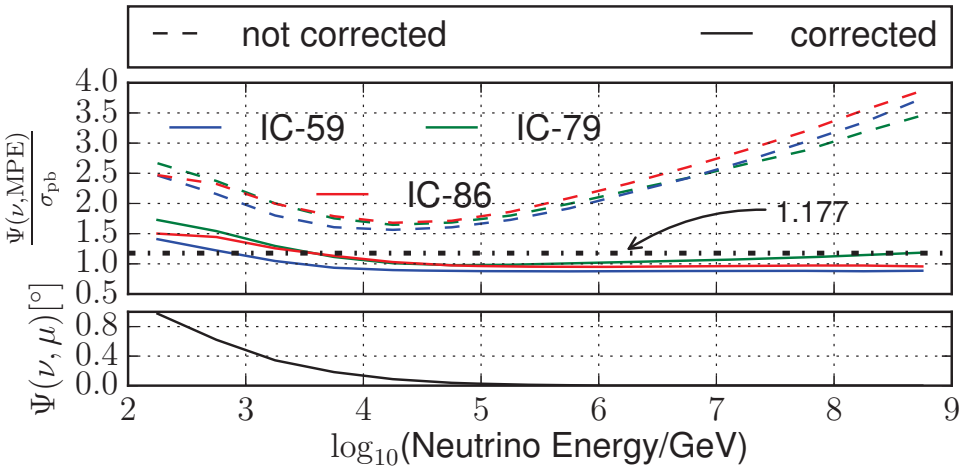

Figure 33: Ratio of the median true reconstructed error with the median paraboloid estimator before (dashed) and after (solid) an energy-dependent correction. The ideal value for this ratio of 1.177 is shown as the dash-dotted line. The lower part of the plot shows the median kinematic angle between the neutrino and emerging muon.

6.1.2 *Energy reconstruction*

Energy reconstructions are applied on a track hypothesis that has been found with a directional reconstruction, in this case on the directional estimate from the MPE reconstruction. Two different energy reconstruction algorithms, named "MuEx" and "MuE", are being used at the final level of this analysis. Both assume a smooth energy loss profile of an infinite muon track and minimize a poisson likelihood (see figure 31, section 5) convolved with a Kernel G that differs between the two approaches.

$$L = \prod_{j=1}^{NDOMs} \int_0^\infty G(\lambda_i, \lambda') \cdot \frac{e^{-\lambda'} \cdot \lambda'^{k_i}}{k_i!} d\lambda' \tag{18}$$

k_i denotes the observed charge and λ_i denotes the expected charge in DOM i. Since λ can be parametrized as a function that depends on the given physics hypothesis and effectively describes the photon flux that arrives at a DOM, it is also called "flux function". The convolution with $G(\lambda_i, \lambda')$ is used to handle potential systematic uncertainties in this quantity. MuE is an older version of MuEx and the two approaches differ in the exact analytic form of the flux function and the convolution term $G(\lambda_i, \lambda')$.

- MuEx

  The analytic expressions for the flux functions of a muon track are given in [Ice14a]. These expressions have been cross-checked with the photon tracking software PPC. The convolution term G takes the following form:

Dataset	Energy Estimator
IC-59	MuE
IC-79	$\theta \leqslant 75^\circ$: MuE
	$75^\circ < \theta < 90^\circ$: $\mathrm{MuE} \cdot ((\theta/\mathrm{Deg}) \cdot \frac{-1}{15} + 6) + \mathrm{MuEx} \cdot ((\theta/\mathrm{Deg}) \cdot \frac{1}{15} - 5)$
	$\theta \geqslant 90^\circ$: MuEx
IC-86	MuEx

Table 4: Energy estimators for the different datasets used in the final analysis. θ denotes the reconstructed zenith angle of an individual event.

$$G(\lambda_i, \lambda') = \frac{\mathrm{const.}}{\lambda'} \cdot \left(e^{-\omega \cdot \ln(\lambda'/\lambda_i)} + \left(\frac{\ln(\lambda'/\lambda_i)}{\sigma} \right)^2 \right) \tag{19}$$

It consists of a student-t version (with 1 DOF) of a log-normal distribution and an additional exponential factor depending on the skewness factor ω which allows for skewed tails. The wide tails of the student-t distribution handle systematic uncertainties and the approximations due to analytic modelling of the light yield. The skewness due to the exponential term is effective in reducing the bias of large stochastic energy losses which are not part of the infinite track hypothesis. The whole expression is derived from a log-normal and not a normal distribution since λ is strictly positive.

- MuE

  MuE is a progenitor variant of MuEx [ZCo8] and was used before IC-79. The analytic functions to model the expected charge differ slightly from the ones used in MuEx. The convolution is not applied, i.e. G is simply a delta function.

  $$G(\lambda_i, \lambda') = \delta(\lambda_i - \lambda') \tag{20}$$

  Because the convolution is not applied, systematics and especially large stochastic losses can not be handled as well as in MuEx and introduce a bias.

Table 4 summarizes the energy estimators in the respective configurations that are used in the final point source analysis. For IC-79 MuE was found in [Sch14] to separate signal and muon-bundles in the downgoing region slightly better, hence this dataset uses MuE up to zenith angles of 75° and then linearly interpolates to MuEx which is used above 90°.

6.2 SELECTION STRATEGY

The strategy to select track-like events is to suppress cascade-like events and suppress or split time-coincident events. It also aims to get rid of event topologies not well-modelled in simulation and to favor tracks that involve a greater number of unscattered hits which tend to provide better angular resolution. For the exact variables and selection criteria in the individual datasets the reader is referred to the descriptions in [Ice14d]. For IC-79, the reprocessed selection is used which is described in detail in [Sch14]. Additionally, in all three years one additional cut is introduced to ensure that all corrected paraboloid estimators are less than 5°.

There are two (nearly) irreducible track-like backgrounds that remain at final cut level: Atmospheric neutrinos and atmospheric downgoing muons [1]. Figure 34 shows these irreducible backgrounds and a diffuse muon-neutrino signal for IC-79 with the currently best fit normalization and spectral index of the measured diffuse neutrino flux. At trigger level the muon background dominates by many orders of magnitude over atmospheric neutrinos. This happens even in the upgoing region due to mis-reconstructions, mostly by muon bundles that strike corners of the detector and appear as showers. After the track selection is applied this background is strongly reduced and is negligible for upgoing directions. The rate reduction over 5 orders of magnitude in the downgoing region is dominantly achieved by the requirement for a high reconstructed energy. This energy cut also reduces the atmospheric neutrino rate (mild red curve) and unfortunately also potential signal in this region (green curve). The data curve lies below the simulated expectation (gray) in the downgoing part because of an air shower veto which is not simulated. This has no effect for this analysis since background estimates are taken from the data (see section 8.4.1). Effectively, the overall selection leads to an energy threshold of around 100 TeV for astrophysical neutrinos in the downgoing sky while the upgoing sky is sensitive down to the sub-TeV regime. This asymmetry in signal acceptance dependent on the neutrino energy is depicted in figure 34 b) for IC-79 and is important to keep in mind when one looks at energy-differential sensitivity curves which effectively trace different regions in the sky for low and high energies.

6.3 PROPERTIES

The final track selection contains around 100000 events per year, dominated by atmospheric neutrinos in the northern (upgoing) sky and atmospheric muons in the southern (downgoing) sky. The exact event numbers are given in table 5. The quite large number of ν_μ signal events, corresponding to the

1 The downgoing muon background is not completely irreducible. The IceTop array can help to veto air shower muons for vertical showers and the stochasticity of the event can also be used to differentiate muon bundles from neutrinos which induce single muon tracks.

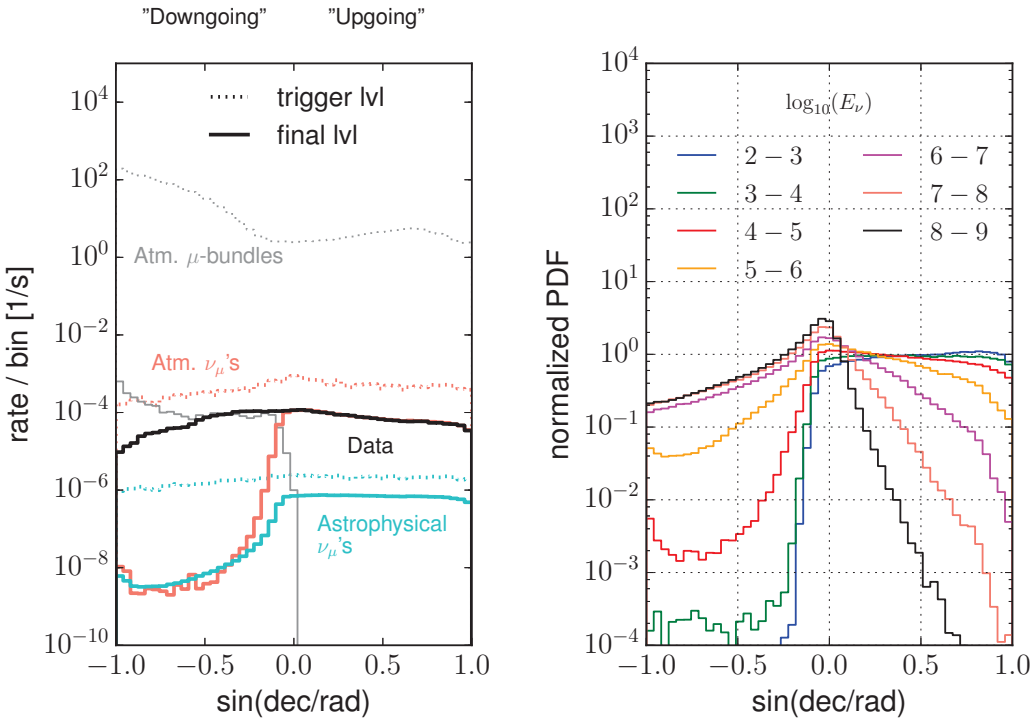

(a) (b)

Figure 34: a) Effects of the event selection demonstrated on the IC-79 dataset. At trigger level (dotted) the dominant number of events are produced by muon bundles from air showers. At final level (solid), the events split up into dominantly atmospheric neutrinos in the upgoing region and air shower events in the downgoing region. The effect of the IceTop-veto can be seen for downgoing events comparing data (black) and air shower simulations (gray) that do not include the veto. At final level, the best fit astrophysical 1-flavor flux from [Ice15] is shown in turquoise.
b) Normalized arrival distributions of interacting muon-neutrinos for different energy regimes at final level in IC-79 (binned per decade and weighted to an E^{-2} spectrum).

best fit in [Ice15], suggests that such a flux should be detectable in a point source stacking analysis which only looks at a small fraction of the sky, if indeed the signal originates from the stacked point source positions.

An important quantity to translate between fluxes and measured event counts is the "effective area". It can be interpreted as the geometrical area of a hypothetical detector that translates a given neutrino flux into an event count with a 100 % detection efficiency (see equation 21), absorbing the muon detection efficiencies and neutrino interaction probabilities. The

Dataset		All sky	$\theta \geqslant 90°$	$\theta < 90°$
IC-59	data	107011	42781	64230
	$\Phi_0 \cdot E^{-2.46}$	364	336	28
IC-79	data	93720	48782	44938
	$\Phi_0 \cdot E^{-2.46}$	428	383	45
IC-86	data	136245	61325	74920
	$\Phi_0 \cdot E^{-2.46}$	527	477	50

Table 5: Total number of data events in the respective datasets of IC-59, IC-79 and IC-86 for different regions in the sky. θ denotes the zenith angle. Also shown is the number of events expected for a diffuse astrophysical flux (over all energies) as measured in [Ice15](Φ_0=4.11 $\times$ 10^{-6} GeV$^{1.46}$ /s/sr /cm^2).

higher the effective area, the higher the event count for a given flux. The flux-to-count relation can be written as

$$N_{\text{Events}} = \int_E A_{\text{eff.}}(E) \cdot \frac{d\Phi}{dE} dE \cdot \Delta T \tag{21}$$

where $A_{\text{eff.}}$ is the energy-dependent effective area, $\frac{d\Phi}{dE}$ the differential flux and ΔT the time interval of observation. Figure 35 a) shows the effective areas of the IC-79 selection for muon neutrinos from three distinct positions in the sky.

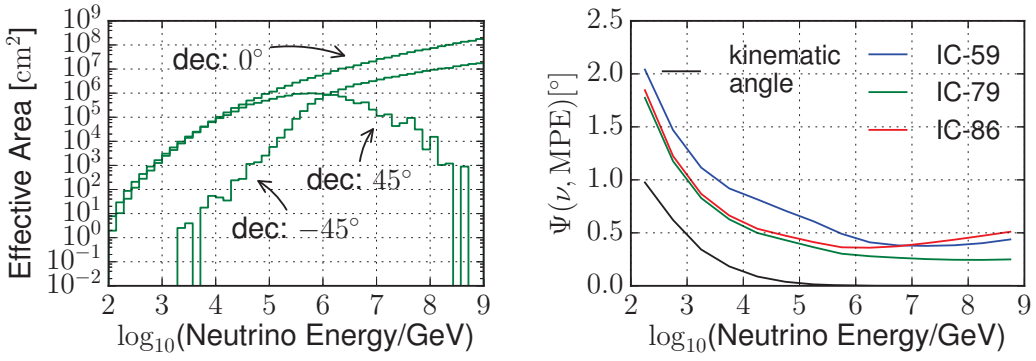

(a) (b)

Figure 35: a) Effective area in IC-79 for muon neutrinos at three different declinations: downgoing (−45°), horizontal (0°), upgoing (45°) b) median angular resolution and kinematic angle between the neutrino and emerging muon.

For IC-59 the effective areas are slightly lower and for IC-86 slightly higher, as can be inferred from the number of signal events in table 5. Qualitatively, however, the effective area curve shapes in the other selections agree with

the ones for IC-79 shown in figure 35(a). Another quantity which is useful to be compared between datasets is the median angular resolution. Figure 35(b) shows the median angular resolution averaged over all directions in the sky. Also included is the kinematic angle between muon and neutrino direction at a given energy which becomes negligible for energies above 10 TeV. Above 10 TeV the resolution is better than 1° in all samples, and substantially better in IC-79 and IC-86 than in IC-59 due to recent improvements of the reconstruction. The degradation in IC-86 above a few PeV is due to downgoing events and most likely caused by the effect of coincident air showers in interplay with the event selection (IC-59 and IC-79 do not contain coincident air shower events within signal simulation). Effects at these energies are however irrelevant for most spectra.

7

BLAZAR SELECTION

7.1 THE FERMI 2LAC CATALOG

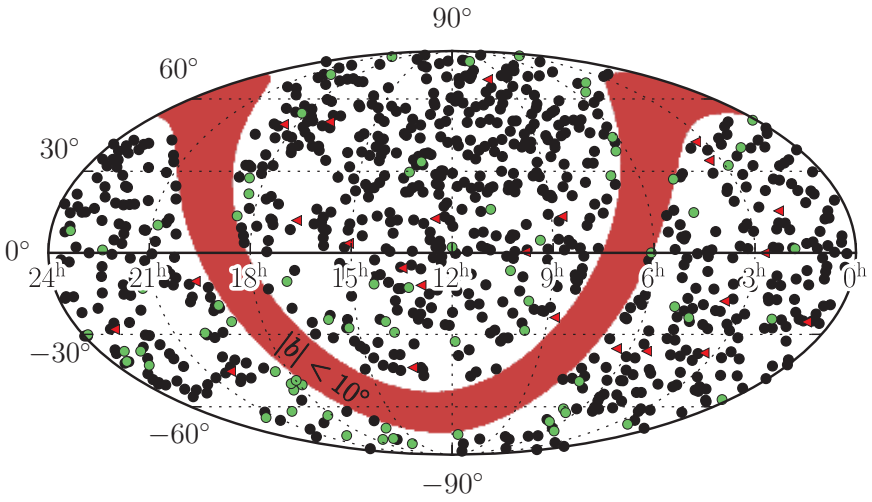

Figure 36: Distribution of all sources in the 2-LAC catalog. The sources are divided into categorized blazars (black), uncategorized blazars (green) and non-blazar AGN (red triangles). For an explanation see the text. The excluded region of galactic latitudes $|b| < 10°$ is highlighted in red.

The catalog of choice for this analysis is the 2LAC AGN catalog [Fer11]. It comprises a large sample of gamma-ray detected blazars (the largest one could find in the literature at the time this analysis was performed[1]) distributed uniformly over the whole sky in the covered region of galactic latitudes larger than $|b| = 10°$, which corresponds to 83 % of the total sky. The gamma-ray data for this catalog has been collected with the Large Area Telescope (LAT) [Fer09] on board of the Fermi space telescope in the energy range between 100 MeV and 100 GeV in 2 years of operation. As can be seen in figure 36, around 97 % (862 objects) of the 886 sources in the catalog are blazars, which split up into "categorized" (89 % / 785 objects) and "uncategorized" (8 % / 77 objects). "Uncategorized" denotes a blazar that could neither be classified according to its spectral properties into BLLac or FSRQ nor according to its synchroton peak into LSP/ISP/HSP object. The remaining 3 % (24 objects) are non-blazar galaxies, dominantly AGN.

1 As of this writing the updated 3LAC catalog has been released, which comprises several hundred more sources.

7.2 DEFINITION OF SAMPLES

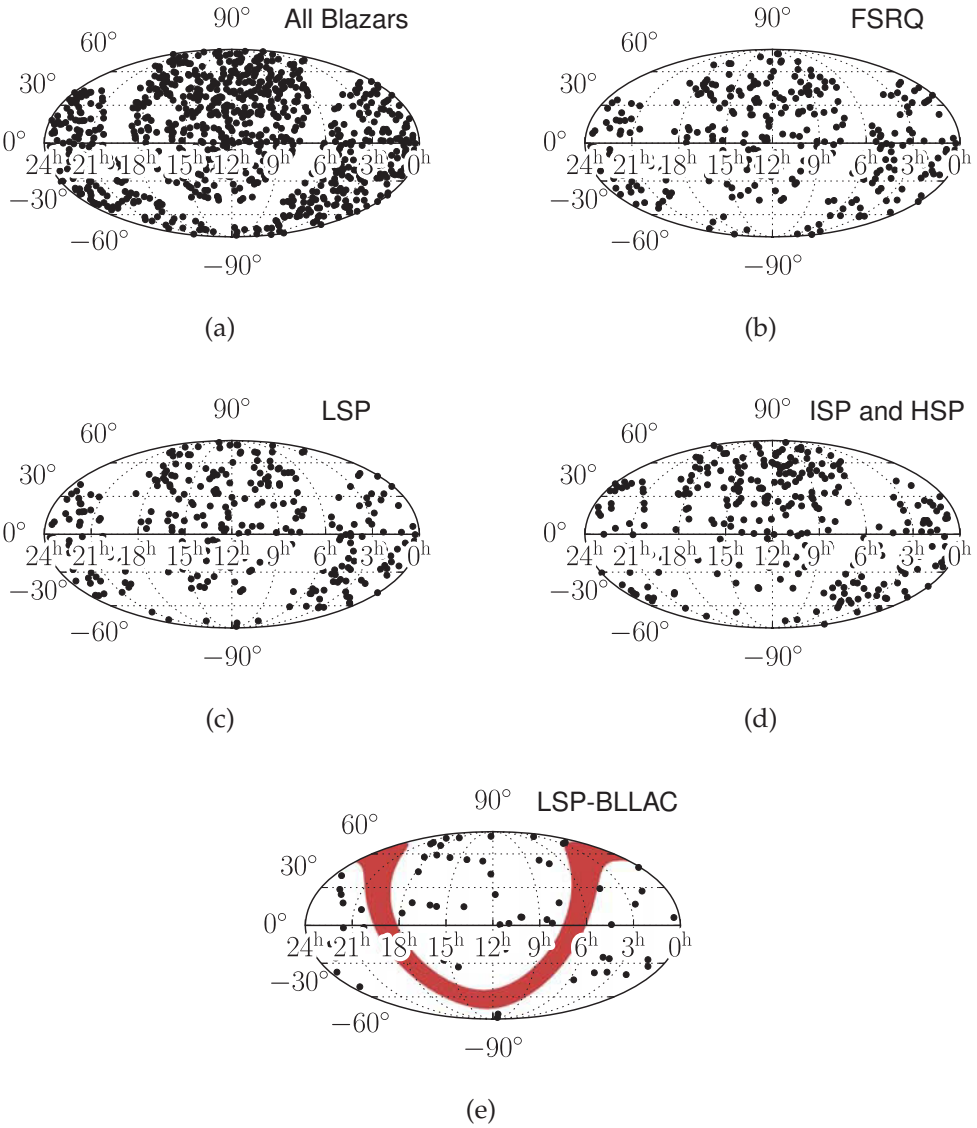

Figure 37: Distribution of the different 2-LAC blazar sub-populations in the sky. For LSP-BLLacs the $|b| < 10°$ region (red) is highlighted due to the sparseness of the sources.

The sub-samples in this thesis are defined via the the observationally distinct characteristics between FSRQ's and BL-LAC's and the synchroton peak classification into LSP/ISP/HSP objects. No pre-cut on the γ-flux to remove weak sources is applied, since it is not beneficial for the overall sensitivity (see section 8.4.2), independent of the weighting scheme. Quite to the contrary, in the equal-weighting scheme it is better to look at more sources to increase the likelihood of detection, since the premise is that there is nearly no correlation to γ observations. The only requirement for the sources is the "clean" flag, which means a blazar does not have source

confusion. The following list summarizes the five populations defined with "clean" blazars from the 2LAC catalog and the motivation behind them.

- All blazars (862 objects)

  The evolutionary blazar sequence within the unified AGN picture suggests that blazars form a continuous spectrum of objects which are connected via cosmological evolution. How the neutrino emission changes with this evolution is not known. It is thus the most unbiased assumption to look at all blazars together, especially with the equal weighting assumption which is most suited if one has no knowledge of the underlying neutrino emission.

- Flat Spectrum Radio Quasars (FSRQs) (310 objects)

  The class of FSRQ's show strong broad emission lines which potentially act as radiation targets for photomeson scenarios in external models (see section 3.5).

- Low Synchroton Peaked Objects (LSPs) (308 objects)

  The majority of FSRQ's are LSP objects. In [Gio+12] it is argued that within the blazar sequence LSP-BLLacs are actually physically similar to FSRQ's but whose emission lines are overwhelmed by the strong jet continuum. This classification thus just groups all LSP objects together.

- Intermediate/High Synchroton Peaked Objects (ISP/HSPS) (301 objects)

  HSP-BLLacs differ from LSP-BLLacs in their luminosity function (see section 3.4). The peak-frequency boundary between the two classes is not sharply defined. In order to have a larger sample, the HS objects are grouped together with the ISP objects as one population.

- Low Synchroton Peaked BLLac objects (LSP-BLLacs) (68 objects)

  LSP-BLLacs have been specifically considered for neutrino emission in [Mue+03]. They form the smallest sub population in this analysis.

Figure 37 show how these individual populations are distributed over the celestial sphere. It is observed that even the smallest population is distributed quasi-isotropically, since roughly an equal amount of sources can be found per steradian when the galactic plane band is ignored. Looking at the source overlap between the samples, visualized in figure 38(a), reveals three nearly independent sub-populations: LSP-BLLacs, FSRQs and ISP/HSPs. The biggest overlap exists between the FSRQs and LSPs, which share around 70% of sources. The 167 sources that are only part of the "All blazar" sample consist of two sub-groups: 77 uncategorized blazars (see section 7.1) and 90 pure BLLac objects which do not have a classification based on the the synchroton peak. Figure 38(b) shows that the majority

of the 2LAC blazars is closer than a redshift of two. Looking again at the cosmic gamma-ray horizon due to EBL absorption (figure 8 in section 2.2), reveals that most of the emitted gamma rays below 100 GeV are therefore not absorbed and reach the Earth directly once they leave the source region.

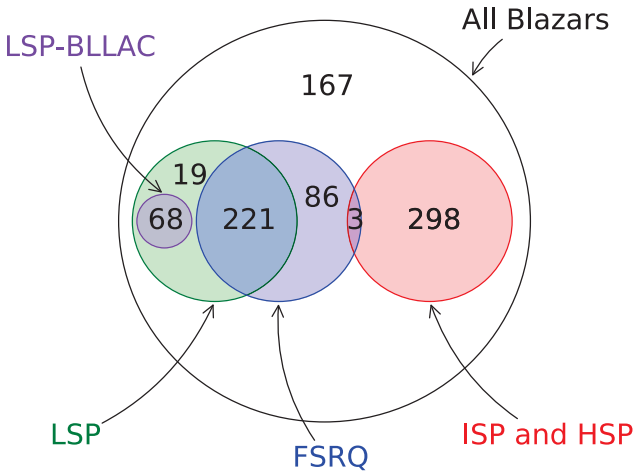

(a)

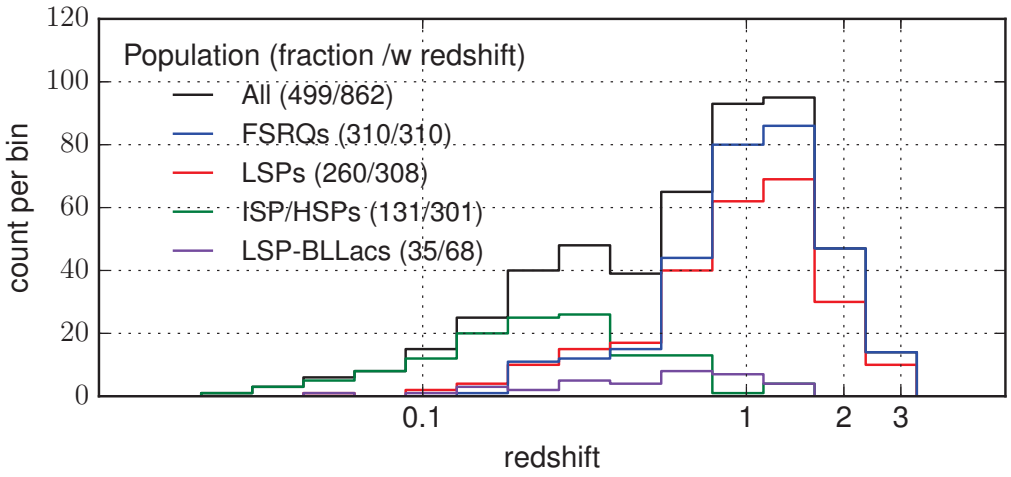

(b)

Figure 38: a) Visualization of the overlap between the different samples including the number of sources within each overlap region. The size of the regions is not to scale. b) Redshift distributions of all sources that have a determined redshift. Values in parenthesis indicate the fraction of sources with a determined redshifts.

7.3 COMPLETENESS

A useful quantity to know about the catalog is its "completeness" if completeness is defined as the fraction of the total flux from all blazars in the observable universe that is resolved into individual point sources in the catalog. While no completeness studies have been published for the 2LAC catalog explicitly, they do exist for the "parent catalog" 2FGL [Fer12], of which the 2LAC catalog is a strict subset. When discussing the completeness, it is instructive to visually inspect $S \cdot dN/d(\log S)$, the arriving flux per logarithmic flux interval, which can be obtained from the source count distribution dN/dS.

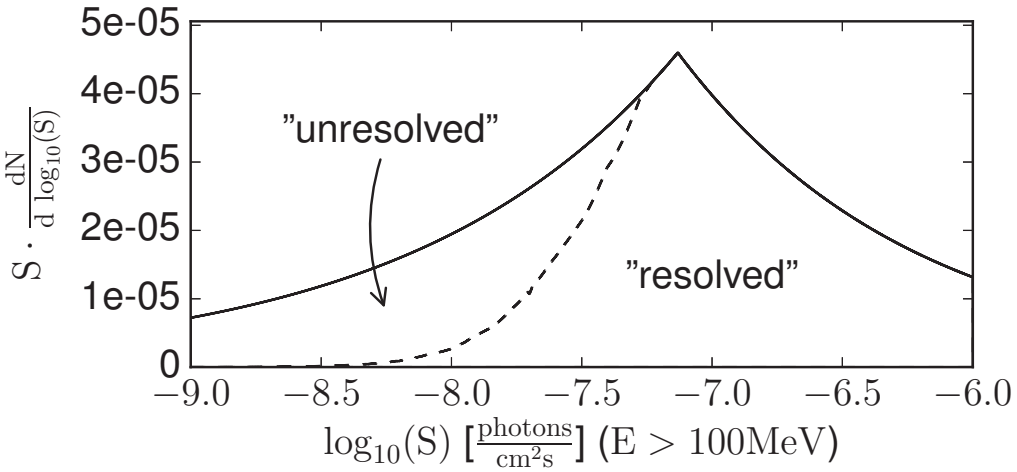

Figure 39: Visualization of the resolved and unresolved fractions of the gamma flux for a subset of the 2-LAC blazars ($b > 20°$) neglecting the efficiency variation with spectral index. The area below the solid line corresponds to the flux from all blazars in the universe while the area below the dotted line corresponds to the flux by resolved 2LAC blazars. The dN/dS distribution and the efficiency curve are taken from [Fer10a].

Figure 39 shows $S \cdot dN/d(\log S)$ for blazars at galactic latitudes $|b| > 20$. The source count distribution of these blazars was taken from table 4 in [Fer10a]. Also included is a curve taking into account the average source detection of the Fermi-LAT (figure 7 in [Fer10a]), resulting in the dashed curve which describes the flux contribution of sources that are resolved by Fermi-LAT. The largest contribution to the total flux arriving at earth comes from sources with a flux of around $1 \times 10^{-7.1}$ Photons/ cm²s, These sources are detected with 100 % efficiency which starts to drop only slightly below this flux value. As the area below the solid curve corresponds to the total flux from all blazars, including the unresolved ones, one can see that around 70 % of the total flux down to sources with fluxes 1×10^{-9} Photons/ cm²s is resolved into point sources. Extrapolating the tail to lower fluxes only changes this result by a few percent. While the preceeding estimate helps to visualize

the sample completeness, it neglects the spectral-index dependence of the detection efficiency. However, the result from the full analysis by the Fermi-LAT collaboration [Aje+15] for sources of $|b| > 15°$, taking into account the whole flux range and the efficiency dependence on the spectral shape, also results in a completeness of 70 %. Importantly, this completeness holds for the sub-populations individually, as it has been shown to be 70 % for FSRQs [Aje+12], which by deduction leaves around 70 % for BL-LACs, since they form the majority of the remaining non-FSRQ blazars. Although the official study has been applied to sources with $|b| > 15°$ (and the simplistic visualization shown in figure 39 to $|b| > 20°$), the quoted "70 %" is applicable to all the 2LAC sources (which go down to $|b| = 10°$) because detection efficiency is not expected to drop to zero sharply at the $|b| = 15°$ boundary. Even if one would assume this extreme scenario, the combined completeness for all $|b| > 10°$ sources would be $\frac{0.08 \cdot 0 + 0.74 \cdot 70}{0.82} \cdot 70\% \approx 63\%$. Here, 0.08 corresponds to the 8% all-sky fraction of the $15° > |b| > 10°$ region and 0.74 to the 74% all-sky fraction of the $|b| > 15°$ region. This hypothetical 7% drop is still smaller than the uncertainty on the 70% completeness value in the first place, which is around $7\% - 14\%$. The completeness of the samples will be important for the discussion of the analysis results.

8

A LIKELIHOOD ANALYSIS FOR POINT SOURCE STACKING

8.1 THE LIKELIHOOD FUNCTION

The likelihood function for a point source search contains a PDF evaluated on the celestial sphere [1]. In the case of a single point source and a background contribution, this celestial PDF f_{PS} can be thought of as a linear superposition of two normalized individual PDFs, the signal $f_s(\vec{x})$ and background $f_b(\vec{x})$, each weighted with a factor depending on the "number of signal events" n_s that steers the relative strength of the signal PDF:

$$f_{PS}(\vec{x}) = \frac{n_s}{N_{tot.}} \cdot f_s(\vec{x}) + (\frac{1 - n_s}{N_{tot.}}) \cdot f_b(\vec{x}) \tag{22}$$

$N_{tot.}$ denotes the overall number of events in the data sample. The vector notation for x emphasizes that the PDFs in general not only depends on spatial coordinates, but also on other observables like the reconstructed energy. As already discussed for the general case in section 5.4, the likelihood function is then given by

$$L = \prod_{i=1}^{N_{tot.}} \frac{n_s}{N_{tot.}} \cdot f_s(\vec{x}_i) + \left(\frac{1 - n_s}{N_{tot.}}\right) \cdot f_b(\vec{x}_i) \tag{23}$$

, which is a direct application of the unbinned likelihood (see case 1, figure 31 in section 5.4). The subscript i denotes individual data events. Leaving n_s as a free parameter, one continues with the standard maximum likelihood procedure (section 5.4.1) and forms the likelihood ratio using a nested hypothesis with $n_s = 0$. However, it is more illuminating to derive the same formula from the "extended likelihood" description (case 2, figure 31 in section 5.4), which encodes the overall normalization by an extra Poisson factor via

$$L = \frac{e^{-\lambda_{tot}} \cdot \lambda_{tot}^N}{N!} \cdot \prod_{i=1}^{N} f(\vec{x}_i) \tag{24}$$

, where λ_{tot} is the total expected number of events. The log-likelihood function is more practical to work with, and one can also write

$$\ln(L) = -\lambda_{tot} + \sum_{i=1}^{N} \ln(\lambda_{tot} \cdot f(\vec{x}_i)) \tag{25}$$

1 The PDF in general also depends on other observables, but it is convenient to first think of the spatial part in isolation.

dropping constant terms. The term $\lambda_{tot} \cdot f(x)$ denotes the overall PDF multiplied by the total number of expected events. One can now assume that $\lambda_{tot} \cdot f(\overline{x})$ consists of several individual sub-PDFs, e.g. of a hypothetical signal and background contribution, whose individual normalizations add up to yield λ_{tot}. More generally, one can assume that λ_{tot} is a sum of k individual normalizations n_k and the term $\lambda_{tot} \cdot f(\overline{x})$ consists of the superposition of k functions $n_k \cdot f_k(\overline{x})$. This turns equation 25 into

$$\ln(L) = -n_1 \cdots - n_k + \sum_{i=1}^{N_{tot.}} \ln(n_1 \cdot f_1(\overline{x_i}) + n_2 \cdot f_2(\overline{x_i}) + \cdots + n_k \cdot f_k(\overline{x_i})) \quad (26)$$

In equation 25 it is clear that $\lambda_{tot} \cdot f(\overline{x_i}) > 0$ for all $\overline{x_i}$, since λ_{tot} is the mean of a Poisson process and $f(\overline{x_i})$ the evaluation of a PDF, both of which can only be positive. This is also the reason one can safely work with the logarithmic likelihood function. It follows that the same has to be true for the replaced term, so $n_1 \cdot f_1(\overline{x_i}) + n_2 \cdot f_2(\overline{x_i}) + \cdots + n_k \cdot f_k(\overline{x_i}) > 0$ for all $\overline{x_i}$. Importantly, the individual n_k's do not have to be positive to fulfill this criterion. Thus, they should not be seen as individual Poisson means anymore, but merely as factors (positive or negative) for the functions f_k. This fact will be important when discussing negative-n_s fits (section 9.3). One can now look at the case for two constituents, a signal and a background term. Equation 26 then writes as

$$\ln(L) = -n_s - n_b + \sum_{i=1}^{N_{tot.}} \ln\left(n_s \cdot f_s(\overline{x_i}) + n_b \cdot f_b(\overline{x_i})\right) \quad (27)$$

Imposing the constraint $N = n_s + n_b$, one ends up with

$$\ln(L) = \sum_{i=1}^{N_{tot.}} \ln\left(n_s \cdot f_s(\overline{x_i}) + (N_{tot.} - n_s) \cdot f_b(\overline{x_i})\right) \quad (28)$$

which is equivalent to equation 23 up to constant factors and the logarithmic notation.

8.1.1 *Signal and background PDF*

The background PDF is a composite PDF consisting of a 1-d spatial term $\mathcal{S}_b$[2], a 1-d energy term $\mathcal{E}_b$ and an additional factor $\frac{1}{2\pi}$.

$$f_b(\cos(\theta_r), E_r) = \frac{1}{2\pi} \cdot \mathcal{S}_b(\cos(\theta_r)) \cdot \mathcal{E}_b(E_r; \cos(\theta_r)) \quad (29)$$

2 Before a discussion of the PDFs, it should be remarked that the zenith angle θ and declination angle δ are always related via $\delta = \theta - \frac{\pi}{2}$ due to the specific location of the detector (see section 8.4.3).

The latter factor arises from the uniform behavior in right ascension in a time-integrated search. θ_r and E_r are the reconstructed zenith direction (from the MPE fit) and energy estimator (MuE or MuEx), respectively. Note that the spatial part is defined over $\cos(\theta_r)$, not linearly in θ_r. Both $\mathcal{S}_b$ and $\mathcal{E}_b$ are normalized to yield unity when they are integrated over $d\Omega$ and dE and are estimated directly from binned data. Importantly, the 1-d energy PDF depends on $\cos(\theta_r)$ and changes from event to event.

The signal PDF of a single point source j at a particular position in the sky is approximated by

$$\begin{aligned} f_{s,j}(\Psi_r, E_r; \sigma_{pb}) &= \mathcal{S}(\Psi_r; \sigma_{pb}) \cdot \mathcal{E}(E_r) \\ &= \frac{1}{2\pi {\sigma_{pb}}^2} \cdot \exp\left(-0.5 \cdot \left(\frac{\Psi_r}{\sigma_{pb}}\right)^2\right) \cdot \mathcal{E}(E_r; \Gamma) \end{aligned} \tag{30}$$

where the spatial term is an analytic 2-d symmetric gaussian which depends on the event-specific paraboloid estimator and serves as an approximation for the point spread function. The quantity Ψ_r is the angle between the position of the source and the direction of the event it is evaluated for. The fact that the spatial term is event-specific (depending on the paraboloid estimator of the event) is to be seen in contrast to the background case where the energy PDF is event-specific (depending on the $\cos(\theta_r)$ of the event). The energy PDF $\mathcal{E}$ for a point source is determined from simulations by histogramming the energy estimators of all events whose neutrino directions stem from a given true zenith band around the source position, and generally depends on the spectral index Γ of the energy spectrum.

The signal PDF in the general stacking case is a weighted linear superposition of signal PDFs of the individual sources, normalized to unity via division by the sum of weights.

$$f_s = \frac{1}{\sum_j w_j} \cdot \sum_{j=1}^{N_{sources}} w_j \cdot f_{s,j} \tag{31}$$

The relative weights w_j are determined by the expected neutrino events for source j (see section 6.3)

$$w_j = \int_{E_{min}}^{E_{max}} \left(\frac{d\Phi_\nu}{dE}\right)_j \cdot A_{eff}(\theta_j, E) dE \tag{32}$$

with $\Phi_{\nu,j}$ being the flux of source j, θ_j its zenith position in the sky and E the true neutrino energy. When the spectral shape of each source is assumed to

be similar, one can further decompose w_j into a "model weight" w_{model} and "acceptance weight" $w_{\text{acc.}}$.

$$\begin{aligned} w_j &= \int_{E_{min}}^{E_{max}} \Phi_{0,j} \cdot f(E) \cdot A_{eff}(\theta_j, E) dE \\ &= \left[\Phi_{0,j}\right] \cdot \left[\int_{E_{min}}^{E_{max}} f(E) \cdot A_{eff}(\theta_j, E) dE\right] \\ &= [C \cdot w_{model}] \cdot [w_{acc.}] \end{aligned} \tag{33}$$

The differential energy spectrum has been split into an overall normalization constant Φ_0 and an energy dependent term $f(E)$ for clarity. The derivation shows that the model weight is some factor that is proportional to the overall normalization of the spectrum (as indicated by the square brackets). Thus, any property that is supposed to be proportional to the overall normalization of the expected neutrino flux can serve as a "model weight", for example the measured gamma flux of the source. The proportionality constant C drops out in the superposition (eq. 31) and is not important. The acceptance weight depends on the position of the source, the limits of energy integration and the assumed differential spectrum. If the spectral index is a free parameter in the likelihood minimization, the acceptance weight will change during the minimization procedure as a consequence.

Given the subtle differences between the signal and background PDFs, one might ask why the point source method works at all. One example is that the spatial part for the background is defined over $\cos(\theta_r)$ while the spatial part in the signal PDF is defined over Ψ_r which is a seemingly different variable. Also, different parts of the PDF are event-specific in the signal and background case, respectively. The resolution to this apparent problem is explained in section 8.4.3.

8.2 ESTIMATING FLUX CONFIDENCE INTERVALS

The right ascension coordinate of each neutrino event in the data sample remains unknown at first. This "blindness" policy ensures one does not bias oneself in any analysis decisions. Nontheless, even with unknown right ascension, one can perform "ensemble tests"[3] and estimate the so-called median sensitivity of the analysis, which is defined as the median expected 90% C.L. flux upper limit if no signal was present. Then, one "unblinds" the data using the real event positions and produces the final measurement or upper limit if no significant signal is seen. In the following the confidence interval construction is described.

Minimizing the negative likelihood function with respect to n_s and spectral index Γ yields a best fit estimate for the given data. One then has to translate the outcome into a confidence interval for the neutrino flux of the

3 Ensemble tests are tests performed on ensembles of simulated skymaps that can be used to determine the sensitivity of the experiment.

sources one is interested in. It is a well-known feature that one does not fit exactly the same number of events as have been injected (see section 8.4.4). Additionally, the analysis in this thesis aims to put limits using an equal weighting scheme, in which one places a limit on average realizations of the source count distribution, which changes the expected number of injected signal events for each simulated skymap. This means, in general there is no one-to-one relationship between the mean number of injected events and the total integrated flux of the tested population.

Before the actual confidence interval is constructed, one determines the p-value of the experimental outcome, which is a measure of the statistical significance. The p-value is defined as $p_0 = \int_{\lambda_{obs.}}^{\infty} g(\lambda; H_0)$, where g is the normalized distribution of test statistic values λ for a large sample of simulated skymaps with no injected signal, i.e. given the null-hypothesis H_0[Oli14]. Analogous to the general description in section 5.4.1, the test statistic in the point-source analysis is defined as

$$\lambda = -2 \cdot \ln \left(\frac{L(n_s = 0)}{L(n_s = n_{s,best}, \Gamma = \Gamma_{best})} \right) \tag{34}$$

or without Γ as a free parameter if the spectral index is fixed. The p-value can also be expressed in gaussian-equivalent sigmas, defined as $Z = \Phi^{-1}(1 - p_0)$ [Cow+11] where Φ^{-1} is the inverse CDF of a standard normal distribution. For simplicity, it was *a priori* decided to perform only an upper limit construction in the case in the case the calculated p-value corresponds to less 3σ, and apply a construction including central confidence intervals[FC98] otherwise. For now we will restrict ourselves to an upper limit construction. The construction is performed following the CL_s method [Rea00], which is a conservative upper limit estimation in the case where one has to deal with contributions from background in the signal region. An important quantity to be determined before unblinding is the "sensitivity". The sensitivity is defined as the median null-hypothesis outcome, i.e. where one performs the upper limit construction assuming the median of $g(\lambda, H_0)$ is the outcome of the experiment.

Figure 40 shows the upper-limit construction using the CL_S method for a point source at dec $= 45°$ with an E^{-2} energy spectrum in comparison to a construction without CL_S.

For demonstrative purposes, the figure contains the test statistic distribution $g(\lambda, H_0)$ for simulated "null skymaps" (no signal). The upper limit construction now proceeds via identifying the integrated flux (y-axis) that produces λ-outcomes larger than the median of in $g(\lambda, H_0)$ in 90% of the cases, or respectively larger than the 10% quantile of the λ-distribution for the sensitivity flux. Here, an analytic parabola fit through "quasi"-10%-quantiles of $g(\lambda)$ [4] for several different signal hypothesis strengths H_1 is used to determine the sensitivity flux. In the case of the non-CL_S construction, 10 %-quantiles are determined via $\int_{-\infty}^{x} g(\lambda; H_1) = 0.1$ which is solved

4 In the CL_S case, they deviate from 10%-quantiles for small λ-outcomes.

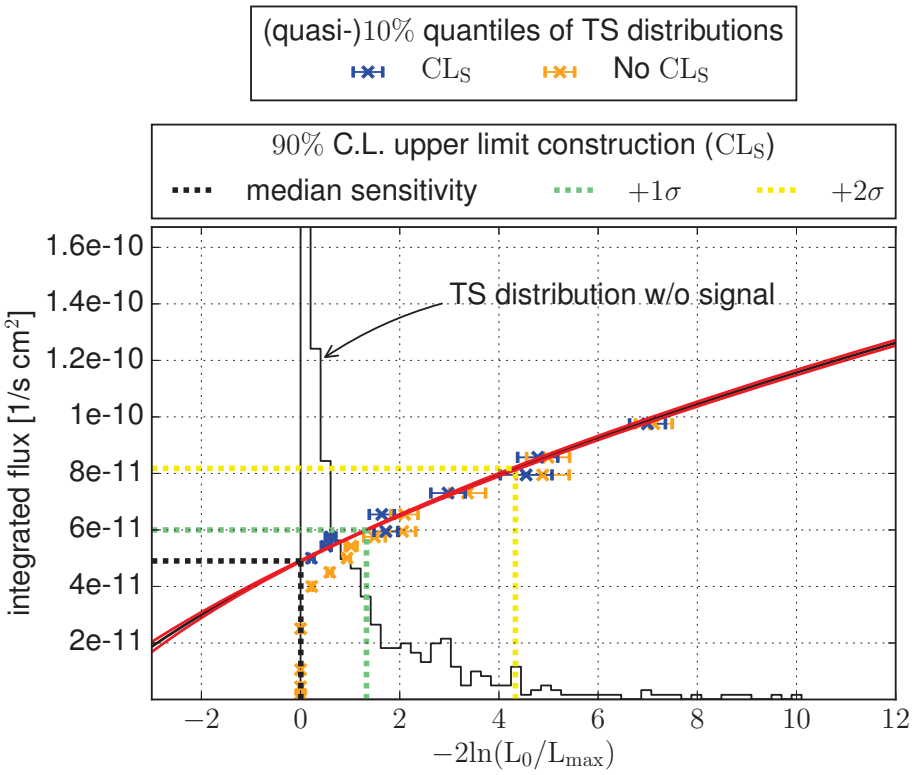

Figure 40: Upper-limit construction for a point source at dec = 45°. The two test statistics (black and blue solid) are plotted for demonstrative purposes and have an arbitrary normalization which is unrelated to the y-axis in the plot. The 10%-quantiles are calculated using individual events and are not depending on any binning. The parabola fit is shown for the best fit (black) and multidimensional one-sigma variation for all parameters (red).

for x. The term H_1 denotes a hypothesis with a particular injected integrated flux and x is the λ value that determines the 10 %-quantile and is used as a data point in the figure. For the CL_S-method, the corresponding relation looks like

$$\frac{\int_{-\infty}^{x} g(\lambda; H_1)\,d\lambda}{1 - p_0} = 0.1 \tag{35}$$

which reduces to the non-CL_S form for small p-values.

The parabola fit empirically describes the flux/quantile relation well for the purpose of retrieving a limit. This is not the case in the standard method, because arbitrarily small fluxes line up at a TS-value of 0 and produce a skewed fit. This could be prevented by removing all data points in the first bin, although a single parabola fit is even then not a good fit as the behavior of the data is linear instead of parabolic towards small test statistic values. The plot emphasizes how the standard method is susceptible to small numerical changes of TS outcomes close to zero, while the CL_S method is not. In previous analyses, e.g. [Ice14d], the upper limit construc-

tion was not done by a parabolic interpolation, but by iteratively narrowing in on the final sensitivity. In this case, the simulations were performed for a large range of injected number of signal events, forming a poisson-weighted mean and exploiting a linear relation between the expected number of signal events and the integrated flux. This has not been an option for this analysis because in the equal weighting scheme the relative injection weights are changed in each trial, which results in no direct correlation between flux and injected events. Also, the standard method is inappropriate when allowing negative n_s, as it will lead to arbitrarily small and ultimately wrong flux limits due to background fluctuations[Rea00]. However, negative n_s are found to be useful for this analysis (see section 9.3). Figure 41 shows the median sensitivity for IC-79 using the CL_S construction presented here in comparison with the standard construction used in [Ice14d]. The CL_S method used here gives upper limits that are on average around

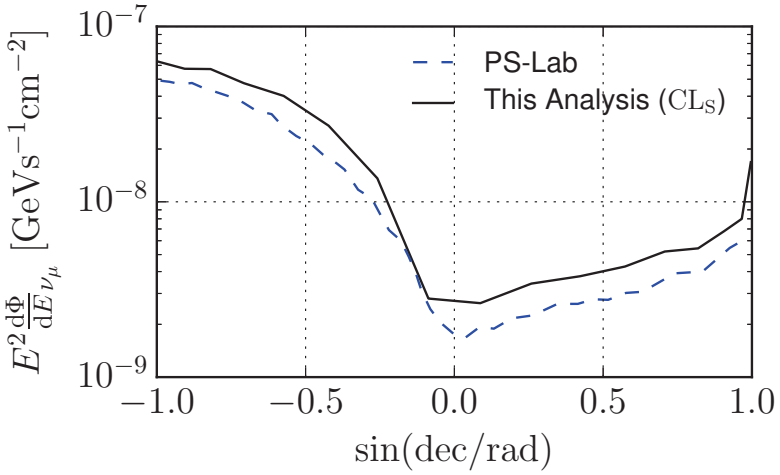

Figure 41: Median sensitivity in IC-79 for an E^{-2} flux using the method presented here a non-CL_S construction (PS-Lab) from [Ice14d].

20% worse than the standard approach, which is expected and reflects the conservative behavior of the CL_S construction. The CL_S-based sensitivities for all datasets are shown in figure 70 in appendix A.2. The construction requires the parabola to describe the sensitivity relation sufficiently. However, it has been found that the final result can shift systematically when a datapoint is added very close to a TS value of 0. A 5% systematic uncertainty has been found empirically to account for such a shift, as the observed changes are of this magnitude once several datapoints are situated in the TS region between 1 and 10. It only applies, though, when the experimental outcome is close to the sensitivity. Overfluctuations should not be affected.

8.3 SOFTWARE IMPLEMENTATION

The whole procedure of simulating skymaps and performing the likelihood minimization and the confidence interval estimation has been implemented

in a self-contained Python framework, specially developed for this purpose. It allows one to test modifications with respect to the standard IceCube point source analysis, in particular features which are not present in other existing software packages. It was also specifically optimized in execution time for stacking searches with thousands of sources and supports to fit multiple populations simultaneously. For example, it takes an equal amount of execution time to evaluate the LLH with two point source populations, each having 1000 sources (and different n_s and Γ_SI), or a single point source population consisting of 2000 sources. The only difference in CPU-time results from the different amount of variables in the fit which leads to a different number of minimization steps. An overview of the procedural flow is shown in figure 42.

Input to the framework are a set of point source population and diffuse flux components.

Each point source within a population can have its own spectrum (but usually does not, as mostly all sources are modelled with the same spectrum), and the spectrum can either be a power-law, a broken power-law, or an arbitrary user-defined spectrum. In the standard mode, only one point source population is given as an input to the framework (whose flux normalization corresponds to one combined n_s value that is fitted). In general, if multiple populations are defined to be used in the LLH minimization, each one can get its own n_s-value in the fit.

At least one diffuse flux has to be given to the framework. A diffuse flux can be either of the "data", "conventional", "prompt" or "astrophysical" type, or it can be a combination of the latter three. It is defined over a certain region in the sky. The spectral index of the diffuse astrophysical hypothesis is held fixed in the combined case. A diffuse flux of the "data"-type means that one uses the PDFs derived from data for event injection or for the likelihood minimization of the diffuse hypothesis.

If more than a single point source population or a single diffuse flux are defined, it is required to use the extended likelihood formalism (see equation 26). If not otherwise stated, however, the default mode uses one point source population and one diffuse component derived from data for the whole sky using the standard point source LLH definition in equation 23. The program then minimizes the given likelihood function (either equation 23 or equation 25) and the results are saved to disk. They are then used to perform the confidence belt constructions.

An important aspect is the fact that different PDFs can be used for event injection and the likelihood minimization (as emphasized in the figure by the red font). For example, one can imagine simulating a sky where one injects events for a defined point source population, but uses a different one as a population hypothesis in the likelihood fit. Such a scenario is for example used to calculate a limit on a small sub-population of the actual population that is studied (see section 11.2). The relative source-weights w_{src} in the constitutive signal PDF can also be different for event injection and llh-minimization. Additionally, the injection weights can be newly ran-

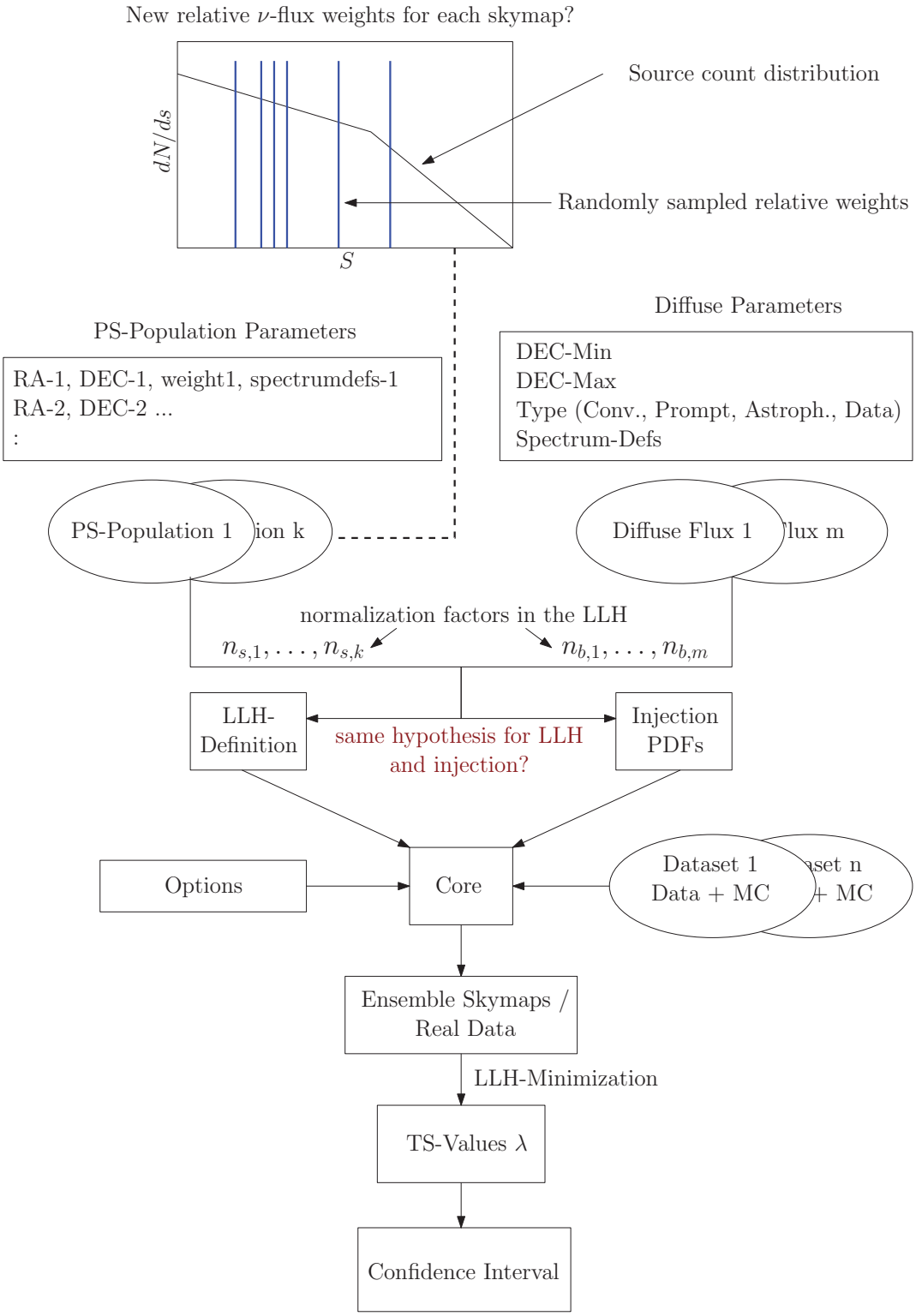

Figure 42: Overview of the software framework which is used to simulate skymaps and perform the stacking analysis. The blue lines in the source count distribution plot at the top of the figure indicate sampled neutrino injection weights. If desired, these can change with each simulated skymap.

domized for each generated skymap. This allows one to construct a median limit for randomized realizations of a particular source count distribution as demonstrated schematically in figure 42.

A list of parameters that can be used to set the binning, the definition of the PDFs, or other options, are given in appendix A.1. If not otherwise stated the default values are being used.

8.4 FEATURES OF THE STANDARD METHOD

8.4.1 *Background injection from data*

In the standard method, background events are injected via randomizing ("scrambling") the right ascension of data events. This is valid since the event density within a given declination band is constant, and the sample retains its statistical properties while washing out any structure. One can also draw events from the data PDFs directly, but the results are indistinguishable from just randomizing the RA positions of the events (see appendix A.2, figure 71).

The scrambling method has the advantage that one does not rely on background Monte Carlo simulations, which can be very time consuming in the case of downgoing muon bundles. It also ensures that one is not biased from possible systematic effects in the simulation. On the other hand it could lead to slight sensitivity losses if the energy PDF is used, as signal-like events that are contained within the data sample can end up close to point source positions and contribute to the LLH. The sensitivity loss can however be assumed to be small as the signal events from a yet undetected source can be assumed to be only a small fraction of the already established diffuse astrophysical events[5].

8.4.2 *Maximal number of sources in a stacking search*

The point source approach is only useful in a regime where the total size of all signal regions (PSF areas around individual sources) is small compared to the total sky. For individual point source searches, this is always the case. For a stacking analysis with many sources, however, it is important to know the critical number of sources where a larger population size starts to deteriorate the sensitivity, or more specifically, the "average sensitivity per source". Since the sensitivity is dominated by the spatial PDF, the energy PDF can be neglected in this estimation. The two weighting scenarios have to be differentiated for this study, as shown in figure 43.

In the γ-energy flux weighting scheme one will never reach the critical point, as additional sources will be added with a contribution w_{src} in the combined signal PDF. The signal PDF will therefore always retain structure

5 Events that belong to the astrophysical diffuse flux are considered as background events in this search and therefore do not pose a problem.

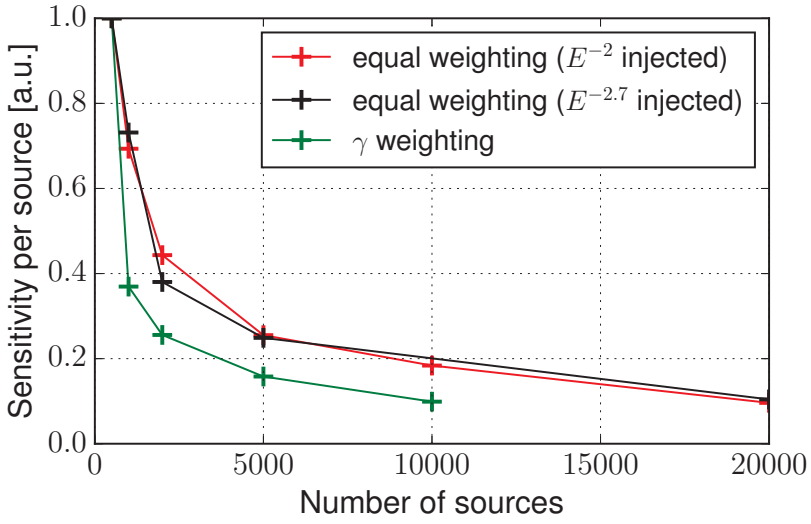

Figure 43: The sensitivity per source for different sizes of the population. The equal weighting scheme uses injection weights sampled from the Fermi-LAT source count distribution. The γ-weighting scheme uses fixed γ weights that are similar for the flux injection and the LLH definition.

on the sky which differentiates it from the background PDF and the average sensitivity per source can only decrease. It is always beneficial to add more sources.

In the equal weighting scheme, on the other hand, the assumed signal region grows roughly linearly by adding more sources as long as the sky-coverage is small enough[6]. In reality, one would not expect equal contributions to the total neutrino flux from each source within the population. Therefore, the behavior is shown for the case where the injection weights are sampled from the gamma-ray source count distribution of blazars for each simulated skymap (see figure 42), which is in line with the equal weigthing limits presented later in chapter 10. At 20000 sources the sensitivity per source does not yet decrease, even if a soft $E^{-2.7}$ is injected which involves low-energy signal events with larger PSFs. Stacking searches with as many sources as possible are therefore desired in all weighting scenarios to maximize detection probability. The only constraint comes from the requirement that the sky-integrated sensitivity flux must be lower than the measured astrophysical diffuse flux. This, however, happens even beyond the maximal population size of 20000 considered here.

8.4.3 *Derivation of the PDFs*

The energy and spatial part in the PDFs in the standard approach (section 8.1.1) can be derived from the general 4-d PDF in a step-by-step manner

6 Sometimes new sources might overlap with old ones, but on average a linear increase is a valid assumption.

as shown in figure 44. This hypothetical 4-d PDF is constructed from the observables declination, right ascension, reconstructed energy, and quality of the reconstruction (paraboloid estimator). The crucial point in the further simplification is to make use of a basic identity of probability theory [Puno3]

$$f(x, y) \equiv f(x \cap y) = f(x|y) \cdot f(y) \equiv f(x; y) \cdot f(y) \tag{36}$$

where f denotes an arbitrary 2-dimensional probability distribution. This means, it is equivalent to evaluate a 2-d PDF in x and y or the product of two 1-d PDFs, where one is the the full 1-d pdf in y and the other is a conditional PDF for x depending on y. This scheme generalizes to higher dimensions. The following list summarizes the individual steps of figure 44 in more detail. Relation 36 is used several times in the process.

- Step 1 involves symmetry arguments. The events are uniformly distributed in right ascension for background, and one can interchange between zenith and declination due to the location of the detector at the South Pole. For signal, one assumes that the PSF is circularly symmetric with respect to the given source position on the sphere. While this might not be the case in individual events, as can be seen from the reconstruction of the paraboloid estimator which involves two paraboloid axes that are usually not equal, it is a reasonable assumption as the behavior averages out because of track-to-track energy deposition differences and alignment variations relative to the string geometry. After step 1 the symmetry arguments have lead to a change of coordinates: the spatial background term is defined over the zenith coordinate θ ($\theta \in [0, \pi]$), while the spatial signal term is defined over Ψ ($\Psi \in [0, \pi]$), the angular distance from the source position in question. While these coordinates are in principle only equivalent if the point source is located at $\theta = 0$, the likelihood method seems to work out mathematically because the coordinates are defined on the sphere which has an intrinsically periodic coordinate system. Due to the periodicity, no data point will ever fall outside the coordinate range in either one of the two cases.

- Step 2 involves a simple coordinate transformation to take the cosine of the respective spatial (angular) coordinate. This is necessary in both cases, since the signal term involves a small angle approximation of a cosine in step 6, and signal and background must always be defined in a way that an integration yields the same result (one linear variable and one cosine would not work).

- Step 3 neglects the paraboloid dependence completely in the background PDF and partially in the signal PDF.

- Step 4 neglects a conditional dependence on the energy in the spatial term and a conditional dependence on the paraboloid estimator in the energy term.

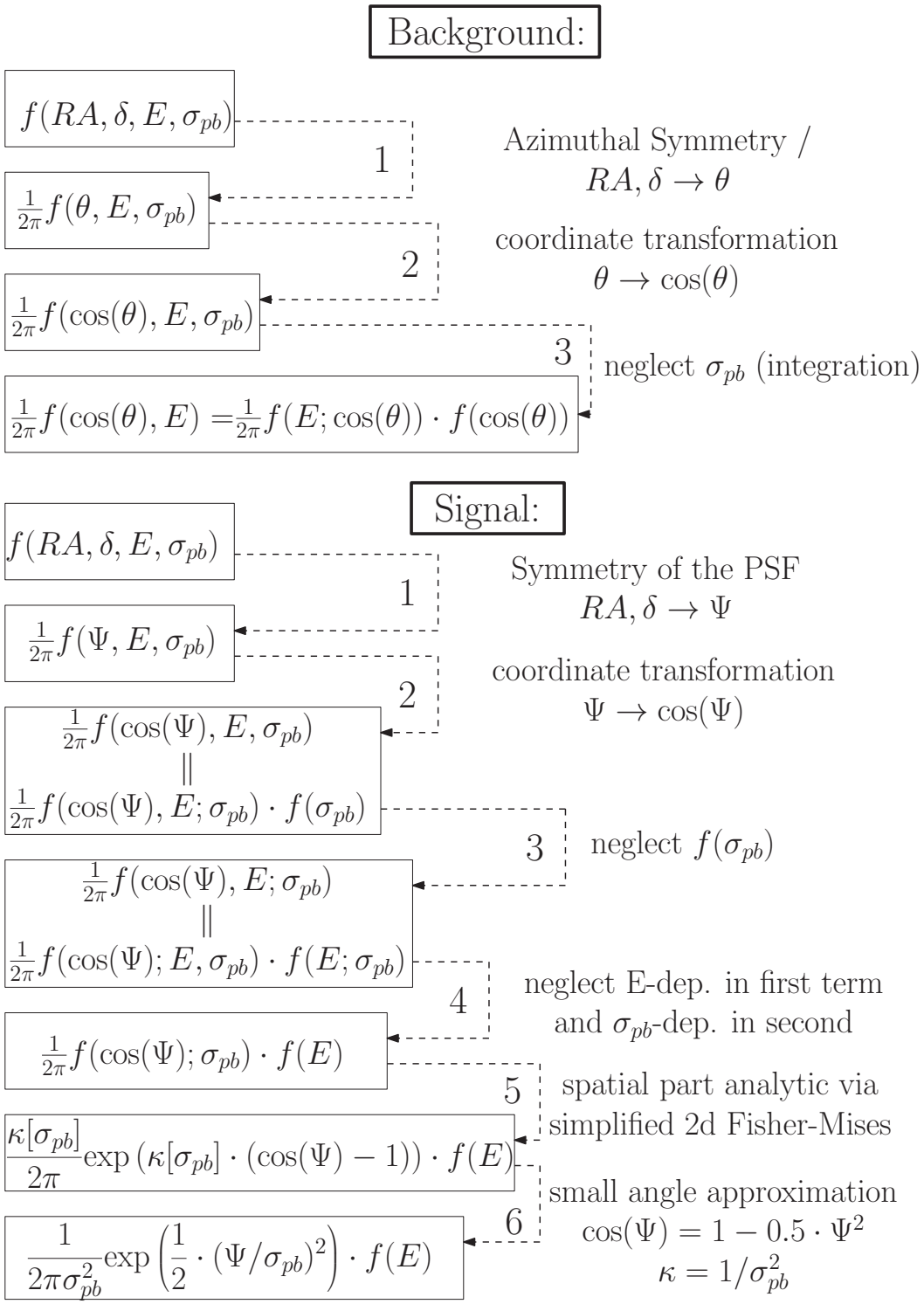

Figure 44: Individual steps in the process of simplification from the full 4d-PDF towards the standard point source form. Flipped equal signs imply the application of equation 36.

- Steps 5 and 6 show the transformation of the spatial part into the analytic Fisher-Von-Mises function and finally into the 2d-gaussian.

Steps 3-6 imply a potential information loss as terms are simplified or approximated. The individual impact of each step on sensitivity is further discussed in section 9.1.

8.4.4 *Disagreement between injected and fitted parameters*

In the standard approach the fitted and injected parameters (n_s and spectral index) do not always agree, as shown in figure 45 in the upper row.

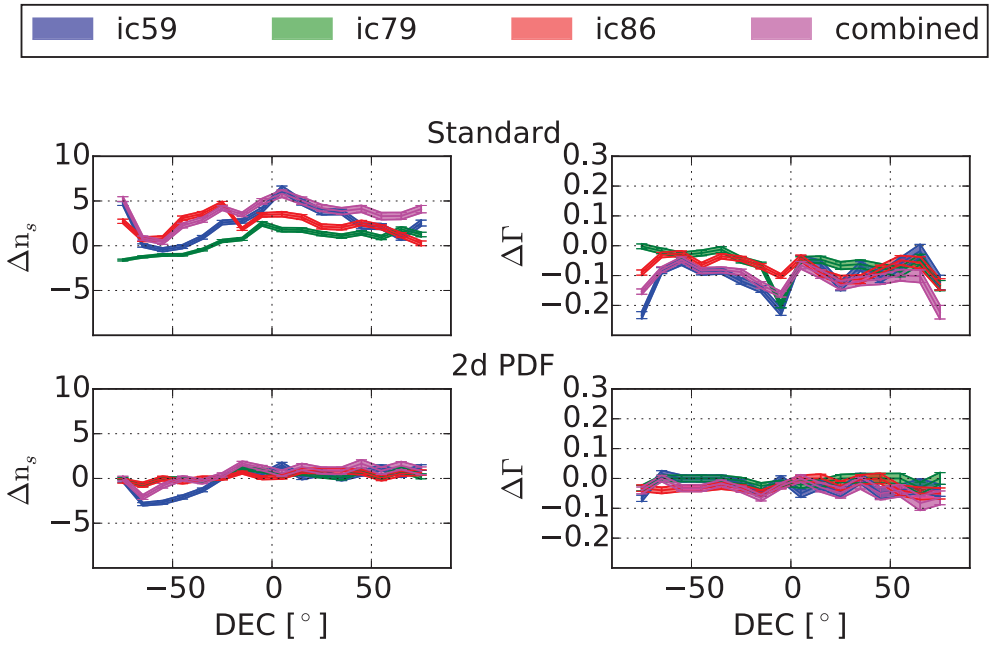

Figure 45: Median of the differences in the injected and reconstructed number of signal events (Δn_s) and spectral index ($\Delta\Gamma$) for a point source with 20 injected events at different declination angles. The error band denotes the 1-σ error on the median. The upper row shows the result using the standard method and the lower row shows the result using the same 2d-PDF for event injection and fitting.

This can be understood as the interplay of two effects. The first is connected to the simplifications described in the previous section, as shown in figure 44. Since one uses the full 3d-PDF (after step 1) during event injection, but an approximation thereof in the fit, it is not suprising to find slight differences in the reconstructed values. A second effect comes from a different binning of the PDFs during injection compared to the binning of the likelihood PDFs which is coarser in the standard approach. This is intending to be precise during injection but conservative in the minimization process. These two effects are eliminated in the lower row in figure 45, which shows the results for a 2d-PDF with an energy and a spatial term (no paraboloid

estimator) using a coarser and equal binning scheme [7] scheme for injection and likelihood minimization. In this particular example, even though the agreement between fitted and injected values is better, the actual sensitivity is worse because the paraboloid estimator is neglected in the 2d-PDF. The slight deviation for IC-59 in the lower left plot is possibly connected to a larger number of misreconstructed events in the down-going region compared to the other two samples.

8.4.5 *Energy pdf and applicability of Wilks' theorem: the "undersampling problem"*

As described in section 5.4.1, the log-likelihood ratio for two nested hypothesis approaches a χ^2 distribution when the sample size N approaches infinity, also called "Wilks' Theorem". The χ^2 distribution then has DOF depending on the difference of the free parameters between two models. In the case of n_s and Γ_{SI}, the DOF are 2. In the case simpler case one only minimizes the normalization parameter n_s the DOF is 1. Three criteria have to be fulfilled for Wilks' Theorem to apply:

- The correct PDFs must be used
- The parameters may not be bounded
- One must reside in the large sample limit ($N \to \infty$)

One can now analyze which of these points apply in the point source method, and how severely they affect the observed test statistic distribution formed by equation 34.

8.4.5.1 *Correct description of the PDFs*

A correct description of the PDFs is an obvious point. As discussed in section 8.4.3, the PDFs that one uses in the likelihood desription are only approximates of the true PDFs (e.g. the analytic approximation for the spatial part) and they differ between signal and background. The effect of some of the simplifications on the sensitivity is discussed in section 9.1. The effect on the TS distribution for the null hypothesis is negligible for nearly all the simplifications that are discussed in this thesis. The exception is the IC-86 test where the background PDF in the northern sky is replaced by a MC-derived PDF one, while events are injected from the data distribution (the corresponding TS distribution a northern-sky source in figure 73, appendix A.2.).

7 Among other parameters, using `numbins_reco_energy_eval=25`, `numbins_reco_energy_inject=25`, `numbins_reco_zenith_eval=25`, `numbins_reco_zenith_inject=25`. See appendix A.1.

8.4.5.2 *Parameter bounds*

Parameter bounds measurably distort the test statistic distribution. In the usual point source approach, n_s is bounded to be non-negative. If the spectral index is fixed, and n_s is the only free parameter, one can show that the LLH-ratio in the large-sample limit [Cow+11] does not asymptotically become a χ^2 distribution but rather behaves as

$$-2 \cdot \ln\left(\frac{L(n_s = 0)}{L(n_{s,\text{bestfit}})}\right) \underset{\lim_{N\to\infty}}{=} 0.5 \cdot \delta(x) + 0.5 \cdot \chi^2_1(x) \tag{37}$$

The delta peak effectively incorporates all under-fluctuations while all over-fluctuations populate a χ^2 distribution with 1 DOF. If one includes the spectral index as a parameter, this "half" χ^2 distribution has 2 DOF (as shown in figure 46(b) in the next section). This result implies that the ideal median cannot be defined properly, as it "sits between" the delta peak and the χ^2 distribution. In a finite simulation, the median either resides in the χ^2 distribution or in the delta peak. When the median outcome resides within the delta-peak distribution, it is ill-defined.

8.4.5.3 *Large sample limit*

The mathematical results from equation 37 only hold in the large sample limit. How quickly this limit is reached depends on the nature of the signal and background PDF. This is illustrated for a toy example in figure 46. The χ^2 distribution for the narrow signal PDF shows a bumpy structure connected to how many background sample events land in the vicinity of the gaussian PDF. Samples with "undersampled" signal PDFs lead to a TS value closer to zero. For the wider signal PDF, on the other hand, 12 background events sample the signal gaussian sufficiently and the theoretical "$0.5 \cdot \chi^2$"-limit is fulfilled. The same situation applies for the real point source analysis. It turns out that around 100000 background events are enough to sample the spatial signal PDF alone, but not enough to sample the spatial signal PDF in combination with an energy PDF with a hard energy spectrum (for example with spectral index -2). This is illustrated in figure 46(b) for a point source at dec=$-5°$ using the IC-79 data sample. The left part of the figure shows the energy PDF for the background derived from scrambled data, for the MC atmospheric neutrino background, and for a point source signal with spectral index -2 at dec=$-5°$. The energy PDF of the point source extends to higher energies than the data PDF and the one from atmospheric neutrinos. As a result, the TS distribution assuming a fixed E^{-2} spectrum strongly overpopulates the delta peak. Judging from the steep drop of the background PDF, even if one used the atmospheric neutrino PDF for background injection, one would require a factor of 10-100 more events than currently present in the data to sample the signal PDF sufficiently. This amounts to 1-10 million events per year. Since this is an unfeasibly large number and present selections have around 10^5 events, the effect is unavoidable. Leaving the spectral index free to vary, however,

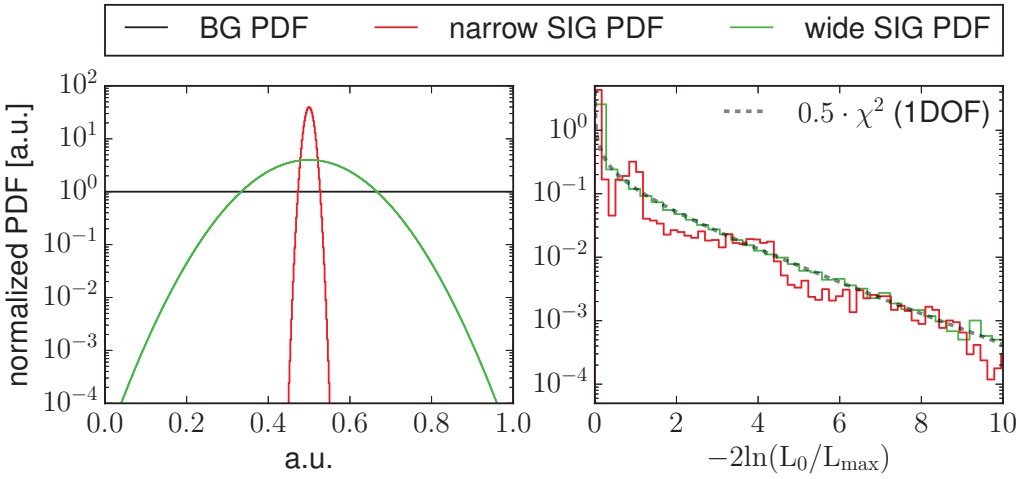

(a)

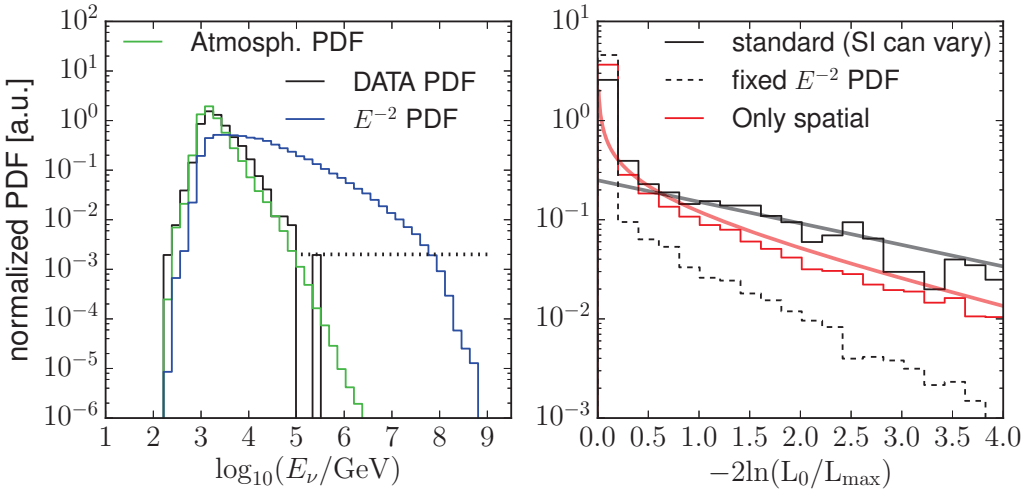

(b)

Figure 46: Illustration of the undersampling problem. a) Toy example with a flat background, a wide signal (green) and a narrow signal (red) PDF. Twelve background events are injected per sample and 100000 samples are produced. The left plot shows the shape of the PDFs and the right plot the resulting TS distribution. The green TS distribution of the wide signal PDF follows the theoretical expectations. b) A point source example using the IC-79 dataset for a source at DEC= 5° in various scenarios. The left side shows the energy PDFs of atmospheric background expectation, an E^{-2} neutrino signal and data. An extension of the data PDF is shown as the dotted line (relevant in section 8.4.6). The right plot shows the normalized TS distributions of three scenarios (n_s and a free spectral index with an energy PDF, n_s and fixed spectral index with an energy term, n_s with a fixed spectral index and no energy term) and the theoretically expected large-sample limit of $0.5 \cdot \chi^2$ distribution with 1 (red) and 2 (black) DOF (smooth curves).

counteracts this behavior by fitting a softer spectral index, which in turn means the final signal energy PDF is more similar to the background PDF and the resulting TS distribution gets closer to the $0.5 \cdot \chi^2$ expectation with 2 DOF. If one does not use the energy PDF in the LLH fit, and does a point source search based on the spatial PDF only, the agreement with the $0.5 \cdot \chi^2$ expectation with 1 DOF is rather close, showing again that the energy PDF is responsible for the effect. For other declination regions the overall behavior changes quantitatively but not qualitatively.

Consequently, due to the inclusion of the energy PDF, one ends up with an overpopulated zero bin. This makes it impossible to define a median of the null hypothesis distribution. For the rest of the thesis, this problem will be referred to as the **"undersampling problem"**. It will be shown in section 9.3 that the removal of the "$n_s \geqslant 0$" restriction in the minimization procedure can mitigate this effect.

8.4.6 *Background pdf from data*

The background PDF in the likelihood minimization is modeled based on experimental data. This has the benefit that the overall shape of the background PDF is correctly described and one does not have to take care of the different backgrounds (atm. ν's vs. atm. μ-bundles) in the southern and northern sky which potentially have different systematic uncertainties in simulation. On the other hand, it reduces sensitivity to the high energy tail of the energy PDF, since any existing signal events are included in the modelling of the background. This effect gets larger, the more signal events are present in the data with respect to background events.

Additionally, one runs into problems for skymaps with injected signal events. This can be understood via the left plot in figure 46(b). Since the signal PDF is defined in areas where the data-driven background PDF is zero, a log-likelihood evaluation for the null hypothesis ($n_s = 0$) results in infinity due to the logarithm in equation 28. In the standard approach this is solved by assuming the smallest non-zero value of the background PDF to be valid at the signal event position, which essentially means a flat extrapolation of the PDF towards higher energies (dotted horizontal line in figure 46(b). This modified background PDF is renormalized to be of unit area. The procedure is in general conservative, as the true background PDF will monotonically fall towards higher energies, and a higher-than-necessary background probability is assigned to the respective signal events.

In an alternative approach one can try to model the background PDF by Monte Carlo simulations, which is described in section 9.2.

9 VARIATIONS OF THE STANDARD METHOD

This chapter describes some modifications of the standard method that address some of the problems raised in the previous chapter.

9.1 REVERSING PDF APPROXIMATIONS

The individual approximations $3-6$ described in section 8.4.3 potentially imply sensitivity losses that have to be quantified. This cannot be done for signal and background separately if the simplification step involves dimensional reduction of the PDF, like for background step 3. If this step was applied only to the background part, the signal PDF would still depend on σ_{pb} and a combined likelihood usage would not work. Therefore, some approximations have to be studied in conjunction. Three approximations are studied in the following:

(A) background step 3 and signal step 3+4

This combined step neglects the dependence of the PDF on the paraboloid estimator for background and reduces the paraboloid-dependence in the signal PDF to the spatial term. This effectively reduces a 3-d PDF to a 2-d PDF for background and a 3-d PDF to two multiplicative 1-d PDFs (where one still depends on the paraboloid estimator) for signal.

(B) signal step 5+6

These steps involve a change of a spatial PDF based on Monte Carlo into the analytic gaussian form. Approximation C) is implicitly contained, but it was chosen to test the effect in this way because the question of exchanging the standard gaussian PSF via a MC-based PSF is interesting by itself.

(C) signal step 6

This step describes the exchange of the Fisher-von-Mises distribution on the sphere with a symmetric 2d-gaussian.

The following three subsections concern describe the potential sensitivity losses that come from these approximations.

9.1.1 *Extension to a 3-d PDF*

Reversing approximation A) (step 3 for background and step 3+4 for signal) yields a single, equally-defined 3d-PDF for signal and background. Figure

47 shows the sensitivity comparison between this 3d-PDF and the standard method, where the analytic gaussian is switched with a MC-derived PSF. The example uses a coarser binning scheme to minimize statistical effects because of the course of dimensionality coming with the 3d-PDF. The gain of the full 3d-PDF is not measurable within statistical uncertainties, if the energy-dependent paraboloid-correction is applied. On the other hand, if it is not applied, the standard point source PDF (with a MC-derived PSF) shows sensitivity losses up to a factor of two, especially in the southern sky. Using the 3d-PDF, all correlations are taken into account, and the sensitivity does not deteriorate.

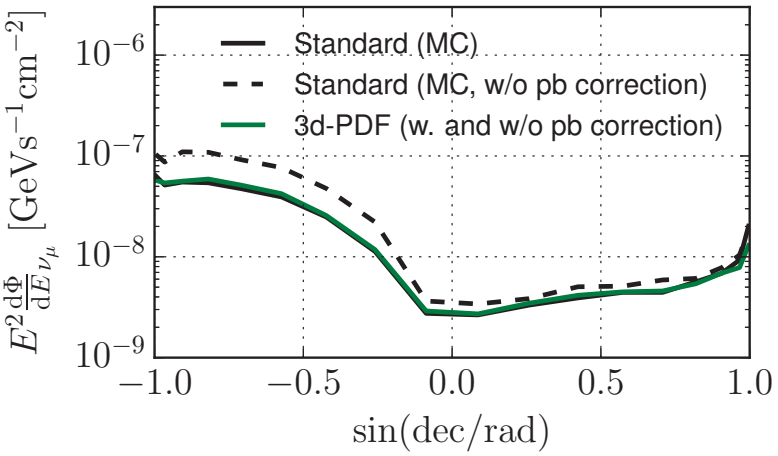

Figure 47: Sensitivity comparison (IC-79) of the 3d-PDF (green) and the standard method based on a MC PSF (black) using corrected (solid) and uncorrected (dashed) paraboloid estimators. All sensitivites are calculated using a coarse binning[a].

a Among other parameters, `numbins_reco_energy_eval=25`, `numbins_reco_energy_inject=25`, `numbins_reco_zenith_eval=25`, `numbins_reco_zenith_inject=25`. In both cases, `combined_pdf_mode` is used to define a complete MC-based PDF. See appendix A.1.

The result shows, that the energy-dependent paraboloid correction effectively eliminates the correlation between reconstructed energy and paraboloid values, which then allows to neglect the paraboloid information for signal in steps 3 and 4 (see figure 44). The similarity of the sensitivities between the two cases using paraboloid correction suggests that the paraboloid estimator does not benefit the background PDF. This motivates background approximation 3.

9.1.2 *Estimating the point spread function from Monte Carlo*

Reversing approximation B) (step 6+5 for signal) replaces the gaussian PDF with a PDF derived from Monte Carlo which is binned in $\cos(\Psi)$. If a gaussian is not an adequate description for the PSF, one might gain sensitivity by instead directly deriving it from Monte Carlo. Figure 48 shows the true and

reconstructed angular errors for an E^{-3} flux in the zenith range between 20 and 40 degrees, which partly motivates such an investigation due to the skewed shape. This example is shown, because the skewness for soft spectra and down-going events has been found to be the largest, much larger than for equally sized zenith bands in the northern sky. Figure 49, however, demonstrates that the gaussian approximation is sufficient, even for a soft E^{-3} spectrum[1]. The same holds true for a harder E^{-2} spectrum (see appendix A.2, figure 72), as expected.

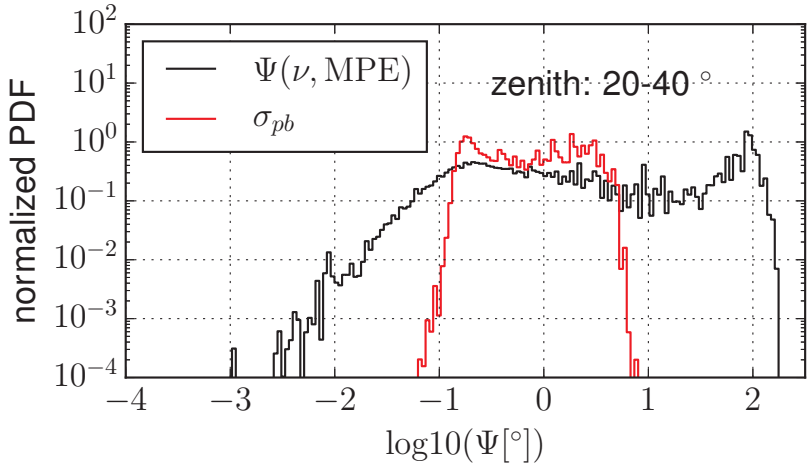

Figure 48: True error (black) and reconstructed error (red) for downgoing events assuming an E^{-3} spectrum using the IC-79 sample.

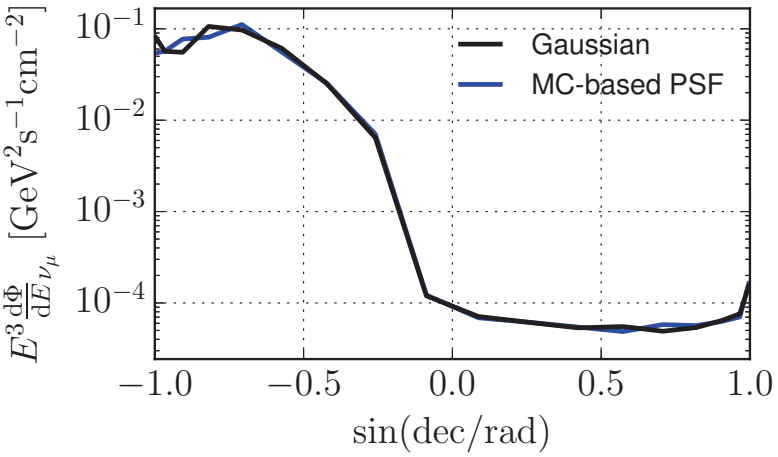

Figure 49: Sensitivity comparison (IC-79) for an E^{-3} spectrum between the standard method and the case where the spatial PDF is derived from MC.

1 The MC-based sensitivity uses `combined_pdf_mode` and `pdf_mode_string` to define the PDFs (see appendix A.1.

9.1.3 *Non-gaussianity due to the curved celestial sphere: the Fisher-von-Mises distribution*

The standard spatial PDF, a 2-d symmetric gaussian, is only an approximation of a distribution that is defined on the two-dimensional sphere: the Fisher-von-Mises distribution in 2 dimensions [Fis53]. Its full expression is shown in equation 38

$$f_{FM,2d}(\theta) = \frac{\exp(\kappa \cdot \cos(\theta))}{2\pi(\exp(\kappa) - \exp(-\kappa))} \tag{38}$$

In this form it is defined symmetrically with respect to an arbitrary point on the sphere, and depends on the angle θ which describes the great arc away from the point around which it is defined. It also depends on the "concentration parameter" κ, which describes how strongly the distribution clusters around its center. A few example distributions are shown in figure 50. The difference to a symmetric gaussian is barely noticable for the

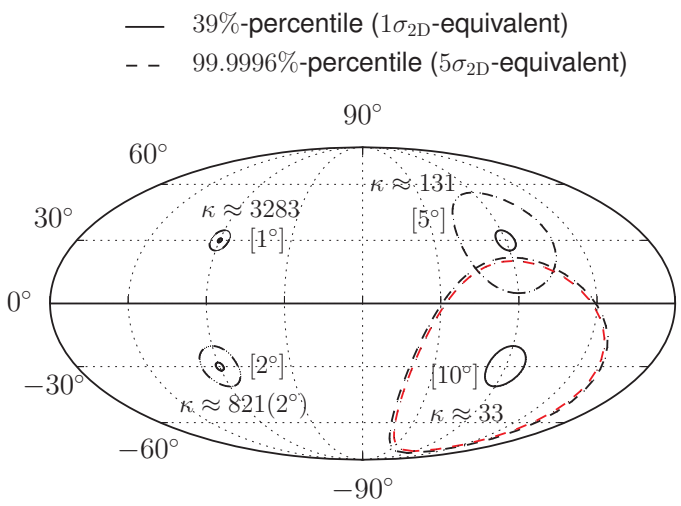

Figure 50: Examples for the Fisher-von Mises distribution in 2 dimensions for different concentration parameters κ. The value in square brackets denotes the 39%-quantile value in degrees. The $5\sigma_{2d}$- line for a symmetric gaussian with $\sigma_{2d} = 10°$ is shown in red.

examples in the figure, as the 5σ line of the gaussian (red line) illustrates for the 10 degree PSF. In the limit $\kappa \to 0$ the distribution approaches $\frac{1}{4\pi}$, i.e. the flat distribution over the sphere without any clustering. In the other limit, $\kappa \to \infty$, two simplifications lead to a 2-d gaussian as will be shown in the following. The first simplification involves restriction to larger κ values, i.e. $\kappa \gtrsim 10$. In this case, one can safely ignore the term $\exp(-\kappa)$ in the denominator of 38, which introduces an error in the overall normalization of $\exp^{-2\kappa}$. It follows that

$$f_{FM,2d}(\theta) \underset{\kappa \gtrsim 10}{\to} f_{FM,2d,1st}(\theta) = \frac{\kappa}{2\pi} \cdot \exp(\kappa \cdot \cos(\theta) - 1) \tag{39}$$

Once this first approximation is taken, one can further make the small angle approximation of the cosine via $\cos(\theta) = 1 - 0.5 \cdot \theta^2$. This yields

$$f_{\mathrm{FM,2d,1st}}(\theta) \underset{\theta \ll 1}{\rightarrow} f_{\mathrm{FM,2d,2nd}}(\theta) = \frac{\kappa}{2\pi} \cdot \exp\left(\frac{1}{2}\kappa \cdot \theta^2\right) = \frac{1}{2\pi\sigma^2} \cdot \exp\left(\frac{1}{2} \cdot (\theta/\sigma)^2\right) \tag{40}$$

Here, κ can be identified with $1/\sigma^2$ where σ is the 39%-quantile of a 2-d symmetric gaussian PDF.

It is interesting to know if the two approximations impose any sensitivity losses for a standard point source analysis, since IceCube has a PSF on the order of a degree (see section 6.3), larger than typical astronomical observatories. While the first approximation is usually safe to make ($\kappa < 10$ corresponds to angles larger than $20°$), the second approximation is exactly step 6 for signal described in figure 44. It is therefore implicit in the sensitivity test from the previous section and the effect due to the small-angle approximation must be negligible for this analysis. However, it is interesting to know at which width of the PSF the effect matters for the sensitivity, which is summarized in appendix D. The small-angle approximation starts to play a role between 5 and 10 degrees.

9.2 THE BACKGROUND PDF FROM MONTE CARLO

Generating the background PDF from data potentially leads to sensitivity losses, as any high energy events would already be contained within the data PDF itself (see section 8.4.1). One can, however, also obtain the PDF from MC-simulations (e.g. the red curve in the left plot of figure 46 (b). It is currently only feasible in the northern sky, where muon bundles are sub-dominant, due to insufficient statistics of air shower simulation and a missing simulation of the IceTop veto. One can include the southern sky by switching to the extended likelihood formalism (equation 26 instead of 28). This is illustrated in figure 51, which shows the sky PDF distribution in the standard point source method (a) with one diffuse background PDF (derived from the data) and the extended option (b). In the new option, the data-derived PDF spans the southern sky and the northern-sky PDF is obtained from Monte Carlo simulation.

The effects are evaluated in two steps. In a first step only the likelihood minimization part is changed, not the injection part which still happens using the data-derived PDF. In a second step, also the event injection part is using the Monte Carlo prediction. The latter option is only meant to be used as a cross-check. For the final significance, one can get biased if the MC-derived PDF is not describing the data sufficiently, for example due to systematic effects.

To simplify the minimization, the MC-derived PDF is described as one effective combined PDF (see section 8.3) including the best fit diffuse astrophysical neutrino flux from [Ice15]. Figure 52 shows the sensitivity curve

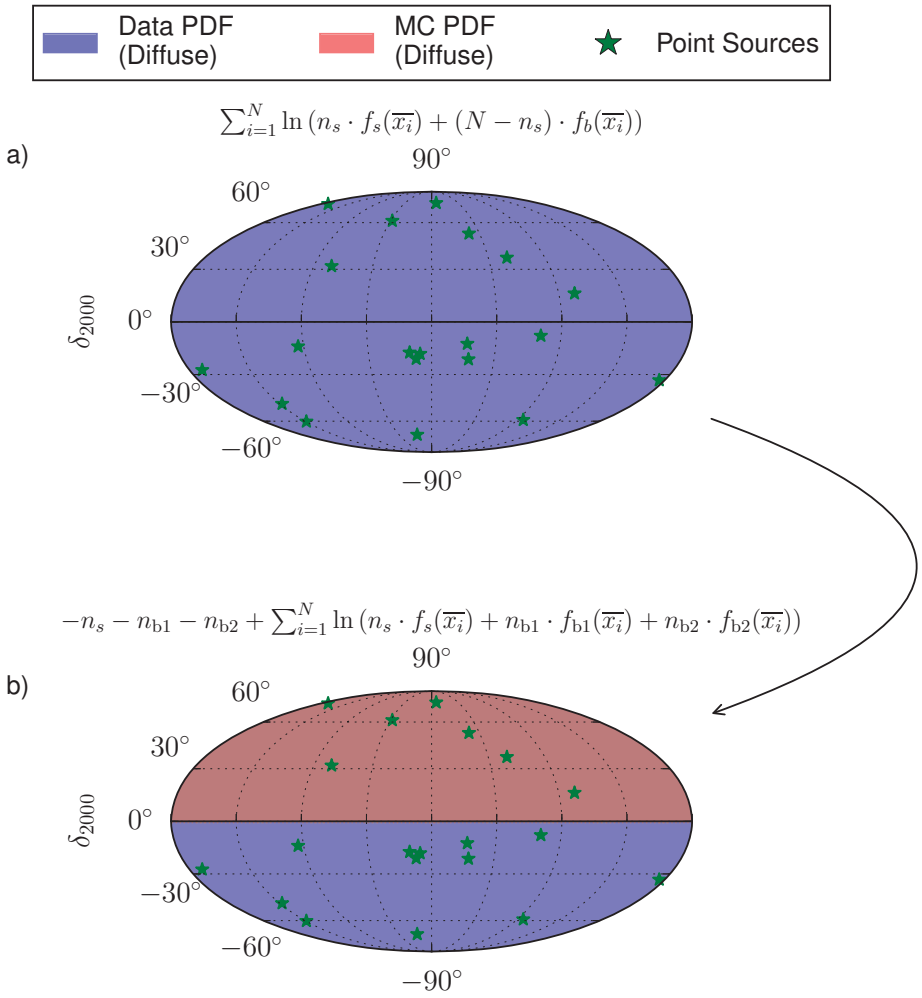

Figure 51: Illustration of the extended likelihood usage for a point source analysis with two diffuse components. (a) The standard approach with one diffuse PDF defined over the entire sky. (b) The extended approach with a data-derived PDF in the southern sky and a MC-derived PDF in the northern sky. The respective likelihood definitions are shown above each skymap.

for an E^{-2} flux using the standard approach and for the two extension steps discussed above.

In the northern sky, where the background PDF is not derived from data, the approach shows a sensitivity gain of about 10%. The gain is smaller than naively expected from the energy PDF gain (see figure 46 b in section 8.4.5), because the reconstructed muon energy is only a lower bound for the true neutrino energy and has a large spread depending on the travel distance of the muon before it enters the detector. It often deviates by orders of magnitude, especially for events with true neutrino energies of a few PeV or larger, which become important for hard spectra. Whether or not one also injects from the Monte Carlo distribution does not have a measurable

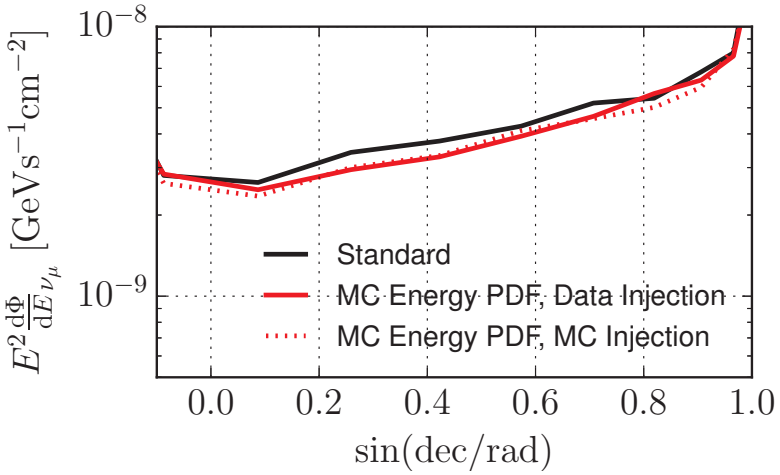

Figure 52: Sensitivity comparison (IC-79) for an E^{-2}-spectrum for the standard approach and a modification where the background PDF in the northern sky is derived from MC and the likelihood fit is performed using the extended likelihood. A third curve (dotted) indicates the sensitivity when the background events are injected from the MC distribution instead of the scrambling of data events.

influence, as can be seen by the dotted curve. This is a sign that the Monte Carlo description is sufficient and does not impose sensitivity losses. For IC-86 the situation is different if standard settings are used (see appendix A.2, figure 73), indicating the influence of a systematic effect. Simulations with a harder spectral index using a much coarser binning indicate (see appendix A.2, figure 74) that this is due to low statistics in the TeV region, since only an E^{-1}-generated dataset is available for IC-86. The IC-79 Monte Carlo, one the other hand, uses an additional E^{-2}-generated dataset that can sufficiently describe the atmospheric spectrum with the standard settings for binning.

9.3 NEGATIVE n_s IN THE MINIMIZATION

Allowing for negative n_s in the fit addresses the problem of the delta peak at zero in the test statistic , which leaves the median often ill-defined as the delta peak usually contains the majority of null outcomes (see section 8.4.5). Moreover, under-fluctuations can not be accounted for as they will also end up in the delta peak. However, there are three potential problems with negative n_s fits that will be addressed in the following. Two are technical and one is conceptual.

1. undefined values appear due to a negative argument in the logarithm
2. the minimizer runs off to $-\infty$
3. conceptual: negative n_s are not physical

The two technical problems can be addressed by looking at the definition of the log-likelihood (eq. 28). The term in the logarithm will in the following be called $T(\overline{x_i})$, with $T(\overline{x_i}) = n_s \cdot f_s(\overline{x_i}) + (N - n_s) \cdot f_b(\overline{x_i})$ where $f_s(\overline{x_i})$ and $f_b(\overline{x_i})$ are the signal and background PDF. When $T(\overline{x_i})$ becomes negative, the logarithm is not defined. It is sufficient, to restrict oneself to the case when this happens due to n_s becoming negative, since the other case where n_s is larger than N is only an artifact of the derivation of the standard form from the extended likelihood function (section 8.1). Besides, one is often interested only in the cases where the expected signal is small compared to the number of background events. It is empirically determined that the true minimum of $-\ln(L)$ is always close to the boundary where the region of undefined values begins, see figure 53 (a). In this example,

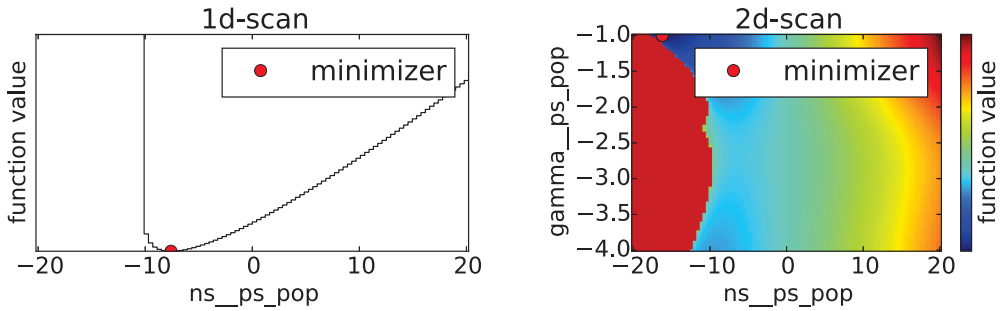

(a) (b)

Figure 53: Likelihood scans for a particular skymap with pure background in IC-86, looking for a point source at DEC=20° and allowing for negative values of n_s. (a) The spectral index is fixed at −2 and a 1-d minimization and scan of n_s is performed. The region with undefined values is at n_s values smaller than around −10. (b) Also the spectral index is minimized. The region of undefined values is the dark red region with a varying n_s boundary.

the region of undefined values begins around −10, where the negative LLH is artificially set to a large value, once the argument $T(\overline{x_i})$ is detected to be negative. In 1-d problems (only n_s), this strategy usually successfully finds the minimum of $-\ln(L)$ with standard minimizer algorithms like MIGRAD. For 2-d minimizations (including a spectral index), the same strategy is less successful, as the boundary which separates the undefined region depends on the spectral index (figure 53 (b) which makes the minimization more intricate. Even if one performs a brute-force minimization and finds the right minimum, it favors hard spectral indices with the largest negative n_s values. This is connected to the undersampling problem of the signal PDF, which depends on the spectral index (see section 8.4.5). Minimizing the spectral index and allowing for negative n_s at the same time will therefore favor minima at the boundary of the allowed spectral index range that also fea-

tures the largest negative n_s values. The problem of a bounded n_s is shifted to the one of a bounded Γ_{SI}.

The second problem, having and unbounded minimum at $-\infty$ that tricks the minimizer into running off, is unrelated to the first problem. It arises in low-count analyses when $f_b(\overline{x}) > f_s(\overline{x})$ for all events in the sample. Automatically, $-\ln(L)$ then has a minimum at $n_s = -\infty$, as will be shown in the following. Comparing the likelihood function from equation 28 for n_s and $n_s - 1$ and forming the difference, one finds

$$\begin{aligned} & L(n_s - 1) - L(n_s) \\ &= \left(\prod_{i=1}^{N} \underbrace{n_s \cdot f_s(\overline{x_i}) + (N - n_s) \cdot f_b(\overline{x_i})}_{\equiv c_i} + \underbrace{f_b(\overline{x_i}) - f_s(\overline{x_i})}_{\equiv \varepsilon_i} \right) - L(n_s) \\ &= \left(\prod_{i=1}^{N} (c_i + \varepsilon_i) \right) - \left(\prod_{i=1}^{N} c_i \right) \\ &> 0 \end{aligned} \tag{41}$$

because ε_i is positive by construction and c_i is positive for all negative values of n_s. Therefore, going to smaller n_s can only increase the likelihood function, or vice versa, decrease $-\ln(L)$. The only solution to this problem is again to restrict n_s to be larger than a minimal n_s, for example $n_s > -N$. One finds that such a case never happens in the analysis presented in this thesis due to sufficient statistics.

The last potential problem is a conceptual one: negative n_s are thought to be unphysical. This proposition, however, is false, as can be seen from the mathematical derivation of the point source likelihood from the extended likelihood in section 8.1. In equation 27 n_s is not a Poisson mean, but adds up only in conjunction with n_b to a Poisson mean. Thus, it is allowed to be negative individually as long as $n_s + n_b > 0$. The name n_s is not always appropriate, as it suggests to describe the number of signal events in all cases. However, as long as the number of signal events is smaller than the average magnitude of background fluctuations in the signal region, the parameter n_s is not to be associated with signal events at all. Only when the analysis outcome has a significance above a certain threshold, for example 3σ, one is allowed to do such an association. Even this is not true, when one encounters the undersampling problem introduced in section 8.4.5 which artificially distorts the fitted n_s value.

One can generally apply negative n_s fits in situations where the two technical problems are not an issue. For a point source analysis with large background, this always applies to differential sensitivity calculations which have a fixed spectral index (usually set to -2) within a given energy band. To distinguish under- from overfluctuations, one has to "mirror" the test statistic at $TS = 0$ for negative values of n_s. Figure 54 illustrates the procedure for two toy examples: a test statistic with a signal PDF that is fully sampled and one that runs into the undersampling problem reported in

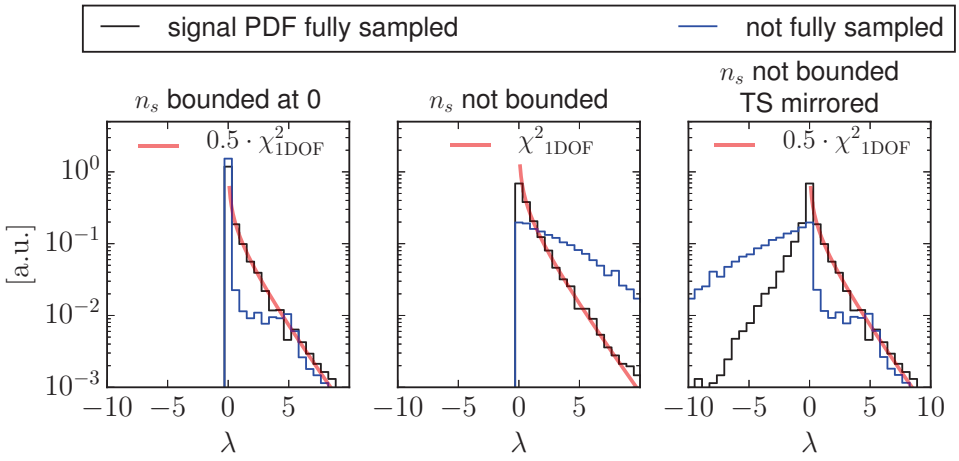

Figure 54: Illustration of the test statistic (λ) construction allowing for negative n_s. One example (black) is simulated for a fully-sampled signal PDF. The other example (blue) possesses the undersampling problem. The same toy-data is used for three different λ constructions. The left column shows the standard construction with only positive n_s. The middle column shows the test statistic distribution allowing for negative n_s. The right column additionally multiplies the test static value by -1 for negative n_s outcomes (mirroring).

section 8.4.5. Using a bound on n_s, the overpopulated delta peak is visible (left column, blue curve). Allowing for negative n_s gets rid of the delta peak, but the distinction between under- and overfluctuations is lost. Multiplying the test statistic by -1 for negative n_s ("mirroring") offers a correct ordering where underfluctuations of background are to the left and overfluctuations are to the right of the distribution, even in cases where the undersampling problem is present. Comparing the first and the last column in the figure, it can be seen that the whole procedure can be interpreted as an "expansion" of the delta peak to negative TS values.

9.3.1 *Application for differential sensitivities*

Permitting negative n_s values allows one to perform confidence belt constructions with a properly defined median even when the undersampling problem is present. This is often the case for differential sensitivities, where one assumes the signal to have a fixed spectral index within a short energy interval. Figure 55 shows an example CL_S construction with negative n_s for a signal present only in the energy interval between 1 TeV and 5 TeV and fixed spectral index of -2.

The test statistic distribution without signal is visibly slightly asymmetric, and the effect becomes larger for higher energies. Instead of a parabola fit which is used in the limit construction with bounded n_s and variable spec-

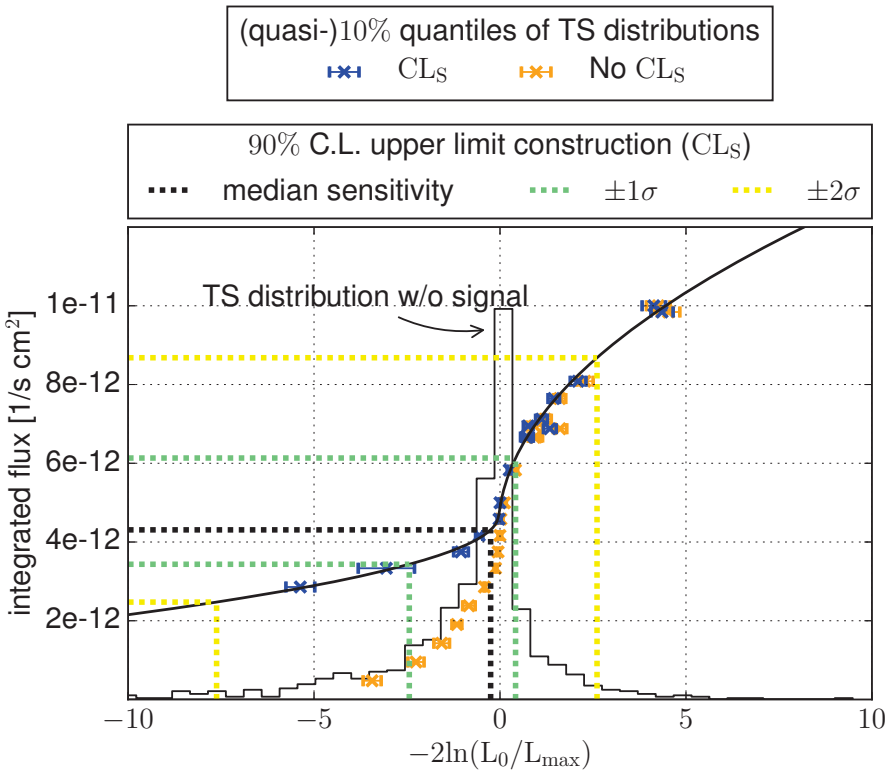

Figure 55: Upper-limit construction in the energy range $4 < \log(E) < 4.5$ using the gamma energy flux weighting allowing for negative n_s (all 2LAC blazars). The construction works similar to the case with bounded n_s (see section 8.2), only that underfluctuations now additionally indicate $-1\sigma/-2\sigma$ regions. The analytic compound function (black solid) consists of two parabolas and one intermediate tangens function fulfilling continuity conditions at the stitching points.

tral index (see figure 40), a three-component function of the form "parabola + tangens + parabola" is used. It is stitched together by imposing continuity in the 0th, 1st and 2nd derivatives and has empirically been found to describe the behavior in the $\pm2\sigma$ region of background fluctuations reasonably well. The positions of the stitching points are free to float in the fit. Doing this construction for a whole range of energy intervals (14 intervals between 100 GeV and 1×10^9 GeV in log-space) gives rise to the differential sensitivity curve shown in figure 56.

The median sensitivity is shown as the central black line, and corresponds to the median outcome of the null test statistic. Additionally, the $\pm1\sigma$ background fluctuations around the median are shown as green bands and the $\pm2\sigma$ background fluctuations around the median are shown as yellow bands. This means, for example, that in 95% of repeated experiments one sets a 90% C.L. upper limit within the yellow band if there is no signal. The red line indicates that the sensitivity improvement allowing for negative n_s is better than a factor of 2 above a few hundred TeV and better than a factor of 3 above energies of a few hundred PeV. Differential limits

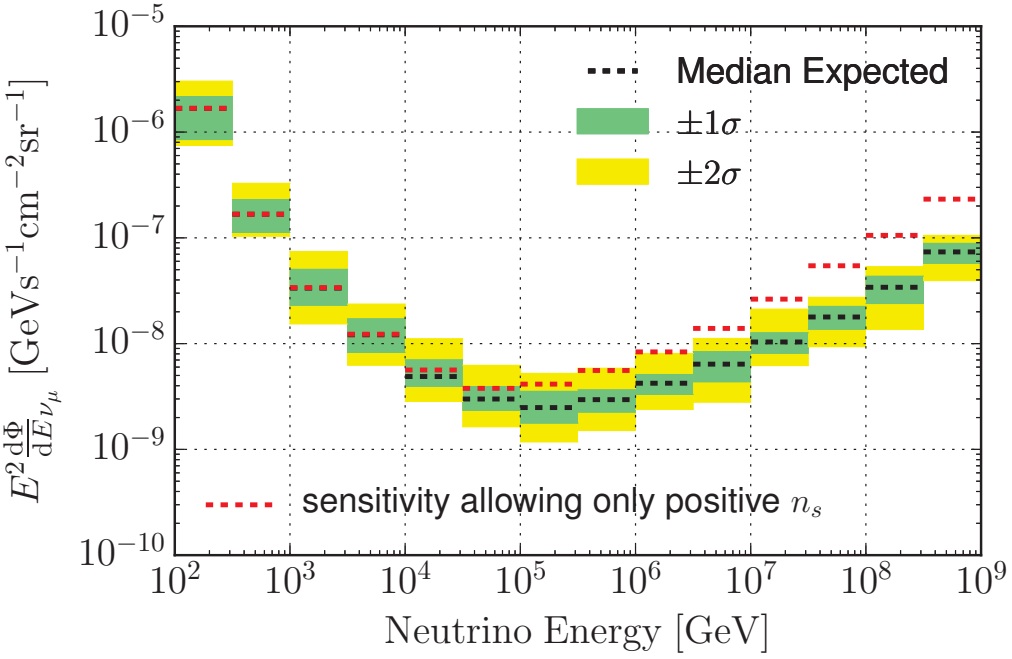

Figure 56: The differential sensitivity for the $(\nu_\mu + \overline{\nu}_\mu)$-flux from all 2LAC blazars using the γ-energy flux weighting scheme. The red line indicates the differential sensitivity with a bounded n_s parameter.

have the advantage that they can be compared to arbitrary energy spectra, but are slightly weaker compared to "integral" limits which only work for a particular spectral model. There is a caveat with any differential sensitivity curve. Its normalization depends on the bin width of the individual energy bins. The sensitivity can become arbitrarily poor the smaller the bin width, as fewer events will end up in a finite-width band for a given flux. A binning finer than the energy resolution of the detector, however, does not give any benefit. Here, a bin width of $0.5 \cdot \log(E)$ was chosen, in accordance with the energy resolution for muons which is around $0.3 \cdot \log(E)$ and larger for muon neutrinos. Too large bins on the other hand would prohibit to compare with arbitrary energy spectra.

9.4 CONCLUSIONS

Table 6 summarizes the effects of the various technical modifications for the point source search itself.

For this analysis, PSFs have a typical extent of a degree and are sufficiently close to the gaussian form that a Monte Carlo based approach does not provide any advantage. Even in the full 3d-PDF form, the result is the same. The last fact can be largely attributed to the paraboloid rescaling, which removes the energy dependence from the spatial distribution and makes an analytic gaussian modeling feasible. If the rescaling was not ap-

Modification	Effect on sensitivity
Analytic → Monte Carlo PSF (signal step 5-6)	negligible for a standard point source analysis
Gaussian → Fisher-von-Mises (signal step 6)	relevant for PSFs > 5° width
Standard Form → Full 3d PDF (signal step 2-4, bg step 3)	σ_{pb}-rescaling: negligible no σ_{pb} rescaling: up to 50% better
Background PDF (Data → MC)	≈ 10% for dec=0 − 60° (hard spectrum)
negative n_s to fit underfluctuations	a factor 2 above a few 100 TeV and a factor 3 above a few 100 PeV (differential sensitivity)

Table 6: Summary of the individual sensitivity impacts of the studied variations to the point source method.

plied, the efficiency loss would be up to a factor two in the southern sky and around 25% in the upgoing sky.

An analytic representation via the Fisher-von-Mises method does not show any significant improvements for PSFs smaller than five degrees. For larger PSFs, one could always switch the analytic Fisher-von-Mises form with a MC-based version, and re-normalize to unity over the sphere. Such approaches might be suitable for extended point source searches or searches using ν-induced cascades, if one assumes a symmetric PSF. In such a case, however, one might also switch to a Monte-Carlo based PSF directly.

From all variations tried, the best positive effect comes from the extension to use a Monte Carlo PDF for the neutrino background in the northern sky, which can potentially yield around 10% in sensitivity in this region. However, it requires that this PDF description has to be sufficiently good to not loose sensitivity again. As this is not the case for the IC-86 dataset using standard parameters, and the procedure additionally requires more CPU-time for the minimization due to the larger number of parameters in the fit, it is not used in the final analysis. It should be emphasized that this improvement would not come at the cost of additional systematics, as the background event injection is still performed with scrambled data.

Finally, allowing for negative n_s was shown to be useful for the calculation of differential sensitivities, which gives a factor three better sensitivity at the highest energies.

10 RESULTS

This chapter presents the results of the thesis to answer the two main questions already introduced in section 5: which constraints can IceCube provide for diffuse neutrino emission models of blazar populations and which maximal share do (2LAC-)blazars have in the diffuse TeV-PeV neutrino flux.

10.1 P-VALUES

This section presents p-values for each individual statistical test. They are reported as "pre-trial" (or "local"), which means they are not corrected for the fact that each test has an independent chance to produce an over-fluctuation if the data is completely uncorrelated. As the number of independent tests increases, one can find lower and lower p-values. Usually, one corrects for this effect and calculates a so-called "post-trial" (or "global") p-value, which is calculated based on the number of independent tests (trials) that have been performed. Since the five blazar populations are not independent (see figure 38 in section 7.2), this post-trial correction is not straight forward to apply here. For the differential p-values, adjacent energy regions are also correlated. Therefore, all p-values in the following sections are presented as pre-trial p-values. A post-trial correction is calculated only for the largest over-fluctuation in the integral and differential tests, respectively, by estimating an "effective" trial-factor[1]. This calculation uses

$$p_{0,\mathrm{post}} = 1 - (1 - p_{0,\mathrm{pre}})^n \tag{42}$$

where n is the number of effective independent tests.

10.1.1 *"Integral" searches*

In the standard "integral" search an unbroken power-law is assumed. The resulting p-values are shown in table 7 for both weighting schemes. Four out of five populations show mild over-fluctuations for the γ-energy flux weighting, the exception being the ISP/HSP population. Using the equal weighting scheme all populations show over-fluctuations, the largest corresponding to a 6% (1.6σ) pre-trial p-value for the "All LAT-blazars" population.

Because of the strong correlation between the two weighting schemes, it is assumed that the trial correction due to the $\gamma - \mathrm{ray}$ energy flux weighting can be neglected. Since the five remaining tests additionally share a large

1 The effective trial factor denotes the effective number of independent tests.

Population	γ energy flux weighting			equal source weighting		
	p-value	n_s	Γ_{SI}	p-value	n_s	Γ_{SI}
All LAT-blazars	36% ($+0.4\sigma$)	19	-2.8	6% ($+1.6\sigma$)	175	-3.0
FSRQs	34% ($+0.4\sigma$)	14	-2.6	34% ($+0.4\sigma$)	30	-2.7
LSPs	36% ($+0.4\sigma$)	13	-2.6	28% ($+0.6\sigma$)	41	-2.8
ISP/HSPs	$> 50\%$	0	-	11% ($+1.2\sigma$)	103	-3.3
LSP-BLLacs	13% ($+1.1\sigma$)	38	-3.2	7% ($+1.5\sigma$)	56	-3.0

Table 7: Pre-trial p-values (and gaussian-equivalent signficances) for the integrated search with bounded n_s and one spectral index over the full energy range. The table shows the results for both weighting schemes, including the respective best fit parameters.

fraction of the sources, it is estimated that the effective trial factor is approximately 2.5 instead of 5. Using equation 42 one finds a post-trial p-value of 14% (1.1σ), which is not significant.

10.1.2 *"Differential" searches*

A useful crosscheck involves a differential test in individual energy bins (here of width 0.5 in $\log(E)$), which is also required for the generation of differential limits. The p-values obtained in this test are summarized in figure 57.

The largest over-fluctuation is again seen in the "All LAT-blazar" sample, tested using equal weighting, as already expected from the integral p-value. The differential test reveals the over-fluctuation happens around 5-10 TeV and has a pre-trial (local) p-value of around 0.004 (2.6σ). It can be related to the combined significance from the three independent sub-populations LSP-BLLacs, FSRQs and ISP/HSPs. In agreement with the integral case, the differential p-values for the ISP/HSP population are the only ones that differ substantially between the two weighting schemes, where the γ-energy flux p-values show flat behavior.

In the differential analysis, 14 (non-independent) trials are performed for each blazar sample instead of one. Two factors enter the trial factor estimation. The first factor is estimated similarly as in the integral test to be 2.5, coming from the source overlap between the different populations. It is multiplied by 5 under the assumption one has approximately 5 independent energy regions, as adjacent energy bins are correlated. This seems to be a reasonable estimate as can be seen from the oscillatory behavior of the p-values versus energy. The resulting effective trial-factor is 12.5. Using equation 42, one finds a post-trial p-value of 5% (1.6σ) for the largest over-fluctuation. While this is also not significant, at first glance it seems to be contradicting the integral outcome of 14%. However, the hypothesis that is being tested is different. One is testing an energy distribution which is flat

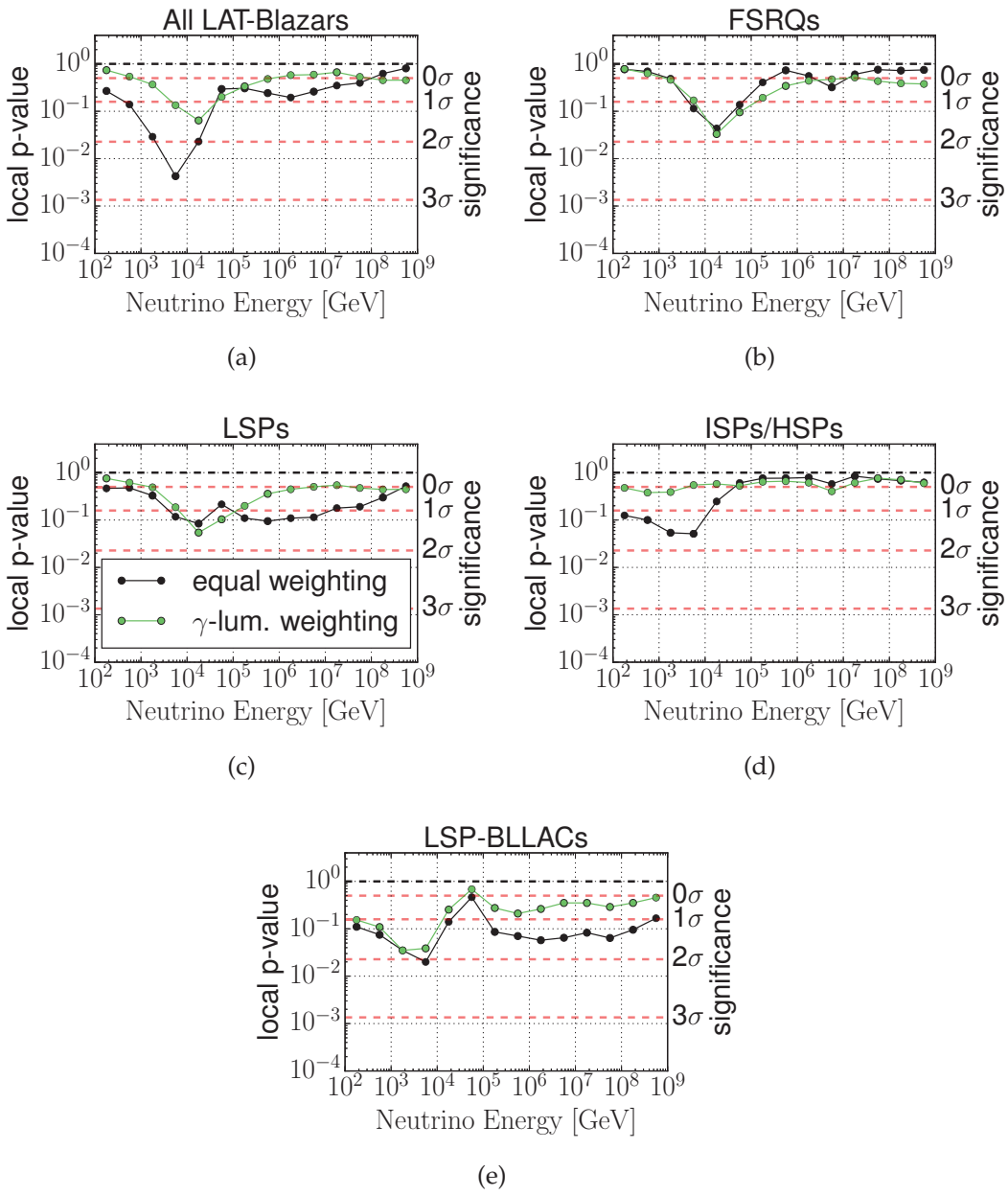

Figure 57: Local p-values for the five blazar populations in the differential test using both weighting schemes. The right y-axis shows the signficance in gaussian-equivalent standard deviations.

in $E^2 \cdot d\Phi/dE$ and only spans half a decade, as opposed to an unbroken power-law for the integral case. Given this difference, the p-value outcomes are comparable.

10.1.3 *Robustness*

The p-values are practically unaffected by any systematic effects, as the data-derived PDF is used for event injection. Even if the PDFs that are

used for the LLH-minimization would be wrong, the ensembles that are used to calculate the p-values are generated using scrambled skymaps with characteristics of the data. This means the final unblinded data-skymap will always produce a TS value that is compatible with the previously produced ensemble and the end-result is robust.

A few a-posteriori (after unblinding) sanity checks are summarized in figures 76, 77,78 in appendix A.2. They show the differential p-values comparing scrambling and injection based on the background PDFs, using different Monte Carlo simulations in IC-79 or using different energy estimators in IC-79, respectively. In general, the results do not deviate significantly from the baseline. Another interesting p-value check, looking at the p-value distribution of each individual year, is discussed separately in section 11.3 in the context of a physical interpretation of the over-fluctuation.

10.2 FLUX UPPER LIMITS

Using the prescription introduced in section 8.2, one can now obtain upper limits on fluxes with arbitrary energy spectra (the "integral" upper limit). All upper limits can also be transformed into the upper limits on the intensity (divided by 4π), which is applicable because the tested blazar samples are large enough that the flux per steradian can be assumed to be constant. All results in the following sections will be presented in these diffuse units.

10.2.1 *Systematic errors*

The systematic uncertainties on the upper limits for this analysis can be categorized into four classes, as outlined in table 8.

The first class is connected to the effective energy scale that is measured in the detector for a particular event. It is affected by scattering and absorption within the ice, by the overall DOM optical efficiency (see appendix B.3 for a definition) and relative DOM efficiency differences in DeepCore DOMs, and by the photon propagation code that is being used. Some of these effects can cancel each other. For example, a higher overall DOM efficiency cancels a larger absorption of photons. Some studies on the light-yield are summarized in appendix B, which eventually contributed to an increase of the overall optical efficiency in simulation by 10% starting with IC-86. The main effect of the combined "energy scale"-systematic is a shift of the reconstructed energy distributions, and therefore has an effect on the LLH analyis itself (through the PDF shape) and for the correction of the paraboloid estimator. There is also a small effect on the directional reconstruction due to the uncertainties in the amount and magnitude of scattered photon hits from the limited knowledge of the ice properties. Its combined effect on the final point source sensitivity has been estimated to be $+5\%/-8\%$ for IC-59 and $+16\%/-8\%$ for IC-79 and IC-86 [Ice14d] where the spline-version of the MPE fit is used compared to the IC-59 analytic

Systematic Type		Uncertainty
Class	Specific	
Energy Scale	Ice Model ($\pm$10% overall scatt. / abs.)	$+16\%/-8\%$
	Absolute DOM optical Efficiency ($\pm$10%) Photon Propagation	$+6\%/-7\%$
	Angular DOM Acceptance	negligible
	Relative DeepCore DOM Efficiency	negligible
Geometry	DOM positions	negligible
Particle Physics	$\nu - N$ cross section rock density muon energy losses	$\pm$4%
Analysis	binning	negligible
	analytic fit in CL_S limit construction	$\pm$5%

Table 8: The four classes of systematic uncertainties which are relevant for this analysis. The uncertainty denotes the uncertainty on the final value of the upper limit.

MPE fit (see section 6.1.1). To be conservative, the larger number is used for all years. Changing the overall DOM optical efficiency by $\pm$10% changes the final sensitivity by $+6\%/-7\%$. Also included in this uncertainty is the effect of the photon propagation technique being used (see section 4.3). Uncertainties in the angular DOM acceptance are negligible compared to this value. Moreover, relative differences in the DeepCore-DOM optical efficiencies have a negligible effect.

The second class of systematics comprises uncertainties on the geometric setup of the detector. A systematic offset of the relative inter-DOM distances from the actual distances could lead to a systematic shift in the directional reconstruction. Absorption of cosmic rays from the direction of the moon can be used to verify that this is not the case as the center of the absorption dip can be reconstructed within 0.2 degrees from the true moon center at 68% C.L. [Ice14b]. This is smaller than the PSF width at the highest neutrino energies and should therefore play only a minor role, even more so towards lower energies.

The third class of systematics concerns with uncertainties on the density of the bedrock below the detector, ν-cross section uncertainties and uncertainties in the muon energy loss profiles. These have been estimated to be around $\pm$4% [Ice11]. Cosmic-ray related uncertainties, like the CR-composition or the CR-spectral index, do not play a role since the background PDFs are estimated from the observed data.

The fourth class of systematics is related to the analysis itself. The binning of the PDFs can have an effect if the MC statistics are not large enough and a "bumpy" PDF is taken as an input for the LLH-minimization. This is tested

by a comparison with a coarser binning scheme (see figure 75, appendix A.2) which shows no visible effect. Another systematic effect comes from the CL_S upper-limit construction which has been estimated to $\pm 5\%$ (see section 8.2).

Taking the individual systematic effects in quadrature one arrives at a final systematic uncertainty of $+18\%/-12\%$ which is applicable to all limits of this analysis. This systematic uncertainty is larger than the expected effect from non-simulated τ-neutrinos (see section 4.1.3) and justifies not taking these into account.

10.2.2 *Energy range*

The exclusion power of the detector is only present within a limited energy range, as the sensitivity is not uniform as a function of ν-energy. The determination of the relevant[2] energy range for a given upper limit is illustrated in figure 58 for the "All LAT-blazar" population.

The upper part shows the differential sensitivity and upper limits for three power-law spectra with indices -1.5, -2.0 and -2.7. The differential sensitivity curve in this example is the same as the one presented in section 9.3.1. One can form a ratio (see middle part of the figure) by the division one of a power-law spectrum by the sensitivity curve template. This ratio is defined in arbitrary units, since the differential limit can in principle be constructed with arbitrarily fine binning. The normalization changes when the binning is changed, but the shape of the ratio stays the same. Empirically one finds, that the fraction of the area below the ratio curve between two given energies with respect to the total area over all energies is directly proportional to the sensitivity fraction that is contributing to the given upper limit. The 90 % central interval of this ratio function thus defines the central energy range from which 90% of the total contribution to an upper limit comes from. To say it differently, if one removes all the signal simulation from regions outside this energy range, the limit becomes weaker by 10 %. For the case of the $E^{-1.5}$ spectrum, the lack of simulation above 1×10^9 GeV artificially weakens the limit.

The method described above is a generalization of the method described in [Ice14d] which only used the 90% central interval of signal events to determine the energy interval. In contrast to this older method, the new construction includes the background events as well. It will be used for all integral limits presented in the following sections. The energy range can vary slightly depending on the weighting scheme being used. For the equal weighting scheme, the energy range corresponds to the median energy range of all skymap realizations that are simulated.

2 "Relevant" here means the range which contributes 90% to the total sensitivity.

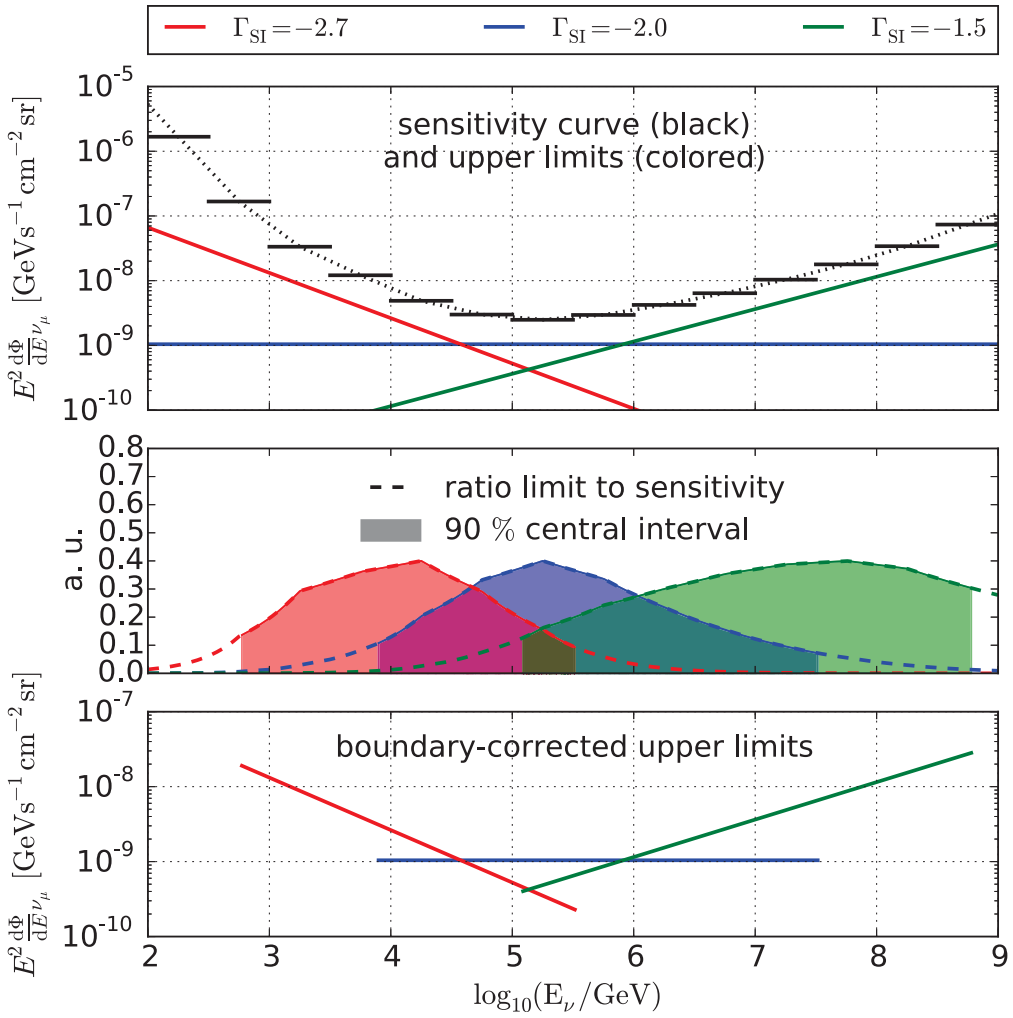

Figure 58: Example construction of the energy range that contributes 90% to the total sensitivity of a given upper limit. The construction is shown for the "All LAT-blazar"-population using the γ-energy flux weighting scheme for three power-law spectra of spectral indices -1.5, -2.0 and -2.7.

10.2.3 *Limit construction in the equal weighting scheme*

Equal weighting upper limits are not calculated assuming equal neutrino injection in each source, but for realizations (or the average of realizations) of a source count distribution handed to the analysis framework, as illustrated in figure 42, section 8.3. Here, it is clarified what implications come with such an approach and which how the result depends on the source count distribution that is being used.

For a given sampling of the source count distribution the weights represent a certain distribution of the total neutrino flux among the sources, and the upper limit has a specific numerical value. Repeating the upper limit calculation for a different set of sampled weights will yield a slightly different upper limit. This calculation is performed 50 times, each time for

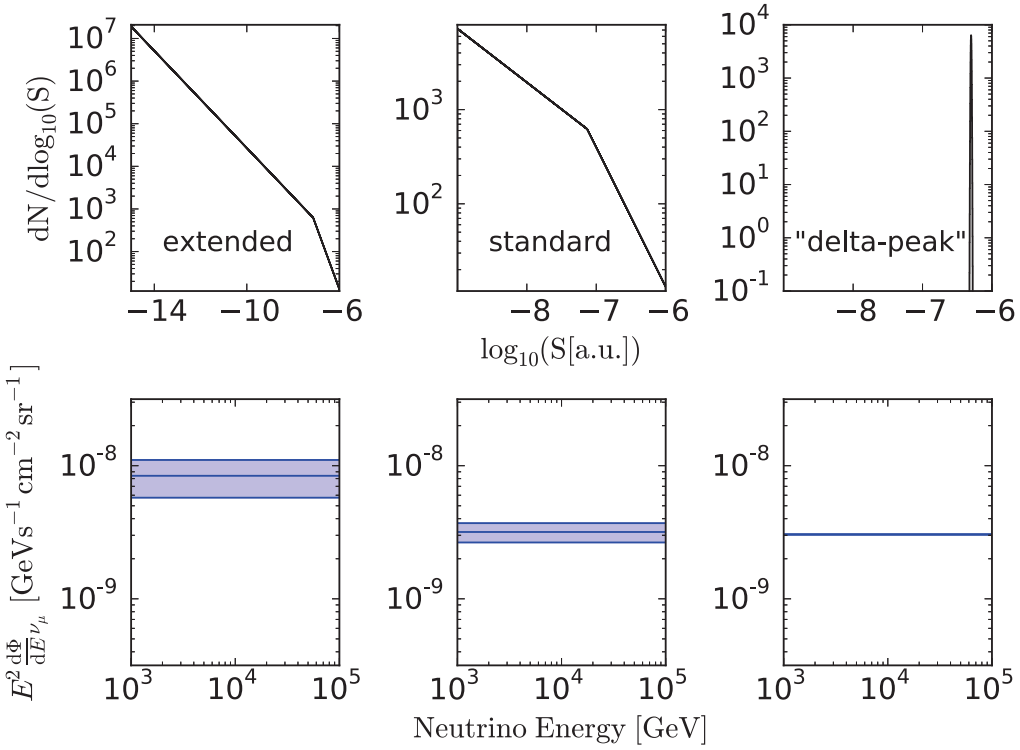

Figure 59: Comparison of equal-weighting upper limits for different source count distributions which are used to sample relative source injection weights. The upper row shows the source count distributions and the lower row the respective upper limit bands for an E^{-2} flux. The blue band marks the 90% central interval of upper limit outcomes for random samplings of the given source distribution. The left-column source count distribution is the same one as in the middle column, but extrapolated to several orders of magnitude lower flux values. The right column shows a delta-peak distribution and corresponds to the injection of events from sources with an equal neutrino flux.

a different distribution of the total flux among the different sources, and the central 90% of these upper limits defines a band. The median value of this band and the magnitude of its spread depends on the form of the source count distribution that is being used for sampling and how far the distribution is sampled towards low-flux values. This is illustrated in figure 59. The upper limit band (bottom row) is calculated for three corresponding source count distributions (top row). The first is the Fermi-LAT blazar source count distribution where the sample range is lowered substantially below the Fermi-LAT detection range, whose lower flux boundary is at $\log_{10}(S/s^{-1}\,m^{-2}) = -9$ (S is measured between 100 MeV and 100 GeV). The second is the same source count distribution, but limited exactly to the Fermi-LAT range of detected fluxes. The third one is a source count distribution which corresponds to an equal neutrino flux per source: a delta function. In practice, the y-axis (the dN/dS value) can be neglected, since

these distributions are used to define relative weights and are treated as normalized probability distributions.

The first and the last example represent unrealistic limiting cases: either a rather large spread of the neutrino flux per source, or equal neutrino flux per source. The resulting band of upper limits therefore gets larger or shrinks to zero, as in the third case the relative injected fluxes correspond exactly to the equal-weighting scheme hypothesis in the PDF definition used for the LLH minimization. The Fermi-LAT blazar source count distribution is chosen for this analysis, because it serves as a template with realistic properties: it is reasonably known beyond the flux region which contributes most to the total flux (figure 39 in section 7.3) and it is also a conservative distribution to use, because of its flattening towards low flux values. An euclidean source count distribution, in comparison, would be unrealistic as the total flux $S \cdot dN/dS$ diverges when integrating over all flux values.

While it is clear why the "delta-peak" source count distribution is unrealistic, it is not so clear with the distribution in the first column. For blazars, the integrated extended source count distribution (figure 59, left column) would correspond to several million objects[3], which can be seen as an interpolation to include all objects in the observable universe. However, since we have a much smaller sample size given by the selection (in this case around 900 objects), sampling the extended distribution will lead to weights that correspond to randomly chosen low-flux sources - a procedure that would imply that no correlation exists between the neutrino flux and gamma-ray flux in the population. The selection itself, however, implies "weak correlation"[4] and therefore an extension to very low fluxes in the source count distribution is not well-motivated. Using exactly the source count distribution observed by the Fermi-LAT (figure 59, central column), the weights have a smaller spread and are sampled more often around the kink region. While the weights are still distributed randomly, i.e. no direct correlation between the gamma-ray and neutrino flux is assumed for individual sources, this procedure is in line with the selection process. The central column source count distribution will be used as a sampling template for all results, also for smaller populations than the "All LAT-blazar" sample for which this represents a conservative choice.

10.2.4 *Generic flux upper limits*

Figure 60 shows the resulting upper limits on the neutrino flux from LAT-resolved blazars for power-law spectra with spectral indices -1.5, -2.0 and -2.7. The limits are to be interpreted differently for the two weighting schemes. The γ-energy flux weighting scheme is valid if one assumes that

3 In the example in the figure, the extension is performed until an arbitrary low-flux value, as the distribution reaches a self-similar form at some point.

4 "Weak correlation" here means the blazars are used as tracers for neutrino emission, but no strict gamma-ray/neutrino flux proportionality is required.

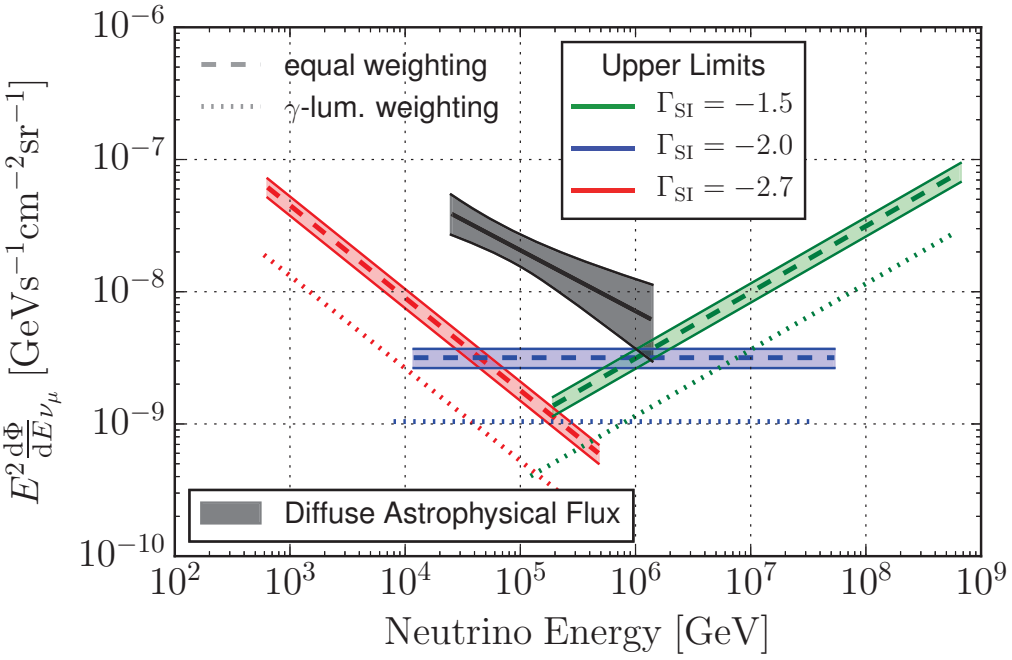

Figure 60: Upper limits on the $(\nu_\mu + \overline{\nu}_\mu)$-flux for generic power-law spectra with spectral indices -1.5, -2.0 and -2.7. Also shown is the diffuse flux measurement from [Ice15] under the assumption of an equal ratio of flavors arriving at Earth.

hadronic emission dominates the gamma-ray flux in the 2LAC energy range (0.1-100 GeV).In this picture, photons generated at higher energies would cascade down and end up in the Fermi-LAT energy range. Since the energy flux is used instead of the flux, the high-energy region (around 100 GeV) gets more relevance in the weight, in line with the reprocessing idea. The upper limit for the equal weighting scheme is to be interpreted as discussed previously in section 10.2.3: it is actually a band corresponding to the 90% central interval of upper limits of randomly sampled realizations of the blazar source count distribution. No assumption about the hadronic contribution to the Fermi-LAT gamma-ray flux except weak correlation (see section 10.2.3) is required .

Table 9 summarizes the flux upper limits on generic power-law spectra for all five populations. For the equal-weighting scheme the median of each band is shown, which is nearly proportional to the number of sources tested in the given population. For the γ-energy flux weighting scheme this proportionality does not apply. The LSP-BLLac population, for example, although it is the smallest one, has its strongest gamma-ray sources in the southern sky (the region with the lowest sensitivity of IceCube) and therefore a rather weak upper limit in this weighing scheme.

10.2.5 *Blazar contribution to the diffuse neutrino flux*

In order to study the contribution of 2LAC blazars to the observed diffuse neutrino signal [Ice15], a spectrum with the currently measured spectral index of -2.5 has been simulated. For such a soft spectral index of $\Gamma_{SI} = -2.5$, the largest contribution to flux upper limit comes from the low-energy bound (as can be seen for the rather similar spectral index -2.7 in

Spectrum	Blazar Class	$\Phi_0{}^{90\%}[\mathrm{GeV}^{-1}\mathrm{cm}^{-2}\mathrm{s}^{-1}\mathrm{sr}^{-1}]$	
		Equal Weighting	γ-E. Flux Weighting
$\Phi_0 \cdot (E/\mathrm{GeV})^{-1.5}$	All LAT-blazars	$31.3\ (26.2 - 36.5) \times 10^{-13}$	11.5×10^{-13}
	FSRQs	$14.1\ (6.6 - 21.6) \times 10^{-13}$	6.7×10^{-13}
	LSPs	$12.9\ (8.1 - 17.6) \times 10^{-13}$	6.8×10^{-13}
	ISPs/HSPs	$17.8\ (13.6 - 21.9) \times 10^{-13}$	12.7×10^{-13}
	LSP-BLLacs	$9.7\ (3.5 - 15.9) \times 10^{-13}$	7.3×10^{-13}
$\Phi_0 \cdot (E/\mathrm{GeV})^{-2.0}$	All LAT-blazars	$3.2\ (2.6 - 3.7) \times 10^{-9}$	9.6×10^{-10}
	FSRQs	$1.2\ (0.5 - 1.8) \times 10^{-9}$	6.5×10^{-10}
	LSPs	$1.5\ (1.0 - 2.1) \times 10^{-9}$	6.5×10^{-10}
	ISPs/HSPs	$1.7\ (1.3 - 2.2) \times 10^{-9}$	9.0×10^{-10}
	LSP-BLLacs	$1.0\ (0.4 - 1.7) \times 10^{-9}$	8.4×10^{-10}
$\Phi_0 \cdot (E/\mathrm{GeV})^{-2.7}$	All LAT-blazars	$5.7\ (4.7 - 6.6) \times 10^{-6}$	1.7×10^{-6}
	FSRQs	$2.3\ (1.1 - 3.5) \times 10^{-6}$	1.1×10^{-6}
	LSPs	$2.6\ (1.6 - 3.5) \times 10^{-6}$	1.1×10^{-6}
	ISPs/HSPs	$3.1\ (2.4 - 3.9) \times 10^{-6}$	1.1×10^{-6}
	LSP-BLLacs	$1.9\ (0.7 - 3.2) \times 10^{-6}$	1.5×10^{-6}

Table 9: 90% C.L. upper flux limits on the $(\nu_\mu + \overline{\nu}_\mu)$-flux for three different power-law spectra ($E^{-1.5}, E^{-2.0}, E^{-2.7}$). The equal-weighting scheme result comprises the median (first value) and the 90% central interval (parentheses) of upper limits.

figure 58). Therefore, it was chosen to simulate a flux starting at 10 TeV, which is close to the lowest energy to which the diffuse flux has been obsered[Ice15]. The diffuse spectrum is unlikely to change significantly within this 15 TeV energy range.

The resulting upper limits for both weighting schemes for the largest population considered (all 2LAC blazars) are shown in comparison to the diffuse flux in figure 61. For the γ-energy flux weighting scheme, the de-

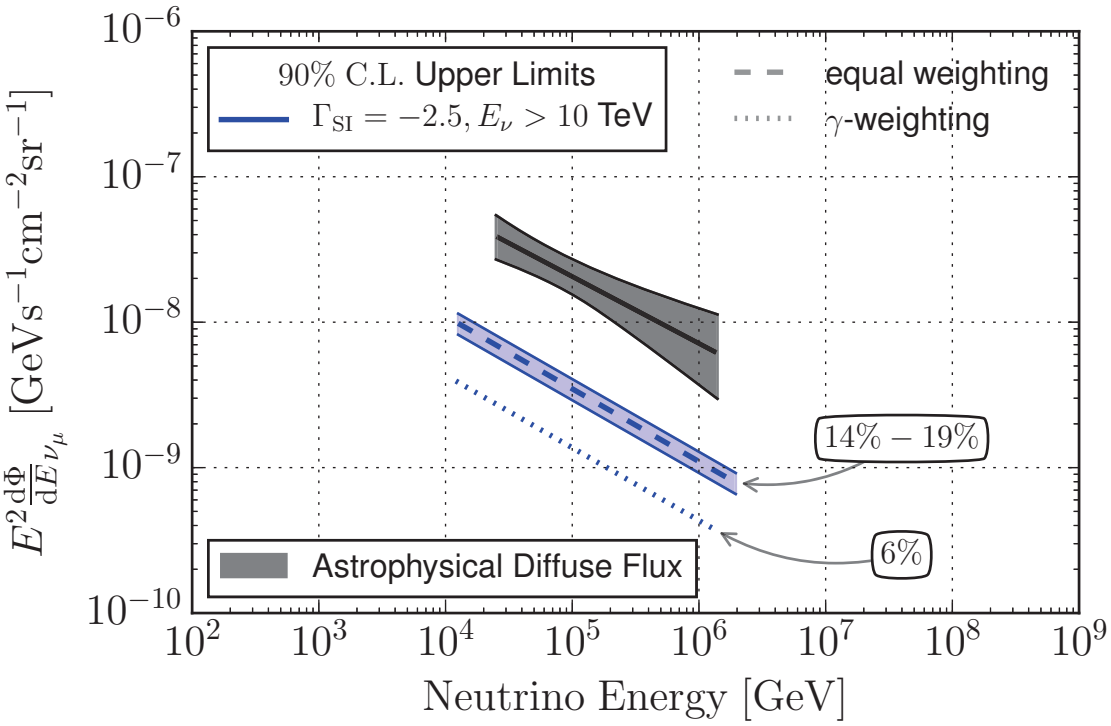

Figure 61: The contribution of all 2LAC blazars to the diffuse astrophysical neutrino flux under assumption of an equal partition of flavors (depicted is the per-flavor flux). In the γ energy flux weighting scheme, the result includes the flux-completeness correction (see text).

picted upper limit is corrected for flux completeness[5] and applies to all GeV-blazars in the observable universe. For the equal weighting scheme, the limit is restricted to the 2LAC blazars. Even in the conservative case of weak correlation to the γ-ray flux, only up to 19% (23% including systematic effects) of the totally measured diffuse signal can be explained by these objects. For a discussion of the robustness of the result with respect to smaller sub-populations, different spectral indices, or other assumptions, see section 11.2.

10.2.6 *Upper limits on models of neutrino emission from blazars*

This section presents upper limits on the diffuse neutrino flux predictions from the models that have been introduced in section 3.5. All upper limits presented in this section assume a correlation between the neutrino flux and γ-ray energy flux, i.e. they apply if the 0.1-100 GeV gamma-ray energy flux is dominated by hadronic processes which are connected to the neutrino

5 The limit is adjusted by a division by 0.7 to account for fact that only 70% of the emission of the entire population of GeV-blazars is resolved into 2LAC sources (see section 7.3).

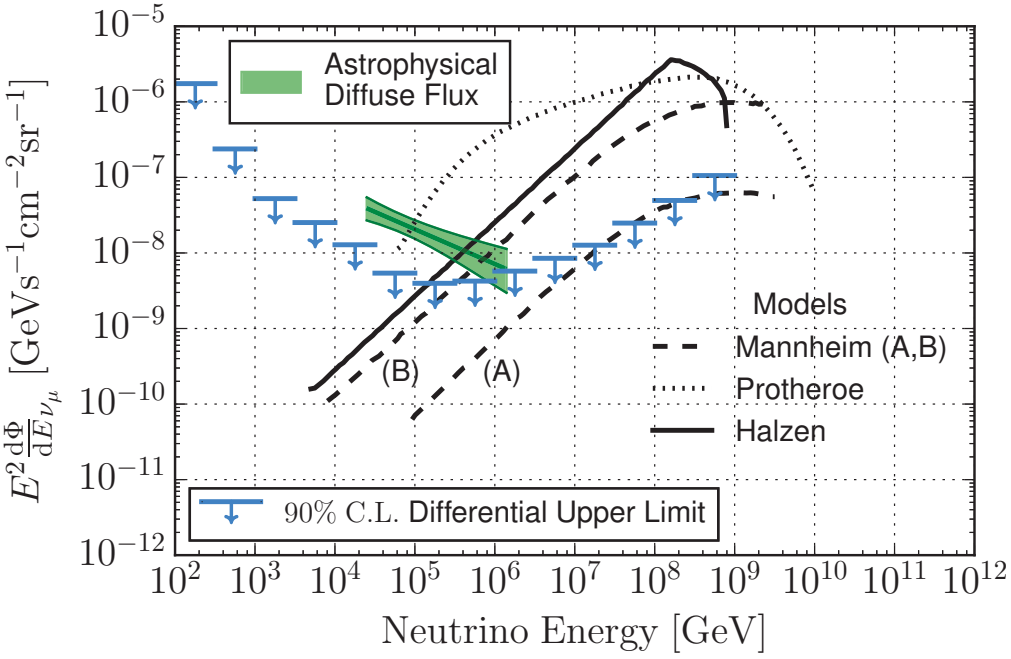

Figure 62: Differential upper limit on the $(\nu_\mu + \overline{\nu}_\mu)$-flux from blazars compared with model predictions by *Mannheim*[Man95],*Halzen et al.* [HZ97] and *Protheroe* [Pro97]. The upper limit uses the γ-energy flux weighting and includes the correction for undetected sources (see text). The astrophysical diffuse neutrino flux (green) is depicted under the assumption of an equal contribution of neutrino flavors arriving at Earth.

production in a given model. To be comparable to the diffuse model predictions all upper limits are corrected for the flux of undetected sources[6].

Figure 62 shows the constraints from this analysis on models of diffuse neutrino emission by (generic) blazars with no distinction between classifications. The differential limit is sufficient to exclude all of them by more than a factor of 10, except model A by *Mannheim* [Man95] which is just at the exclusion boundary. Model A (*Mannheim*) and the model by *Protheroe* [Pro97] assume a correlation to the extragalactic gamma-ray background above 0.1 GeV, which makes the assumption of gamma-ray/neutrino correlation implicit. The other models assume a correlation to the 0.2-30 GeV flux (*Halzen et al.* [HZ97]) and to the gamma-ray flux for energies larger than 1 MeV (*Mannheim* model B), respectively. These energy ranges are slightly different than the 2LAC range but have some overlap. Therefore, the gamma-ray/neutrino correlation assumption is at least partially implied by these models.

6 The limit is adjusted by a division by 0.7 to account for fact that 70% of the emission of the entire population of GeV-blazars is resolved into 2LAC sources (see section 7.3).

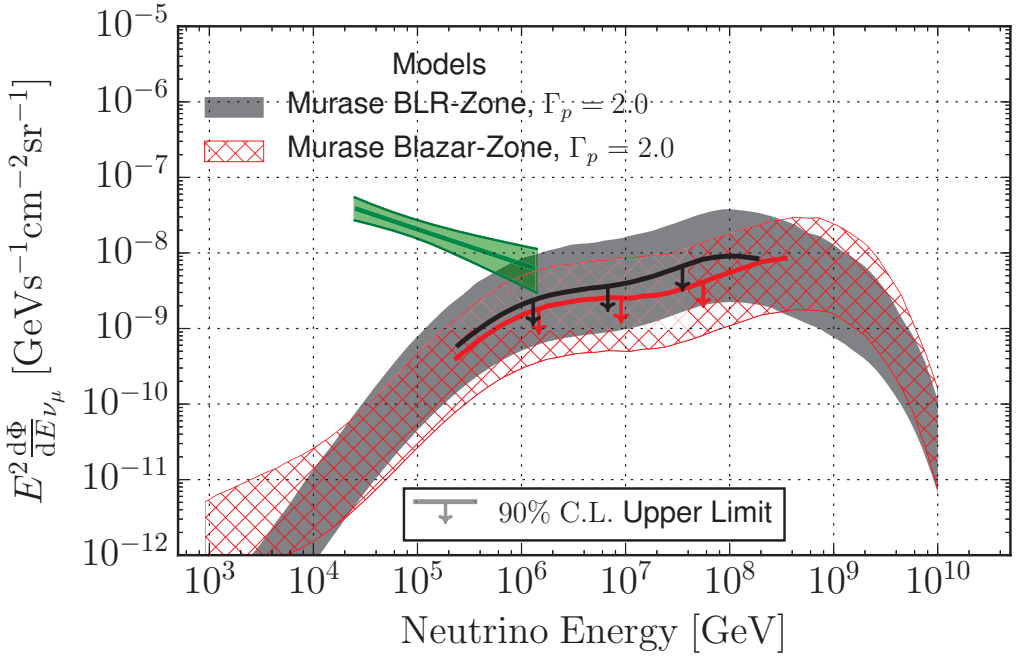

(a)

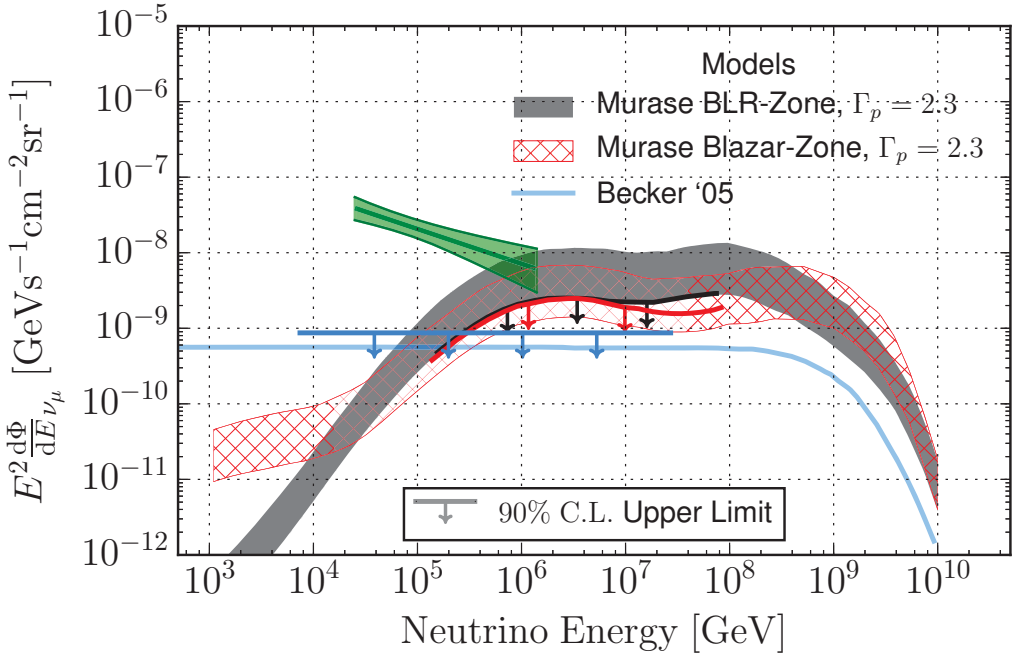

(b)

Figure 63: Upper limits on the diffuse ($\nu_\mu + \overline{\nu}_\mu$)-flux predictions from FSRQs by *Becker et al.*[BBR05] and *Murase et al.*[MID14]. The limits use the γ-energy flux weighting and include the correction for undetected sources (see text). The astrophysical diffuse neutrino flux (green) is depicted under the assumption of an equal contribution of flavors arriving at Earth.

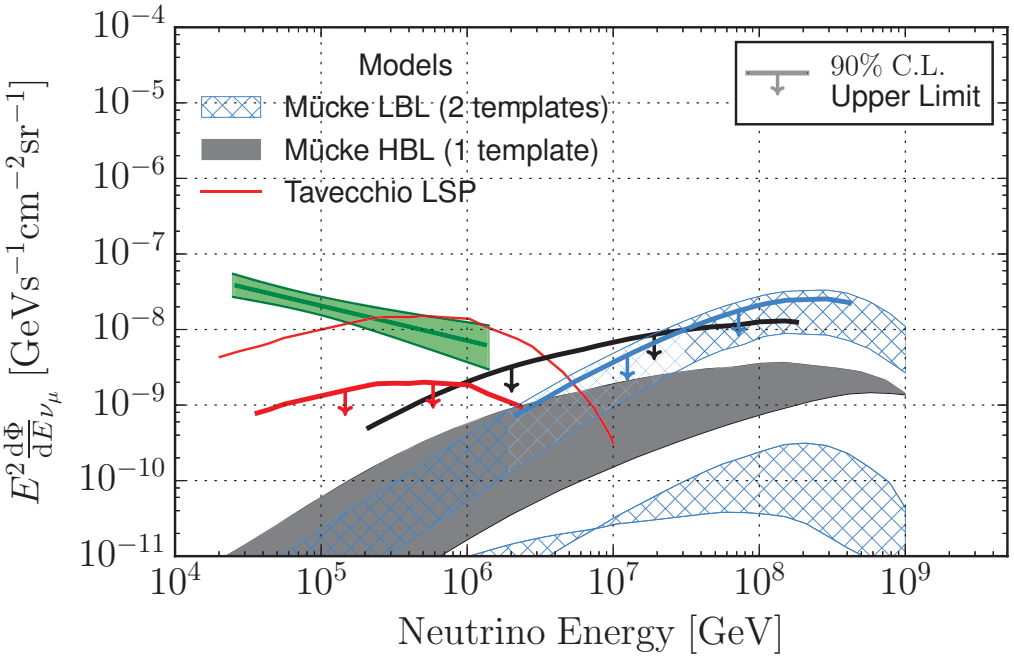

Figure 64: Upper limits on the diffuse $(\nu_\mu + \overline{\nu}_\mu)$-flux predictions from BLLacs by *Mücke et al.* [Mue+03] and the LSP model by *Tavecchio et al.* [TGG14]. The limits use the γ-energy flux weighting and include the correction for undetected sources (see text). The astrophysical diffuse neutrino flux (green) is depicted under the assumption of an equal contribution of neutrino flavors arriving at Earth.

Figure 63 shows upper limits on the neutrino flux from FSRQs. The upper limit on the spectrum predicted by *Becker et al.* [BBR05] is above the model prediction by around a factor of 1.5. The neutrino flux predictions by *Murase et al.* [MID14] for different proton spectra and different photon production zones ("Blazar" and "BLR" zone) are substantially constrained within the assumed parameter space of cosmic ray loading factors ξ_{CR}. The strongest upper limit can be set for the BLR-zone and a soft proton spectrum with a spectral index -2.3, for which the whole parameter space of ξ_{CR} is excluded.

Figure 64 shows the results for BLLac models. The HSP model by *Mücke et al.* [Mue+03] is lower by a factor of around five than the corresponding upper limit and can not be constrained. The most optimistic LSP model range (based on the spectral template of *PKS 0716+714*) is just in the excluded region. The SpineSheath model by *Tavecchio et al.*[TGG14][TG15] is depicted for the LSP dominated case and for both HSP models. It is excluded by an order of magnitude. The constraints on the SpineSheath HSP-related models 1 and 2 are not shown in the figure, but are summarized in table 10 later in this section. Model 1 is slightly constrained, while model 2 is excluded by a factor of around 4. The upper limit calculation uses the ISP/HSP population, assuming that the inclusion of the ISP objects does not change the

Type	Model		MRF
Generic blazars	Mannheim (1995) [Man95]	(A)	0.89
		(B)	< 0.1
	Halzen et al. (1997) [HZ97]		< 0.1
	Protheroe (1997) [Pro97]		< 0.1
FSRQs	Becker et al. (2005) [BBR05]		1.58
	Murase et al. (2014) [MID14]	$\Gamma_{SI} = -2.0$ (BLR)	0.24 ($\xi_{CR} < 12$)
		$\Gamma_{SI} = -2.0$ (blazar)	0.29 ($\xi_{CR} < 15$)
		$\Gamma_{SI} = -2.3$ (BLR)	0.22 ($\xi_{CR} < 108$)
		$\Gamma_{SI} = -2.3$ (blazar)	0.35 ($\xi_{CR} < 173$)
BLLacs	Mücke et al. (2003) [Mue+03]	LSP (optimistic)	0.76
		HSP (optimistic)	3.52
	Tavecchio et al. (2014) [TGG14][TG15]	LSP-dominated	0.13
		HSP-dominated (1)	0.71
		HSP-dominated (2)	0.24

Table 10: Summary of model rejection factors for the diffuse neutrino flux predictions from blazar populations.

result significantly. This is justified as the boundary between the two classes is set artificially.

Included in several of the figures is the all-sky diffuse measurement [Ice15]. For the generic predictions of neutrino emission from blazars (figure 62) this represents an independent measurement in tension with these models. For the BLLac and FSRQ models, the all-sky diffuse flux is higher than the model predictions. Table 10 summarizes the IceCube constraints on the models in terms of model rejection factors [HR03]. The model rejection factor is defined as the ratio of the upper limit to the model prediction, which means the model is excluded if its value is less than one. The models which remain unconstrained are the *Becker et al.* model for FSRQs and the HSP-BLLac calculations by *Mücke et al.*.

11 DISCUSSION

11.1 IMPLICATIONS FOR MODELS OF NEUTRINO EMISSION

The implications for the diffuse neutrino flux predictions from blazar populations have to be differentiated. The generic blazar models from the 90's have in principle been in tension with an earlier all-flavor high-energy diffuse upper limit [Aar+13] and the all-sky diffuse measurement [Ice15]. However, these tensions have rarely been discussed in the literature, if at all. Here, these tensions have been spelled out explicitly, and the results of this thesis provide the strongest model rejection factors on these models, so far.

For the FSRQ and BLLac models, the situation is different. This analysis is the first one to provide upper flux limits that are in tension with some of the parameter space of these model predictions. The upper limits on the most recent models by *Murase et al.*[MID14] and *Tavecchio et al.*[TGG14] are the most interesting ones, since their works utilize the latest multi-wavelength information. The *Tavecchio et al.* model has been explicitly constructed to explain part or all of the all-sky diffuse flux, but is in its current form not viable anymore. For the various *Murase et al.* models, the cosmic-ray to photon luminosity ratio (cosmic ray loading factor ξ_{CR}) within FSRQs has to be small, and a considerable range of the values that have been considered by the authors are excluded. One must, however, caution that the these newer model predictions are not implicitly containing the direct gamma-ray/neutrino correlation assumption of the upper flux limits via pion decay. Indirectly, however, a correlation can be present (for example in the case of the *Murase et al.* predictions), as discussed in section 3.5.

In general, the results provide an experimental benchmark for future model building. Some of the predictions for BLLac-objects (e.g. the HSP models by *Mücke et al.*[Mue+03]) lie a few orders of magnitude below the upper limits presented here and only the most optimistic of these predictions might be reachable in the forseeable future.

11.2 IMPLICATIONS FOR THE OBSERVED DIFFUSE NEUTRINO FLUX

As has been shown in section 10.2.5, the contribution of the 2LAC blazars to the diffuse astrophysical neutrino flux observed by IceCube is less than 23% including systematic uncertainties. While a simple power-law with a spectral index of around -2.5 is currently the favored model to describe the data, this might change in the future. In a few years the sum of a soft and a hard component, or a harder component with a spectral cutoff might

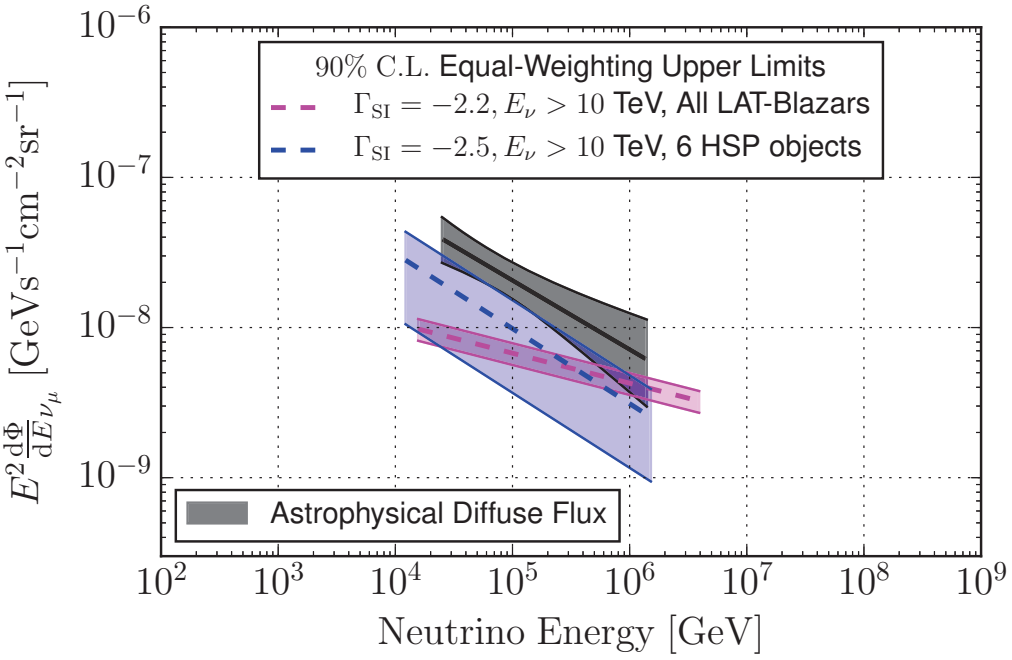

Figure 65: The 2LAC blazar contribution to the diffuse neutrino flux for a harder spectral index of -2.2 and for a small sub-sample of HSP objects (*MKN421*, *H2356-309*, *PG1553+113*, *1RXSJ054357.3*, *1H1914-194*, *PMNJ0816-1311*).

be preferred by the data. Figure 65 shows the equal-weighting result for a harder spectral index of -2.2. While the limit at high energies (around a PeV) becomes compatible with the current best-fit diffuse estimates, one can see that blazars cannot contribute much to the bulk of the emission at lower energies. As such, it seems unlikely that the result presented here will change significantly based on a potentially different spectral fit for the diffuse flux in the future.

Another question that can arise, is whether certain sub-populations (for example the TeVCat blazar sub-sample of the 2LAC catalog) might account for the diffuse flux, because they have not explicitly been tested in this analysis. Figure 65 contains an upper limit for an extreme sub-population: a sample of 6 HSP objects which have been discussed in [PR14] and [Pet+15] to explain either all or fractions of the astrophysical diffuse flux. For this comparison the ISP/HSP population result is used.

The test with the 6 HSP BLLac objects reveals a large spread in allowed upper limits based on the distribution of injected events over the sources (see section 10.2.3 for the derivation of the spread). Some might be compatible with the diffuse flux at first consideration. However, the extremes of this distribution are made up of neutrino flux distributions in which a single source has a dominant share of the neutrino flux and is sitting either in the southern sky (very bad constraint) or northern sky/equatorial region (very good constraint). As such, one has to argue if a quasi-diffuse

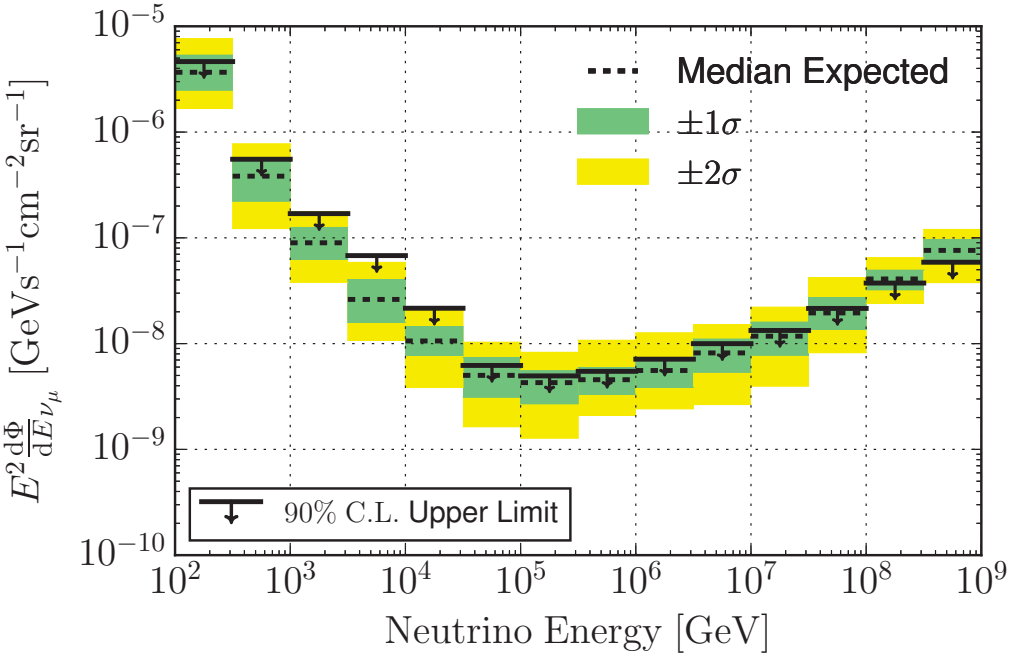

Figure 66: Differential upper limit on the $(\nu_\mu + \overline{\nu}_\mu)$-flux in the equal-weighting scheme for the "All LAT blazar" population. The median sensitivity and expected $\pm1\sigma/\pm2\sigma$ range of outcomes are depicted with colored bands.

description makes sense, since one source dominates the sky with respect to the others. If the allowed spread in neutrino flux between the strongest and weakest source in this sample is constrained, this band gets smaller and the median will shift to lower values (in line with figure 59 in section 10.2.3). As a result, the 6 sources cannot explain the bulk of the diffuse neutrino emission. The same arguments apply to larger sub-samples, like the complete set of TeV-detected blazars [WH08] that are a subset of the blazars in the 2LAC catalog.

Lastly, it is important to emphasize that the overall result applies to the 2LAC blazars. It is still possible that blazars which are currently below the γ-ray detection threshold or do not produce γ-rays at all can cumulatively produce a neutrino flux of the magnitude of the bulk emission. In this case, the neutrino flux would be correlated either to lower energies (which would point to very opaque sources) or to higher energies beyond the reach of the Fermi-LAT.

11.3 A POTENTIAL PHYSICAL NATURE OF THE OBSERVED EXCESS

Figure 66 shows the differential limit for the "All LAT-blazar" population using the equal weighting scheme (the median of the equal-weighting band) which shows the largest over-fluctuation of all tests of this analysis. The slight excess is visible in the 5-10 TeV region. Although it is not yet significant, one can still ask the following questions: What if the overfluctuation

is of a physical nature? What can we expect by adding more data? Does an estimated flux that would produce such an over-fluctuation make sense in the global picture together with Fermi-LAT observations?

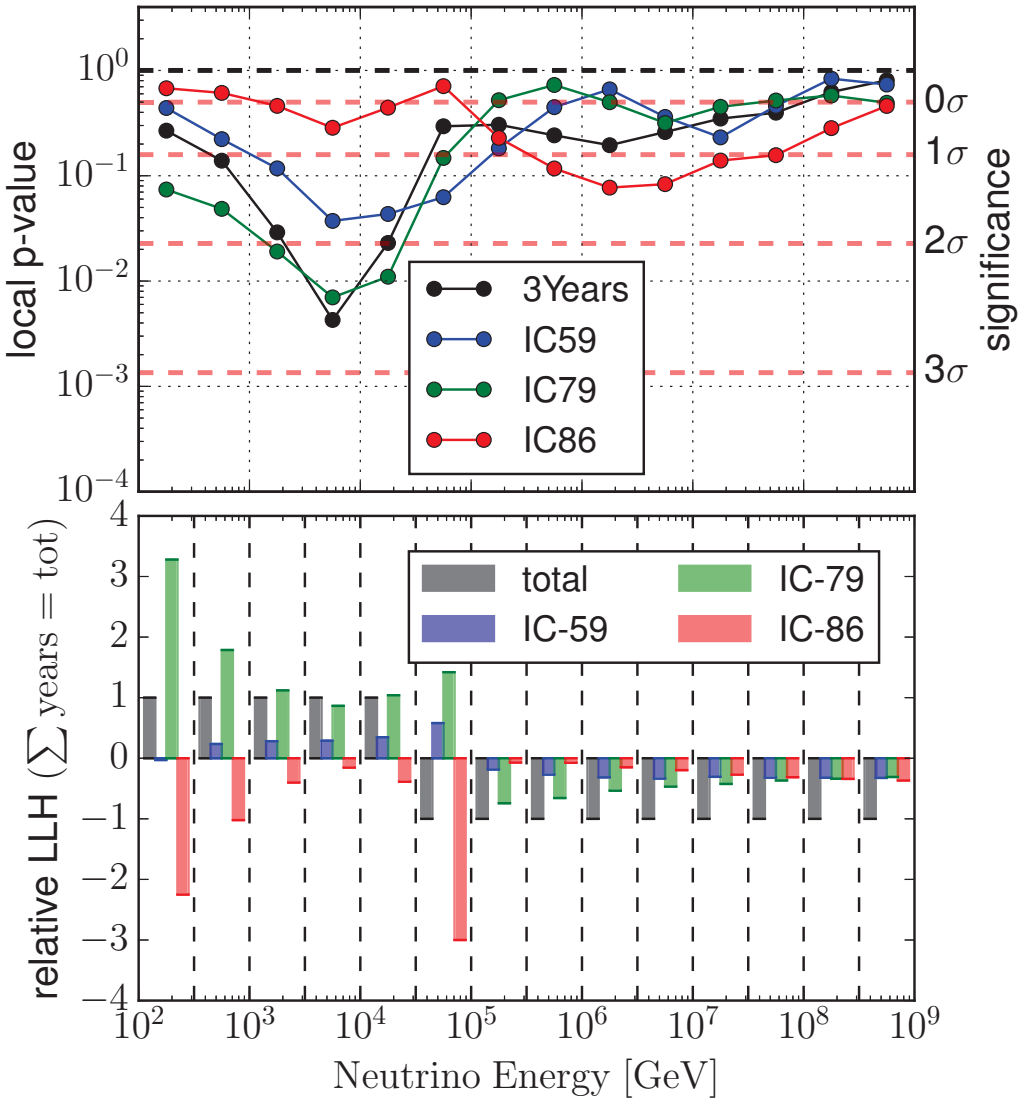

Figure 67: A per-year analysis of the contributions of each dataset to the final significance in the All LAT-blazar sample and the equal-weighting scheme. Upper plot: The a-posteriori p-value distributions for each year individually compared to the 3-year result. Lower plot: The contributions to the total LLH value in each energy bin for the final result. The individual contributions are shown relative to the total contribution in the given bin which itself is normalized to 1. For high energies the total log-likelihood is negative (due to the negative n_s construction with mirroring), which is indicated by a negative bar. Still, in these cases, a larger value for a given dataset (or often the least negative one) has the highest signal-like contribution to the LLH.

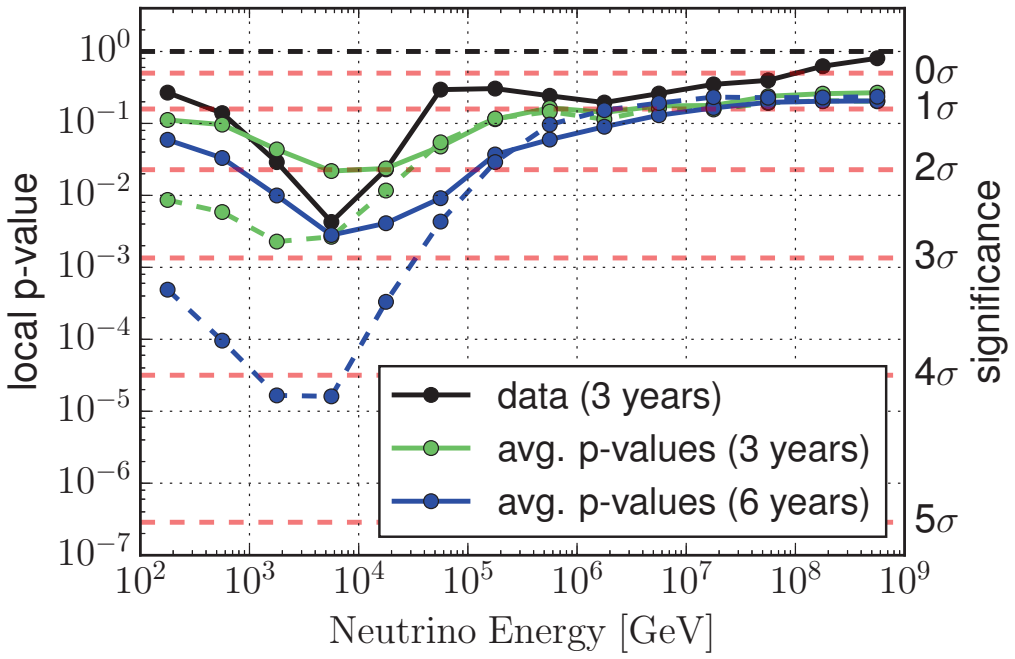

Figure 68: The p-value distribution of the data (black) in comparison to the average expected p-value distribution for the two benchmark fluxes (see text) in 3 years and 6 years. The larger benchmark flux is shown with dashed lines, the lower benchmark flux with solid lines.

It is first useful to look at the p-value distributions of each year of data individually or at the relative contribution to the total likelihood value, shown in figure 67. The information in the lower part of the plot is nearly identical as in the upper one, but is obtained from the final result directly, without doing a year-by-year analysis. The upper part of the figure reveals that the overfluctuation is mostly caused by IC-79, followed by IC-59 and only very mildly by IC-86. In the lower part, it can be seen that this "too mild" excess in IC-86 actually contributes negatively to the final LLH best fit value. At first sight, this seems to strengthen the case that the excess is caused by a statistical fluctuation, since IC-86 is the most sensitive detector configuration, if only by a small margin. However, tests with simulated skymaps demonstrate that a simulated signal flux with a substantial amount of signal events in IC-86 (above 50) can still cause an over-fluctuation as observed in the data, with IC-86 having sub-dominant share in the likelihood contribution (see figure 79 in appendix A.2). A background under fluctuation of equal magnitude as the 50 signal events is responsible for this situation. In summary, from the fact that IC-86 is showing the smallest over-fluctuation in the 5-10 TeV region in data, one can not exclude a potential physics origin of the excess.

To estimate a range of fluxes that would be compatible with the data, two specific power-law spectra have been identified whose p-value distributions encompass the one measured in data. One of them follows an E^{-3} spectrum

(with normalization $\Phi = 0.001$ - in the following called "larger benchmark flux") and one an $E^{-2.7}$ spectrum (with normalization $\Phi = 3.84 \cdot 10^{-5}$ - in the following called "lower benchmark flux"). As a reminder, the best-fit spectral index from the power-law fit assuming equal weights is -2.9. Figure 68 shows the resulting p-value distributions for data and the average p-value distribution expected for the two benchmark fluxes after 3 and 6 years. The p-value curves are the average of 100 realizations, where for each realization the injection weights were randomly sampled from the Fermi-LAT source count distribution. If the signal was real, with 3 more years of data the largest p-value is expected to reach a local significance between 3 to 4 sigma on average.

Finally, it is also interesting to compare the estimated flux range to extragalactic gamma-ray observations and see if the joint picture can make sense and what it would imply. Figure 69 shows Fermi-LAT EGB data and the diffuse neutrino flux measured by IceCube.

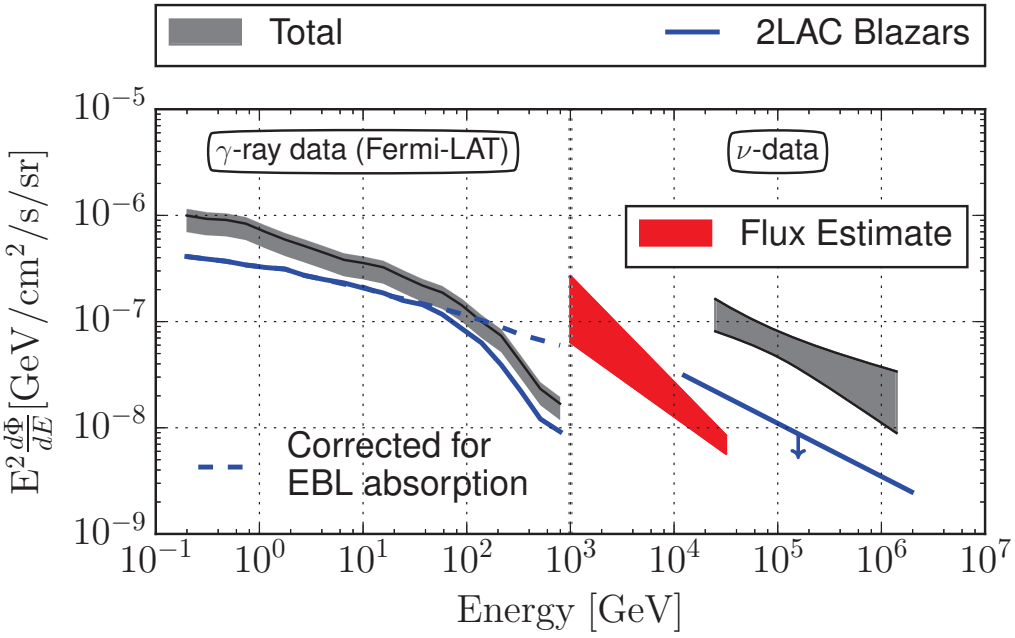

Figure 69: The EGB measurement by the Fermi-LAT experiment and the contribution of 2LAC blazars (adapted from [Aje+15]) is compared to the diffuse astrophysical neutrino flux and the upper limit (median from the equal weighting scheme) on the neutrino flux of 2LAC blazars derived here. The separation between the two regimes is indicated by the dotted vertical line. The 2LAC blazar fraction is calculated assuming 70% of the total blazar EGB fraction are resolved. The flux range that would be compatible with the observed small excess is shown in red. It includes the uncertainty band (approximately ± 15 %) expected from equal-weighting upper limits.

It also depicts the fraction of the EGB originating from the 2LAC blazars and the upper limit on the fraction of 2LAC-blazars to the astrophysical neutrino flux (the result from figure 61). The flux range stretching between the two benchmark fluxes is shown in red and would be situated in-between the two regimes. As discussed in section 2.4, the diffuse neutrino flux has to become harder in this energy range to remain compatible with the EGB, at least in p-p interaction scenarios. At the same time, the soft spectral index of the blazar best-fit estimate presented here seems to suggest a strong increase in flux towards lower energies. Both facts taken together would imply that the neutrino-flux fraction from blazars would actually increase below 10 TeV until it dominates the total neutrino flux. A consequence of that would be that most gamma rays at the highest energies in the Fermi-LAT data (beyond 100 GeV) are actually of hadronic origin. Since this scenario works most naturally in the p-p case, one would have to rethink neutrino production in blazars, which is modeled dominantly via photo-hadronic interactions in the literature.

In summary, a physical origin is possible and the current best-fit estimate indicates a scenario which is currently not discussed in the literature: low-energy (likely p-p) neutrino emission from blazars (in the 5-10 TeV region), that fills the gap between photon and neutrino observations. Several more years of IceCube data will either rule out or confirm this picture.

12

SUMMARY AND OUTLOOK

In this thesis, five samples of GeV-emitting blazars - the full population of blazars summarized in the 2LAC catalog and four spectrally selected sub-populations - have been analyzed for a cumulative neutrino flux using three years of IceCube muon-track data. The analysis uses an unbinned likelihood stacking, which treats all sources of a given population as a single effective neutrino source. Two schemes of relative flux weights - equal weights per source and weights proportional to the photon energy flux in the 100 MeV-100 GeV energy range - were used to define the combined signal PDF for each population, resulting in a total of ten combinations.

This study represents the largest blazar stacking search for neutrinos that has ever been performed. It is also the first to use an equal weighting scheme, motivated by the lack of knowledge about the potential correlation between the neutrino and gamma-ray flux.

For each combination of a given population and weighting scheme, the data has been analyzed in two steps. The first involved an unbroken power-law fit and the second a differential analysis in which short, step-wise E^{-2} spectra were separately fitted in 14 logarithmic energy bins between 100 GeV and 1 EeV. Nine out of the ten tests show mild over-fluctuations. The largest one comes from the total 2LAC-blazar sample using equal weighting, which has a significance of 1.1 σ (1.6 σ differentially) after trial-factor corrections.

Given that the excess is not significant enough to claim evidence for a detection, upper limits on the $(\nu_\mu + \overline{\nu}_\mu)$-flux for $E^{-1.5}$, $E^{-2.0}$ and $E^{-2.7}$ generic power-law spectra have been calculated for each of the five tested populations and each weighting scheme. All equal-weighting upper limits are constructed assuming a "realistic injection" scenario, where the relative neutrino emission of each source within a population is randomly sampled from the differential Fermi gamma-ray source count distribution for blazars. The result is a band of upper flux limits, corresponding to the 90% central interval of these neutrino flux realizations. No strict $\nu - \gamma$ flux proportionality and no flux equipartition among the sources is required.

Performing the equal-weighting upper limit construction for an $E^{-2.5}$ spectrum starting at 10 TeV, the resulting upper flux limit has been compared to the recently detected diffuse astrophysical neutrino flux. The total contribution of all Fermi-2LAC blazars to the TeV-PeV diffuse flux is less than 23%. This result assumes an equal composition of flavors, but again does not require strict proportionality to the gamma-ray flux in the Fermi-LAT range because of the equal-weighting construction. The constraint is not changing significantly (at most a factor of two) when harder spectra up to a spectral index of -2.2 are assumed and also applies to smaller

sub-populations, for example the TeVCat blazars, as long as they emit an approximately equal flux per solid angle.

The analysis outcome was also used to calculate limits on specific spectral models for the diffuse neutrino emission from blazar populations found in the literature. Assuming a dominantly hadronic production of the gamma-rays in the Fermi-LAT energy range, which is implicit already in many of the theoretical predictions, this analysis provides the so-far strongest experimental constraints or exclusions for all of these models. 12 of 14 considered spectral models are constrained, nine of these with model rejection factors better than 0.5.

For the purpose of this thesis a software framework has been developed optimized for unbinned stacking analyses of large samples of objects. It was used to perform an in-depth analysis of the standard unbinned likelihood method for point source searches in IceCube. The method has been derived in a step-by-step construction from a more general starting point, its properties have been evaluated, and five possible extensions and variations have been studied. None of these showed measurable sensitivity improvements for the unbroken power-law fit, except to use a MC-derived background PDF in the northern hemisphere which can yield up to a 10% better sensitivity in this region. However, due to longer minimization timescales and systematic differences between the individual datasets, it has not been applied. One variation, allowing for under-fluctuations in the signal region via "negative n_s", was adopted for the final analysis in the differential tests. It improves the sensitivity above TeV energies by a factor of 2 and above PeV energies by a factor of 3. For the first time, all upper limits were calculated using the CL_s construction, which was found useful because of the robustness for analysis outcomes close to the median sensitivity and because it naturally supports under-fluctuations.

Simulations have shown that the largest possible population sizes are desired, even in equal-weighting scenarios, at least up to the maximum population size (20000 objects) which has been studied. It therefore seems sensible to extend the blazar population analysis to larger population sizes in future searches beyond the trivial extension to more livetime, for example to the 3LAC-catalog that has been published in the meantime.

The differential analysis shows that the small 1.6σ excess in located in the 5 -10 TeV region. A year-by-year statistical analysis and a comparison to the extragalactic gamma-ray observations by Fermi reveals that there is no immediate contradiction for the excess to be of a physical nature. The allowed spectral range favors a soft flux (with spectral index around -2.9) situated in-between current EGB observations by Fermi and the diffuse astrophysical TeV-PeV flux observed by IceCube. It would fit into a scenario where the highest-energy extragalactic gamma-rays measured by Fermi (beyond 100 GeV) originate in the same hadronic interactions as the hypothetical soft signal. If confirmed, blazars would become the first identified extragalactic hadronic acceleration site. Already more than 3 years of additional data are

taken with the full IceCube detector which might either rule out or support this scenario in the near future.

A

SUPPLEMENTARY INFORMATION

A.1 ANALYSIS FRAMEWORK

The code of the analysis framework is made available for other collaboration members and can be found under `http://code.icecube.wisc.edu/svn/sandbox/gluesenkamp/population_stacking/`. Example scripts and a program to interactively inspect the output data is included.

The following list summarizes the steering parameters for the analysis framework in alphabetical order. The default values are used in all standard results of this thesis if not explicitly mentioned otherwise. The parameters to control the point source and diffuse populations (e.g. the spectral index fitting) are defined separately. Examples can be found in the scripts.

parameter name	description	possible values	default value
`absolute_inputspectrum_weighting`	Use full integration over assumed spectrum to calculate LLH-weight. No acceptance and model weights are used (see section 8.1.1 for details).	**0** or **1**	**0**
`angular_improvement`	Scaling factor for the paraboloid estimator (not the true error).	any float	**1.0**

`apriori_scatter_function`
 	
`apriori_scatter_parameter`
	Modification of injection weights each trial in a predefined way.	**"None"**: No multiplication
		"scatter_log_gauss": draw from log-normal with width set to `apriori_scatter_parameter`
		"anti_correlation": injection weights are inverse of LLH model weights
			"None"

`bg_injection`	Determines the background injection mode.	**"scramble_ra":** scrambling RA of data events **"standard":** sample from background PDF **"real_data":** injecting real data	**"scramble_ra"**

table continued on next page

Table 11 – continued from previous page

parameter name	description	possible values	default value
`burnsample_mode`	Only events with a `run_id` ending on 0 are used. Effectively reduces the livetime by a factor of 10.	**0** or **1**	**0**
`cache_injection_histos`	Toggle weather the injection PDFs should be cached. Saves time for large populations.	**0** or **1**	**1**
`combined_pdf_mode`	This mode makes use of user-defined PDF definitions (derived purely from MC) for background and signal.	**0** or **1**	**0**
`combine_years_in_minimization`	Use one combined n_s for all years (assumes constant signal) or individual n_s for each year.	**0** or **1**	**1**
`cospsi_binning_mode`	Determines the binning used for the true error (Ψ) in the LLH evaluation. Only used if the spatial PDF is determined from MC.	**1:** linear binning **2:** same binwidth as option 1, but transformed to cosine **3:** predefined binning in $\cos(\Psi)$	3
`coszencut_min`	Additional cut on the reconstructed direction for all data and MC (a minimum in $\cos(\theta_{zen})$).	at least **-1.0** and smaller than `coszencut_max`	**-1.0**
`coszencut_max`	Similar to `coszencut_min`, but defines the maximum in $\cos(\theta_{zen})$.	larger than `coszencut_max` and max. **1.0**	**1.0**
`custom_pdf_eval`	Uses non-powerlaw spectra as defined in the skymap files for the LLH-evaluation (currently works only simultaneously for all signal hypotheses).	**0** or **1**	**0**
`debug`	Produce debugging plots during the runtime process.	**0** or **1**	**0**
`debug_folder`	Specifies the folder for debugging plots.	any path	`"./debug"`
`dnds_injection`	Toggles injection mode with new sampled injection weights from a sourcecount distribution each trial.	**0** or **1**	**0**

table continued on next page

Table 11 – continued from previous page

parameter name	description	possible values	default value
`do_param_scan`	Produces an LLH-scan of spectral index and/or n_s to be saved in the debug folder. Works without debug mode.	**0** or **1**	**0**
`energycut`	Additional cut on the reconstructed energy for all data and MC.	**-1:** no cut **positive float c:** $E_{reco} > 10^c$ GeV	**-1**
`equidistant_dnds_sampling`	To be used in connection with `dnds_injection`. Instead of standard random sampling the sampling happens in equidistant steps. Potentially prevents strong outliers of the sampling distribution.	**0** or **1**	**0**
`fix_sig_sigma`	Fix the reconstructed error (paraboloid) for all signal events to be exactly `fix_sig_sigma`. To be used with `redraw_fixed_sigma`.	**-1:** no effect **positive float:** error in degrees	**-1**
`fix_bg_sigma`	Fix the reconstructed error (paraboloid) for all background events to be exactly `fix_bg_sigma`. To be used with `redraw_fixed_sigma`.	**-1:** no effect **positive float:** error in degrees	**-1**
`individual_source_injection`	If switched on, each source injects events based on its own spectrum. Otherwise the first source in a population file is representative of the population in terms of the spectrum. Influences memory load.	**0** or **1**	**0**
`limit_n_to_zero`	A lower bound at zero on n_s.	**0** or **1**	**1**
`minimization_algorithm`	The algorithm used for the LLH minimization.	**simplex** or **migrad**	**migrad**
`ns_to_start`	Seed value for n_s.	**-1:** Scan n_s to find best seed **positive float:** seed value	**-1**
`numbins_reco_energy_eval`	Number of bins in the reconstructed energy dimension ($\log_{10}(E)$) for LLH evaluation.	**positive integer**	**50**

table continued on next page

Table 11 – continued from previous page

parameter name	description	possible values	default value
`numbins_reco_energy_inject`	Number of bins in the reconstructed energy dimension ($\log_{10}(E)$) for injection.	**positive integer**	**200**
`numbins_reco_zenith_eval`	Number of bins in the reconstructed zenith dimension ($\cos(\theta)$) for LLH evaluation.	**positive integer**	**50**
`numbins_reco_zenith_inject`	Number of bins in the reconstructed zenith dimension ($\cos(\theta)$) for injection.	**positive integer**	**100**
`numbins_truezen_weighting`	Number of true zenith bands to determine acceptance weights for different sources.	**positive integer**	**40**
`pdf_mode_string`	Defines the PDF structure if `combined_pdf_mode` is used.	**string**	""
`precache_sis`	Toggles table lookup of LLH PDFs for different spectral indices.	**0** or **1**	**1**
`precache_numbins`	Defines no. of spectral index bins between -1 and -4. To be used with `precache_sis`.	positive integer	**30**
`realistic_injection`	Toggle weather the true error is injected separately from the reconstructed error.	**0** or **1**	**1**
`redraw_fixed_sigma`	Redraw a new reconstructed error (paraboloid) each trial from a fixed predetermined given error. To be used with `toy_binning_mode`.	**0:** not used **1:** redraw only for injected signal events **2:** redraw for both signal and background events	**0**
`renormalize_rows_for_zero_evals`	Renormalize the LLH PDF (usually energy PDF) in the respective dimension(s) if it is changed in regions where the data PDF is zero due to signal injection from MC.	**0** or **1**	**1**
`reweight_percentile`	Rescale all reconstructed errors, which ideally correspond to the respective 39% quantile, to another value corresponding to the percentile given by `reweight_percentile`.	**-1:** no rescaling **float between 0 and 1:** the new percentile	**-1**

table continued on next page

Table 11 – continued from previous page

parameter name	description	possible values	default value
`save_detailed_events`	Saving detailed event information for diagnostics (intended for unblinding).	**0** or **1**	**0**
`seed`	Initial random seed given to the instance of the framework.	**-1:** use system seed **positive integer:** any seed	**-1**
`share_eval_pdf`	Sharing the table lookup of spectral indices between different signal populations. Requires `splitup_true_zenith_bands`.	**0** or **1**	**0**
`sigma_binning_mode_inject`	Binning mode for the injection PDFs of the true error.	**0:** linear **1:** logarithmic **2:** cosine	**1**
`sigma_binning_numbins_inject`	Number of bins in the true error dimension for injection.	**positive integer**	**50**
`sigma_binning_max_value_inject`	Maximum value of the binning scheme in the true error dimension for injection (in logarithmic units in standard mode).	**float**	**0.87**
`sigma_binning_numbins_eval`	Number of bins in the true error dimension for LLH evaluation.	**positive integer**	**50**
`sigma_binning_max_value_eval`	Maximum value of the binning scheme in the true error dimension for LLH evaluation (in logarithmic units in standard mode).	**float**	**0.87**
`sigma_reco_mode`	Binning mode for the injection and LLH PDFs of the reconstructed error (paraboloid).	**0:** linear **1:** logarithmic **2:** cosine	**0**
`sigma_reco_numbins`	Number of bins in the reconstructed error (paraboloid) dimension for LLH evaluation and injection.	**positive integer**	**50**
`splitup_true_zenith_bands`	Determines weather SI table-lookup should occur for each true zenith bin (defining a point source position) independently. Allows for shared table lookup between populations with different spectral indices. To be used with `precache_sis`.	**0** or **1**	**1**

table continued on next page

Table 11 – continued from previous page

parameter name	description	possible values	default value
`superscramble_mode`	Extra null-skymaps are produced via RA scrambling, including all injected signal events which normally are not part of the scrambling process.	**0:** superscramble off **positive integer:** produce this amount of scrambled skymaps per trial	**0**
`true_zenith_numbins`	Number of true zenith bands to determine LLH PDFs for different sources.	**positive integer**	**40**
`true_zenith_use_cosinus`	Use cosine of true zenith instead of zenith.	**0** or **1**	**0**
`truezen_bandwidth_for_injection`	The binwidth of true zenith bins used for injecting signal in degrees.	**positive float**	**1**
`use_acceptance`	Use acceptance weights. Can be switched off for a purely spatial test without any energy considerations.	**0** or **1**	**1**
`use_energy_pdf`	Use the standard energy PDF term. Will be ignored if `combined_pdf_mode` is used.	**0** or **1**	**1**
`use_fisher`	Use the Fisher-von-Mises distribution instead of the gaussian for the spatial term. The paraboloid sigma is converted to the 39% quantile in this case.	**0** or **1**	**0**
`use_logloge_for_injection`	Use a double-logarithmically binned energy distribution for event injection.	**0** or **1**	**1**
`use_theory_weights`	Main weighting-mode option.	**0:** use equal model weights **2:** use model weights from skymap definition	**2**
`use_space_pdf`	Use the analytic spatial PDF term. Will be ignored if `combined_pdf_mode` is used.	**0** or **1**	**1**

Table 11: List of steering parameters used for the analysis framework. Values in parentheses denote strings.

A.2 SUPPLEMENTARY FIGURES

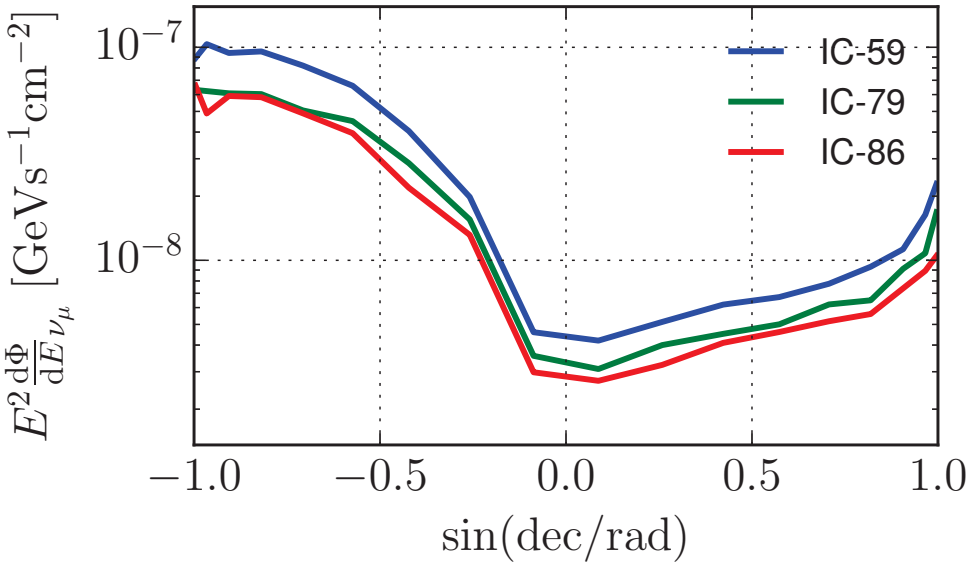

Figure 70: Sensitivity for an E^{-2} flux comparing IC-59, IC-79 and IC-86.

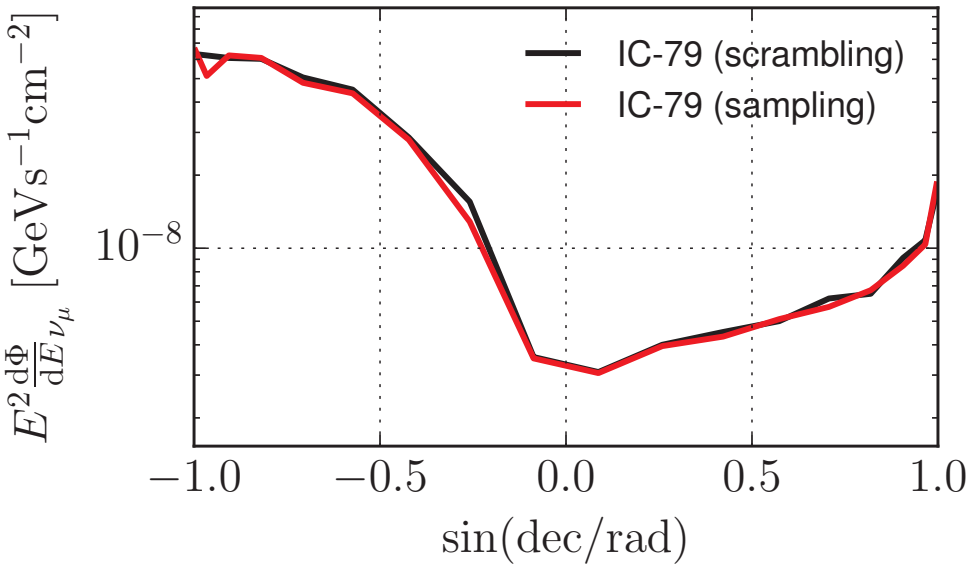

Figure 71: Sensitivity for an E^{-2} flux (IC-79) comparing event injection via RA scrambling with full sampling from the background PDFs[a].

a Sampling uses `bg_injection="standard"` instead of "scramble_ra". See appendix A.1.

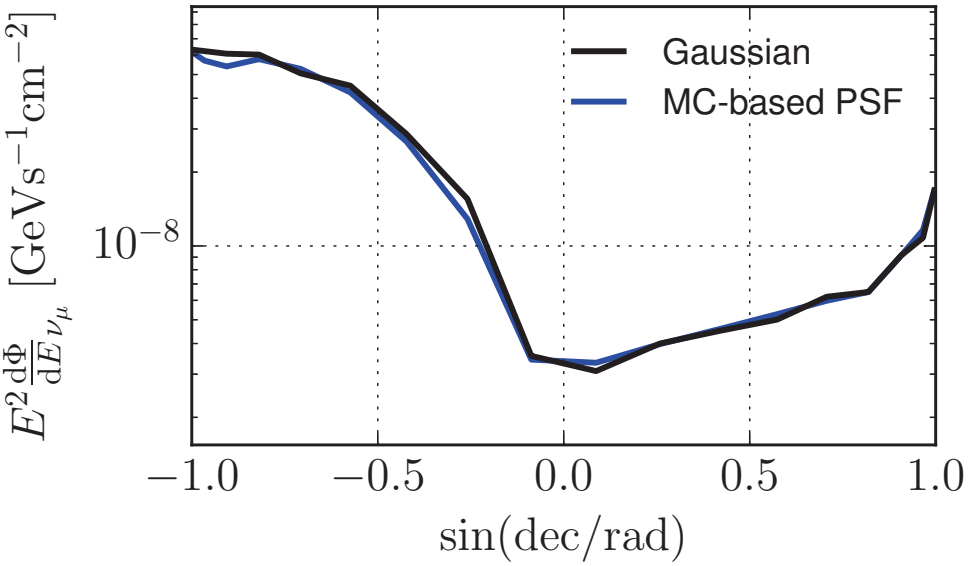

Figure 72: Sensitivity comparison (IC-79) for an E^{-2} spectrum between the standard method and the case where the spatial PDF is derived from MC[a].

a The MC-based version uses `combined_pdf_mode`. See appendix A.1.

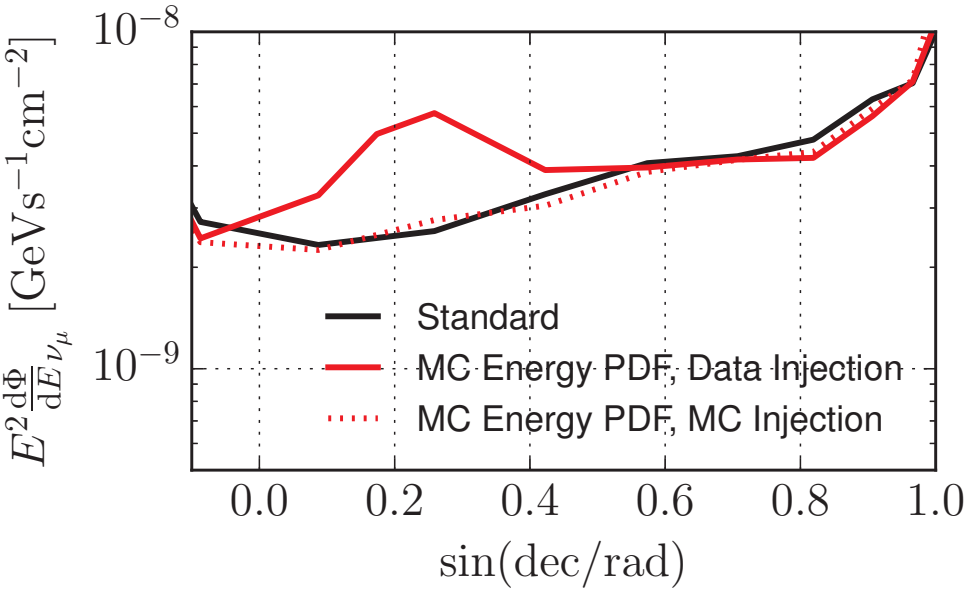

Figure 73: Sensitivity comparison (IC-86) for an E^{-2}-spectrum for the standard approach and a modification where the background PDF is derived from MC in the northern sky. The modification is shown for event injection via scrambling (solid) or via sampling from the MC distribution (dotted).

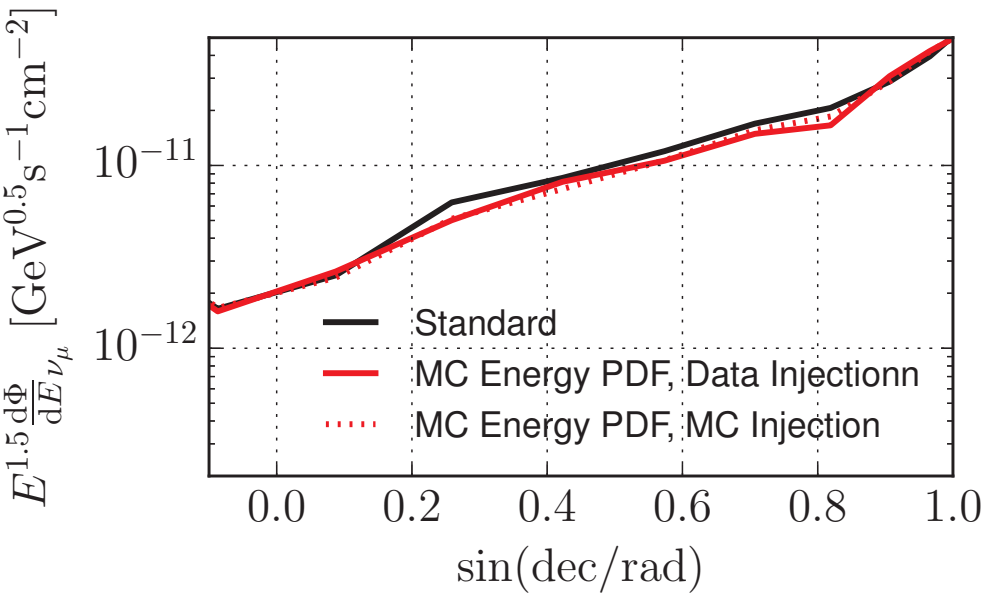

Figure 74: Sensitivity comparison (IC-86) for an $E^{-1.5}$-spectrum for the standard approach and a modification where the background PDF is derived from MC in the northern sky. The modification is shown for event injection via scrambling (solid) or via sampling from the MC distribution (dotted). The simulations use a coarser binning than in the standard method[a].

a Among other parameters, using `numbins_reco_energy_eval=25`, `numbins_reco_energy_inject=25`, `numbins_reco_zenith_eval=25`, `numbins_reco_zenith_inject=25`. See appendix A.1.

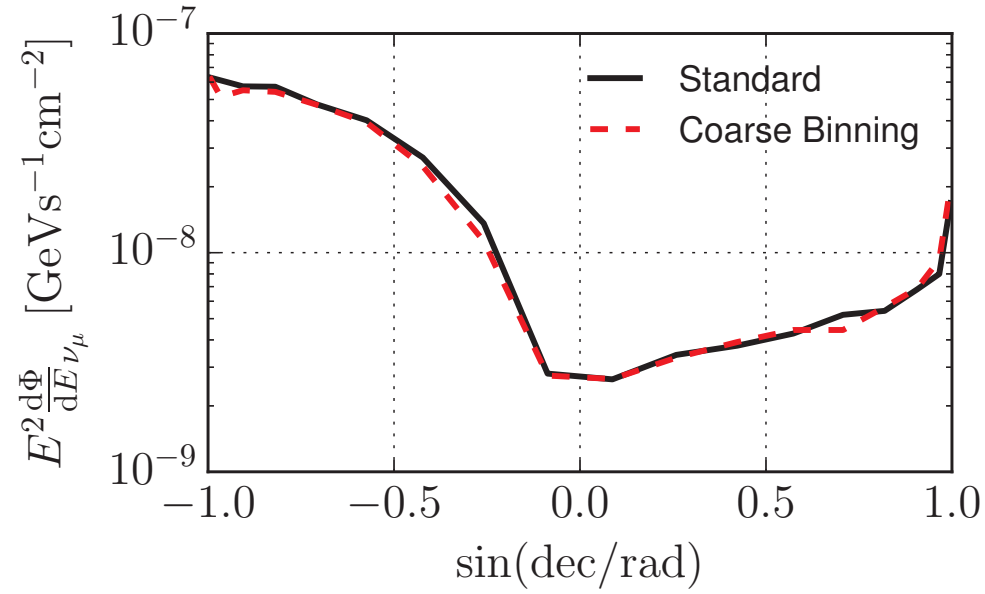

Figure 75: Sensitivity comparison using the standard method with a coarser binning scheme[a] in IC-79 for an E^{-2} spectrum.

a Among other parameters, using `numbins_reco_energy_eval=25`, `numbins_reco_energy_inject=25`, `numbins_reco_zenith_eval=25`, `numbins_reco_zenith_inject=25`. See appendix A.1.

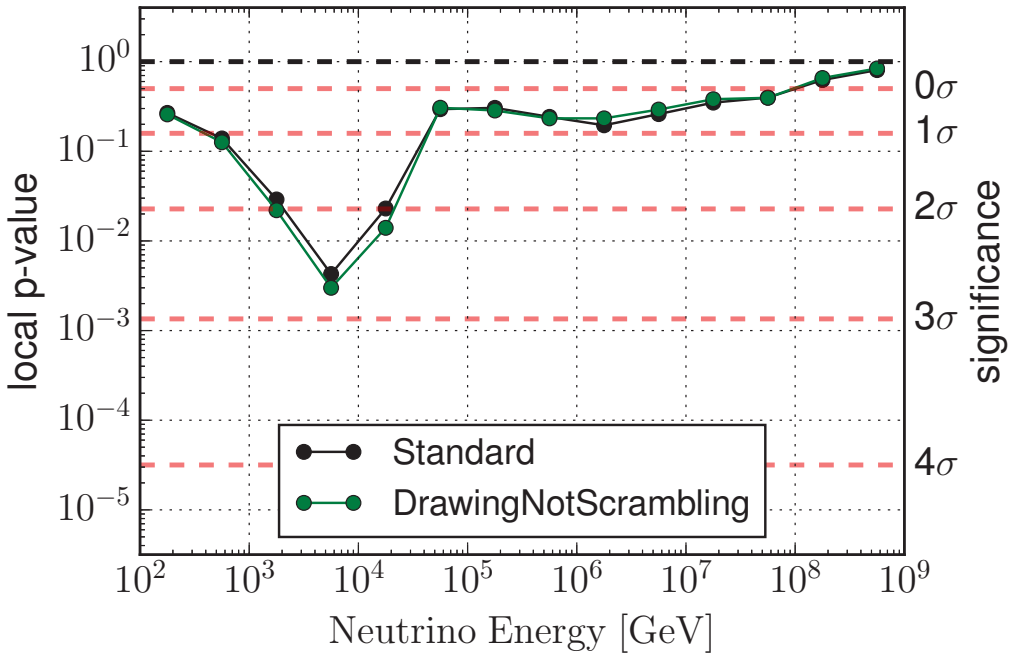

Figure 76: Differential p-value distributions for injection with simple RA scrambling versus injection via sampling from the background PDF.

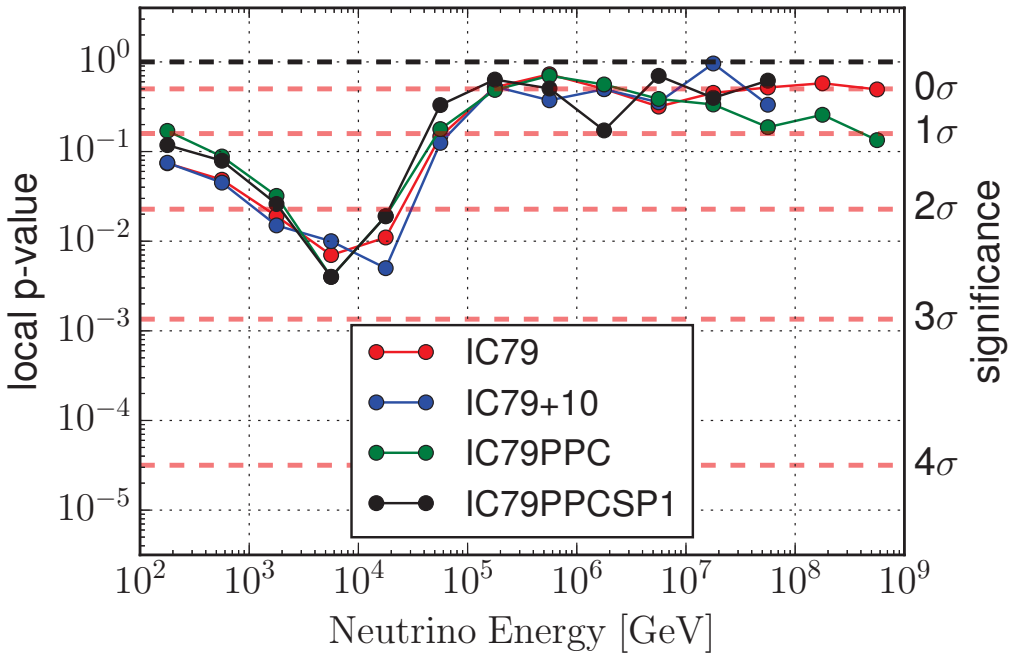

Figure 77: Differential p-value distributions in IC-79 for photonics (SpiceMIE), the baseline, comparing to photonics (SpiceMIE/+10% optical efficiency), PPC (SpiceMIE), PPC (Spice1) using the equal weighting scheme and looking at the "All Blazar" sample.

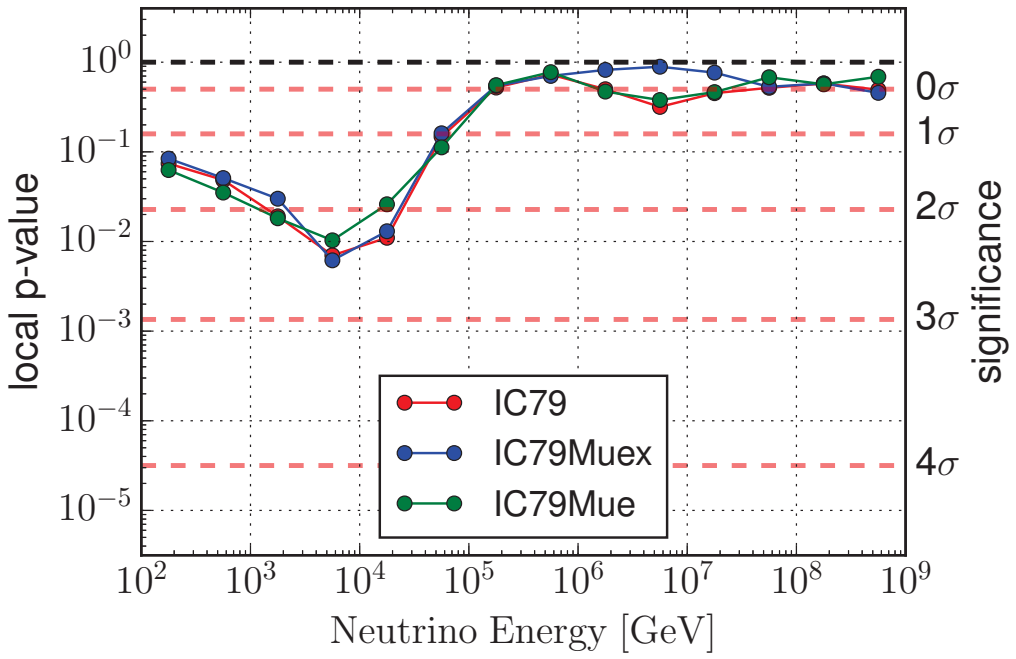

Figure 78: Differential p-value distributions in IC-79 for different energy estimators using the equal weighting scheme and looking at the "All Blazar" sample.

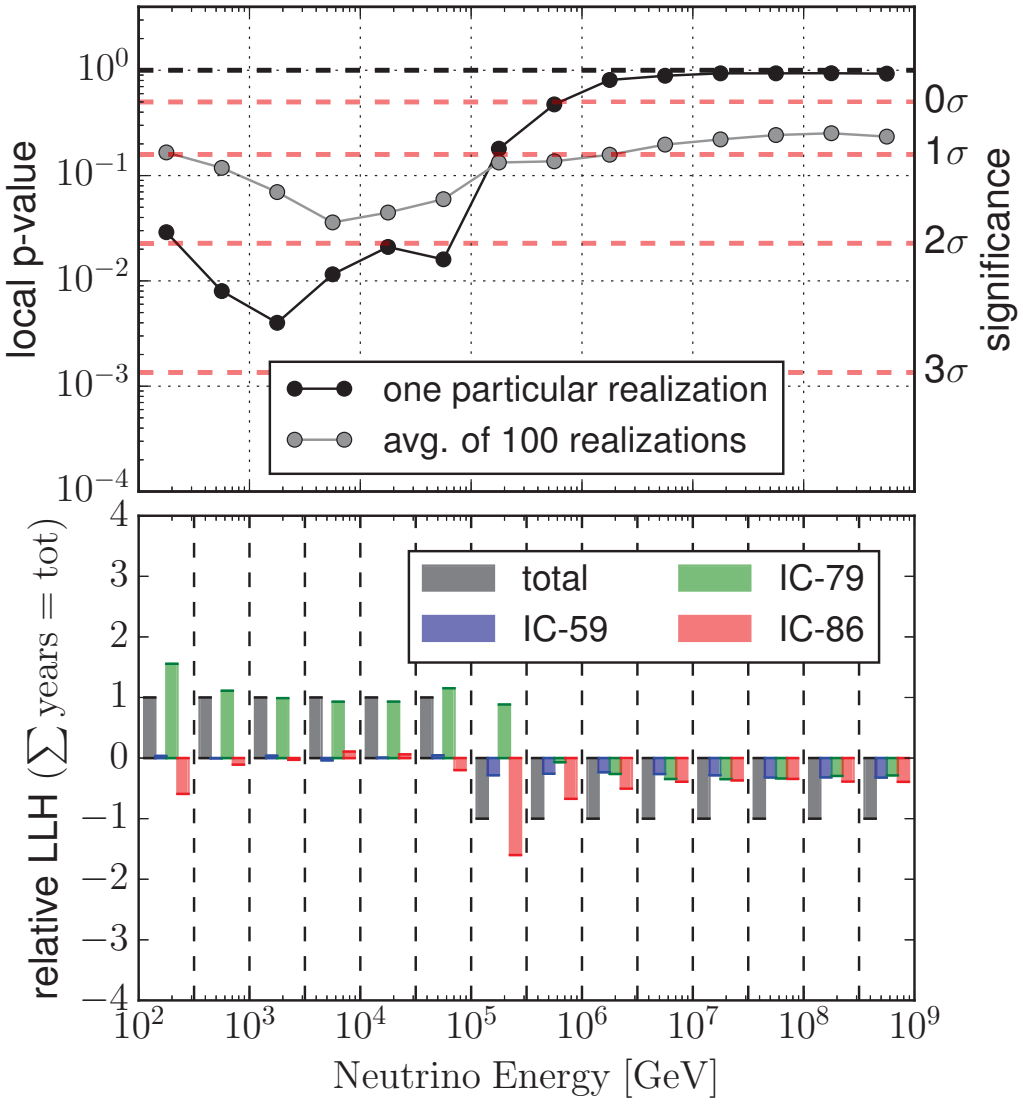

Figure 79: Upper plot: Differential p-values obtained from a particular realization (black) of a soft $E^{-2.7}$ flux with relative neutrino fluxes proportional to the LAT energy flux. The average of 100 such realizations is shown in gray. Lower plot: Relative contributions to the LLH value for each energy bin for the particular realization from the upper plot. In this realization, 39 signal events are injected in IC-59, 54 signal events are injected in IC-79, and 55 signal events are injected in IC-86.

B

LIGHTYIELD STUDIES

Systematic uncertainties connected to the exact energy scale of physical processes (sometimes summarized in a parameter called "optical efficiency", see later this section) are one of the important systematic uncertainties regarding the final sensitivity of the point source analysis. Among others, the following studies presented here have contributed to the decision made in 2012 to increase the baseline optical efficiency in simulation by 10%, starting with IC-86. All numbers presented here therefore apply to the IC-79 period and earlier.

B.1 IMPLEMENTATION OF A MIN.-BIAS TRIGGER

At trigger level, a "min.-bias physics trigger" had been running in the DAQ until IC-86, which would capture short (a few µs) readout windows centered around randomly-chosen HLC hits. Given this behavior, it had only limited use and could barely be utilized for studies aimed at low-energy events, noise, or at studying longer-term behavior exceeding a few microseconds. With increased software capabilities, it became possible to capture much longer data streams and save them as single events in the standard data-flow scheme in 2011.

At this opportunity a new minimum bias readout trigger called "FixedRateTrigger" was implemented in the DAQ, which captures long frames of pure readout data in fixed time intervals (up to several tens of microseconds in length), disconnected to any DOMLaunch criteria. This data is readable in a data-friendly format, as it is directly connected to the standard data stream. It has been used since then to study noise rates, detect noise variability over time or estimate background for slow-particle analyses [Ice14c]. It has also been utilized to estimate the relative DOM efficiency of high-QE DOMs, as described in the next section.

B.2 RELATIVE DOM EFFICIENCY

The photon detection efficiency (**R**elative **D**OM **E**fficiency - **RDE**) in certain DeepCore DOMs, the high-QE DOMS (see section 4.2.1), has been determined to be $30\% - 40\%$ larger than for standard DOMs in laboratory measurements [Wie09].

In this section, data from the FixedRateTrigger is used to study if the laboratory value is reproducible with InIce data. The high-QE DOMs should have a larger amount of detected photons from air-shower muons compared to standard DOMs situated at the same depth. Figure 80 (left side)

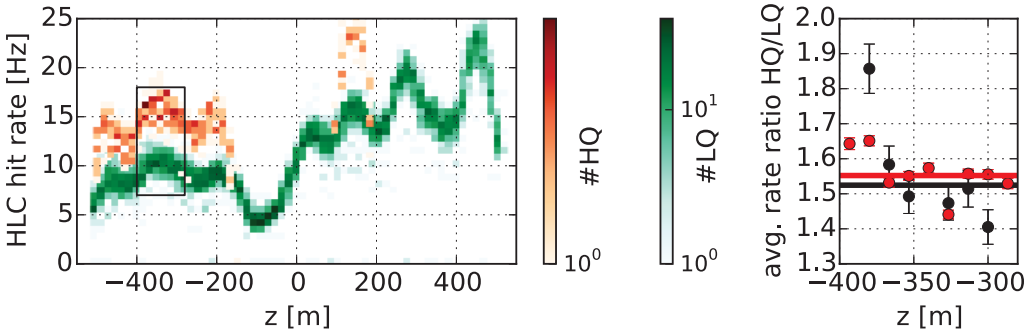

Figure 80: Left plot: 2d histogram containing all High-QE and Low-QE DOMs for different HLC-NCh rates and different depths z ($z = 0$ corresponds to the detector center). The clear-ice region between $z = -400$m and $z = -280$m is marked with a rectangle. Right plot: Ratios of the average rate of High-QE DOMs versus Low-QE DOMs in the clear-ice region. The ratios are calculated using all DOMs in a given depth (red) or using only the central DeepCore string and the six DeepCore-surrounding strings (black). Their ratio mean is indicated by a constant function fit (horizontal bars).

shows the DOMLaunch rate of HLC DOMLaunches ("HLC-Nch") versus the instrumented depth in IceCube coordinates (where z=0 corresponds to the center of the detector) using a cumulative livetime of around 80 seconds. The larger rate of high-QE DOMs is visible in the plot. The restriction to HLC DOMLaunches increases the likelihood of the launch being caused by an atmospheric muon rather than random noise. However, HLC-coincidence conditions and noise hits are still included in these rates which distort the measured ratio from the true high-QE efficiency gain. This can be seen in figure 80 (right side), which shows the ratio of the average high-QE to low-QE rates in the region of the clearest ice between -280 m and -400 m. The ratio is depicted with a constant fit function for two different cases. In the first case (red), the ratio is calculated taking into account all high-QE and low-QE DOMs in a given depth. In the second case, the high-QE DOMs are only taken from the central string within DeepCore and the low-QE DOMs from the six strings surrounding DeepCore (see figure 27 in section 4.2.1). The central string is the only one which has high-QE DOMs with a "standard" vertical DOM spacing of 17m, which therefore share the same HLC coincidence conditions as normal DOMs. The different spacing in the two cases explains the observed difference in ratios, both of which are still different from the true RDE value. The outlier datapoints possibly come from DOMs which are malfunctioning - however the effect on the overall mean is rather small.

Simulations with PPC (see section 4.2.2) and the SpieMIE ice model (see section 4.3) corresponding to 100 seconds of pure livetime were performed to determine the relation between the RDE value and the measured HLC-Nch ratio. To include relevant systematic effects in the study the following

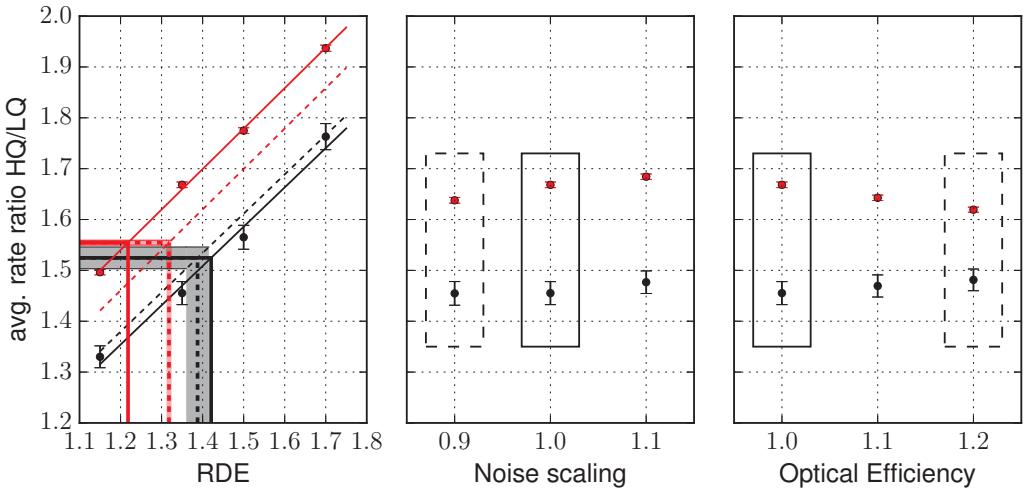

Figure 81: Estimation of the RDE using FixedRateTrigger data. The left part shows the relation between the measured HLC-Nch ratio and the RDE value. The central and right part show the relation between the measured HLC-Nch ratio versus the noise rate scaling or the overall optical efficiency scaling. Solid rectangles and solid lines correspond to nominal values for the parameters. Dashed rectangles and lines correspond to simulation settings using a noise scaling of 0.9 and an overall optical efficiency of +20%.

settings were simulated: relative DOM efficiencies of 1.15, 1.35 (nominal in this study), 1.5 and 1.7, absolute DOM optical efficiencies (see next section for a definition of optical efficiency) of +0% (nominal in this study), +10%, +20% and three different noise rate scalings of 0.9, 1.0 (nominal in this study[1]) and 1.1 relative to a measured baseline rate.

The results are shown in figure 81. The first part depicts the RDE/HLC Nch ratio relation which is fitted with a linear function. The measured ratios of 1.52 and 1.55 from figure 80 , using the nominal simulation values (solid lines), translate into different values for the RDE which do not agree. However, the RDE values should agree if the data and simulation are consistent.

The effect of the noise rate scaling and overall optical efficiency on the measured ratio is shown in the second and third part, showing different scaling relations due to the different effective HLC conditions from the different vertical DOM spacing in the two cases. The nominal values are indicated by solid rectangles. Assuming that the effect due to noise scaling and optical efficiency are uncorrelated among themselves and to the actual RDE value, the difference to the nominal HLC-Nch outcome can be added to the RDE/HLC Nch relation in the first part of the figure. Using a noise scaling of 0.9 (which was actually used in the standard simulation at the time) and

1 0.9 was the nominal value at the time - however all simulations in this study use 1.0 for the noise scaling parameter

an overall optical efficiency increase of 20% (dashed rectangles), one obtains the shifted linear RDE/HLC Nch ratio relation (dashed). If one uses this new relation to obtain RDE values from the data ratio, the results are closer together and fall into the region between 1.3 and 1.4, which now also agrees with results from the laboratory measurements. The statistical error from the constant fit is shown as the shaded region, whose regions do still not entirely overlap. This is expected to come from other non-simulated systematics (i.e. no malfunctioning DOMs in simulation or non-optimal noise simulation) or a still too low value of the optical efficiency. Systematic effects related to physics (for example on hadronic interaction cross sections or on cosmic ray composition) should not play any role since they cancel out in the ratio.

Since the HLC-Nch rate is dominantly produced by downgoing muons, the 20% value for the overall optical efficiency indicated here is only valid for the downgoing region. An independent method to study the optical efficiency parameter is described in the next section, which comes to a similar conclusion.

B.3 ABSOLUTE OPTICAL EFFICIENCY

The absolute DOM efficiency describes the photon transmission efficiency from the moment the photon traverses the outer DOM pressure sphere to the point it launches the PMT. This quantity, however, is degenerate with other quantities that manifest themselves as "absolute light-yield", such as the ice parameters or the photon propagation code. Additionally, in simulation, the estimated effect of the "cable shadow", which is not known but thought to block about 10% of the light, is included into this quantity. Therefore, one often talks of "optical efficiency" to denote the overall light-yield scaling factor that is in principle able to balance all of these effects in simulation in case partial aspects of the simulation do change.

It turns out that the ratio of the number of HLC Domlaunches between different datasets is a quantity that reveals this information and can be used for Data/MC verification. All further comparisons are performed on trigger level with some extra "high-quality" cuts to suppress coincident events. These cuts retain events that have a large amount of unscattered hits with respect to the reconstructed MPE track (`n_dir` > 8), that have a long maximal distance between the unscattered hits along the MPE track (`l_dir` > 800) and that have a good likelihood value in the reconstruction ($\texttt{logl}/(\texttt{NCh} - 5) < 9.5$). Figure 82(a) shows the slope of the HLC-Nch ratio comparing different optical efficiency settings for downgoing muon bundles simulated with PPC using the Spice Mie ice model. A slope of 0.025 for this ratio equals an optical efficiency difference of about 10%. It was further studied how systematic uncertainties related to physical properties of the cosmic-ray spectrum would influence the measured slope.

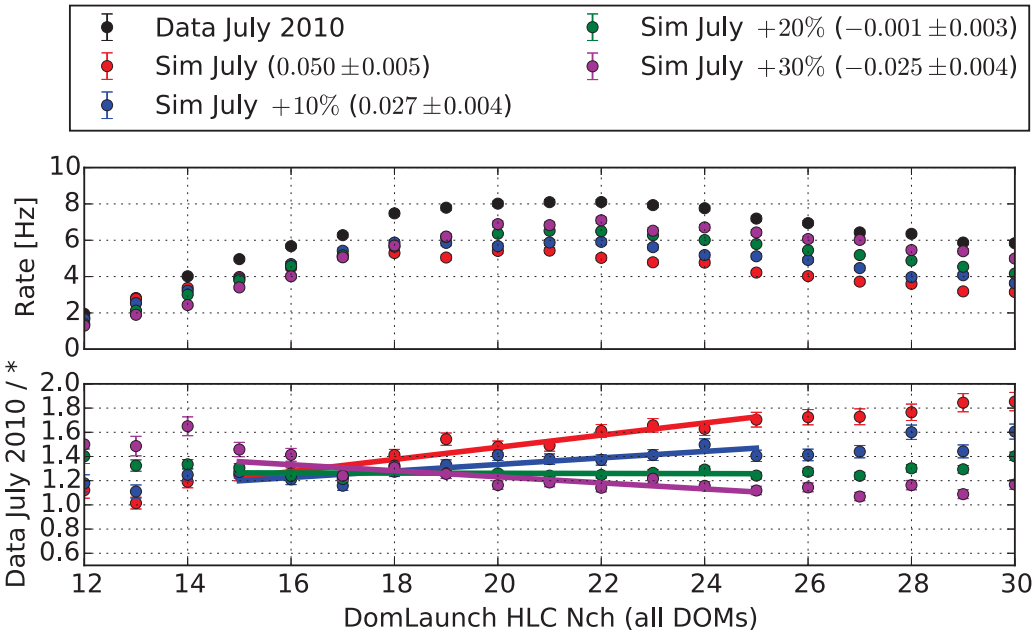

(a)

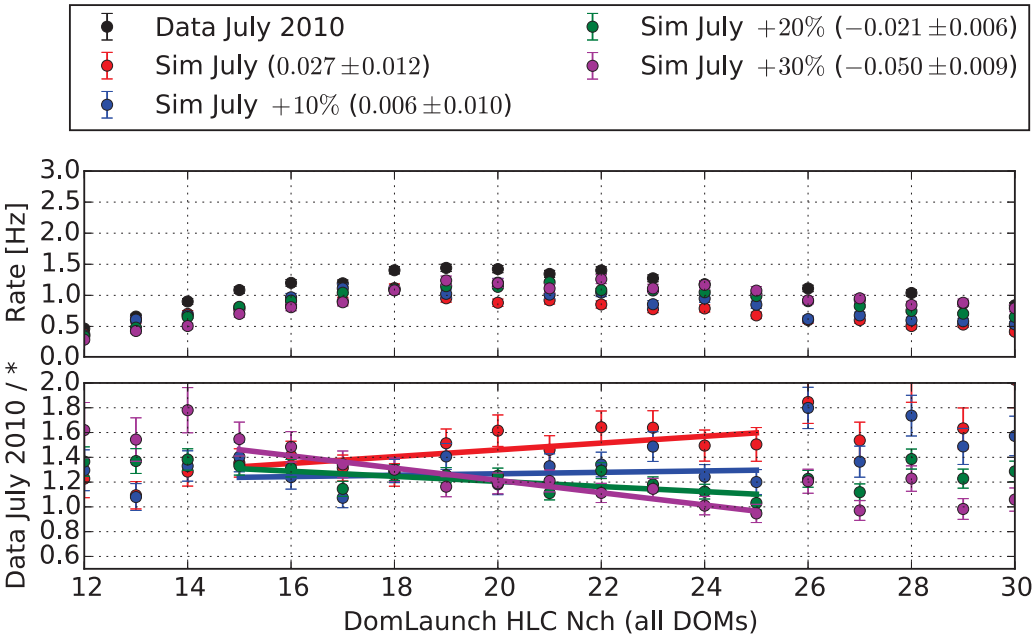

(b)

Figure 82: Determination of the optical efficiency from the HLC-Nch ratio between data and simulations with different optical efficiencies (upper row: rates - lower row: ratios with respect to data). All data is processed after trigger level with high quality cuts to remove coincident events (see text). Slopes of the linear fits to the ratios are shown in parentheses in the legend. a) All tracks. b) Only tracks with a reconstructed zenith direction larger than 50 degrees.

Varying the cosmic-ray composition (Gaisser-Hillas model[Gai12] or Polygonato model[Hoe03]) showed a barely noticable difference in the slope corresponding to less than 1% optical efficiency equivalent. Changing the cosmic-ray spectral index of a pure proton spectrum by $\Delta\Gamma_{CR} = 0.1$ changes the slope by around 0.003 corresponding to around 1%-2% optical efficiency equivalent. The impact of different hadronic interaction models has not been studied, but it is expected the impact should not be much larger than from different compositions.

The different values are taken in quadrature as a systematic uncertainty on the final optical efficiency measurement which results in $20 \pm 3\%$. This value is applicable to all IC-79 simulation with the SpiceMie ice model[2]. As the majority of muon bundles is downgoing, the value might not hold for all track directions. Figure 82(b) shows the same study for tracks with zenith angles larger than 50 degrees. Here, the HLC-Nch slope indicates an optical efficiency discrepancy of only 10%. This value is in agreement with another study conducted with inclined minimally ionizing muons [Fei14], which has lead to the acceptance of a 10% increased optical efficiency as the the new baseline for IC-86. The angular variation of the optical efficiency deviation is not completely understood, but likely connected to the properties of the ice in the bore holes.

2 An older ice model (SPICE1), for example, shows a slope difference to the Spice Mie model equivalent to 14% increased optical efficiency, which would result in 6% instead of 20% as the optimal value compared to data.

C

OUTLOOK ON THE DIRECTIONAL RECONSTRUCTION

Improvements in the directional reconstruction lead to a direct sensitivity improvement for any analysis looking for point sources. Studies have been conducted with a track reconstruction that has at least the potential to be better than the standard MPE reconstruction discussed in section 6.1.1. In this method (which will be denoted as "energy-unfolding" in the following), the track hypothesis is not an infinitely long muon track with a quasi-continuous energy loss, but individual electromagnetic showers are fitted simultaneously in small segments along the track hypothesis to allow the description of a stochastic energy-loss profile [Ice14a]. This is done using a Poisson likelihood fit, in which the energy losses are re-fit for each step in the positional or angular change of the track hypothesis using a semi-analytic Poisson minimizer. Thus, the energy-loss hypothesis changes in the course of the track minimization. In initial tests, likelihood scans revealed that the energy solutions were numerically not stable, showing large fluctuations for nearly identical directions of the parent track hypothesis. However, if the timing information within a DOM was neglected (by effectively handling each DOM in a single time bin) the problem did not appear. This hinted at a numerical issue connected to the binning scheme. In a follow-up study [Gor+14], this was confirmed to be part of the problem. The solution was to change the time-binning scheme and the algorithm used for the semi-analytic Poisson solver.

Having in mind the possible likelihood relations from section 5.4 (figure 31) one can try to find compatible LLH descriptions that solve the known problems. Figure 83, example A), shows that the time binning issues can be avoided, if one uses the extended likelihood instead of a Poisson description and works with the unbinned hypothesis directly. Since the Poisson minimization in the standard energy unfolding is performed semi-analytically via algorithms like NMML or PCG[Ang+11] which are only suited for Poisson likelihoods, one would switch to an algorithm like L-BFGS-B[Byr+94], which has been shown to compete with these semi-analytical methods in terms of execution time [KSD13], but can handle the extended unbinned likelihood form. In this first extension, the extended unbinned likelihood would not only be used for the unfolding of the energy losses, but also for the directional reconstruction itself.

The MPE likelihood, using the time residual PDF for the first hit within each DOM, is known to perform better than using the total time residual PDF for all hits. Again inspired by figure 31, one can therefore also try another route and extend the MPE likelihood with a Poisson term (see example B). This has been used before in a modification of MuEx (in a specific "angular" mode), but only using an analytic representation of the light yield

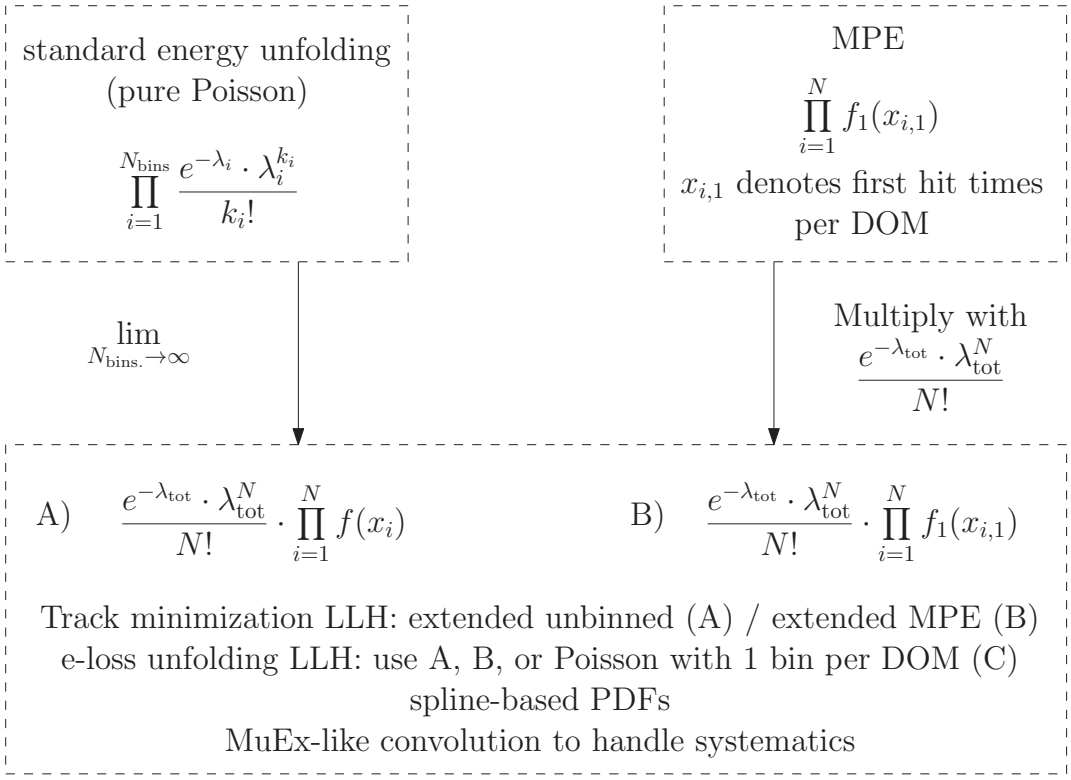

Figure 83: Possible LLH extensions of existing directional reconstructions that avoid time binning issues of the energy unfolding method (A) or include energy unfolding into the MPE reconstruction (B).

and the time residual PDF. A full description of such a reconstruction using spline tables has not been studied, yet. However, it is known from the standard MPE reconstruction, that the change to spline tables considerably improves the resolution [Sch14].

Given these reasons, routes A and B seem reasonable to explore in future studies. A hybrid mode (C), using the MPE (extended MPE) likelihood for the directional part, and using a pure Poisson likelihood with 1 bin per DOM for the energy unfolding within each directional minimization might also be worthwhile to test, as in this case the energy unfolding is known to work without any problems. Additionally, one can try to compensate for systematic effects, for example by an extra convolution of the expected charge as it is implemented in MuEx.

D

STUDIES ON THE FISHER-VON-MISES DISTRIBUTION

This section describes the validity of the approximations of the Fisher-von-Mises distribution in equations 39 and 40 in section 9.1.3.

The first approximation should safely hold for $\kappa \gtrsim 10$ which corresponds to a 39%-quantile of around 30°, i.e. it should hold for rather extended PSFs. All examples in figure 50 have larger concentration parameters and reside in this limit.

For the second simplification, a toy simulation has been performed to determine where the approximation breaks down under "standard point source conditions". The toy simulation involves a single point source on a flat background distribution, but other than that uses realistic IC-79 simulation: around 90000 background events and simulated reconstruction errors. For simplicity, only two skymaps are simulated: a background-only skymap and a skymap with 50 injected signal events. The LLH function in the minimization process only involves a spatial term, the energy estimator is not used. 3 diagnostic variables are then employed to quantify at which PSF-width the gaussian approximation breaks down:

- Median number of fitted signal events. This number should reflect the 50 injected signal events.
- 50% quantile of the LLH-ratio distribution $g(\lambda; H_{50})$ with 50 injected signal events . The higher this value, the more sensitive the analysis.
- 90% quantile of the LLH-ratio distribution $g(\lambda; H_0)$ with no injected signal events. As this toy example involves only one parameter in the minimization (n_s), the null hypothesis test statistic follows equation 37 in section 8.4.5. The 80% quantile of this combined test statistic is equal to the 90% quantile of a χ^2 distribution with one DOF and was thus chosen as a diagnostic parameter. Its numerical value is 1.682.

Three cases have been considered:

1. Injected from a gaussian, PDF is a gaussian (Inj G / Reco G)
2. Injected from the FM distribution, PDF is a gaussian (Inj F / Reco G)
3. Injected with the FM distribution, PDF is a FM distribution (Inj F / Reco F)

Figure 84 shows the results. At around 5 degrees, the approximation breaks down and the diagnostic parameters begin to change. At 10 degrees, the number of reconstructed events is already less than a third of the injected number and the test statistic distributions have changed dramatically, an

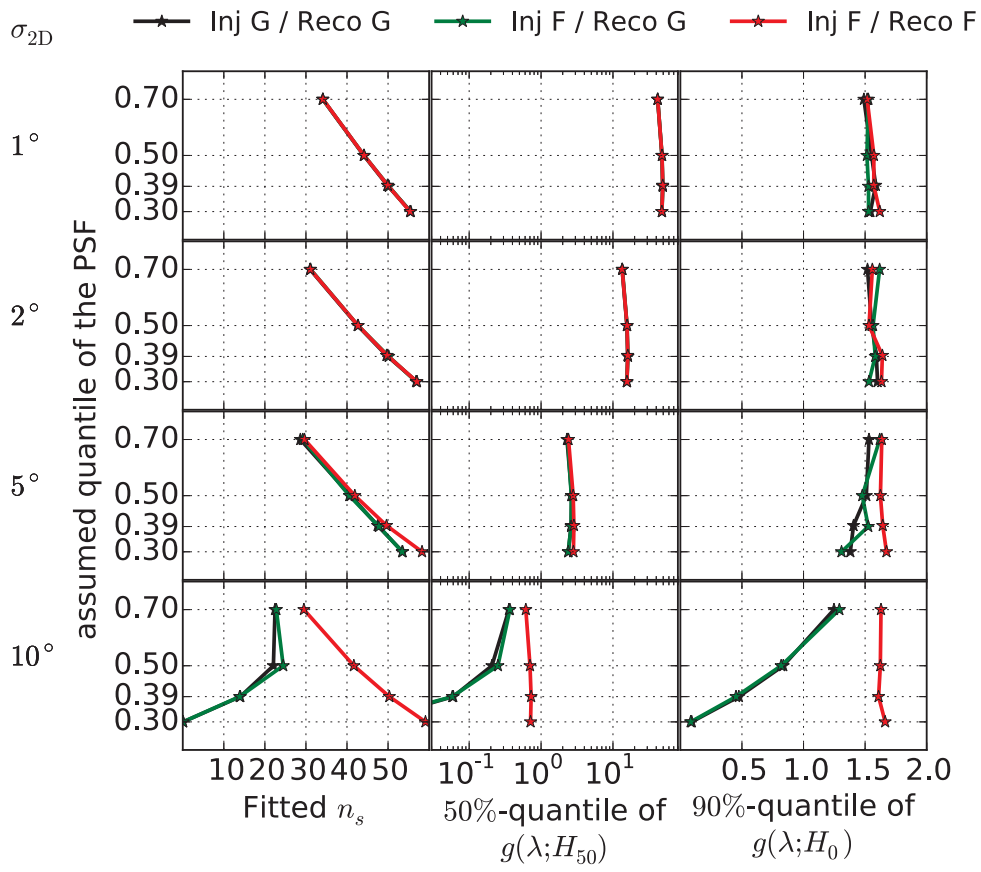

Figure 84: Diagnostic plots to determine when the gaussian approximation of the PSF breaks down. Each row corresponds to a simulated PSF with a different width ($\sigma_{2d} = 1°, 2°, 5°, 10°$) during injection. The y-axis shows the quantile that the paraboloid reconstruction is assumed to represent: it is the value that is used in the LLH-minimization and ideally equals σ_{2d} (the 39%-quantile). The first two columns are created using skymaps with 50 signal events, the last column using skymaps without any signal (see section 8.2 for a definition of $g(\lambda)$).

indication of sensitivity loss. Also shown is the effect for different assumptions of the paraboloid estimator. For example, one can assume that the paraboloid estimator should correspond to the 50% quantile of the PSF (which happens for example, when the ratio of true error versus paraboloid estimator is corrected to be 1.0, and not 1.177). The number of fitted events is only reconstructed correctly when the assumed quantile of the paraboloid corresponds to 39%, i.e. only when it really is the 1-σ width of the PSF.

As most paraboloid estimators are around one degree or smaller, a standard point source search should not be affected by the gaussian approximation. For analyses where a substantial fraction of the events has reconstructed errors larger than 5 degrees, as it is the case for cascade-like events or potentially for extended sources modelled as point sources with a bad resolution, a gaussian approximation for the spatial part inevitably involves

sensitivity losses. The magnitude of these losses will depend on the details of the respective analysis. One could avoid this by re-normalizing the gaussian such that its integral is unity within a given interval, e.g. up to 180 degrees in the radial direction. On the other hand, it is then much easier to take the FM-distribution directly, as one can always identify $\sigma = \sqrt{1/\kappa}$ as long as the first simplification is valid.

LIST OF FIGURES

Figure 1 The primary cosmic ray spectrum between 1×10^{13} eV and 2×10^{20} eV. 6
Figure 2 Diffusive Shock Acceleration. 7
Figure 3 Magnetic field strength versus Larmer radius - the "Hillas" plot. 9
Figure 4 Schematic of a cosmic ray shower. 10
Figure 5 The Extragalactic Gamma-Ray Background between 100 MeV and 820 GeV. 11
Figure 6 Scenarios to produce high energy photons. 12
Figure 7 Reprocessing of a gamma-ray. 13
Figure 8 The cosmic gamma ray horizon. 14
Figure 9 The cosmic neutrino background above 1 TeV 16
Figure 10 The three basic messenger particles. 17
Figure 11 Compatibility of the IceCube diffuse flux with the EGB. 18
Figure 12 Optical rest-frame spectra of the typical FSRQ and BLLac object. 22
Figure 13 The unified scheme of AGN. 24
Figure 14 The typical SED of a blazar (object *1ES-0229*). 26
Figure 15 The blazar sequence. 27
Figure 16 Luminosity and density evolution of blazars. 30
Figure 17 Model predictions and upper bounds for the diffuse neutrino flux from generic blazars. 33
Figure 18 Model predictions and upper bounds for the diffuse neutrino flux from BLLac objects. 34
Figure 19 Model predictions and upper bounds for the diffuse neutrino flux from FSRQs. 35
Figure 20 Diagram of CC and NC muon neutrino scattering on a nucleus. 37
Figure 21 DIS neutrino cross sections and optical thick boundary for a neutrino flux arriving at an underground detector. 38
Figure 22 Schematic of the Cherenkov effect. 39
Figure 23 Effective Cherenkov profiles due to energy loss of an electromagnetic shower and a quasi-continuous track. 40
Figure 24 Shower-like neutrino signatures. 41
Figure 25 Track-like neutrino signatures. 42
Figure 26 Illustration of typical stochastic and smooth event signatures of muon-bundles. 43

Figure 27 Geometry and construction of the IceCube Neutrino Observatory. 45
Figure 28 Scattering and absorption coefficients of the Antarctic ice. 47
Figure 29 The data acquisition chain. 49
Figure 30 The simulation chain. 50
Figure 31 Relations between possible likelihood functions. 57
Figure 32 Derivation of the MPE PDF. 60
Figure 33 Energy-dependent correction of the paraboloid estimator. 62
Figure 34 a) Zenith distribution of event at trigger level and final level. b) Zenith distribution of neutrino signal for different energies at final level. 65
Figure 35 a) Effective area for IC-79 at three different positions in the sky. b) Median angular resolution for the different datasets. 66
Figure 36 Distribution of sources from the 2-LAC catalog in the sky. 69
Figure 37 Distribution of the different 2-LAC blazar sub-populations in the sky. 70
Figure 38 The overlap between the different blazar populations. 72
Figure 39 The resolved and unresolved gamma flux of the $b > 20^\circ$ 2-LAC blazars. 73
Figure 40 Upper-limit construction with the CL_S method. 80
Figure 41 Sensitivity comparison of CL_S construction with standard approach. 81
Figure 42 Overview of the software framework. 83
Figure 43 Sensitivity per source for different popluation sizes. 85
Figure 44 Schematic of the point source PDF simplifications for signal and background. 87
Figure 45 Differences between injected and fitted number of signal events. 88
Figure 46 Illustration of the "undersampling problem" via the experimental large sample limit. 91
Figure 47 Sensitivity comparison between the standard method (with a MC-based PSF) and using a single 3d-PDF in energy/position/paraboloid. 94
Figure 48 Non-gaussianities for different zenith bands. 95
Figure 49 Sensitivity comparison (IC-79) for an E^{-3} spectrum between the standard method and the case where the spatial PDF is derived from MC. 95
Figure 50 Examples for the 2d-Fisher-von-Mises distribution on the sphere. 96
Figure 51 Illustration how to use a MC-based PDF for the atmospheric background in the northern sky with the extended likelihood. 98

Figure 52 Sensitivity comparison (IC-79) between the standard method and using a MC-based background PDF for the northern sky. 99
Figure 53 Likelihood scans with 1 and 2 DOF allowing for negative n_s. 100
Figure 54 Illustration of the test statistic (λ) construction for negative n_s. 102
Figure 55 Upper-limit construction allowing for negative n_s. 103
Figure 56 Differential sensitivity curve for the $(\nu_\mu + \overline{\nu}_\mu)$-flux from all 2LAC blazars using γ-energy flux weighting. 104
Figure 57 Differential-test p-values for the 5 blazar populations 109
Figure 58 Construction of the relevant energy interval for upper limits. 113
Figure 59 Comparison of equal-weighting upper limits for different source count distributions. 114
Figure 60 Upper limits for generic spectra with spectral indices -1.5, -2.0 and -2.7. 116
Figure 61 Contribution of All 2LAC blazars to the diffuse neutrino flux. 118
Figure 62 Constraints of the differential upper limit on diffuse neutrino models for generic blazars. 119
Figure 63 Upper limits on models of diffuse neutrino emisson from FSRQs. 120
Figure 64 Upper flux limits on diffuse neutrino models for BLLac objects. 121
Figure 65 The 2LAC blazar contribution to the diffuse neutrino flux for small sub-samples or a harder spectral index. 124
Figure 66 Differential upper limit on the $(\nu_\mu + \overline{\nu}_\mu)$-flux in the equal-weighting scheme for the "All LAT blazar" population. 125
Figure 67 Per-year significance analysis for the "All LAT-blazar" sample in the equal-weighting scheme. 126
Figure 68 Expected p-value distribution with 3 years more data. 127
Figure 69 EGB and diffuse neutrino flux with respective 2LAC fractions and a best-fit neutrino flux estimate for the largest excess. 128
Figure 70 Sensitivity for an E^{-2} flux comparing IC-59, IC-79 and IC-86. 141
Figure 71 Sensitivity for an E^{-2} flux (IC-79) comparing event injection via RA scrambling and PDF sampling. 141
Figure 72 Sensitivity comparison (IC-79) for an E^{-2} spectrum between the standard method and the case where the spatial PDF is derived from MC. 142

Figure 73 Sensitivity comparison (IC-86) for an E^{-2} spectrum between the standard method and using a MC-based background PDF for the northern sky. 142
Figure 74 Sensitivity comparison (IC-86) for an $E^{-1.5}$ spectrum between the standard method and using a MC-based background PDF for the northern sky. 143
Figure 75 Sensitivity comparison using different binning schemes. 143
Figure 79 One realization of a soft flux and individual dataset contributions to differential p-values. 146
Figure 80 High-QE and Low-QE DOM occupancies and ratios in data. 148
Figure 81 Estimation of the RDE using FixedRateTrigger data. 149
Figure 82 Determination of the optical efficiency from the HLC-Nch ratio. 151
Figure 83 Possible LLH extensions of existing directional reconstructions. 154
Figure 84 Diagnostic plots to determine when the gaussian approximation of the 2d-Fisher-von-Mises distribution breaks down. 156

LIST OF TABLES

Table 1 Change of flavor ratio over cosmological distances. 17
Table 2 Summary of of the two blazar classification schemes used in this thesis. 27
Table 3 Overview of models for the diffuse $\nu_\mu + \overline{\nu}_\mu$-flux from blazar populations. 32
Table 4 Energy estimators used in the final point source analysis. 63
Table 5 Events per year in the different track selections for data and the diffuse astrophysical flux. 66
Table 6 Summary of the variations of the point source method. 105
Table 7 Pre-trial p-values for the integral search. 108
Table 8 Systematic uncertainties 111
Table 9 Limits on generic spectra. 117
Table 10 Model rejection factors on diffuse neutrino flux predictions from blazar populations. 122
Table 11 List of parameters for the analysis framework. 140

ACRONYMS

AGN Active Galactic Nucleus

BLR Broad Line Region

CDF Cumulative Density Distribution

CMB Cosmic Microwave Background

CR Cosmic Ray

DIS Deep Inelastic Scattering

DOM Digital Optical Module

EBL Extragalactic Background Light

EGB Extragalactic Gamma Ray Background

FSRQ Flat Spectrum Radio Quasar

HBL High Peaked BLLac

HSP High Synchroton Peaked (object)

IBL Intermediate Peaked BLLac

IC Inverse Compton

IGRB Isotropic diffuse Gamma Ray Background

ISP Intermediate Synchroton Peaked (object)

LBL Low Peaked BLLac

LDDE Luminosity Dependent Density Evolution

LLH Log-Likelihood

LSP Low Synchroton Peaked (object)

MHD Magneto Hydro Dynamics

ML Maximum Likelihood

MRF Model Rejection Factor

NLR Narrow Line Region

PDF Probability Density Distribution

PMT Photo Multiplier Tube

QE Quantum Efficiency

RDE Relative DOM Efficiency

SED Spectral Energy Distribution

SSC Self-Synchroton Compton

QSO Quasi-Stellar Object

UHE Ultra High Energy

UV Ultra Violet

BIBLIOGRAPHY

[Aar+13] M. G. Aartsen et al. (The IceCube Collaboration). "Probing the origin of cosmic rays with extremely high energy neutrinos using the IceCube Observatory." In: *Physical Review* D88 (2013), p. 112008. DOI: 10.1103/PhysRevD.88.112008. arXiv: 1310.5477 [astro-ph.HE].

[AD01] A. Atoyan and C.D. Dermer. "High-energy neutrinos from photomeson processes in blazars." In: *Physical Review Letters* 87 (2001), p. 221102. DOI: 10.1103/PhysRevLett.87.221102. arXiv: astro-ph/0108053 [astro-ph].

[Aje+12] M. Ajello et al. "The Luminosity Function of Fermi-detected Flat-Spectrum Radio Quasars." In: *The Astrophysical Journal* 751 (2012), p. 108. DOI: 10.1088/0004-637X/751/2/108. arXiv: 1110.3787 [astro-ph.CO].

[Aje+14] M. Ajello et al. "The Cosmic Evolution of Fermi BL Lacertae Objects." In: *The Astrophysical Journal* 780 (2014), p. 73. DOI: 10.1088/0004-637X/780/1/73. arXiv: 1310.0006 [astro-ph.CO].

[Aje+15] M. Ajello et al. "The Origin of the Extragalactic Gamma-Ray Background and Implications for Dark-Matter Annihilation." In: *The Astrophysical Journal* 800.2 (2015), p. L27. DOI: 10.1088/2041-8205/800/2/L27. arXiv: 1501.05301 [astro-ph.HE].

[AKC08] F. Aharonian, D. Khangulyan, and L. Costamante. "Formation of hard VHE gamma-ray spectra of blazars due to internal photon-photon absorption." In: *Monthly Notices of the Royal Astronomical Society* 387 (2008), pp. 1206–1214. DOI: 10.1111/j.1365-2966.2008.13315.x. arXiv: 0801.3198 [astro-ph].

[Ale+87] E.N. Alekseev et al. "Possible Detection of a Neutrino Signal on 23 February 1987 at the Baksan Underground Scintillation Telescope of the Institute of Nuclear Research." In: *Journal of Experimental and Theoretical Physics Letters* 45 (1987), pp. 589–592.

[Ali+14] E. Aliu et al. "A three-year multi-wavelength study of the very-high-energy γ-ray blazar 1ES 0229+200." In: *The Astrophysical Journal* 782.1 (2014), p. 13. DOI: 10.1088/0004-637X/782/1/13. arXiv: 1312.6592 [astro-ph.HE].

[AMA06] M. Ackermann et al. (The AMANDA Collaboration). "Optical properties of deep glacial ice at the South Pole." In: *Journal of Geophysical Research* 111.D13 (2006), p. D13203. DOI: 10.1029/2005JD006687.

[Ang+11] G.I. Angelis et al. "The performance of monotonic and new non-monotonic gradient ascent reconstruction algorithms for high-resolution neuroreceptor PET imaging." In: *Physics in Medicine and Biology* 56.13 (June 2011), pp. 3895–3917. DOI: 10.1088/0031-9155/56/13/010.

[Ant82] R. Antonucci. "Optical polarization position angle versus radio source axis in radio galaxies." In: *Nature* 299.5884 (1982), pp. 605–606. DOI: 10.1038/299605a0.

[Ant83] R. Antonucci. "Optical polarization position angle versus radio structure axis in Seyfert galaxies." In: *Nature* 303.5913 (1983), pp. 158–159. DOI: 10.1038/303158a0.

[AS80] J.R.P. Angel and H.S. Stockman. "Optical and Infrared Polarization of Active Extragalactic Objects." In: *Annual Review of Astronomy and Astrophysics* 18.1 (1980), pp. 321–361. DOI: 10.1146/annurev.aa.18.090180.001541.

[Aug08] J. Abraham et al. (The Pierre Auger Collaboration). "Correlation of the highest-energy cosmic rays with the positions of nearby active galactic nuclei." In: *Astroparticle Physics* 29 (2008), pp. 188–204. DOI: 10.1016/j.astropartphys.2008.06.004, 10.1016/j.astropartphys.2008.01.002. arXiv: 0712.2843 [astro-ph].

[Aug10] P. Abreu et al. (The Pierre Auger Collaboration). "Update on the correlation of the highest energy cosmic rays with nearby extragalactic matter." In: *Astroparticle Physics* 34 (2010), pp. 314–326. DOI: 10.1016/j.astropartphys.2010.08.010. arXiv: 1009.1855 [astro-ph.HE].

[Bar90] R.J. Barlow. "Extended maximum likelihood." In: *Nuclear Instruments and Methods in Physics Research* A297 (1990), pp. 496–506. DOI: 10.1016/0168-9002(90)91334-8.

[Bay+10] R.C. Bay et al. "South Pole paleowind from automated synthesis of ice core records." In: *Journal of Geophysical Research* 115.D14 (2010). DOI: 10.1029/2009jd013741.

[BB09] J.K. Becker and P.L. Biermann. "Neutrinos from active black holes, sources of ultra high energy cosmic rays." In: *Astroparticle Physics* 31 (2009), pp. 138–148. DOI: 10.1016/j.astropartphys.2008.12.006. arXiv: 0805.1498 [astro-ph].

[BBR05] J.K. Becker, P.L. Biermann, and W. Rhode. "The Diffuse neutrino flux from FR-II radio galaxies and blazars: A Source property based estimate." In: *Astroparticle Physics* 23 (2005), pp. 355–368. DOI: 10.1016/j.astropartphys.2005.02.003. arXiv: astro-ph/0502089 [astro-ph].

[BD02] M. Boettcher and C.D. Dermer. "An evolutionary scenario for blazar unification." In: *The Astrophysical Journal* 564 (2002), p. 86. DOI: 10.1086/324134. arXiv: astro-ph/0106395 [astro-ph].

[Bei+09] B. Beischer et al. "Perspectives for indirect dark matter search with AMS-2 using cosmic-ray electrons and positrons." In: *New Journal of Physics* 11 (2009), p. 105021. DOI: 10.1088/1367-2630/11/10/105021.

[Bel78] A.R. Bell. "The Acceleration of cosmic rays in shock fronts. I." In: *Monthly Notices of the Royal Astronomical Society* 182 (1978), pp. 147–156.

[Bha+11] A. Bhattacharya et al. "The Glashow resonance at IceCube: signatures, event rates and pp vs. pγ interactions." In: *Journal of Cosmology and Astroparticle Physics* 1110 (2011), p. 017. DOI: 10.1088/1475-7516/2011/10/017. arXiv: 1108.3163 [astro-ph.HE].

[BK79] R.D. Blandford and A. Konigl. "Relativistic jets as compact radio sources." In: *The Astrophysical Journal* 232 (1979), p. 34. DOI: 10.1086/157262.

[BM09] P.M. Bauleo and J.R. Martino. "The dawn of the particle astronomy era in ultra-high-energy cosmic rays." In: *Nature* 458N7240 (2009), pp. 847–851. DOI: 10.1038/nature07948.

[BM54] W. Baade and R. Minkowski. "Identification of the Radio Sources in Cassiopeia, Cygnus a, and Puppis a." In: *The Astrophysical Journal* 119 (1954), p. 206. DOI: 10.1086/145812.

[BO78] R.D. Blandford and J.P. Ostriker. "Particle Acceleration by Astrophysical Shocks." In: *The Astrophysical Journal* 221 (1978), pp. L29–L32. DOI: 10.1086/182658.

[BP82] R.D. Blandford and D.G. Payne. "Hydromagnetic flows from accretion discs and the production of radio jets." In: *Monthly Notices of the Royal Astronomical Society* 199 (1982), p. 883.

[Bra+05] N.E. Bramall et al. "A deep high-resolution optical log of dust, ash, and stratigraphy in South Pole glacial ice." In: *Geophysical Research Letters* 32.21 (2005). DOI: 10.1029/2005gl024236.

[BS95] M. Böttcher and R. Schlickeiser. "Pair bremsstrahlung radiation from relativistic jets in γ-ray blazars." In: *Astronomy and Astrophysics* 302 (1995), p. L17.

[BS96] M. Böttcher and R. Schlickeiser. "Pair annihilation radiation from relativistic jets in gamma-ray blazars." In: *Astronomy and Astrophysics Supplement Series* 120 (1996), pp. 575–578. arXiv: astro-ph/9506112 [astro-ph].

[BW01] J.N. Bahcall and E. Waxman. "High-energy astrophysical neutrinos: The Upper bound is robust." In: *Physical Review* D64 (2001), p. 023002. DOI: 10.1103/PhysRevD.64.023002. arXiv: hep-ph/9902383 [hep-ph].

[Byr+94] R.H. Byrd et al. "A Limited-Memory Algorithm for Bound Constrained Optimization." In: *Siam Journal On Scientific Computing* 16 (1994), pp. 1190–1208. DOI: 0.1137/0916069.

[BZ77] R.D. Blandford and R.L. Znajek. "Electromagnetic extractions of energy from Kerr black holes." In: *Monthly Notices of the Royal Astronomical Society* 179 (1977), pp. 433–456.

[CD02] A. Cavaliere and V. D'Elia. "The blazar main sequence." In: *The Astrophysical Journal* 571 (2002), pp. 226–233. DOI: 10.1086/339778. arXiv: astro-ph/0106512 [astro-ph].

[Čer37] P. Čerenkov. "Visible Radiation Produced by Electrons Moving in a Medium with Velocities Exceeding that of Light." In: *Physical Review* 52.4 (1937), pp. 378–379. DOI: 10.1103/physrev.52.378.

[Chi03] D. Chirkin. "Cosmic Ray Energy Spectrum Measurement with the Antarctic Muon and Neutrino Detector Array (AMANDA)." PhD thesis. University of California, 2003.

[Chi13] D. Chirkin. "Photon tracking with GPUs in IceCube." In: *Nuclear Instruments and Methods in Physics Research* A725 (2013), pp. 141–143. DOI: 10.1016/j.nima.2012.11.170.

[Cle+98] B.T. Cleveland et al. "Measurement of the solar electron neutrino flux with the Homestake chlorine detector." In: *The Astrophysical Journal* 496 (1998), pp. 505–526. DOI: 10.1086/305343.

[Cow+11] G. Cowan et al. "Asymptotic formulae for likelihood-based tests of new physics." In: *The European Physical Journal* C71 (2011), p. 1554. DOI: 10.1140/epjc/s10052-011-1554-0, 10.1140/epjc/s10052-013-2501-z. arXiv: 1007.1727 [physics.data-an].

[CR04] D. Chirkin and W. Rhode. "Propagating leptons through matter with Muon Monte Carlo (MMC)." In: *arXiv* (2004). arXiv: hep-ph/0407075 [hep-ph].

[Cur18] H.D. Curtis. "The planetary nebulae." In: *Publications of Lick Observatory* 13 (1918), pp. 55–74.

[DA81] A.M. Dziewonski and D.L. Anderson. "Preliminary reference earth model." In: *Physics of the Earth and Planetary Interiors* 25 (1981), pp. 297–356. DOI: 10.1016/0031-9201(81)90046-7.

[Der95] C.D. Dermer. "On the Beaming Statistics of Gamma-Ray Sources." In: *The Astrophysical Journal* 446 (1995), p. 63. DOI: 10.1086/187931.

[DeY05] T. DeYoung. "IceTray: A software framework for IceCube." In: *International Conference on Computing in High Energy and Nuclear Physics* (2005), pp. 463–466.

[Dom+11] A. Domínguez et al. "Extragalactic Background Light Inferred from AEGIS Galaxy SED-type Fractions." In: *Monthly Notices of the Royal Astronomical Society* 410 (2011), p. 2556. DOI: 10.1111/j.1365-2966.2010.17631.x. arXiv: 1007.1459 [astro-ph.CO].

[Dom+13] A. Domínguez et al. "Detection of the cosmic γ-ray horizon from multiwavelength observations of blazars." In: *The Astrophysical Journal* 770 (2013), p. 77. DOI: 10.1088/0004-637X/770/1/77. arXiv: 1305.2162 [astro-ph.CO].

[DS93] C.D. Dermer and R. Schlickeiser. "Model for the high-energy emission from blazars." In: *The Astrophysical Journal* 416 (1993), p. 458. DOI: 10.1086/173251.

[Ess+10] W. Essey et al. "Secondary photons and neutrinos from cosmic rays produced by distant blazars." In: *Physical Review Letters* 104 (2010), p. 141102. DOI: 10.1103/PhysRevLett.104.141102. arXiv: 0912.3976 [astro-ph.HE].

[FB95] H. Falcke and P.L. Biermann. "The jet-disk symbiosis. 1. Radio to X-ray emission models for quasars." In: *Astronomy and Astrophysics* 293 (1995), p. 665. arXiv: astro-ph/9411096 [astro-ph].

[FC98] G.J. Feldman and R.D. Cousins. "A Unified approach to the classical statistical analysis of small signals." In: *Physical Review* D57 (1998), pp. 3873–3889. DOI: 10.1103/PhysRevD.57.3873. arXiv: physics/9711021 [physics.data-an].

[Fei14] J. Feintzeig. "Searches for Point-like Sources of Astrophysical Neutrinos with the IceCube Neutrino Observatory." PhD thesis. University of Wisconsin, Madison, 2014.

[Fer09] W.B. Atwood et al. (The Fermi-LAT Collaboration). "The Large Area Telescope on the Fermi Gamma-ray Space Telescope Mission." In: *The Astrophysical Journal* 697 (2009), pp. 1071–1102. DOI: 10.1088/0004-637X/697/2/1071. arXiv: 0902.1089 [astro-ph.IM].

[Fer10a] A.A. Abdo et al. (The Fermi-LAT Collaboration). "The Fermi-LAT high-latitude Survey: Source Count Distributions and the Origin of the Extragalactic Diffuse Background." In: *The Astrophysical Journal* 720 (2010), pp. 435–453. DOI: 10.1088/0004-637X/720/1/435. arXiv: 1003.0895 [astro-ph.CO].

[Fer10b] A.A. Abdo et al. (The Fermi-LAT Collaboration). "The Spectral Energy Distribution of Fermi bright blazars." In: *The Astrophysical Journal* 716 (2010), pp. 30–70. DOI: 10.1088/0004-637X/716/1/30. arXiv: 0912.2040 [astro-ph.CO].

[Fer11] M. Ackermann et al. (The Fermi-LAT Collaboration). "The Second Catalog of Active Galactic Nuclei Detected by the Fermi Large Area Telescope." In: *The Astrophysical Journal* 743 (2011), p. 171. DOI: 10.1088/0004-637X/743/2/171. arXiv: 1108.1420 [astro-ph.HE].

[Fer12] P.L. Nolan et al. (The Fermi-LAT Collaboration). "Fermi Large Area Telescope Second Source Catalog." In: *The Astrophysical Journal Supplement Series* 199 (2012), p. 31. DOI: 10.1088/0067-0049/199/2/31. arXiv: 1108.1435 [astro-ph.HE].

[Fer13] M. Ackermann et al. (The Fermi-LAT Collaboration). "Detection of the Characteristic Pion-Decay Signature in Supernova Remnants." In: *Science* 339 (2013), p. 807. DOI: 10.1126/science.1231160. arXiv: 1302.3307 [astro-ph.HE].

[Fer15] M. Ackermann et al. (The Fermi-LAT Collaboration). "The spectrum of isotropic diffuse gamma-ray emission between 100 MeV and 820 GeV." In: *The Astrophysical Journal* 799.1 (2015), p. 86. DOI: 10.1088/0004-637X/799/1/86. arXiv: 1410.3696 [astro-ph.HE].

[Fis53] R. Fisher. "Dispersion on a sphere." In: *Proceedings of the Royal Society*. Vol. 217. 1130. The Royal Society. 1953, pp. 295–305.

[Fos+98] G. Fossati et al. "A Unifying view of the spectral energy distributions of blazars." In: *Monthly Notices of the Royal Astronomical Society* 299 (1998), pp. 433–448. DOI: 10.1046/j.1365-8711.1998.01828.x. arXiv: astro-ph/9804103 [astro-ph].

[FTV14] D.V. Forero, M. Tortola, and J.W.F. Valle. "Neutrino oscillations refitted." In: *Physical Review* D90.9 (2014), p. 093006. DOI: 10.1103/PhysRevD.90.093006. arXiv: 1405.7540 [hep-ph].

[FZ12] J.A. Formaggio and G.P. Zeller. "From eV to EeV: Neutrino Cross Sections Across Energy Scales." In: *Reviews of Modern Physics* 84 (2012), p. 1307. DOI: 10.1103/RevModPhys.84.1307. arXiv: 1305.7513 [hep-ex].

[Gai12] T.K. Gaisser. "Spectrum of cosmic-ray nucleons, kaon production, and the atmospheric muon charge ratio." In: *Astroparticle Physics* 35 (2012), pp. 801–806. DOI: 10.1016/j.astropartphys.2012.02.010. arXiv: 1111.6675 [astro-ph.HE].

[Ghi+11] G. Ghisellini et al. "The transition between BL Lac objects and Flat Spectrum Radio Quasars." In: *Monthly Notices of the Royal Astronomical Society* 414 (2011), p. 2674. DOI: 10.1111/j.1365-2966.2011.18578.x. arXiv: 1012.0308 [astro-ph.CO].

[Ghi89] G. Ghisellini. "Pair production in steady synchrotron self Compton models." In: *Monthly Notices of the Royal Astronomical Society* 238 (1989), pp. 449–479.

[Gio+12] P. Giommi et al. "A simplified view of blazars: clearing the fog around long-standing selection effects." In: *Monthly Notices of the Royal Astronomical Society* 420 (2012), p. 2899. DOI: 10.1111/j.1365-2966.2011.20044.x. arXiv: 1110.4706 [astro-ph.CO].

[GK05] A. Gazizov and M.P. Kowalski. "ANIS: High energy neutrino generator for neutrino telescopes." In: *Computer Physics Communications* 172 (2005), pp. 203–213. DOI: 10.1016/j.cpc.2005.03.113. arXiv: astro-ph/0406439 [astro-ph].

[Gor+14] D. Gora et al. *Internal report - icecube/201404001*. Tech. rep. 2014.

[Gra12] J. Granot. "The effects of sub-shells in highly magnetized relativistic flows." In: *Monthly Notices of the Royal Astronomical Society* 421 (2012), pp. 2467–2477. DOI: 10.1111/j.1365-2966.2012.20474.x. arXiv: 1109.5315 [astro-ph.HE].

[GS64] V.L. Ginzburg and S.I. Syrovatskii. *The Origin of Cosmic Rays*. Pergamon Press, 1964.

[GS66] R.J. Gould and G. Schréder. "Opacity of the Universe to High-Energy Photons." In: *Physical Review Letters* 16.6 (1966), pp. 252–254. DOI: 10.1103/PhysRevLett.16.252.

[GS67] R.J. Gould and G. Schréder. "Opacity of the Universe to High-Energy Photons." In: *Physical Review* 155 (1967), pp. 1408–1411. DOI: 10.1103/PhysRev.155.1408.

[HBW10] M. Houjun, F. van den Bosch, and S. White. *Galaxy Formation and Evolution*. Cambridge University Press, 2010.

[Hec+98] D. Heck et al. *CORSIKA: A Monte Carlo code to simulate extensive air showers*. 1998.

[Hil84] A.M. Hillas. "The Origin of Ultrahigh-Energy Cosmic Rays." In: *Annual Review of Astronomy and Astrophysics* 22 (1984), pp. 425–444. DOI: 10.1146/annurev.aa.22.090184.002233.

[Hoe03] J. Hoerandel. "On the knee in the energy spectrum of cosmic rays." In: *Astroparticle Physics* 19 (2003), pp. 193–220. DOI: 10.1016/S0927-6505(02)00198-6. arXiv: astro-ph/0210453 [astro-ph].

[Hop+05] P.F. Hopkins et al. "Black holes in galaxy mergers: Evolution of quasars." In: *The Astrophysical Journal* 630 (2005), pp. 705–715. DOI: 10.1086/432438. arXiv: astro-ph/0504190 [astro-ph].

[HR03] G.C. Hill and K. Rawlins. "Unbiased cut selection for optimal upper limits in neutrino detectors: The Model rejection potential technique." In: *Astroparticle Physics* 19 (2003), pp. 393–402. DOI: 10.1016/S0927-6505(02)00240-2. arXiv: astro-ph/0209350 [astro-ph].

[HZ97] F. Halzen and E. Zas. "Neutrino fluxes from active galaxies: A Model independent estimate." In: *The Astrophysical Journal* 488 (1997), pp. 669–674. DOI: 10.1086/304741. arXiv: astro-ph/9702193 [astro-ph].

[Ice06] A. Achterberg et al. (The IceCube Collaboration). "On the selection of AGN neutrino source candidates for a source stacking analysis with neutrino telescopes." In: *Astroparticle Physics* 26 (2006), pp. 282–300. DOI: 10.1016/J.ASTROPARTPHYS.2006.06.012. arXiv: astro-ph/0609534 [astro-ph].

[Ice09] R. Abbasi et al. (The IceCube Collaboration). "The IceCube Data Acquisition System: Signal Capture, Digitization, and Timestamping." In: *Nuclear Instruments and Methods in Physics Research* A601 (2009), pp. 294–316. DOI: 10.1016/j.nima.2009.01.001. arXiv: 0810.4930 [physics.ins-det].

[Ice10] R. Abbasi et al. (The IceCube Collaboration). "Calibration and Characterization of the IceCube Photomultiplier Tube." In: *Nuclear Instruments and Methods in Physics Research* A618 (2010), pp. 139–152. DOI: 10.1016/j.nima.2010.03.102. arXiv: 1002.2442 [astro-ph.IM].

[Ice11] R. Abbasi et al. (The IceCube Collaboration). "Time-Integrated Searches for Point-like Sources of Neutrinos with the 40-String IceCube Detector." In: *The Astrophysical Journal* 732 (2011), p. 18. DOI: 10.1088/0004-637X/732/1/18. arXiv: 1012.2137 [astro-ph.HE].

[Ice13a] M.G. Aartsen et al. (The IceCube Collaboration). "Evidence for High-Energy Extraterrestrial Neutrinos at the IceCube Detector." In: *Science* 342 (2013), p. 1242856. DOI: 10.1126/science.1242856. arXiv: 1311.5238 [astro-ph.HE].

[Ice13b] M.G. Aartsen et al. (The IceCube Collaboration). "Measurement of South Pole ice transparency with the IceCube LED calibration system." In: *Nuclear Instruments and Methods in Physics Research* A711 (2013), pp. 73–89. DOI: 10.1016/j.nima.2013.01.054. arXiv: 1301.5361 [astro-ph.IM].

[Ice14a] M.G. Aartsen et al. (The IceCube Collaboration). "Energy Reconstruction Methods in the IceCube Neutrino Telescope." In: *Journal of Instrumentation* 9 (2014), P03009. DOI: 10.1088/1748-0221/9/03/P03009. arXiv: 1311.4767 [physics.ins-det].

[Ice14b] M.G. Aartsen et al. (The IceCube Collaboration). "Observation of the cosmic-ray shadow of the Moon with IceCube." In: *Physical Review* D89.10 (2014), p. 102004. DOI: 10.1103/PhysRevD.89.102004. arXiv: 1305.6811 [astro-ph.HE].

[Ice14c] M.G. Aartsen et al. (The IceCube Collaboration). "Search for non-relativistic Magnetic Monopoles with IceCube." In: *The European Physical Journal* C74.7 (2014), p. 2938. DOI: 10.1140/epjc/s10052-014-2938-8. arXiv: 1402.3460 [astro-ph.CO].

[Ice14d] M.G. Aartsen et al. (The IceCube Collaboration). "Searches for Extended and Point-like Neutrino Sources with Four Years of IceCube Data." In: *The Astrophysical Journal* (2014). DOI: 10.1088/0004-637X/796/2/109. arXiv: 1406.6757 [astro-ph.HE].

[Ice15] M.G. Aartsen et al. (The IceCube Collaboration). "Atmospheric and astrophysical neutrinos above 1 TeV interacting in IceCube." In: *Physical Review* D91.2 (2015), p. 022001. DOI: 10.1103/PhysRevD.91.022001. arXiv: 1410.1749 [astro-ph.HE].

[IMB87] R.M. Bionta et al. (The IMB Collaboration). "Observation of a Neutrino Burst in Coincidence with Supernova SN 1987a in the Large Magellanic Cloud." In: *Physical Review Letters* 58 (1987), p. 1494. DOI: 10.1103/PhysRevLett.58.1494.

[Ino+10] Y. Inoue et al. "The Cosmological Evolution of Blazars and the Extragalactic Gamma-Ray Background in the Fermi Era." In: *arXiv* (2010). arXiv: 1001.0103.

[IT09] Y. Inoue and T. Totani. "The Blazar Sequence and the Cosmic Gamma-Ray Background Radiation in the Fermi Era." In: *The Astrophysical Journal* 702 (2009), pp. 523–536. DOI: 10.1088/0004-637X/728/1/73,10.1088/0004-637X/702/1/523. arXiv: 0810.3580 [astro-ph].

[Jam06] F. James. *Statistical Methods in Experimental Physics (2nd Edition)*. World Scientific Publishing Co. Pte. Ltd., 2006.

[JR07] G. Japaridze and M. Ribordy. "Realistic arrival time distribution from an isotropic light source." In: *arXiv* (2007). arXiv: astro-ph/0506136.

[Kam87] K. Hirata et al. (The Kamiokande-II Collaboration). "Observation of a Neutrino Burst from the Supernova SN 1987a." In: *Physical Review Letters* 58 (1987), pp. 1490–1493. DOI: 10.1103/PhysRevLett.58.1490.

[Kel+89] K.I. Kellermann et al. "VLA observations of objects in the Palomar Bright Quasar Survey." In: *The Astronomical Journal* 98 (1989), pp. 1195–1207. DOI: 10.1086/115207.

[KMO14] M. Kachelriess, I.V. Moskalenko, and S.S. Ostapchenko. "Nuclear enhancement of the photon yield in cosmic ray interactions." In: *The Astrophysical Journal* 789 (2014), p. 136. DOI: 10.1088/0004-637X/789/2/136. arXiv: 1406.0035 [astro-ph.HE].

[KSD13] D. Kim, S. Sra, and I.S. Dhillon. "A non-monotonic method for large-scale non-negative least squares." In: *Optimization Methods and Software* 28.5 (Oct. 2013), pp. 1012–1039. DOI: 10.1080/10556788.2012.656368.

[LB85] K.R. Lind and R.D. Blandford. "Semidynamical models of radio jets - Relativistic beaming and source counts." In: *The Astrophysical Journal* 295 (1985), p. 358. DOI: 10.1086/163380.

[LLM07] P. Lipari, M. Lusignoli, and D. Meloni. "Flavor Composition and Energy Spectrum of Astrophysical Neutrinos." In: *Physical Review* D75 (2007), p. 123005. DOI: 10.1103/PhysRevD.75.123005. arXiv: 0704.0718 [astro-ph].

[Lun+07] J. Lundberg et al. "Light tracking through ice and water—Scattering and absorption in heterogeneous media with Photonics." In: *Nuclear Instruments and Methods in Physics Research* A581 (2007), pp. 619–631. DOI: 10.1016/j.nima.2007.07.143. arXiv: astro-ph/0702108 [astro-ph].

[MAL13] K. Murase, M. Ahlers, and B.C. Lacki. "Testing the Hadronuclear Origin of PeV Neutrinos Observed with IceCube." In: *Physical Review* D88.12 (2013), p. 121301. DOI: 10.1103/PhysRevD.88.121301. arXiv: 1306.3417 [astro-ph.HE].

[Man95] K. Mannheim. "High-energy neutrinos from extragalactic jets." In: *Astroparticle Physics* 3 (1995), pp. 295–302. DOI: 10.1016/0927-6505(94)00044-4.

[MBQ08] A. Meli, J.K. Becker, and J.J. Quenby. "On the origin of ultra high energy cosmic rays: subluminal and superluminal relativistic shocks." In: *Astronomy and Astrophysics* 492.2 (2008), pp. 323–336. DOI: 10.1051/0004-6361:20078681. arXiv: 0709.3031 [astro-ph].

[MD01] M.A. Malkov and L.O.C. Drury. "Nonlinear theory of diffusive acceleration of particles by shock waves." In: *Reports on Progress in Physics* 64.4 (2001), pp. 429–481. DOI: 10.1088/0034-4885/64/4/201.

[MHB70] G.K. Miley, D.E. Hogg, and J. Basart. "The Fine-Scale Structure of Virgo A." In: *The Astrophysical Journal* 159 (1970), p. L19. DOI: 10.1086/180469.

[MID14] K. Murase, Y. Inoue, and C.D. Dermer. "Diffuse Neutrino Intensity from the Inner Jets of Active Galactic Nuclei: Impacts of External Photon Fields and the Blazar Sequence." In: *Physical Review* D90.2 (2014), p. 023007. DOI: 10.1103/PhysRevD.90.023007. arXiv: 1403.4089 [astro-ph.HE].

[Mie08] G. Mie. "Beiträge zur Optik trüber Medien, speziell kolloidaler Metallösungen." In: *Annalen der Physik (4)* 25 (1908), p. 377.

[Mis93] A. Misaki. "The Landau-Pomeranchuk-Migdal (LPM) effect and its influence on electromagnetic cascade showers at extremely high-energies." In: *Nuclear Physics B - Proceedings Supplements* 33AB (1993), pp. 192–199. DOI: 10.1016/0920-5632(93)90091-J.

[MPR01] K. Mannheim, R.J. Protheroe, and J.P. Rachen. "Cosmic ray bound for models of extragalactic neutrino production." In: *Physical Review* D63 (2001), p. 023003. DOI: 10.1103/PhysRevD.63.023003. arXiv: astro-ph/9812398 [astro-ph].

[Mue+03] A. Muecke et al. "BL Lac Objects in the synchrotron proton blazar model." In: *Astroparticle Physics* 18 (2003), pp. 593–613. DOI: 10.1016/S0927-6505(02)00185-8. arXiv: astro-ph/0206164 [astro-ph].

[Neu06] T. Neunhoffer. "Estimating the angular resolution of tracks in neutrino telescopes based on a likelihood analysis." In: *Astroparticle Physics* 25 (2006), pp. 220–225. DOI: 10.1016/j.astropartphys.2006.01.002. arXiv: astro-ph/0403367 [astro-ph].

[NMB93] L. Nellen, K. Mannheim, and P.L. Biermann. "Neutrino production through hadronic cascades in AGN accretion disks." In: *Physical Review* D47 (1993), pp. 5270–5274. DOI: 10.1103/PhysRevD.47.5270. arXiv: hep-ph/9211257 [hep-ph].

[NR09] A. Neronov and M. Ribordy. "IceCube sensitivity for neutrino flux from Fermi blazars in quiescent states." In: *Physical Review* D80 (2009), p. 083008. DOI: 10.1103/PhysRevD.80.083008. arXiv: 0905.0509 [astro-ph.HE].

[Oli14] K.A. Olive. "Review of Particle Physics." In: *Chinese Physics C* 38.9 (2014), p. 090001. DOI: 10.1088/1674-1137/38/9/090001.

[Par57] E.N. Parker. "Sweet's mechanism for merging magnetic fields in conducting fluids." In: *Journal of Geophysical Research* 62.4 (1957), pp. 509–520. DOI: 10.1029/jz062i004p00509.

[Pet+15] M. Petropoulou et al. "Photohadronic origin of γ-ray BL Lac emission: implications for IceCube neutrinos." In: *Monthly Notices of the Royal Astronomical Society* 448.3 (2015), pp. 2412–2429. DOI: 10.1093/mnras/stv179. arXiv: 1501.07115 [astro-ph.HE].

[Pet06] B.M. Peterson. "The Broad-Line Region in Active Galactic Nuclei." In: *Lecture Notes in Physics* (2006), pp. 77–100. DOI: 10.1007/3-540-34621-x_3.

[Pet61] B. Peters. "Primary cosmic radiation and extensive air showers." In: *Il Nuovo Cimento* 22.4 (1961), pp. 800–819. DOI: 10.1007/bf02783106.

[Pet97] B.M. Peterson. *An Introduction to Active Galactic Nuclei*. Cambridge University Press, 1997.

[PG95] P. Padovani and P. Giommi. "The Connection between x-ray and radio-selected BL Lacertae objects." In: *The Astrophysical Journal* 444 (1995), p. 567. DOI: 10.1086/175631. arXiv: astro-ph/9412073 [astro-ph].

[PR14] P. Padovani and E. Resconi. "Are both BL Lacs and pulsar wind nebulae the astrophysical counterparts of IceCube neutrino events?" In: *Monthly Notices of the Royal Astronomical Society* 443.1 (2014), pp. 474–484. DOI: 10.1093/mnras/stu1166. arXiv: 1406.0376 [astro-ph.HE].

[Pri06] P.B. Price. "Attenuation of acoustic waves in glacial ice and salt domes." In: *Journal of Geophysical Research* 111.B2 (2006). DOI: 10.1029/2005jb003903. arXiv: astro-ph/0506648 [astro-ph].

[Pro97] R.J. Protheroe. "High-energy neutrinos from blazars." In: *ASP Conference Series* 121 (1997), p. 585. arXiv: astro-ph/9607165 [astro-ph].

[Pun03] G. Punzi. "Comments on likelihood fits with variable resolution." In: *eConf* C030908 (2003), WELT002. arXiv: physics/0401045 [physics.data-an].

[Pur+13] T. Pursimo et al. "The Micro-Arcsecond Scintillation-Induced Variability (MASIV) Survey III. Optical Identifications and New Redshifts." In: *The Astrophysical Journal* 767 (2013), p. 14. DOI: 10.1088/0004-637X/767/1/14. arXiv: 1302.3409 [astro-ph.CO].

[Rac+10] J.P. Rachen et al. "Radio-submm flares from blazars in a discontinuous jet model." In: *Fermi meets Jansky Proceedings* 2010, (2010), p57. arXiv: 1006.5364.

[Raj03] R. Raja. "A Measure of the goodness of fit in unbinned likelihood fits: End of Bayesianism?" In: *eConf* C030908 (2003), MOCT003. arXiv: physics/0401133 [physics.data-an].

[Ran12] G. Ranucci. "The Profile likelihood ratio and the look elsewhere effect in high energy physics." In: *Nuclear Instruments and Methods in Physics Research* A661 (2012), pp. 77–85. DOI: 10.1016/j.nima.2011.09.047. arXiv: 1201.4604 [physics.data-an].

[RB10] P. Roustazadeh and M. Böttcher. "VHE Gamma-Ray Induced Pair Cascades in Blazars and Radio Galaxies: Application to NGC 1275." In: *The Astrophysical Journal* 717 (2010), pp. 468–473. DOI: 10.1088/0004-637X/717/1/468. arXiv: 1005.2379 [astro-ph.HE].

[Rea00] A.L. Read. "Modified frequentist analysis of search results (the CL_s method)." In: CERN-OPEN-2000-205 (2000).

[San65] A. Sandage. "The Existence of a Major New Constituent of the Universe: the Quasistellar Galaxies." In: *The Astrophysical Journal* 141 (1965), p. 1560. DOI: 10.1086/148245.

[SBR94] M. Sikora, M.C. Begelman, and M.J. Rees. "Comptonization of diffuse ambient radiation by a relativistic jet: The source of gamma rays from blazars?" In: *The Astrophysical Journal* 421 (1994), p. 153. DOI: 10.1086/173633.

[Sch10] O. Schulz. "The design study of IceCube DeepCore : Characterization and veto studies." PhD thesis. Universität Heidelberg, 2010.

[Sch14] K. Schatto. "Stacked searches for high-energy neutrinos from blazars with IceCube." PhD thesis. Universität Mainz, 2014.

[Sch63] M. Schmidt. "3C 273 : A Star-Like Object with Large Red-Shift." In: *Nature* 197.4872 (1963), p. 1040. DOI: 10.1038/1971040a0.

[Sch68] J.L. Schmitt. "BL Lac identified as a Radio Source." In: *Nature* 218.5142 (1968), p. 663. DOI: 10.1038/218663a0.

[Sey43] C.K. Seyfert. "Nuclear Emission in Spiral Nebulae." In: *The Astrophysical Journal* 97 (1943), p. 28. DOI: 10.1086/144488.

[Spa+01] M. Spada et al. "Internal shocks in the jets of radio-loud quasars." In: *Monthly Notices of the Royal Astronomical Society* 325 (2001), p. 1559. DOI: 10.1046/j.1365-8711.2001.04557.x. arXiv: astro-ph/0103424 [astro-ph].

[SPS02] C. Schuster, M. Pohl, and R. Schlickeiser. "Neutrinos from active galactic nuclei as a diagnostic tool." In: *Astronomy and Astrophysics* 382 (2002), p. 829. DOI: 10.1051/0004-6361:20011670. arXiv: astro-ph/0111545 [astro-ph].

[SS14] L. Sironi and A. Spitkovsky. "Relativistic Reconnection: an Efficient Source of Non-Thermal Particles." In: *The Astrophysical Journal* 783 (2014), p. L21. DOI: 10.1088/2041-8205/783/1/L21. arXiv: 1401.5471 [astro-ph.HE].

[Sti+91] M. Stickel et al. "The complete sample of 1 Jansky BL Lacertae objects. I - Summary properties." In: *The Astrophysical Journal* 374 (1991), p. 431. DOI: 10.1086/170133.

[Str+72] P.A. Strittmatter et al. "Compact Extragalactic Nonthermal Sources." In: *The Astrophysical Journal* 175 (1972), p. L7. DOI: 10.1086/180974.

[TG15] F. Tavecchio and G. Ghisellini. "High-energy cosmic neutrinos from spine-sheath BL Lac jets." In: *Monthly Notices of the Royal Astronomical Society* 451.2 (2015), pp. 1502–1510. DOI: 10.1093/mnras/stv1023. arXiv: 1411.2783 [astro-ph.HE].

[TGG14] F. Tavecchio, G. Ghisellini, and D. Guetta. "Structured Jets in BL Lac Objects: Efficient PeV Neutrino Factories?" In: *The Astrophysical Journal* 793 (2014), p. L18. DOI: 10.1088/2041-8205/793/1/L18. arXiv: 1407.0907 [astro-ph.HE].

[Tra01] H.D. Tran. "Hidden broad line seyfert 2 galaxies in the cfa and 12micron samples." In: *The Astrophysical Journal* 554 (2001), p. LL19. DOI: 10.1086/320926. arXiv: astro-ph/0105462 [astro-ph].

[UNO87] M. Aglietta et al. (The UNO Collaboration). "On the event observed in the Mont Blanc Underground Neutrino observatory during the occurrence of Supernova 1987a." In: *Europhysics Letters* 3 (1987), pp. 1315–1320. DOI: 10.1209/0295-5075/3/12/011.

[UP95] C.M. Urry and P. Padovani. "Unified Schemes for Radio-Loud Active Galactic Nuclei." In: *Publications of the Astronomical Society of the Pacific* 107 (1995), p. 803. DOI: 10.1086/133630.

[Vel+12] S. van Velzen et al. "Radio galaxies of the local universe: all-sky catalog, luminosity functions, and clustering." In: *Astronomy and Astrophysics* 544 (2012), A18. DOI: 10.1051/0004-6361/201219389. arXiv: 1206.0031 [astro-ph.CO].

[VPR09] T.M. Venters, V. Pavlidou, and L.C. Reyes. "The Extragalactic Background Light Absorption Feature in the Blazar Component of the Extragalactic Gamma-ray Background." In: *The Astrophysical Journal* 703 (2009), pp. 1939–1946. DOI: 10.1088/0004-637X/703/2/1939. arXiv: 0909.1571 [astro-ph.HE].

[WB99] E. Waxman and J.N. Bahcall. "High-energy neutrinos from astrophysical sources: An Upper bound." In: *Physical Review* D59 (1999), p. 023002. DOI: 10.1103/PhysRevD.59.023002. arXiv: hep-ph/9807282 [hep-ph].

[WH08] S.P. Wakely and D. Horan. "TeVCat: An online catalog for Very High Energy Gamma-Ray Astronomy." In: *International Cosmic Ray Conference* 3 (2008), pp. 1341–1344.

[Wie09] C. Wiebusch (The IceCube Collaboration). "Physics Capabilities of the IceCube DeepCore Detector." In: *International Cosmic Ray Conference* (2009). arXiv: 0907.2263 [astro-ph.IM].

[Wie95] C. Wiebusch. "The Detection of faint light in deep underwater neutrino telescopes." PhD thesis. RWTH Aachen, 1995.

[Wil38] S.S. Wilks. "The Large-Sample Distribution of the Likelihood Ratio for Testing Composite Hypotheses." In: *Annals of Mathematical Statistics* 9.1 (1938), pp. 60–62. DOI: 10.1214/aoms/1177732360.

[Win12] W. Winter. "Neutrinos from Cosmic Accelerators Including Magnetic Field and Flavor Effects." In: *Advances in High Energy Physics* 2012 (2012), p. 586413. DOI: 10.1155/2012/586413. arXiv: 1201.5462 [astro-ph.HE].

[WSL13] N. Whitehorn, J. van Santen, and S. Lafebre. "Penalized Splines for Smooth Representation of High-dimensional Monte Carlo Datasets." In: *Computer Physics Communications* 184 (2013), pp. 2214–2220. DOI: 10.1016/j.cpc.2013.04.008. arXiv: 1301.2184 [physics.data-an].

[ZC08] J. Zornoza and D. Chirkin. "Muon energy reconstruction and atmospheric neutrino spectrum unfolding with the IceCube detector." In: *International Cosmic Ray Conference* 5 (2008), pp. 1275–1278.

ACKNOWLEDGEMENTS

I would like to thank PD Dr. Alexander Kappes for taking the responsibility for this thesis and Prof. Dr. Marek Kowalski and Prof. Dr. Lutz Köpke for the willingness to be the second and third referee. I am also very grateful for Prof. Dr. Matthias Staudacher and Prof. Dr. Heiko Lacker who agreed on very short notice to be the fourth and fifth members in my committee.

A very special thanks goes to Dr. Markus Ackermann who has been a great supervisor during the years in Zeuthen. His deep knowledge, oversight and support has been crucial and his proof reading of the thesis invaluable.

Additionally, I thank David Altmann, Dr. Patrick Berghaus, Marcel Usner and Dr. Juan-Pablo Yanez for more proof reading support.

Many thanks go to Dr. Christian Spiering, who gave me the opportunity to work in the Zeuthen group and also to Prof. Dr Elisa Bernadini, Dr. Dariusz Gora, Prof. Dr. Hermann Kolanoski and Dr. Rolf Nahnhauer who were always open for advice. I am very grateful for the opportunity to visit the South Pole for a few weeks - an experience I will never forget.

I thank all the people from the DESY institute who made the time here run by very quickly and with whom I had many good discussions - be it in physics or outside.

Lastly, my warmest gratitude goes to my parents and to you Kathrin, who have always supported me, especially during the intensive periods.

SELBSTSTÄNDIGKEITSERKLÄRUNG

Hiermit erkläre ich, die vorliegende Arbeit selbständig ohne fremde Hilfe verfasst, und nur die angegebene Literatur und Hilfsmittel verwendet zu haben.

Thorsten Glüsenkamp,
August 2015